Title
Size-related Mechanical Properties of Pure Magnesium

Author
YU, QIAN

Publication Date
2012

Peer reviewed|Thesis/dissertation

Size-related Mechanical Properties of Pure Magnesium

By

Qian Yu

A dissertation submitted in partial satisfaction of the

requirements for the degree of

Doctor of Philosophy

in

Engineering - Materials Science and Engineering

in the

Graduate Division

of the

University of California, Berkeley

Committee in charge:

Professor Andrew M. Minor, Chair
Professor John. W. Morris
Professor Mark D. Asta
Professor Peter Hosemann

Fall 2012

SIZE-RELATED MECHANICAL PROPERTIES OF PURE MAGNESIUM

by

Qian Yu

Abstract

Size-related Mechanical Properties of Pure Magnesium

by

Qian Yu

Doctor of Philosophy in Engineering - Materials Science and Engineering

University of California, Berkeley

Professor Andrew M. Minor, Chair

Magnesium (Mg) is the lightest structural metal in the world. Therefore, Mg alloys hold great promise for weight-saving applications in the automotive and aerospace industries. However, the hexagonal close-packed (HCP) structure of Mg alloys results in limited dislocation plasticity and alternative deformation mechanisms such as deformation twinning that leads to poor formability and mechanical performance of Mg alloys. This inherent low ductility in Mg restricts its broad applicability as a high performance structural material. Further understanding of the fundamental deformation behavior in Mg and its alloys is therefore critical in order to identify potential processing routes that could enable high strength and ductility performance in Mg alloys.

Dimensional refinement is regarded as an efficient way to tune the mechanical properties of materials. To probe the size-related mechanical properties of Mg and also the related fundamental deformation mechanisms, a series of *in situ* transmission electron microscopy nanocompression (TEM), nanotension and nanobending tests were conducted on single crystal and polycrystalline Mg with different crystallographic orientations. The external dimensions of the samples studied ranged from approximately 100 to 900 nm. The effect of crystal size was studied in regard to both deformation twinning behavior and dislocation behavior in single crystal Mg oriented for deformation twinning and basal slip, respectively. The influence of different grain boundary structures on the mechanical properties of polycrystalline Mg were also investigated using bicrystalline Mg specimens with constrained physical dimensions.

For deformation twinning in Mg, it was found that there is strong crystal size effect. The formation of nanotwins was obtained in small specimens resulting in high strength (GPa level), high ductility and significant strain hardening, characteristics that have not been observed before in bulk materials. The nanotwinned structure is explained to be a result of the confined volume and large surface area in the small samples. The nucleation mechanism for deformation nanotwins was studied by computational simulations, and it was found that intrinsic nucleation of deformation twinning in Mg can be influence by the correlated nucleation of twinning dislocations, resulting in a nanotwinned structure.

A strong size effect on the dislocation behavior in Mg was also discovered through the in situ TEM tests. Through systematic investigation three different size regimes were identified where the strength levels and dislocation plasticity were distinctly different. In the largest samples, three-dimensional dislocation plasticity was found; both the microstructure and the mechanical behavior were similar to those found in bulk. As the sample size decreased, two-dimensional dislocation plasticity became dominant, resulting in limited ductility and localized shear along the basal plane. Finally, in the extremely small samples ($\leq$ 100 nm), multiple slip systems were activated under ultra-high stresses and exceptional ductility was reached. Corresponding high-resolution TEM (HRTEM) observations revealed a significant contribution from non-basal slip systems to the entire plastic deformation in these smallest samples. Presumably, the ultra-high stress decreased the anisotropy of the critical resolved shear stress (CRSS) between different slip systems, resulting in non-basal slip that generated a more homogenous deformation and much better ductility. The *in situ* TEM experiments were further compared to detailed molecular dynamic simulations. These observations of the reduction of CRSS anisotropy and ultra-high strength plasticity are discussed in light of future processing opportunities for high strength and high ductility structural materials.

Lastly, the influence of different grain boundary structures on the deformation mechanisms and the mechanical properties of Mg at small scales was investigated by performing *in situ* SEM/TEM compression tests on polycrystalline Mg. Using electron backscatter diffraction (EBSD), it was observed that a low angle grain boundary served neither as an effective source of dislocation nucleation nor an effective barrier to mobile dislocations, resulting in localized shear. By comparison, high angle grain boundaries served

as effective sources for dislocations and deformation twins, resulting in more stable and sustained plastic deformation.

Taken together, the observations and analysis in this thesis give novel and powerful insight into the fundamental plasticity mechanisms in pure Mg. The experiments presented here are both rigorous and creative, generating insightful and powerful conclusions into Mg metallurgy with a high potential impact for light-weighting strategies in structural materials.

Contents

ABSTRACT ----------1

CONTENTS ----------i

LIST OF FIGURES ----------v

LIST OF TABLES ---------- xii

ACKNOWLEDGEMENTS ----------xiii

CHAPTER 1. INTRODUCTION----------1

1.1 Background----------1

1.1.1 Geometry of Magnesium crystal----------2

1.1.2 Dislocations in HCP materials ----------3

1.1.3 Slip modes in HCP materials----------5

1.1.4 Deformation twinning in HCP materials----------9

1.1.5 Mechanical property---------- 15

1.1.5.1 Elastic property ----------15

1.1.5.2 Plastic deformation-Basal slip----------15

1.1.5.3 Plastic deformation-Non-basal slip ----------17

1.1.5.4 Plastic deformation-deformation twinning ----------21

1.1.5.5 Strength and ductility ----------25

1.1.6 Size effect---------- 28

1.1.6.1 Internal dimension refinement-Grain boundary strengthening---
----------28

1.1.6.2 External dimension refinement---------- 30

1.1.7 In situ transmission electron microscope (TEM) mechanical tests ------
---------- 32

1.2 Objectives and achievements of the present research work ----------38

CHAPTER 2. SIZE-RELATED DEFORMATION TWINNING BEHAVIOR IN SINGLE CRYSTAL MG ---------- 41

2.1 Sample preparation ----------42

2.2 Mechanical tests and microstructure analysis ----------46

2.2.1 Bulk material behavior ---------- 47

2.2.2 Submicron samples behavior---------- -------50

2.2.2.1 Nanocompression and Nanotension tests ----------50

2.2.2.2 Nanobending tests ----------60

2.3 Discussion ----------65

2.3.1 Twin induced plasticity ----------65

2.3.2 Molecular dynamic simulation for stress field of nanotwin ----------67

2.3.3 Molecular dynamic simulation for twin nucleation in tension tests-------
----------68

2.3.4 Kinetic Monte Carlo simulation ----------72

2.4 Movies ----------76

2.5 Conclusion ----------77

CHAPTER 3. SIZE-RELATED DISLOCATION BEHAVIOR IN SINGLE CRYSTAL MG ----------79

3.1 Sample preparation----------80

3.2 Initial microstructure ----------82

3.3 Mechanical properties and microstructure analysis ----------83

3.3.1. DFT calculation of ideal strength of Mg ----------83

3.3.2 Mechanical data ----------84

3.3.2.1 Regime 1-“Bulk” behavior ----------87
3.3.2.2 Regime 2-limited ductility----------90
3.3.2.3 Regime 3-Ultrahigh strength ductility ----------92
3.4 Discussion ----------98

CHAPTER 4. IN SITU TEM STUDY ON GRAIN BOUNDARY-MEDIATED PLASTIC DEFORMATION IN POLYCRYSTALLINE MG ----------108
4.1 The grain boundary structures in bulk polycrystalline Mg----------110
4.2 Grain boundary structure of polycrystalline micron/nanpillars ----------112
4.3 In situ SEM/TEM nanocompression----------115
4.3.1 The deformation of micron/nanopillars with low angle grain boundary ----------116
4.3.1.1 In situ SEM mechanical tests ----------116
4.3.1.2 In situ TEM mechanical tests ----------119
4.3.2 The deformation of micron/nanopillars with high angle grain boundary---------- 129
4.3.2.1 In situ SEM compression tests ---------- 130
4.3.2.2 In situ TEM compression tests ---------- 132
4.3.2.2.1 Grain boundary enhanced dislocation plasticity ------- 132
4.3.2.2.2 Grain boundary sliding ---------- 134
4.4 Discussion---------- 136

CHAPTER 5 CONCLUSIONS ---------- 144
5.1 Summery ---------- -144
5.1.1 Size-related deformation twinning behavior ---------- -144

5.1.2 Size-related dislocation behavior ----------144
5.1.3 Grain boundary-mediated plasticity in polycrystalline Mg----------145
5.2 Future work ----------145

REFERENCES ----------147

List of Figures

Figure 1.1 The crystal lattice in HCP. The stacking sequence is in ABAB…
Figure 1.2 The dislocations in HCP structure in Bi-pyramidal construction.
Figure 1.3 The slip planes and directions in HCP Mg
Figure 1.4 A twinning shear event representing bulk material
Figure 1.5 The most common deformation twinning in Mg
Figure 1.6 Periodicity on twin plane $\{10\bar{1}2\}$.
Figure 1.7 Atomic structures of an A-type $\{10\bar{1}2\}$ plane.
Figure 1.8 Changes in stacking sequence of $\{10\bar{1}2\}$ planes associated with twinning in HCP structures.
Figure 1.9. Basal dislocations in a 45-degree compression specimen. ~5% Strain.
Figure 1.10 The typical engineering stress-strain curves for single crystal Mg deformed for basal slip at different temperatures. Bhattacharya et al., 2011)
Figure 1.11 Evolution of the dislocation source for <a+c> pyramidal slip system. a) cross slip of a-dislocation, b) formation of a+c dislocation junction, and c) cross slip of a+c dislocation. (Yoo et al., 2001)
Figure 1.12 The typical deformation twinning structure in Mg.
Figure 1.13 The twin is usually in the lens-shape with a sharp twin tip.
Figure 1.14 The "Hall-Petch" type power-law size strengthening for deformation twinning in single crystal Ti alloy.
Figure 1.15 Channel-die compression tests of pure Mg single crystal: Simulation results and tests (Kelley and Hosford 1968a).
Figure 1.16 Channel-die compression tests of textured Mg rolled plate material, simulation results and tests (Kell and Hosford, 1968b).
Figure 1.17 The plot of yield stresses versus grain size showing the transition from Hall-petch relation to inverse-Hall petch relation
Figure 1.18 The FIB-machined micron pillar before and after compression test.
Figure 1.19 The engineering stress strain curves for micron pillars with different sizes. Smaller is stronger.
Figure 1.20 Bragg Law. Bragg reasoned that constructive interference would

occur only when the path length difference between rays scattered from parallel crystal planes would be an integer number of wavelengths of the radiation.

Figure 1.21 The TEM images captured from the movie for the generation of dislocations in a Al grain.

Figure 1.22 The load-displacement curve corresponding to the test in Figure 1.21.

Figure 1.23 TEM dark field images of a submicron Ni pillar before and after in situ TEM compression test.

Figure 1.24 The setup of the in situ TEM tension test.

Figure 2.1 The crystal orientation of the bulk single crystal Mg rod.

Figure 2.2 The geometry and crystal orientation of bulk compression samples. The loading direction is along [0001].

Figure 2.3 The procedures for preparing a Mg thin film with the electron transparent area at one side. That edge should be perpendicular to [0001] direction.

Figure 2.4 The steps for FIB-milling.

Figure 2.5 The procedures for final cutting in FIB.

Figure 2.6 The TEM bright field images of the samples before test. (a) tensile sample, (b) compression sample, (c) bending sample. The diffraction conditions are all g=[0002].

Figure 2.7 The tensile stress-strain curves of polycrystal Mg with {0001} texture. The grain sizes were different after different number of pass. 4 pass presented the smallest grain size.

Figure 2.8 One typical engineering strain-stress curve for bulk single crystal Mg oriented along [0001].

Figure 2.9 The typical TEM images of the twinning structure in our bulk materials after tension, where the long twinning band can be seen and also the dislocations interaction at the twin boundaries.

Figure 2.10 A TEM bright-filed image of a tensile specimen and its corresponding diffraction pattern.

Figure 2.11 The TEM image shows the position of the tensile sample and the gripper. (a) before alignment. (b) after alignment.

Figure 2.12 The uniaxial compression curves from in situ TEM tensile tests on submicron samples.

Figure 2.13 The uniaxial tensile curves from in situ TEM compression tests on submicron samples.

Figure 2.14 TEM from an in situ compression test of [0001] oriented Mg. A dark field image showing the in situ compression sample post-deformation, the diffraction condition is g= $[\bar{2}112]_t$. The twin boundary is indicated by blue arrows, and the shear displacement is marked in red. One typical HRTEM image of compression sample is inserted showing the $\{10\bar{1}1\}$ twinning structure.
Figure 2.15 mXRD pole figure of the compressed sample.
Figure 2.16 A tensile sample before test (left) and just after the formation of twinned region (right); the diffraction pattern for twinning is inserted.
Figure 2.17 The bright field TEM image that shows an example of the formation of nanotwins and the structure of nanotwinned arrays formed in tension.
Figure 2.18 Fracture event in tensile test, which occurred at the end of the twinned region; the image of the same sample before test is inserted for comparison.
Figure 2.19 High-resolution TEM image of the nanotwins in deformed tensile sample, which revealed even finer twin structures along the edge of the gage section where the spacing between twins could be only several atomic layers as shown in.
Figure 2.20 The bright field TEM image of a bending bar before *in situ* TEM bending test.
Figure 2.21 The bright field TEM image for the crack formation.
Figure 2.22 The formation of the nanotwinned region at the crack tip, which strongly deflected the crack propagation.
Figure 2.23 HRTEM images of nanotwined structure formed in in situ TEM bending tests. Both extension twin and contraction twin can be observed.
Figure 2.24 The "stimulated slip" model for the formation of deformation twinning.
Figure 2.25 The distribution of atomic shear stress σ_{xy} was calculated by molecular static simulation.
Figure 2.26 (a) Stress-strain curve for MD tensile test of $10 \times 10 \times 30$ nm^3 sample with clean surfaces at T = 300 K and under strain rate of 2×10^7 s^{-1}. Mg EAM potential from Ref. 4 was applied. (b) and (c): Nucleation and propagation of extension twin embryo on the edge between two facets at the critical stress obtained from MD simulations. (d): Cross section of a $(2\bar{1}\bar{1}0)$ plane near the sample

surface after twin nucleation. (e): 50 steps of conjugate gradient relaxation were performed to the MD configuration of (d) to remove the effect of thermal fluctuation in order to obtain a clear illustration.
Figure 2.27 (a) MD sample with rough surfaces of $(2\bar{1}\bar{1}0)$ and $(01\bar{1}0)$ and periodic boundary conditions along $<0001>$ directions. (b) Changes of critical nucleation stress of deformation twinning with strain rates for samples with different sizes, surface conditions and EAM potentials.
Figure 2.28 2-D twinning dislocation (TD) model
Figure 2.29 The stress filed produced by a twin from continuum calculations.
Figure 2.30 Kinetic Monte Carlo simulation results of nanotwins and corresponding shear stress field based on model in Figure 2.28. Zero in x-axis is the surface and twin boundaries are plotted in solid lines. Comparing the evolution from left to right, we can clearly see the new TDs nucleated from high stress areas (red color) but no TDs from low stress areas (blue).
Figure 3.1 The crystal orientation of Mg thin film oriented for basal slip.
Figure 3.2 The crystal orientation of Mg samples oriented for basal slip.
Figure 3.3 (a), (b) and (c) are the dark field images showing the dislocation distribution before tension in samples with size ~600 nm, 200 nm and 80 nm, respectively, g=[-1012].
Figure 3.4 The relaxed shear stress-strain relation of Mg on basal plane along [11-20] direction.
Figure 3.5 Quantitative results showing three different regimes of mechanical behavior. (a) typical stress strain curves of samples with different sizes. (b) The plot of yield strength versus the inverse of the sample gage size, d^{-1}, showing the increase of strength with decreasing size. (c) Plot of fracture strain versus sample gage size d showing a significant transition in plasticity when the sample size approaches ~100 nm.
Figure 3.6 The dark field images showing the sample before test, plastic deformed and necking and failure. The sample size is ~800 nm, g=[10-12].
Figure 3.7 The bright field images showing the sample before test and necking and failure. The sample size is ~600 nm, g=[10-12].

Figure 3.8 The dark field images of a sample with size ~300 nm before deformation, after plastic deformed and after fracture. BD=[4-2-23].
Figure 3.9 Bright field images captured from the movie of the in situ tensile test showing the large elongation in a sample with size ~100 nm. The initial image of the sample is on top.
Figure 3.10 The dark field images captured from the movie of a ~90 nm sample showing the motion of a <c+a>dislocation.
Figure 3.11 The dark field TEM images of a <c+a> dislocation under different g vectors.
Figure 3.12 The cone shape failure surface in a sample with size ~ 80 nm. BD=[4-2-23].
Figure 3.13 HRTEM images of the edge of a deformed sample, where many small slip steps can be seen, BD=[2-1-10].
Figure 3.14 The HRTEM image that shows multiple types of dislocations.
Figure 3.15 The HRTEM image of the slip steps at the surface of a deformed sample with size ~90 nm, Beam Direction=[10-10].
Figure 3.16 (a) and (b) are MD samples with two different types of orientations. In both samples, the basal plane has 45^o angle with the tensile axis. In type A (a), one <a>-axis ([2-1-10]) has 45^o angle with tensile axis, so the corresponding slip system has highest Schmid factor of 0.5. In type B (b), one a-axis ([2-1-10]) has 90^o angle with tensile axis, so the corresponding slip system has zero Schmid factor. But the other two a-axis ([-12-10] and [-1-120]) have Schmid factor smaller than 0.5.
Figure 3.17 Stress-strain curves from MD samples with different types of orientations and different sizes.
Figure 3.18 The atomic configurations of samples after deformation. Here different colors means different coordinate number, so the tracks of dislocation lines can be observed clearly.
Figure 3.19 The nucleation of multiple types of dislocations, even though the crystal orientation heavily favors basal slip.
Figure 3.20 Mapping the dislocation plasticity in Mg
Figure 4.1 The bright field images of nanocrystalline Mg and the related diffraction patterns.
Figure 4.2 Dislocations in some nano-sized grains.
Figure 4.3. The SEM image of micron Mg pillars.
Figure 4.4 The bright field images of bicrystalline nanopillars with low angle grain boundary.

Figure 4.5 The dark field image of bicrystalline nanopillar with high angle grain boundary. The related diffraction patterns are shown at right. Rotation angles are about 43 degrees and 52 degrees respectively.
Figure 4.6 The setup of the in situ SEM compression test.
Figure 4.7 load-displacement curve from the in situ SEM compression test on a micron pillar with low angle grain boundary.
Figure 4.8 (a) Left: The SEM image of a deformed micron pillar with low angle grain boundary showing the localized shear. Right: the EBSD orientation map of the pillar shown at left. (b) The EBSD map of the pillar in figure 4.7 and the related misorientation profile.
Figure 4. 9 (a) and (b) The typical engineering stress-strain curves of the nanopillars with low angle grain boundary.
Figure 4.10 The bright field image of the nanopillar before the compression test and the related diffraction patterns.
Figure 4.11 The bright field image captured from the movie to show the dislocation activities from the contact surface.
Figure 4.12 The grain boundary dissociated gradually from top to bottom with the dislocation motion.
Figure 4.13 The nanopillar after compression, bright field image and diffraction pattern; only grain “A” and grain “C” can be seen. Grain “B” disappeared.
Figure 4.14 The bright field image of the nanopillar in the lower case in figure 4.6 before compression test.
Figure 4.15 The bright field images captured from the movie, the dissociation of grain boundary processed gradually.
Figure 4.16 A significant shear step was produced; the offset along the shear direction was about 20 nm.
Figure 4.17 The pillar after compression test. The related diffraction spots from original grain “D” disappeared.
Figure 4.18 The load-displacement curve from a micron pillar with high angle grain boundary.
Figure 4.19 The SEM image of the deformed micron pillar and its corresponding EBSD map.
Figure 4.20 The EBSD orientation map and the misorientation profile of the micron pillar in figure 4.19.
Figure 4.21 Example H1 of nanopillars with high angle grain boundary. The dark field TEM image shows two individual grains, which are labeled as grain “A” and grain “B” and have their related

diffraction spots shown in diffraction pattern.
Figure 4.22 The engineering stress-strain curve corresponding to H1.
Figure 4.23 The evolution of dislocation activities during the compression test (left to rigth).
Figure 4.24 The dark field image of the pillar before the test and the related diffraction pattern that shows the ~52 rotation angle.
Figure 4.25 The related engineering stress-strain curve for the sample in figure 4.17.
Figure 4.26 HRTEM image for the low angle grain boundary, dislocation arrays were observed at the grain boundary.
Figure 4.27 The lattice orientation in the nanopillar shown in figure 4.14
Figure 4.28 A typical HRTEM image for the high angle grain boundary before compression.
Figure 4.29 A typical dark field image for the high angle grain boundary after compression; large number of dislocations can be observed near the grain boundary. The related diffraction pattern is shown at right.
Figure 4.30 Illustration of both diffusional and dislocation accommodation of grain boundary sliding in a polycrystalline solid.

List of Tables

Table 1. Physical properties of magnesium
Table 2: Dislocations in HCP metals (Partridge, 1967)
Table 3: Possible slip systems in HCP metals (Partridge, 1967)
Table 4: Slip systems and the CRSS for Mg
Table 5: Definition of the different orientations used with the channel-die compression tests on single crystals by Kelley and Hosford (1968a)

Acknowledgement

I would like to take this opportunity to express my thanks to all my significant.

I would like to express my sincere gratitude and deep appreciation to my supervisor, Prof Andrew Minor, for his support and guidance and for providing the opportunity to undertake research in a fascinating field. He has always guided me with constructive suggestions, and has provided assistance in many ways. His patience and encouragement helped me through the hard times. I also deeply appreciate his help on developing my academic career and communication. I'd like to also thank Prof John Morris for his useful discussion and advise during my PhD study.

I am grateful for the funding that has allowed me to complete the project. Foremost, the PhD funding from General Motors. In addition, the National Center for Electron Microscopy, Lawrence Berkeley National Lab is generous enough to support experiments. My sincere thanks and gratitude go to Dr Raj Mishra at R&D, General Motors, as well as everybody at NCEM for their technical support.

I am indebted to Dr Liang Qi and Prof Ju Li at MIT for providing their respective models in collaboration. Their models support my research and provide more theoretical understanding for the mechanism study.

Finally, my special thanks go to my parents Zhifu Yu and Qilin Zhao for their support and encouragement. They are my strongest confidence always. Also a huge thank to my husband, Dr Liang Qi, for his understanding, encouragement, support and patience. Life will be easy or hard, but with their strength, there is and will be no bad time.

Chapter 1

Introduction

1.1 Background

Magnesium (*1*) is the lightest structural metal currently available in the world (density 1.738 g/cm^3). It is approximately 34% lighter by volume than aluminum (density of Al is 2.7g/cm^3) and 50% lighter than titanium (density 4.506 g/cm^3) (*2*). Magnesium was first isolated by Sir Humphrey Davy in 1808, by electrolyzing a mixture of magnesia (magnesium oxide, MgO) and mercuric oxide (HgO) (*3*). Mg can be found abundantly. It is the eighth most abundant element in the earth's crust and the third most plentiful element dissolved in the seawater. Mg has a hexagonal close-packed (HCP) structure with c/a ratio of 1.623, which is close to the ideal HCP structure. Some physical properties of Mg are listed in Table 1. Besides the lightweight construction, magnesium offers some other advantages: 1) excellent specific strength. The strength-to-weight ratio of Mg is about 158 kN.m/kg; 2) great damping capacity. Mg has the highest known damping capacity of any structural metal - as much as 10 times greater than steel, titanium, or aluminum, which indicates the excellent ability to absorb vibration; 3) recyclability; 4) dimensional stability. Because of these attractive properties, the increased use of Mg for structural applications would immediately and directly impact areas such as automotive fuel economy and aerospace applications.

Table 1 Physical properties of magnesium

Atomic number	Melting point	Young's modulus	Shear modulus	Poisson ratio
12	632°C	45 GPa	17 GPa	0.29

For structural materials, mechanical properties such as strength and ductility are the critical criteria in application. Firstly strength describes the ability of materials to withstand an applied stress without failure. The yield strength of a material is defined as the stress at which a material begins to deform plastically. It is usually corresponding to the initiation of dislocation motion. Prior to the yield point the material will deform elastically and will return to its original

shape when the applied stress is removed. Once the yield point is passed, plastic deformation will be permanent and non-reversible. For plastic deformation, ductility in metals is determined by the ability of defects to move under an applied stress, usually in the form of dislocation motion, and the ability of the material to store these defects. The high symmetry of cubic crystals readily enables five independent dislocation slip systems that accommodate arbitrary shape changes at relatively low stresses. As a result, for most structural applications where formability is a major requirement one will predominately find cubic crystals such as steel and aluminum alloys or hexagonal close-packed (HCP) Ti where basal, prismatic and pyramidal slip systems with nearly similar critical resolved shear stress (CRSS) values can provide enough slip systems. For Mg alloys with HCP structure, however, the highly anisotropic CRSS values for activation of different slip mechanisms results in limited dislocation plasticity, leading to alternative deformation mechanisms such as twinning(*4-6*). So that although Mg and Mg alloys have many attractive properties, their relative low ductility and low elastic modulus restricts its application as the structural materials.

Generally the engineering strategies, which target to develop the mechanical performance of materials, must be associating with the microstructure engineering. Dimension refinement is one method, which can shape the microstructure evolution to tune the mechanical properties of materials. A profound understanding on the size-related deformation mechanisms, microstructure and their correlation with the mechanical properties of Mg is highly required. However, because of the texture characteristics in polycrystalline bulk Mg and Mg alloys and the ex situ testing methods, the relationship of the dynamic microstructure evolution during deformation process and the corresponding mechanical properties of materials has not been systematically investigated. So presumably, by performing *in situ* electron microscope mechanical study on the single crystal systems with well-defined crystal orientation and polycrystalline Mg with well defined grain boundary structure, we could be able to develop the understanding on the size-related mechanical properties and the fundamental deformation mechanisms in this anisotropic structure and supply new information on physical metallurgy for materials design.

1.1.1 Geometry of Mg crystal

Magnesium has a hexagonal close-packed structure with ABAB.....stacking

sequence , as shown in Figure 1.1. In the hexagonal closest-packed structure, $a_1 = a_2 = a_3 = 2r$ lying on the basal plane and $c = 4(2/3)^{1/2} r$, which is perpendicular to the a axis, where r is the atomic radius of the atom. The sides of the unit cell are perpendicular to the base, thus $\alpha = \beta = 90^o$. The base has a diamond (hexagonal) shape corresponding with $\gamma = 120^o$. The ratio of the unit cell of magnesium is 1.623, which is very close to an ideal HCP lattice (c/a =1.633). There are two atoms associated with each primitive unit cell, one locates at (0,0,0) and another is at $(\frac{2}{3},\frac{1}{3},\frac{1}{2})$. (*7*)

Different from cubic structure, the four-axis system, which is called Miller-Bravais indices is usually used to index the HCP structure, which is based on vectors a_1, a_2, a_3 and c. In principle, $a_3 = -(a_1 + a_2)$. Then the direction can be expressed as $d=ua_1+va_2+ta_3+wc$, where u+v = -t. The close packed directions in HCP is indexed as <2-1-10> (Barrett et al., 1966)(*8*). The Miller indices for the planes can be derived directly by taking the reciprocal of the intercepts of the planes on the respective axis. These values are then reduced to the smallest integers, having the same ratio, which gives the indices of the planes. The conversion of a plane (*hkil*) to a direction representing the plane normal is given by $[uvtw] = [hki\frac{3}{2}(\frac{c}{a})^2 l]$(*8*).

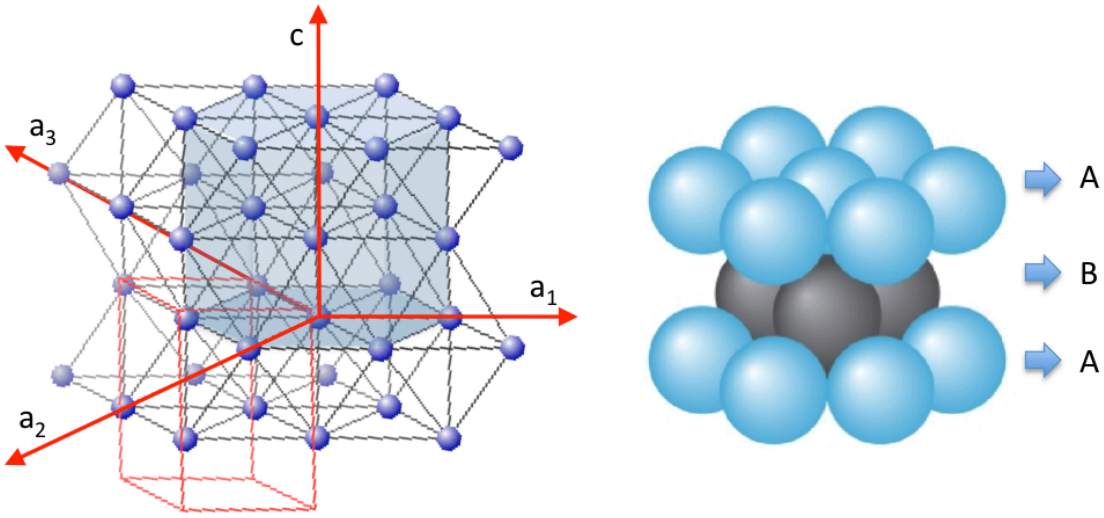

Figure 1.1 The crystal lattice in HCP structure. The stacking sequence is ABAB…

1.1.2 Dislocations in HCP Mg

Berghezan et al., described the dislocations in HCP structure as Bi-pyramidal construction(*9*). This construction set a unit, which has three atoms on the basal plane (0001) and two mirror atoms at $(\frac{2}{3},\frac{1}{3},\frac{1}{2})$ and $(\frac{2}{3},\frac{1}{3},-\frac{1}{2})$ as shown in Figure 1.2. The full dislocations on basal plane are along the sides of the triangular base of the pyramid. In Figure 1.2, the full dislocations are marked out as AB, BC and CA. These are called <a>-dislocation with the Burgers vectors parallel to basal plane and magnitude one "a", the lattice parameter. Another type of full dislocation is called <c>-dislocation, which is perpendicular to the basal plane, as that be labeled by ST or TS. The magnitude of ST and TS is one "c".

In addition, as shown in Figure 1.2, Aδ, Bδ, Cδ, Sδ and Tδ are partial dislocations in the HCP structure. δ is on basal plane. So Aδ, Bδ and Cδ are also on basal plane but with magnitude $\frac{\sqrt{3}}{3}a$. Sδ and Tδ are perpendicular to basal plane with magnitude $\frac{1}{2}c$.

Other type of the partial dislocations are the combination of the latter two types, which is called <c+a> dislocation and can be described by AS= Aδ+ Sδ.

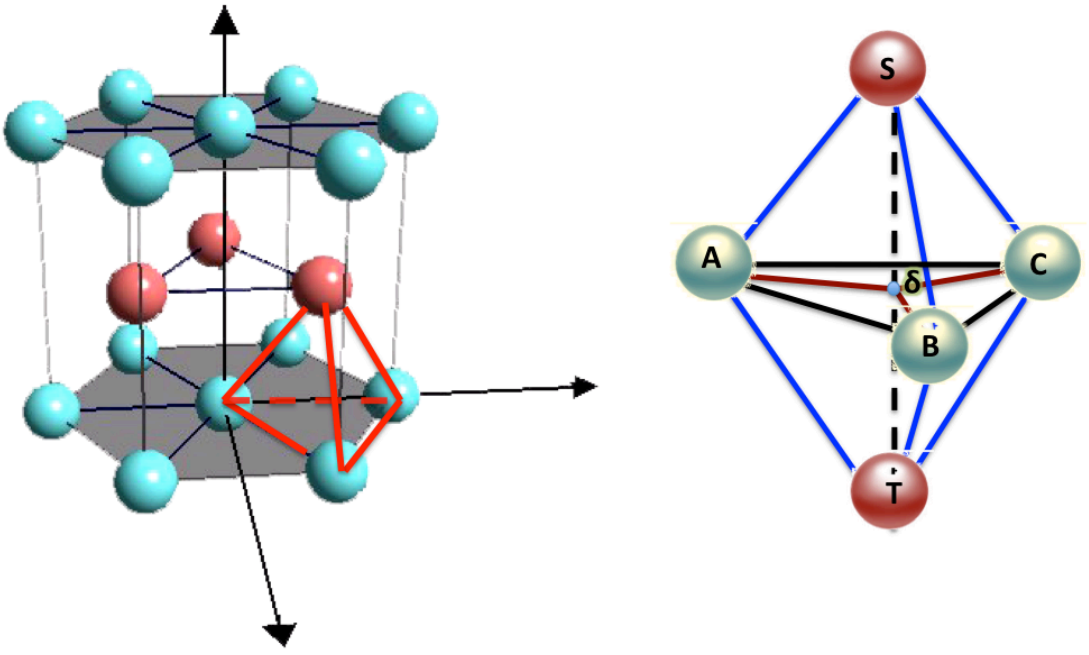

Figure 1.2 The dislocations in HCP structure in the Bi-pyramidal construction.

To sum, all the reported dislocations in HCP metals are listed in Table 2 below by Partridge at 1967(*7*).

Table 2: Dislocations in HCP metals (*7*)

Number	1	2	3	4	5	6
Bi − pyramid designation	*AB* (*perfect*)	*TS* (*perfect*)	*ST + AB* (*partial*)	*A* (*partial*)	*S* (*partial*)	*AS* (*partial*)
b	$\frac{1}{3}<11\bar{2}0>$	[0001]	$\frac{1}{3}<11\bar{2}3>$	$\frac{1}{3}<10\bar{1}0>$	$\frac{1}{2}$[0001]	$\frac{1}{6}<2\bar{2}03>$
b	a_1,a_2,a_3	*c*	*c + a*	$\frac{1}{2}(2a_1+a_2)$	$\frac{c}{2}$	4 + 5
b^2	a^2	c^2	c^2+a^2	$\frac{a^2}{3}$	$\frac{c^2}{4}$	$\frac{a^2}{3}+\frac{c^2}{4}$
Total	3	1	6	3	2	6

1.1.3 Slip modes in HCP Mg

The basal glide system is the easiest one and the most active one for magnesium at ambient temperature, which can be easily explained by the stable dissociation of <a>-dislocations in the basal planes (Legrand, 1984)(*10*). There are three basal slip systems $(0001)<11\bar{2}0>$, but only two of them are independent. In addition, basal slip cannot produce the strain along <c>-axis, so that non-basal slip is highly required for arbitrary shape change of Mg crystal. There are two types of non-basal slip in theory, one is prismatic slip, where the first order slip plane is $(10\bar{1}0)$ and the second order prismatic plane is $(11\bar{2}0)$. Both <a>-dislocation with Burgers vector $\frac{1}{3}<11\bar{2}0>$ and <c>-dislocation with Burgers vector along c axis can slip on the first order prismatic planes. But only <c>-dislocation can slip on the second order prismatic planes. Another type of non-basal slip is pyramidal slip, where <a>-dislocation can slip on the first order pyramidal plane $(10\bar{1}1)$ and <c+a>-dislocation with Burgers vector along

$<11\bar{2}3>$ can slip on both the first order pyramidal plane $(10\bar{1}1)$ and the second order pyramidal planes $(11\bar{2}2)$ *(11)*. Figure 1.3 shows the slip planes and directions in HCP Mg; Table 3 lists the possible slip systems and Table 4 lists the critical resolved shear stress (CRSS) for different slip systems in Mg (*12, 13*). It is obvious that the CRSS for basal slip is about 100 times smaller than that for prismatic and pyramidal slip, indicating the predominance of basal slip during plastic deformation and the remarkable CRSS anisotropy.

However, according to the Taylor criteria, in order to have an arbitrary shape change at least five independent slip systems are required to activate. As we discussed above, Taylor's criterion is usually not satisfied for HCP Mg and Mg alloys because it has only two independent slip systems along <11-20> direction in basal plane. This makes twinning one of the important modes of deformation in magnesium.

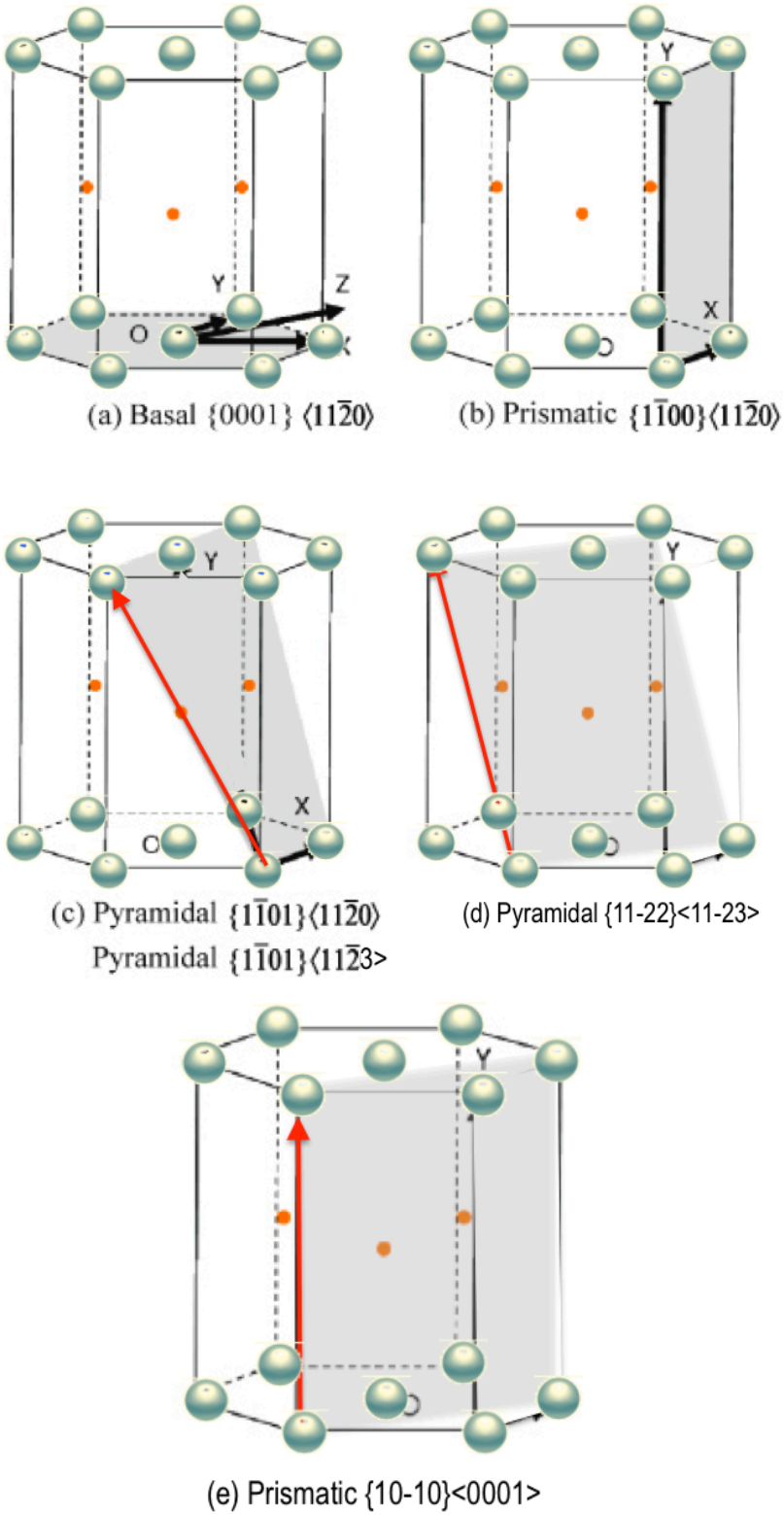

Figure 1.3 The slip planes and directions in HCP Mg

Table 3: Possible slip systems in HCP metals (*7*)

Slip system	*Burgers vector type*	*Slip direction*	*Slip plane*	No. of slip system	
				Total	*Independent*
1	a	$<11\bar{2}0>$	*Basal plane* (0001)	3	2
2	a	$<11\bar{2}0>$	1^{st}*order prism plane* $<10\bar{1}0>$	3	2
3	a	$<11\bar{2}0>$	1^{st}*order pryramidal plane* $<10\bar{1}1>$	6	4
4	$c+a$	$<11\bar{2}3>$	2^{nd}*order pyramidal plane* $<11\bar{2}2>$	3	2
5	c	$< 0001 >$	1^{st}*order prism plane* $<10\bar{1}0>$	3	2
6	c	$< 0001 >$	2^{nd}*order prism plane* $<11\bar{2}0>$	3	2

Table 4: Slip systems and the CRSS for Mg (*12, 13*)

Deformation mode	Basal	Prismatic	Pyramidal-1	Pyramidal-
Slip / Twin plane	(0001)	$\{10\bar{1}0\}$	$\{10\bar{1}1\}$	$\{11\bar{2}2\}$
Slip / Twin direction	$\langle 11\bar{2}0\rangle$	$\langle 11\bar{2}0\rangle$	$\langle 11\bar{2}0\rangle$	$\langle 11\bar{2}3\rangle$
CRSS [MPa]	0.5	40	40	40

1.1.4 Deformation twinning in HCP Mg

Twinning is the region of a crystal, which has undergone displacive transformation, resulting in the new atomic structure with mirror symmetry. The mirror plane is called twinning plane. Deformation twinning forms during mechanical deformation. As we discussed above, the number of the easy-glide systems in HCP metals is not enough to satisfy the Von Mises criteria, which requires at least five independent slip systems to achieve arbitrary plastic deformation. So that in many cases, it is not possible for the strain to be totally accommodated by dislocation motion, instead it is done by the twinning. So deformation twinning is a very important deformation mode in HCP structured metals.

Deformation twinning, like slip, occurs by shear. However, they have significant differences (*14*):

1) For slip, the magnitude of the shear displacement in the slip plane is variable, but it is an integral number of interatomic distance nb, where b is the Burgers vector. For twinning, the shear displacement is a fraction of an interatomic distance and each atomic plane shears relative to its adjacent planes.
2) For twinning, the shear is always directional, which means that the shear in one direction is not equivalent to the shear in the opposite direction. For example, the {111} twin in face centered cubic (FCC) shears along [11-2] direction, but cannot shear along [-1-12] direction. Slip in FCC, however, can happen on {111} plane in either [-110] or the [1-10] direction.
3) Slip rotates the lattice gradually, but twinning reorients the lattice abruptly.

A formal notation system is used to describe twinning in crystalline lattices. Figure 1.4 shows a twinning shear event representing bulk material, the first atomic layer in the top half having undergone twinning shear. There are two planes that remain undistorted during twinning. K_1 is the first undistorted plane, which is also the twinning plane and K_2 is the second undistorted plane. η_1 is the direction of the twinning shear corresponding to K_1 and η_2 is the second characteristic direction. This second direction lies in K_2 plane, which is also perpendicular to the intersection of K_1 and K_2. The plane of shear contains η_1, η_2, and also normal to the planes K_1 and K_2. Depending on whether or not, K_1, K_2, η_1 and η_2 are rational or irrational, twinning can be classified into two groups,

namely twinning of first kind (or type I) and twinning of second type (type II) (*15, 16*). If the K_1 plane is parallel to a lattice plane and η_1 is parallel to a lattice direction i.e., if K_1 and η_2 are rational then one has twinning of the first kind. K_2 and η_1 in this case, need not to be parallel to lattice elements, i.e. they can be irrational (*15*). If the K_2 is parallel to a lattice plane and η_1 is parallel to a lattice row i.e., if K_2 and η_1 are rational and K_1 and η_2 are irrational then one has twinning of the second kind. Twinning of the second kind is observed only in crystals having low symmetry. Here we basically concern the first kind twinning only.

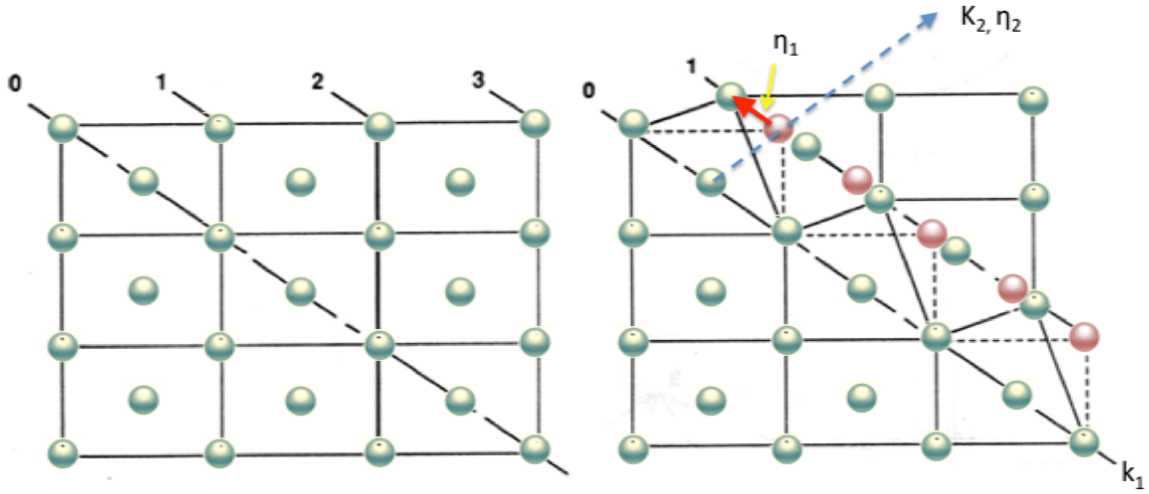

Figure 1.4 A twinning shear event representing bulk material

The most common twinning system in HCP structured metals is $\{10\bar{1}2\}<\bar{1}011>$. The direction of the shear associated with this twin system depends on the c/a ratio. If c/a ratio is greater than $\sqrt{3}$, such as that in zinc and cadmium, $\{10\bar{1}2\}<\bar{1}011>$ twinning system would produce shortening parallel to the c-axis, which is called contraction twin. From other hand, if c/a ratio is smaller than $\sqrt{3}$, such as that in Magnesium and Titanium, $\{10\bar{1}2\}<\bar{1}011>$ twinning produces elongation along <c>-axis, which is then called extension twin.

Another important type of twin in Mg is $\{10\bar{1}1\}<10\bar{1}\bar{2}>$. This type of twin would produce the shortening along <c>-axis in Mg, so it is named contraction twin. It has been commonly found that if we load Mg crystal along <c>-axis, $\{10\bar{1}1\}<10\bar{1}\bar{2}>$ twin would form under compression and $\{10\bar{1}2\}<\bar{1}011>$ twin would form under tension, as shown in Figure 1.5.

Twinning also occurs on other planes, such as $\{10\bar{1}1\},\{1\bar{1}03\},\{1\bar{1}05\}$ and $\{30\bar{3}4\}$. Twinning on the $\{1\bar{1}03\}$ plane in magnesium occurs at low temperatures, and are often obtained at or near the fracture surface (Reed-Hill and Robertson,1957)(*4*). $\{30\bar{3}4\}$ twins are found to be produced in the form of clusters and plastic deformation occurs inside the twin bands (Reed-Hill and Robertson, 1957a)(*4*).

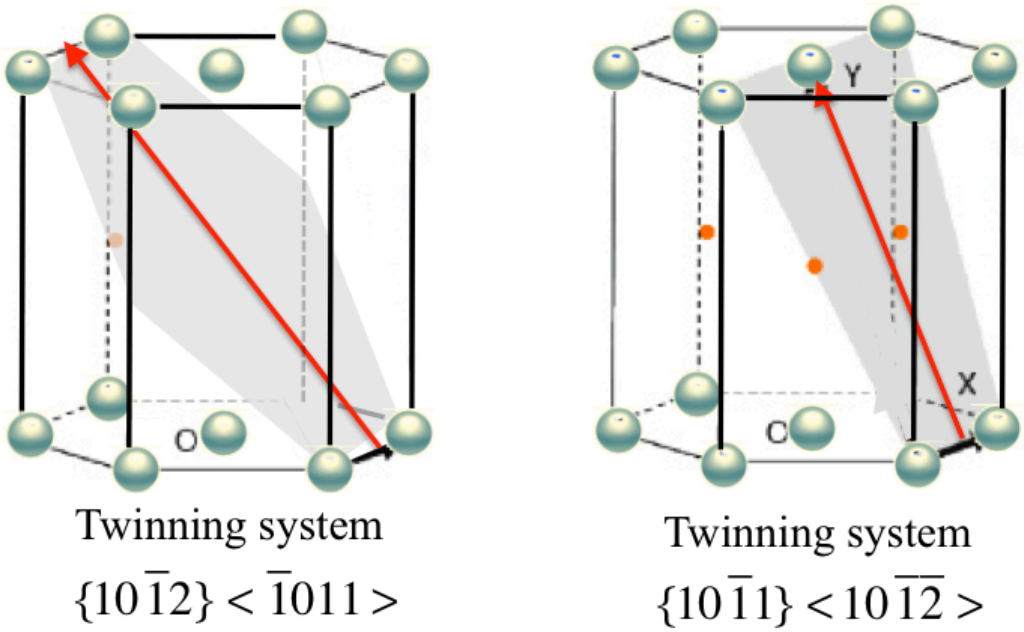

Twinning system $\{10\bar{1}2\}<\bar{1}011>$

Twinning system $\{10\bar{1}1\}<10\bar{1}\bar{2}>$

Figure 1.5 The most common deformation twinning in Mg are $\{10\bar{1}1\}<10\bar{1}\bar{2}>$ and $\{10\bar{1}2\}<\bar{1}011>$ twin. $\{10\bar{1}1\}<10\bar{1}\bar{2}>$ twin would form under compression and $\{10\bar{1}2\}<\bar{1}011>$ twin would form under tension.

It is very important to emphasize that the twinning mechanism in HCP structural materials is much more complicated compared with that in FCC materials. Because of the anisotropic structure, the formation of twinning cannot be achieved by pure shear. Therefore, atomic shuffle is required also to adjust the mismatching on the twin boundary.

Twinning mechanisms were attributed to the glide of defects (TD) called twinning dislocations or twinning disconnections on their twin planes (*17, 18*). The concept of a TD in HCP crystals was first introduced in by Thompson and Millard(*19*), and later in the work by Kronberg(*20*), Westlake et al., (*21*) with its description as a disconnection characterized by a dislocation with the value of "b"

and a step of height "h" by Pond and Hirth(*22*). Different from the dislocations for twinning formation in FCC materials, which are basically partial dislocations, twinning dislocation in HCP usually has the height, which is in the order of several lattice spacing.

The dynamic twinning nucleation mechanism in HCP is still in mystery. Orowan et al., introduced a homogeneous twin nucleation model, where the twin is considered to grow a uniformly sheared lenticular-shaped twin embryo(*23*). Even through homogeneous nucleation theory requires unreasonable high stress, the observation of twinning nucleation from the defect free Zn whiskers proved its possibility indirectly (Price et al.,) (*24*).

More likely, heterogonous nucleation of twinning from a defect site such as grain boundary or surface requires much lower stress. Thompson et al.,(*19*) first introduced this heterogonous nucleation model and proposed that a twin is formed from the non-planar dissociation of a <c>-dislocation, <a>-dislocation and/or <c+a> dislocation, which led to the generation of glissile twinning dislocations in the respective twin plane.

Recently, a new twinning mechanism was reported by studying the atomic structure of an extension twin nucleus in Mg through density function theory and empirical potential (Wang et al., 2009)(*25, 26*). This study proposed that the pole mechanism, the commonly used twinning nucleation theory in FCC materials, could not be simply applied in HCP metals. It also showed that the minimal stable nucleus of twin has to be several atomic layers and partial dislocation is also required in growth of twin.

They latter described more detailed atomic dynamic process in a twinning event in Mg. The basic concept combines twinning dislocation motion and also atomic shuffle at the twin boundary. For $\{10\bar{1}2\}$ twin, one periodicity on twin plane $\{10\bar{1}2\}$ actually contains four atomic layers, as shown in Figure 1.6. We labeled them as AaBb.

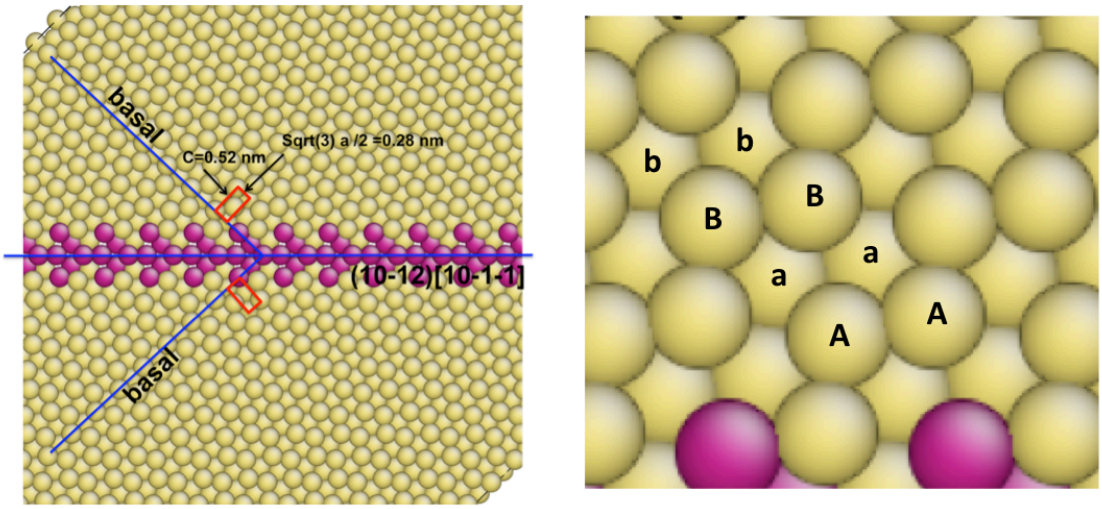

Figure 1.6 Periodicity on twin plane $\{10\bar{1}2\}$, one periodicity on twin plane $\{10\bar{1}2\}$ actually contains four atomic layers Aa-Bb.(*26*)

To build a twin structure, the slip of twinning dislocations is required on each plane to induce a shear that can replace atoms into their corresponding mirror (twinning) positions. As shown in Figure 1.7, twinning dislocation with b_{tw} is needed, which has a relatively small Burgers vector. Atoms on C-layer all move a distance induced by the twinning dislocation, which has the value of b_{tw}; then C-layer becomes the mirror of A-layer. This indicates that the atoms on each layer in the twinned region must shear to the position of atoms on the layer, which is two atomic layers' distance in front, to form twin symmetry. At the same time, the atoms on the twin boundary need to go shuffling.

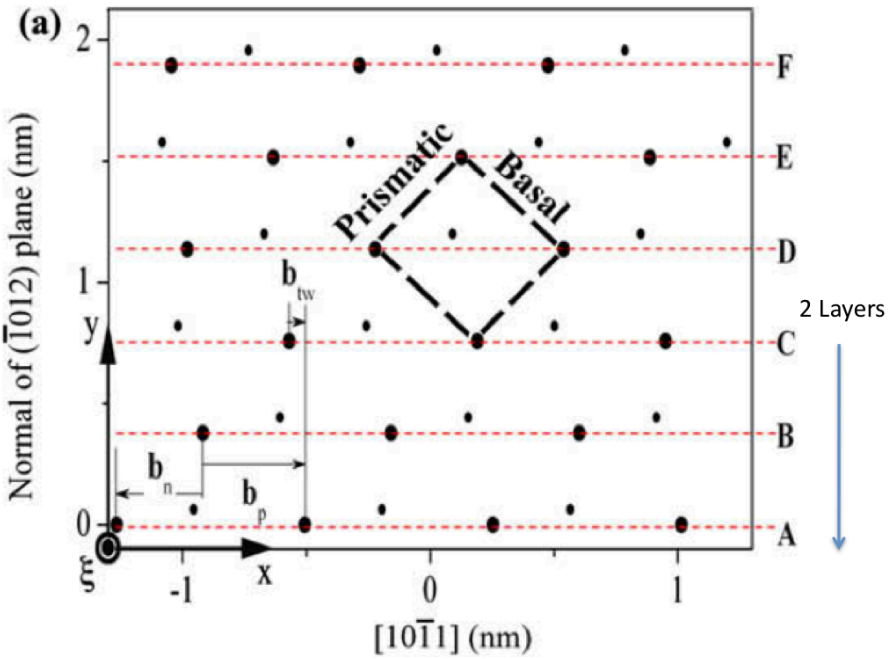

Figure 1.7 Atomic structures of an A-type $\{10\bar{1}2\}$ plane, showing the stacking character of $\{10\bar{1}2\}$ planes. b_{tw} represents one twinning dislocation.(*26*)

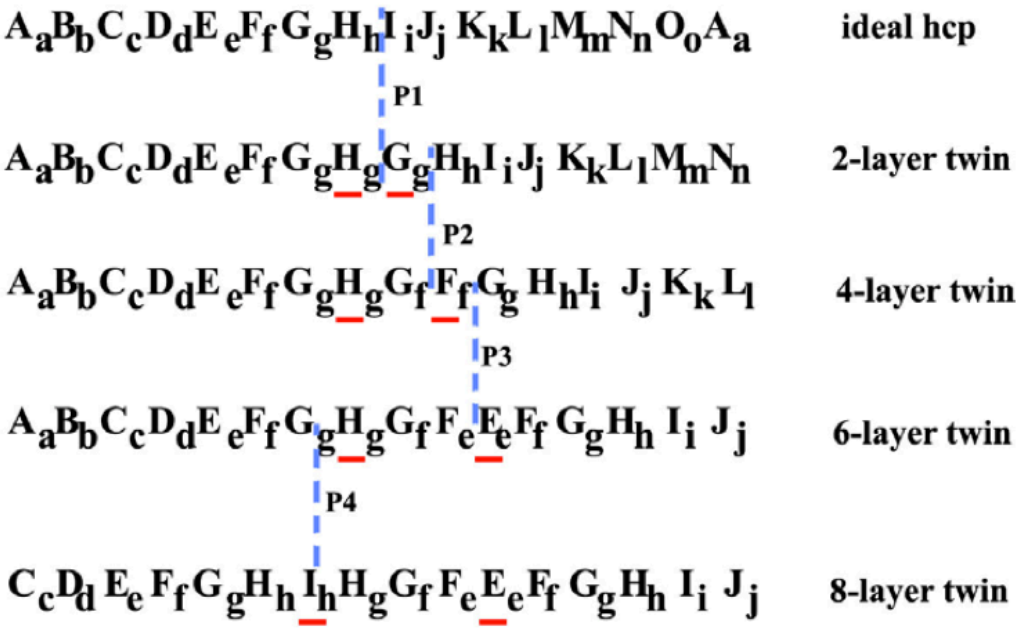

Figure 1.8 Changes in stacking sequence of $\{10\bar{1}2\}$ planes associated with twinning in HCP structures. The dashed lines represent glide planes. With respect to the four operations, an eight-layer twin forms. From a perfect HCP structure, the first three operations are accomplished by shifting the right crystal relative to

the left over planes P1, P2 and P3 corresponding to the glide of a TD b_{tw}. The fourth operation is to shift the left crystal of plane P4 relative to the right corresponding to the glide of a TD btw. The underlines indicate the twin boundary planes (23).

As we can see in Figure 1.8, by the slip of twinning dislocation, atoms on I-layer shear to the new positions, which are the original positions of atoms on G-layer. We can equally consider that I-layer goes back two layers and becomes G-layer, and every layers in the twinned region shear with I-layer. The original "h" needs to be shuffled to become "g" so that mirror symmetry can be produced. With twinning dislocations, the twin will grow thicker following the same principle.

According to the previous studies, the twinning dislocation in HCP materials has no clear definition so far. The twinning dislocation in Wang et al.,'s study is actually called zonal dislocation in the modeling of B Li et al., (*27*) since it contains four atomic layers and has a certain "height".

1.1.5 Mechanical Properties

1.1.5.1 Elastic properties

The elastic modulus is the mathematical description of an object or substance's tendency to be deformed elastically when a force is applied to it. The elastic modulus of an object is defined as the slope of its stress–strain curve in the elastic deformation region. The elastic properties of single crystal Mg vary with different crystal orientations due to the anisotropic structure. Slutsky et al., measured the elastic constants of pure Mg in the temperature range between 4.2K to 300K by using ultrasonic pulse technique(*28*). The value of Young's modulus at room temperature is about 45 GPa.

1.1.5.2 Plastic deformation-Basal slip

Basal slip is the main deformation mode in Mg. Burke et al., (1952)(*29*) reported that the basal slip would dominate the deformation when basal plane is within 6 degree to 72 degree of the tensile direction. They also found that when basal plane is oriented perpendicular to the tensile axis, twinning deformation is the most active one; when basal plane is along the tensile axis the pyramidal slip would be the most favorable deformation mechanism. Basal slip supplies two independent slip vectors, which allow deformation to proceed in the {0001} closed packed plane perpendicular to the c-axis of the hexagonal lattice. The crystals show critical resolved shear stress values (CRSS) for a basal slip system

in the range of 0.5–1.5 MPa(*30*). Basically the easiest one would be activated first during deformation. So that basal slip dominates the plastic deformation in many cases. Large number of basal dislocations can be usually observed in the deformed microstructure, as that shown in Figure 1.9.

Figure 1.9. Basal dislocations in a 45-degree compression specimen. ~5% Strain. (R.T. Tsui, 1967)(*31*). Large number of basal dislocations can be usually observed in the deformed microstructure.

Burke et al., 1952 (*29*) and Hirsch et al., 1965 (*30*) studied the basal slip mechanism in Mg single crystals at room temperature. B. Bhattacharya et al., recently reported their research results on the work hardening behavior in Mg single crystal oriented for basal slip at different temperatures (*32*). As a common phenomena, two stages in the deformation process were found in all; the typical engineering stress-strain curves are shown in Figure 1.10 below (B. Bhattacharya et al., 2011)(*32*): 1) stage A, which is called a long easy glide stage. Work hardening rate is about 2×10^{-5} μ, μ is the shear modulus of Mg, which is about 17 GPa. In this stage, dislocations sources operate simultaneously, and dislocations emitted from these sources trap one another and form dipole bands for both edge

and screw dislocations. The screw dislocations cross slip and then annihilate, leaving the edge dislocations and also the residual of the screw component of the same sign. Because of the dislocation annihilate, the work hardening rate in this stage is low. Dislocations have relatively small interaction radii with the mobile dislocations, so that they have limited contribution to the work hardening. So the flow stress in stage A is mainly controlled by the internal stress field from the edge clusters, residual screw dislocations and also non-primary dislocations. Dislocations undergo easy glide in this stage. 2) Stage B, which is called a rapid hardening stage terminated by failure. The work hardening rate in this stage is about 5×10^{-5} μ. The higher hardening rate can be directly related with the formation of dislocation tangles and stronger dislocation network. Three types of <a>-dislocations with different Burgers vectors interact with each other in the basal plane. The angle between each of them is 120 degree. So that the glide of non-primary dislocations on basal plane gives rise to the formation of hexagonal networks. Some also reported the formation of deformation twinning in this stage, which would also contribute to the high work hardening rate.

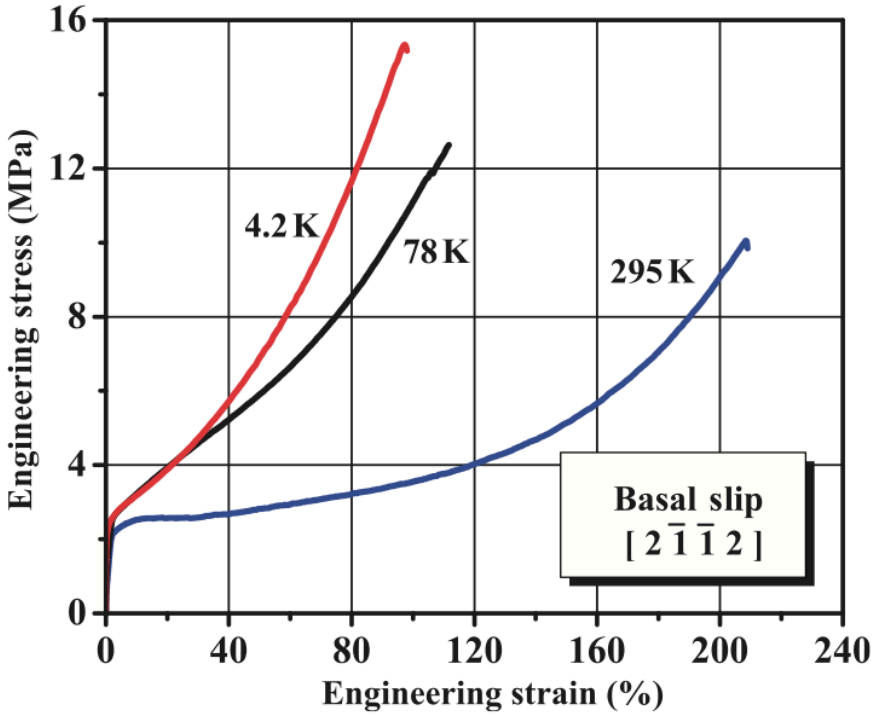

Figure 1.10. The typical engineering stress-strain curves for single crystal Mg deformed for basal slip at different temperatures. (B. Bhattacharya et al., 2011) (*32*)

1.1.5.3 Plastic deformation-Non-basal slip

As we just discussed above, basal slip is the primary slip system in Mg, which can be accomplished by two independent slip systems. However, in order to satisfy the Von-Mises criterion for polycrystal deformation and to explain the reasonably good ductility of polycrystalline Mg alloys, non-basal slip must be taken into account. The non-basal slip should be able to accommodate the strain change along c-axis, because basal slip does not induce this strain. Strain along the <c>-axis is very important in order to explain the good ductility of magnesium polycrystals especially in compression (Groves et al., 1963)(*33*).

<c+a> slip

<c+a> slip is the important deformation mode in Mg, which can induce strain along both <a> and <c>-axis. It has been reported that the secondary pyramidal slip $(11\bar{2}2)<11\bar{2}3>$ (<c+a> slip) plays an important role in plastic deformation of polycrystalline magnesium and its alloys (Agnew et al., 2002)(*34*). Stohr et al., 1972 (*35*); Obara. et al., (1973) (*36*) studied this secondary pyramidal slip system in magnesium in compression along the <c>-axis and Ando et al., (2000) studied this in tension along the $<11\bar{2}0>$ direction (*37*). Obara et al., found that $(11\bar{2}2)<11\bar{2}3>$ <c+a> slip is actually the dominant slip mode in Mg in a wide range of temperature if compression load is applied along <c>-axis (*36*). The work hardening rate is much higher than that for basal slip.

From recent simulations, it is realized that their contribution to the nucleation and growth of deformation twinning is also significant where they are considered as zonal dislocations that can generate shear with both <a> and <c> components. However, since one independent slip system must have its own independent dislocation source, what are the source and operation mechanisms for <c+a> slip become a critical issue that directly questions the validity of the five independent <c+a> slip systems. Many efforts have been made to solve these problems. For example, Yoo et al., proposed a possible source mechanism for non-basal <c+a> slip dislocations based on the formation of an attractive junction between glissile <a> and sessile <c> dislocations from the prismatic plane into a pyramidal plane (*38*). As shown in Figure 1.11, one possible source mechanism for <c+a> dislocations of a pyramidal slip system is proposed.

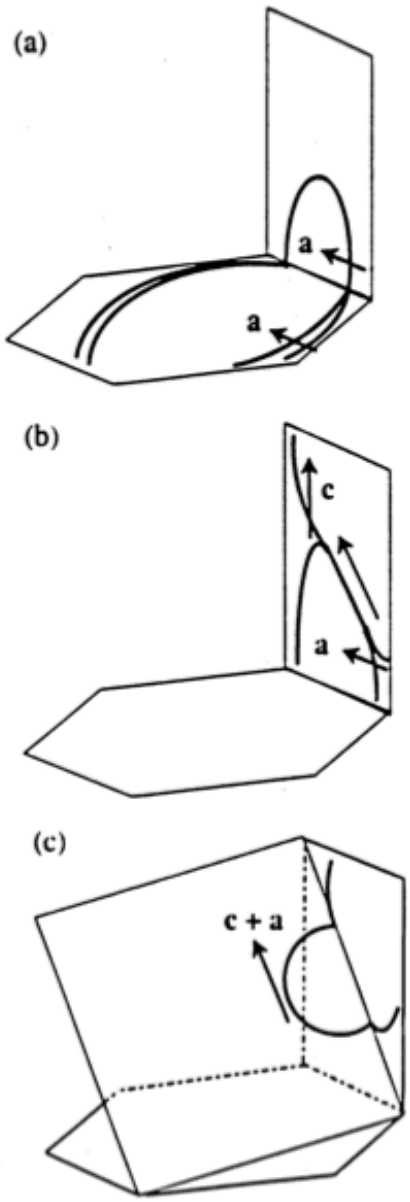

Figure 1.11. Evolution of the dislocation source for <a+c> pyramidal slip system. A) cross slip of <a>-dislocation, b) formation of <a+c> dislocation junction, and c) cross slip of <a+c> dislocation. (Yoo et al., 2001)(*38*)

In this mechanism, the first step is the cross slip of an <a>-dislocation from the basal plane to a prismatic plane ☒. Then it would form a <c+a> dislocation junction along its near-screw orientation when an active prismatic slip dislocation interacts with a sessile <c>-dislocation. The <c>-dislocation here is considered as a pre-existing dislocation in the material lying on the prismatic plane. The

sequent cross slip of the <c+a> screw dislocation from $(10\bar{1}0)$ plane to $(11\bar{2}2)$ plane happens afterwards. Since the c/a ratio for Mg is 1.624, there is no resolved shear stress to assist the cross slip from the basal plane to prismatic plane, so there must be attractive force between a <c>-dislocation on the prismatic plane and the basal <a>-dislocation to pull the <a>-dislocation out of the plane. However, because that the <c+a> slips on $\{11\bar{2}2\}$ plane with $<11\bar{2}\bar{3}>$ slip direction are associated with the largest Burgers vector and the smallest interplanar spacing, their importance in plastic deformation usually comes after <a> and <c> slip, which makes it difficult to experimentally isolate the <c+a> dislocation activities, so that there is still lack of direct experimental observation of its operation.

Because of the large Burgers vector, the dissociation of <c+a> dislocations may happen. Frank and co-workers, (Frank et al., 1953) (*39*) suggested dissociation of a <c+a> type dislocation into two partials of type $<20\bar{2}3>$. Liang et al., (1986) have done a series of atomistic simulation studies of HCP metals to understand core structure of different dislocations (*40, 41*). Minonishi et al., (1982) (*42*) and Morris et al., (1997) (*43*) also reported the similar reaction for the dissociation of this type of dislocation. They suggested two possible types of dissociations. First one was the dissociation of a <c+a> dislocation into two <c+a> types of dislocations with a stacking fault in the $\{11\bar{2}2\}$ glide plane, which can be expressed as:

$$\frac{1}{3}[11\bar{2}3] \rightarrow \frac{\eta}{3}[11\bar{2}3] + \frac{1-\eta}{3}[11\bar{2}3] + SF(11\bar{2}\bar{2})$$

The other was dissociation of <c+a> dislocation into $\frac{1}{3}[10\bar{1}0]$ and $\frac{1}{3}[01\bar{1}3]$ type dislocations with a stacking fault in the basal plane.

<c+a> dislocation may also dissociate into a <a>-dislocation and a <c> dislocation.

Prismatic slip

Prismatic slip $\{1\bar{1}00\}<11\bar{2}0>$ is also reported in HCP Mg. Reed-Hill et al., 1957 (*4*) and Ward Flynn et al., 1961 (*44*) found the operation of the first order prismatic slip at room temperature in single crystal Mg with the loading direction parallel to the basal plane, Especially at the corner of the grain boundaries.

However, prismatic <a>-slip cannot induce the strain along <c>-axis, so that pyramidal slip on $\{10\bar{1}1\}$ would actually take place at higher temperature.

The CRSS for the first order prismatic <a>-slip is about 40 MPa at room temperature as listed in Table 4. Couret et al., reported that the CRSS for prismatic slip in Mg has strong temperature dependence. Comparing with basal slip, the dislocation core on the prismatic plane is metastable due to the high stacking faults energy (Couret et al 1985)(*45*).

Prismatic <c>-slip is also possible theoretically. The Burgers vector of <c>-dislocations are along [0001] direction. They can induce the strain along <c>-axis. The experimental observation on the prismatic <c>-slip is rare, mainly because of the high general stacking fault energy required, which directly limits the mobility of <c>-dislocations in Mg. However, <c>-dislocations have been experimentally observed in some studies. Morozumi et al., (1976) and Angrew et al., (2005) studied the dislocation structure in a Mg alloy by using TEM analysis. Large number of <c>-dislocations were observed, especially at the grain boundary regime(*46, 47*).

1.1.5.4 Plastic deformation- deformation twinning

As we discussed above, the most active slip mode in Mg is basal slip, which however, cannot induce strain change along <c>-axis. Therefore, twinning deformation in Mg is the very important deformation mode at ambient temperature. The typical structure of twin in Mg is shown in Figure 1.12 below. They usually have a large length-to-thickness ratio. The tip of the twin is in a lens-shape, as shown in Figure 1.13, where high density of dislocations are generated from the tip due to the high local-stress concentration. Dislocation density within the twin is usually higher than that in the matrix. Small twin embryos can also be observed when the strain is less than 5%. The structure of the twin embryo is shown in the bright field TEM image in Figure 1.13 b.

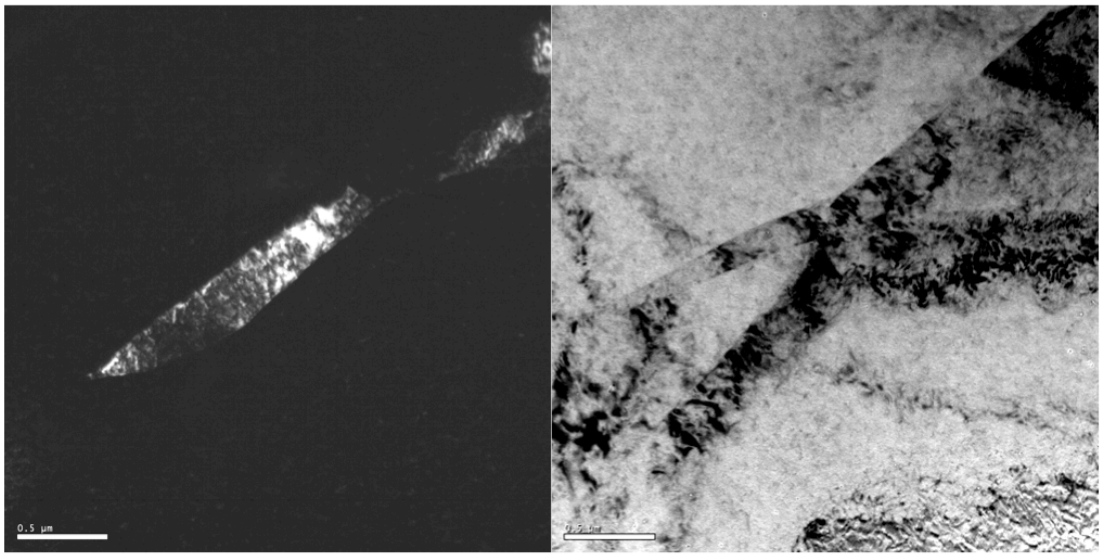

Figure 1.12. A typical deformation twinning structure in Mg.

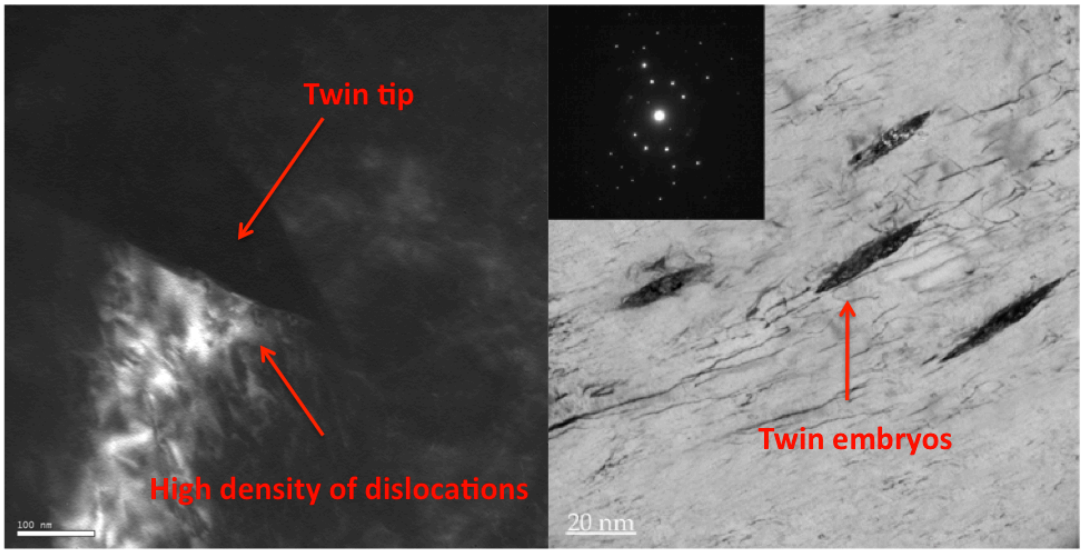

(a) (b)

Figure 1.13. (a) The twin is usually in the lens-shape with a sharp twin tip; dislocation density there is higher due to the stress concentration. (b) Twin embryos in Mg are shown in the right bright field image.

The size-related twinning behavior in HCP materials is very different from that of FCC metals. For FCC metals, with decreasing grain size it becomes more difficult to deform by twinning in the coarse-grain size range, but twinning becomes easier once the grain size is smaller than 100 nm, although twinning

may become difficult again when the grain size is too small. The corresponding size regime where the deformation twinning disappears again is usually 5-10 nm (*48*). In contrast, coarse-grained HCP metals usually need twinning to accommodate plastic deformation in addition to dislocation slip due to the lack of sufficient slip systems. However, twinning is rarely observed in nanocrystalline Mg as the grain size reduced to about 100 nm. The high stacking faults energy might be one important reason. Wu et al., reported the formation of deformation twinning in nanocrystaline Mg-10 at.% Ti alloy, where the stacking faults energy is reduced by making alloy.(*49*)

In single crystal HCP Ti, strong crystal size effect on deformation twinning is reported by Yu et al., (*50*). By employing the state-of-the-art *in situ* Transmission electron microscopy and nanomechanical testing on Ti alloy single-crystal pillars to investigate the spatial-temporal correlations and effect of sample size on deformation twinning. Interestingly, deformation twinning subsided and gave way to ordinary dislocation plasticity when the sample diameter is reduced to below ~1μm, a mechanism transition that is easily accessible in practice. In addition, accompanying the deformation mechanism transition, the strength of the materials was observed to saturate, too. This suggests that by simply reducing the sample dimension, the strain bursts resulting from deformation twinning can be replaced by continuous plastic flow at theoretical high level stress, a feature that are highly desirable for plastic forming and structural applications.

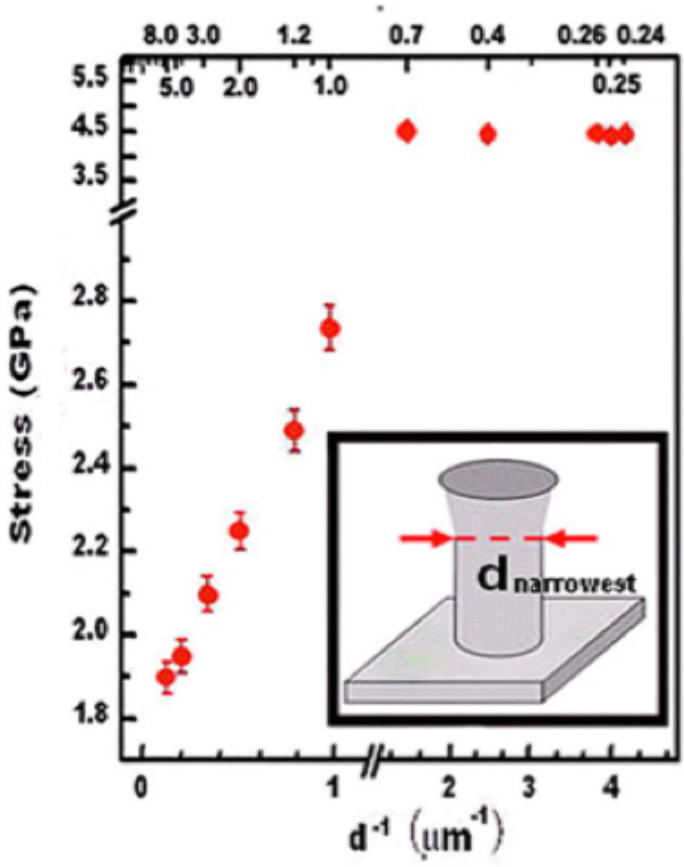

Figure 1.14 The "Hall-Petch" type power-law size strengthening for deformation twinning in single crystal Ti alloy.(*50*)

A general mathematical model is built to explain the "Hall-Petch" type power-law size strengthening for deformation twinning, its anomalously high strengthening coefficient, and its breakdown. Figure 1.14 illustrates this phenomenon. The model is inspired by the "stimulated emission" concept in laser (light amplification by stimulated emission of radiation) theory: if ordinary dislocation plasticity is like normal light, then deformation twinning is analogous to laser.

However the critical size for transition should be material dependent. Micropillar compression results for single crystal Mg oriented for twinning found no twinning in samples from about 2 to 10 microns in diameter. Both Lilleodden(*51*) and Byer et al.,(*52*) tested pure Mg single crystal pillars with the same [0001]

crystal orientation. Pyramidal and <c> type dislocations were observed in the deformed pillars, but not twins. Here the size regime where the deformation twinning vanished is larger than that observed in the Ti alloy, but the trend of the deformation mode transition from deformation twinning dominated to dislocation plasticity dominated is similar, since larger Mg single crystals would be expected to twin in this orientation. But it was also observed that deformation twinning reoccurred during compression of Mg in extremely small samples with diameters around 200 nm. Ye et al., reported the formation of deformation twinning by performing in situ TEM nanocompression tests on submicron single crystal pure Mg and Mg-0.2.wt%Ce alloy samples oriented for deformation twinning (*53*). The sample sizes were around 200 nm diameter. Twinning deformation was observed including the migration of the twin boundary until almost the entire pillar had been converted to a twinned orientation. The critical stress for twinning nucleation in this case was approximately 1.26 GPa, demonstrating the significant size effect associated with the twining mechanism, consistent with what had been observed previously in the Ti–Al alloy.

1.1.5.5 Strength and ductility

Kelley et al., 1968 tested a series of singe crystal Mg oriented from A to G by channel-die compression tests, see Table 5 for orientations. (*54*)

Different deformation modes were activated in the single crystal tests depending on the respective orientations of specimens. This allows for selectively identifying the hardening parameters for a particular slip mechanism.

Table 5. Definition of the different orientations used with the channel-die compression tests on single crystals by Kelley and Hosford (1968a)(*54*)

Test	Loading (1)	Constraint (2)
A	⟨0001⟩	⟨10$\bar{1}$0⟩
B	⟨0001⟩	⟨1$\bar{2}$10⟩
C	⟨10$\bar{1}$0⟩	⟨0001⟩
D	⟨1$\bar{2}$10⟩	⟨0001⟩
E	⟨10$\bar{1}$0⟩	⟨1$\bar{2}$10⟩
F	⟨1$\bar{2}$10⟩	⟨10$\bar{1}$0⟩
G	⟨0001⟩ at 45°	⟨10$\bar{1}$0⟩

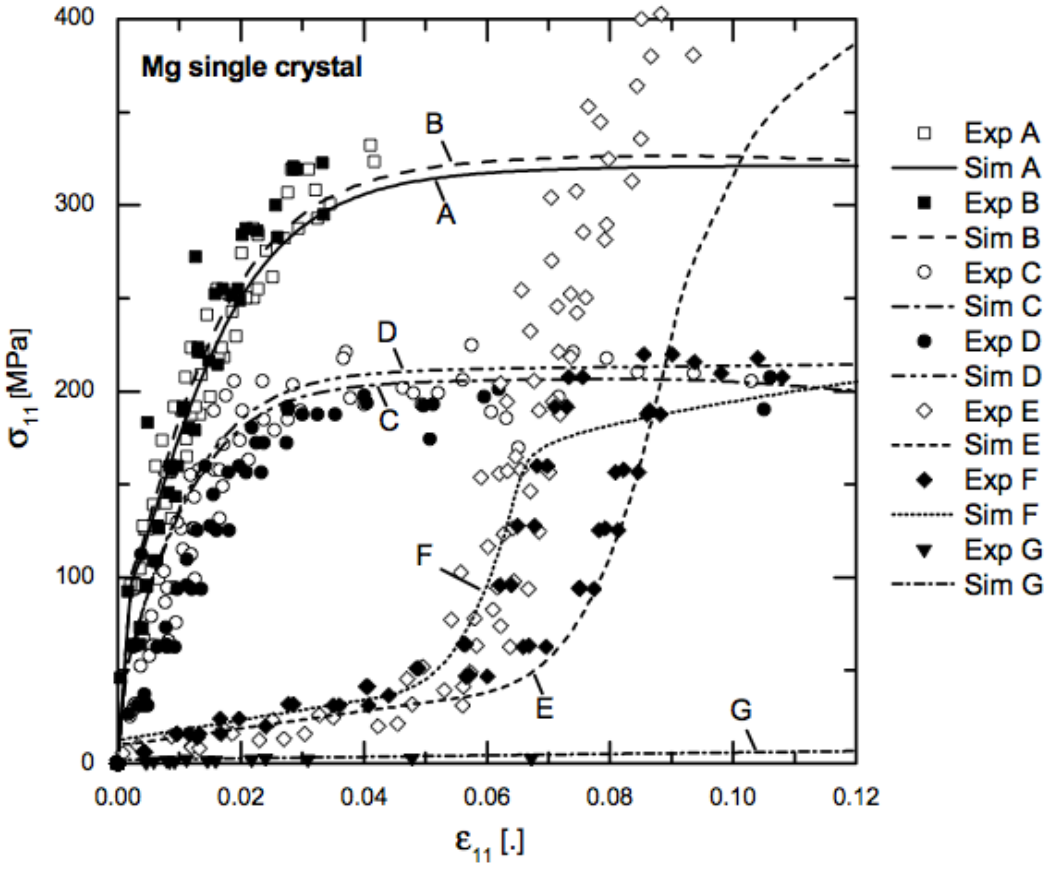

Figure 1.15 Channel-die compression tests of pure Mg single crystal: Simulation results and tests (Kelley and Hosford 1968a).(*54*)

Figure 1.15 shows the stress-strain curves for different samples. A and B shows much higher flow stress. And from the related microstructure analysis, only the curves A and B show more than one family of slip mechanisms acting at the same time, namely prismatic and pyramidal slip. Curves C and D are dominated by prismatic slip and curve G by basal slip over the whole range of strain. For orientations E and F the transition from twinning to pyramidal slip occurs within a very small range of strains. Orientations E and F favor twinning deformation resulting in an elongation of the c-axis. Because of its low critical resolved shear stress (CRSS), tensile twinning is easily activated; elastic deformation increases the stresses until they reach the CRSS of pyramidal glide, which explains the sudden increase of stresses at about 0.06 strain.

They also studied the mechanical behavior of polycrystalline Mg with different textures. As shown in Figure 1.16, in the specimens of orientations LT and TL, about 60% of the plastic deformation results from prismatic slip with yield

strength at about 35 MPa, and highest flow stress at about 150 MPa. For the specimensof orientations SL and ST, pyramidal slip dominates, which shows yield strength at about 40 MPa, and highest flow stress at about 260 MPa. Basal slip contributes nearly equally by about 40% and prismatic slip by about 20%. The low yield strength and hardening for the orientations LS and TS is due to the activation of tensile twinning (CRSS at about 5 MPa), which contributes to the plastic deformation by about 40%, and the sudden increase of stresses beyond 5% strain results from the saturation of twinning and the further activation of pyramidal slip.

Compression Direction	Constraint Direction	Corresponding Polycrystalline Orientations
[0001]	$<10\bar{1}0>$	SL, ST
[0001]	$<1\bar{2}10>$	
$<10\bar{1}0>$	[0001]	LT,
$<1\bar{2}10>$	[0001]	
$<10\bar{1}0>$	$<1\bar{2}10>$	
$<1\bar{2}10>$	$<10\bar{1}0>$	

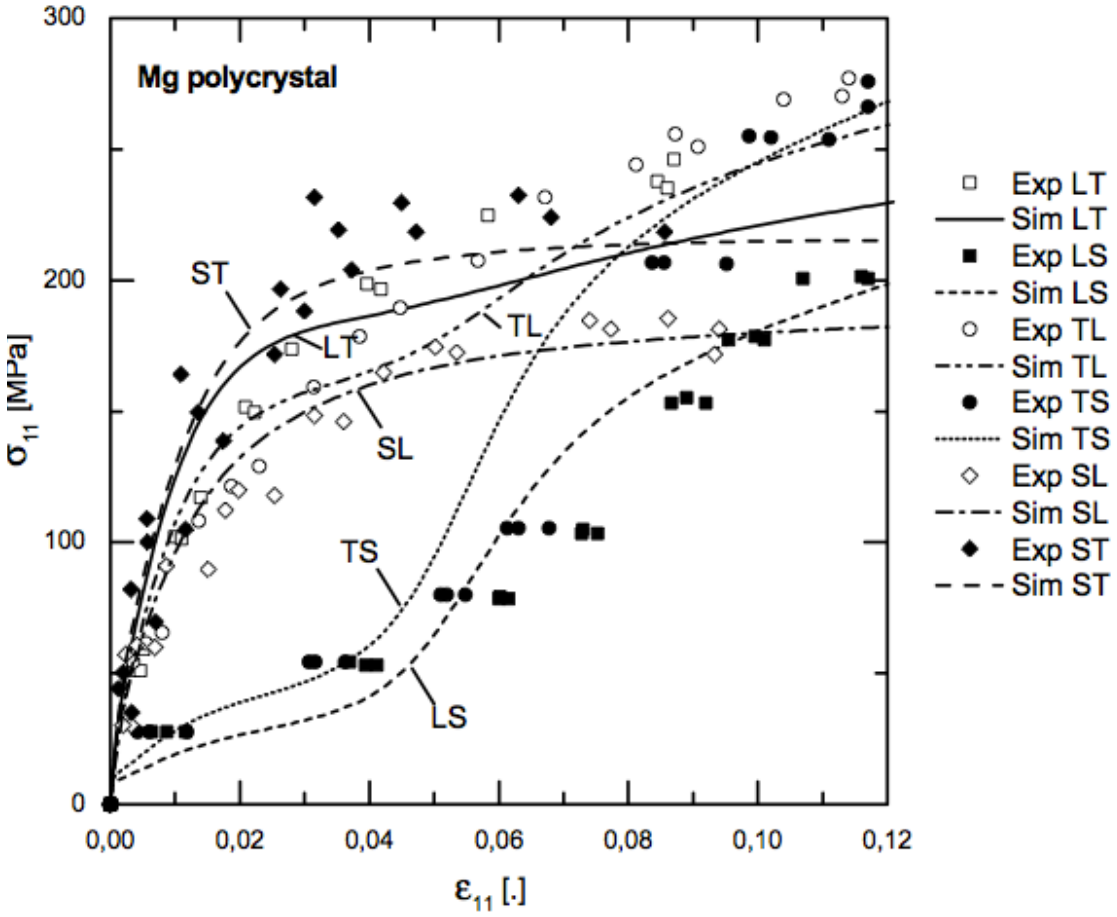

Figure 1.16 Channel-die compression tests of textured Mg rolled plate material, simulation results and tests (Kelley and Hosford, 1968b).(*54*)

1.1.6 Size effect

Mechanical properties of materials will change with their internal and external dimensions. Generally, external dimension is determined by the sample size. Internal dimension usually determined by grain sizes. Phase boundaries and twin boundaries can also tune the internal dimension. As we mentioned, the yield strength of materials is defined as the stress at which a predetermined amount of permanent deformation occurs, which is the term that directly related to the initiation of dislocations movement. The ductility of materials is usually determined by the dislocation activities also. Both of them are size-dependent.

1.1.6.1 Internal-dimension refinement-grain boundary strengthening

Once the stress reaches the CRSS of the dislocation, dislocation starts to move.

The grain boundaries act as pinning points impeding further dislocation propagation. Since the lattice structure of adjacent grains differs in orientation, it requires more energy for a dislocation to change directions and move into the adjacent grain. The grain boundary is also much more disordered than inside the grain, which also prevents the dislocations from moving in a continuous slip plane. So impeding the dislocation motion will hinder the onset of plasticity and hence increase the yield strength of the material.

The details are described below. Under an applied stress, pre-existing dislocations and the dislocations generated by Frank–Read Sources will move through a crystalline lattice until encountering a grain boundary, where the large atomic mismatch between different grains creates a repulsive stress field to oppose continued dislocation motion. As more dislocations propagate to this boundary, dislocation 'pile up' occurs and they are unable to move past the boundary easily. As dislocations generate repulsive stress fields, each successive dislocation will apply a repulsive force to the previous dislocation against the grain boundary. These repulsive forces act as a driving force to reduce the energetic barrier for diffusion across the boundary, such that additional pile up causes dislocation diffusion across the grain boundary, allowing further deformation in the material. Decreasing grain size decreases the amount of possible pile up at the boundary, increasing the amount of applied stress necessary to move a dislocation across a grain boundary.(*55*) Thus, the materials with smaller grains will be stronger. This is demonstrated by the Hall–Petch equation:

$$\sigma = \sigma_0 + kd^{-0.5}$$

where σ is the yield strength, k is a constant and d is the grain size.

The Hall–Petch relation was experimentally found to be an effective model for materials with grain sizes ranging from 1 millimeter to 1 micrometer. However, experiments on many nanocrystalline materials demonstrated that if the size of the grains reduced to a critical value, which was typically less than 100 nm, the yield strength would either remain constant or decrease with decreasing grain size. This phenomenon has been named the inverse Hall–Petch relation. Several possible reasons for Hall-petch to inverse Hall-petch relation transition were proposed. The basic concern is that the dislocation activity would be very hard to achieve in extremely small grains, so that other deformation modes, such as grain boundary sliding or grain rotation might take place and dominate the plastic

deformation. As a consequence, strain softening may happen instead of strain hardening. Other explanations that have been proposed to rationalize the apparent softening of metals with nano-sized grains include poor sample quality and the suppression of dislocation pileups (*56*). One example of the Hall-petch relation and inverse-Hall petch relation is shown in Figure 1.17.

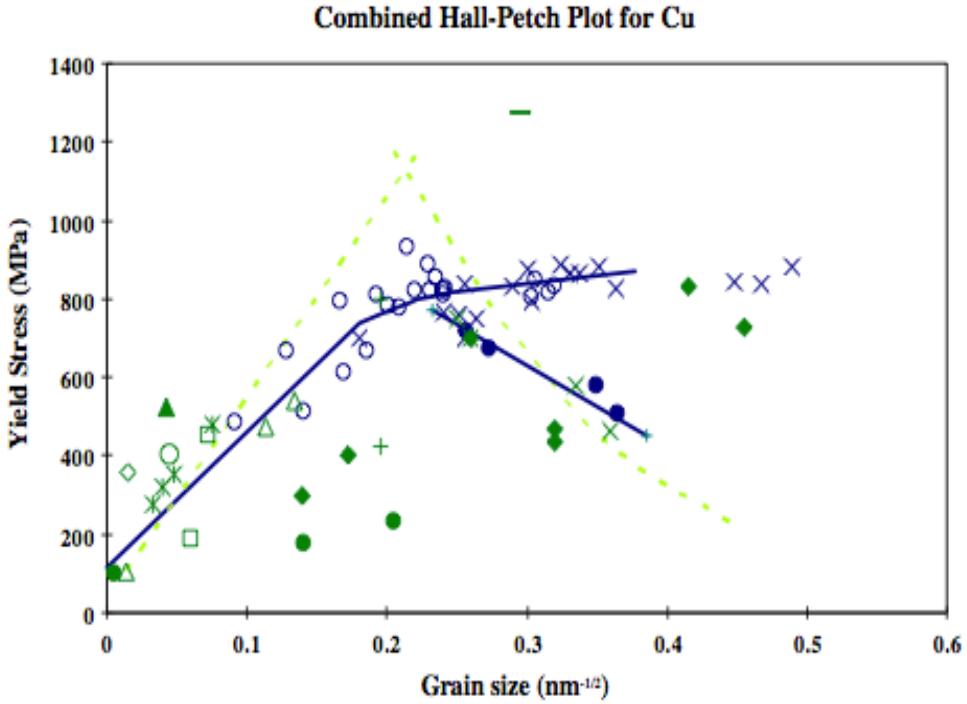

Figure 1.17 The plot of yield stresses versus grain size showing the transition from Hall-petch relation to inverse-Hall petch relation. (*56*)

1.1.6.2 External dimension refinement

The strength and plasticity can be also affected by the external geometry of materials. For example, the near ideal strength of materials was obtained in micron-sized single-crystal metallic whiskers but unfortunately with little plasticity. Similar to those high-perfection whiskers, significant strengthening, where the yield strength could be 5-10 times higher than that in bulk materials, is also achieved in Focused ion beam (FIB)-machined micro/submicro-sized single crystal samples (*57-60*). One example of the micron pillars and the deformed micron pillar is shown in Figure 1.18. Different from that in whiskers, here the pre-existing defects in the initial crystals can carry plasticity, but usually in the

form of intermittent strain bursts, as shown in the engineering stress-strain curves in Figure 1.19.

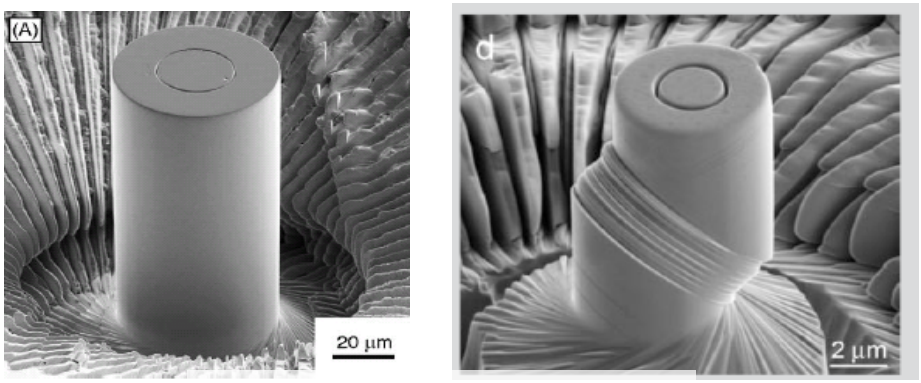

Focused ion beam-machined

Figure 1.18 The FIB-machined micron pillar before and after compression test.(*61*)

Dislocation-source truncation mechanism and exhausting hardening mechanisms are proposed to explain the observed size effects (*56*). For source truncation mechanism, it is proposed that the length of free arm dislocation source is directly regulated by the sample dimension as the sample dimension reduces to the same order of that of line defects, so that $L \propto \alpha D$, where L is the length of dislocation source, D is the sample dimension and α is a positive number. In the principle of size effect, the critic resolved shear stress for a dislocation source is inversely proportional to the length of the dislocation source, which can be simply expressed as $\tau \sim Gb / L$, where τ is the CRSS, G is the shear modulus, b is the Burgers vector. Since the length of dislocation is constrained by the external dimension of sample, decrease the sample size will shorten the length of the dislocation source, resulting in the increase of CRSS. In exhausting hardening mechanism, the main concept is also based on the size-related operation of the dislocation source. It is demonstrated that once deformed the primary dislocation source in a small volume might start to operate first but quickly run to "exhausted", so that the secondary dislocation source is required to operate but higher stress is needed. This phenomenon would be more significant when decreases the external dimension of specimen to micron/submicron scale and is commonly called "smaller is stronger". However, since the samples in previous studies are usually tested by compression and deformed in the form of discontinuous strain bursts, although the GPa level strength is very attractive for application, the precise characterizations on materials' ability of plastic

deformation still requires further investigation to develop the understanding on the size-related plastic behavior of materials.

In addition, microstructure is critical to the mechanical properties of materials. As we mentioned above, the activities of dislocations and the operation of Frank-Read source directly determine the strength and ductility of materials. Since the previous ex situ studies cannot supply the real-time information during plastic deformation, more effort is required to establish the relation between the microstructure evolution and the size-related mechanical response of materials.

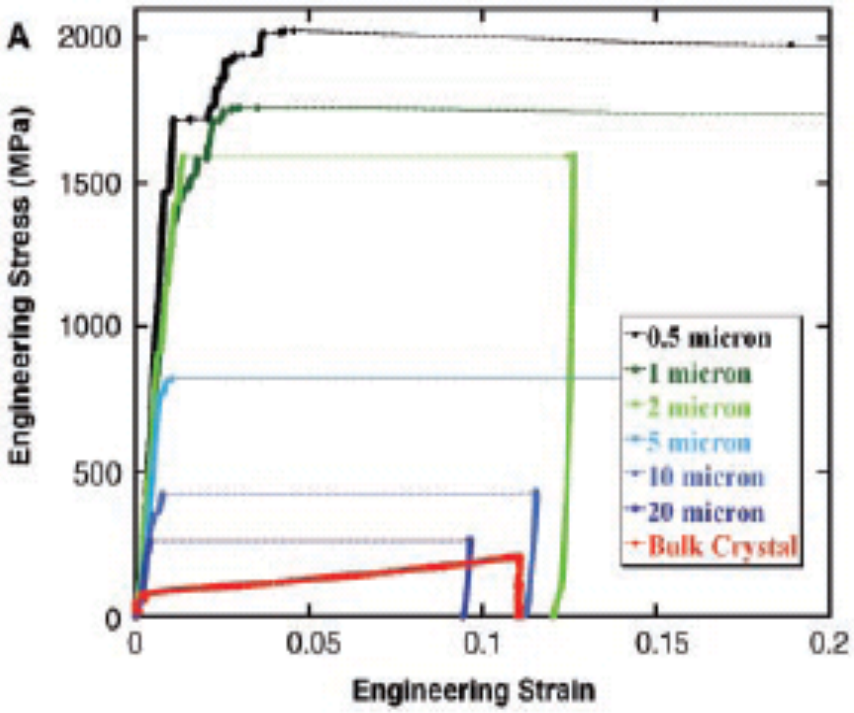

Figure 1.19 The engineering stress strain curves for micron pillars with different sizes. Smaller is stronger.(*56*)

1.1.7 *In situ* transmission electron microscopy TEM mechanical tests

TEM has been commonly agreed as a powerful tool for microstructure analysis. The first TEM was built by Max Knoll and Ernst Ruska in 1931. This is the important event in the history of materials science and engineering due to the special contribution of TEM technique to the development of this academic field. Transmission electron microscopy is a microscopy technique, where a beam of

electrons is transmitted through an ultra thin specimen, which is usually less than 250 nm thick, interacting with the specimen as it passes through. Electrons come out from the filament, which can be LaB_6 or Tungsten, and are accelerated by an electrostatic potential. The whole system is operating in vacuum. The TEM then uses electromagnetic lenses to focus the electrons into a very condensed beam. The electron beam then travels through the specimen and is affected by the structures and objects. Unlike X-rays and neutrons, electrons are charged particles and interact with matter through the Coulomb forces. This means that the incident electrons feel the influence of both the positively charged atomic nuclei and the surrounding electrons. TEM basically uses three different interactions of electron beam-specimen; they form the transmitted beam, elastically diffracted beam and inelastically scattered electrons. (*62*)

Transmitted beam is the electron beam that transmitted through the thin specimen without any interaction occurring inside the specimen. The intensity of transmitted beam is inversely proportional to the specimen thickness. So in bright-field TEM image, where the image is formed by transmitted beam, areas of the specimen that are thicker will have fewer transmitted electrons and will appear darker. The low magnification images are usually formed in the mass-thickness contrast. The TEM image is then magnified and focused onto an imaging device, such as a fluorescent screen, on a layer of photographic film, or to be detected by a sensor such as a CCD camera.

Another part of the incident beam is scattered by atoms in the specimen. It is elastic scattering so that there is no loss of energy. These scattered electrons are then transmitted through the remaining portions of the specimen. The diffraction of electrons follows Bragg's Law, which is $2d\sin\theta = n\lambda$, where λ is the wavelength of the rays, θ is the angle between the incident rays and the surface of the crystal and d is the spacing between layers of atoms (Figure 1.20). So all incident electrons that are scattered by the same atomic spacing will be scattered by the same angle.

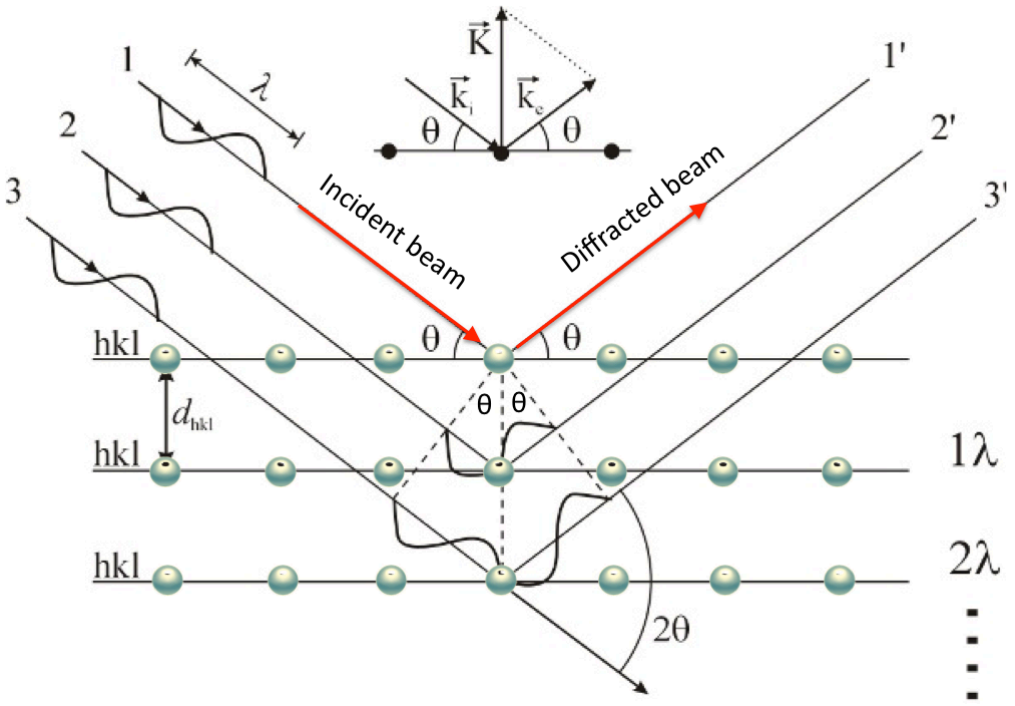

Figure 1.20. Bragg Law. Bragg reasoned that constructive interference would occur only when the path length difference between rays scattered from parallel crystal planes would be an integer number of wavelengths of the radiation.

Constructive beam can be formed if the certain d and θ can fit the Bragg's law. These scattered electrons can be collated using magnetic lenses to form a pattern of spots; each spot corresponding to a specific atomic spacing (a plane). This is called diffraction pattern. This pattern can then yield information about the orientation, atomic arrangements and phases present in the area being examined. So the image of the diffraction pattern is formed by Bragg contrast. In addition, since the defects, such as dislocations and twinning, will all affect the interaction between electrons and materials, the diffraction condition will also change, so we can directly image the 2-dimensional projection of the defects by the Bragg contrast. This enables TEM to be the attractive tool for microstructure analysis.

Another way that incident electrons can interact with the specimen is inelastic interaction. Incident electrons interact with specimen atoms in an inelastic fashion, loosing energy during the interaction. These electrons are then transmitted through the rest of the specimen. Electron Energy Loss Spectroscopy (EELS) and Kikuchi Bands are formed in this way. EELS can be used to analyze the elemental composition and atomic bonding state. Because of the high magnification in TEM, the selected area EELS analysis can be very small, which

enable us to study the local chemical composition and further map the elemental composition. Kikuchi lines appear in relatively thick crystals due to Bragg reflection of the inelastically scattered electrons. They are alternating light and dark lines that are related to atomic spacing in the specimen.

TEM studies have solved many problems and significantly improved our understanding on the deformation mechanisms and the mechanical behaviors of materials. However, since most of the previous studies are performed before and/or after the deformation, the ex situ studies usually lack of the spatial and the time resolution to investigate the dynamic process. In contrast, *in situ* studies can offer more dynamic information, especially the *in situ* transmission electron microscopy study, which can directly record the defects evolution and the change of crystallography during the deformation process. Many efforts have been made to develop the technique of *in situ* TEM test; and the quantitative *in situ* TEM mechanical tests technique is one important branch.

Quantitative *in situ* TEM mechanical tests are usually performed by employing the specially designed TEM holder. The movement of the indenter and the measurement of force and displacement can be accomplished by the transducer and piezo system. Since the specimens need to be electron transparent, their thickness should be normally less than 300 nm. Focused ion beam milling process or lithography technique is usually employed to fabricate the specimens. Through *in situ* TEM mechanical tests, the dynamic microstructure evolution can be recorded by the TEM during mechanical deformation, and the time-to-time mechanical response from the specimens can be recorded by the indentation system. So it is possible for us to generate a clear picture to exploit the fundamental deformation mechanism. Minor et al., used this technique to study the onset of the plasticity in a single grain in 2006. They reported that plasticity in a dislocation-free volume of polycrystalline aluminum can begin at very small forces, however, the shear stresses associated with these very small forces do approach the theoretical shear strength of aluminum (2.2 GPa) (*63*). This study provided direct evidence for the earlier molecular dynamics simulations results, which proposed that the shear stress at the onset of plasticity could approach the theoretical shear strength of an ideal, defect-free lattice. The generation of dislocations from the contact between indenter and the grain boundary was recorded in the *in situ* movie. Figure 1.21 shows the TEM images captured from the movie for the generation of dislocations. The related mechanical data is shown in Figure 1.22.

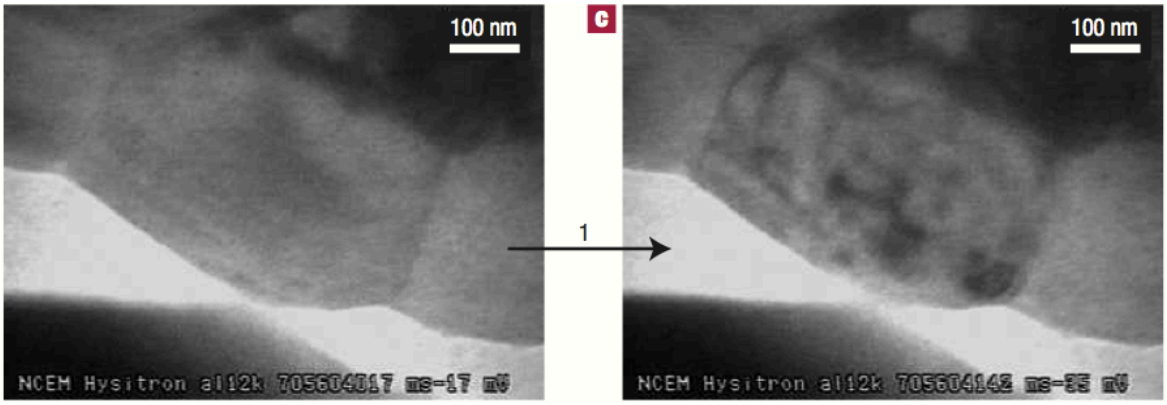

Figure 1.21 The TEM images captured from the movie for the generation of dislocations in an Al grain.(*63*)

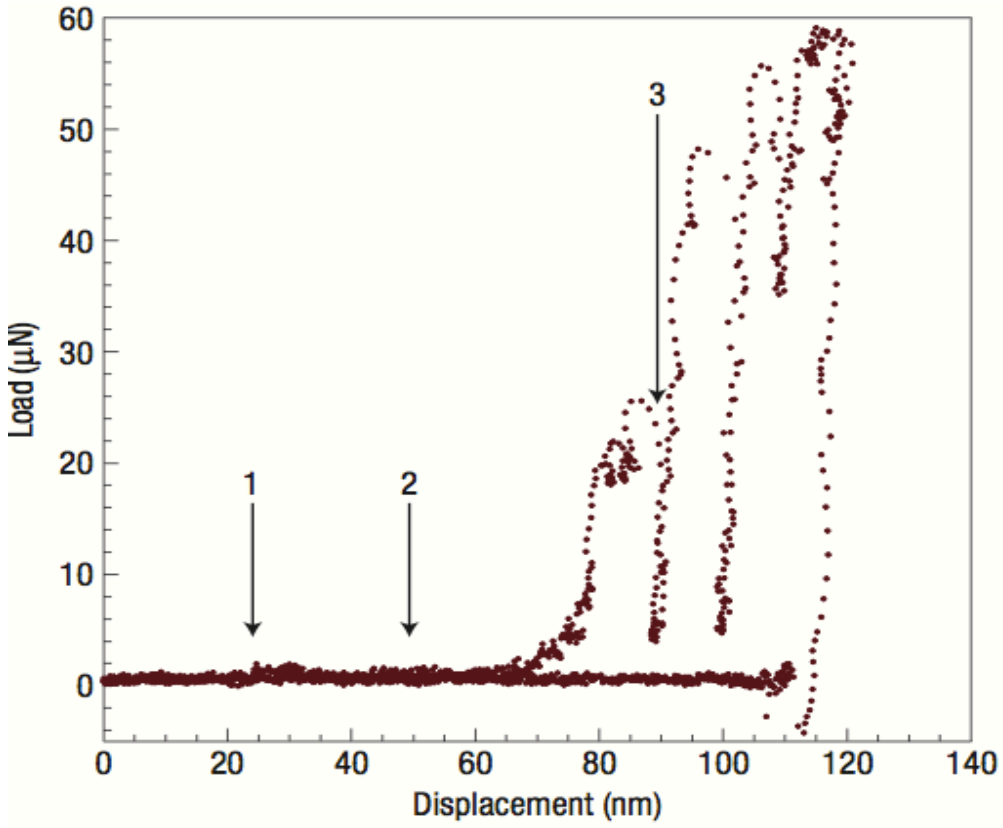

Figure 1.22 The load-displacement curve corresponding to the test in Figure 1.21.

The quantitative *in situ* TEM study was further developed for small sample tests. Freestanding compression or tension specimens were cut out by FIB. Shan et al., tested Ni single crystal pillars in this method and reported the mechanical annealing phenomenon (*64*). Pre-existing dislocations and FIB-induced damage

in the surface layer would escape from the surface once the force was applied, as shown in Figure 1.23, resulting in a defect-free pillar. This result provided direct evidence for the proposed dislocation-starvation mechanism, which was used to understand the "smaller is stronger" trend in small specimens.

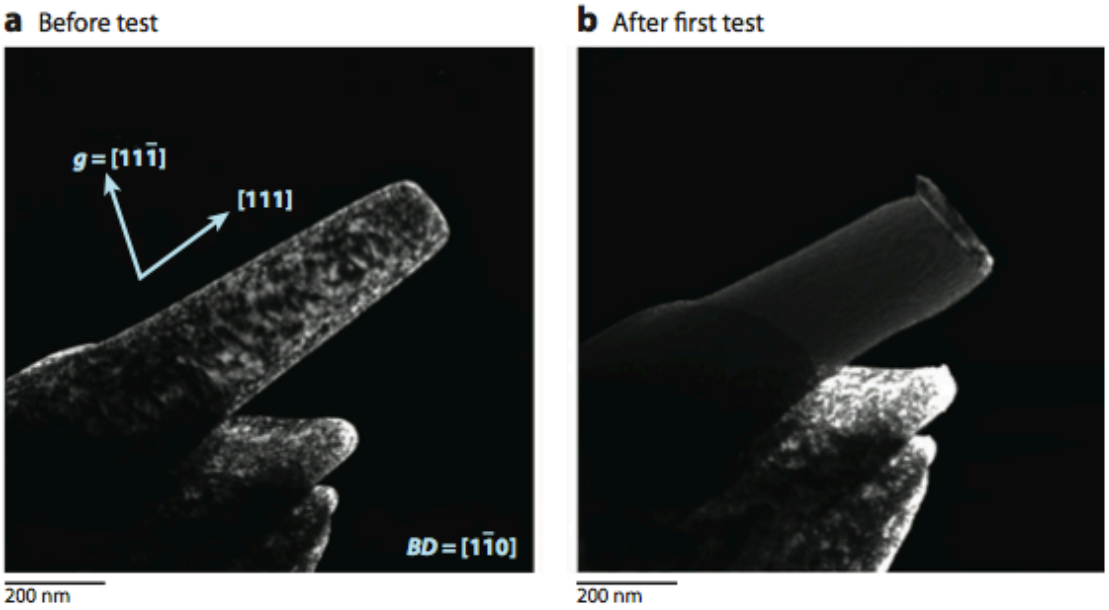

Figure 1.23 TEM dark field images of a submicron Ni pillar before and after in situ TEM compression test. (*64*)

However, the influence of contact surface (nano-level surface roughness) and the sample taper issue in the nanocompression tests usually complicate the results, which makes the analysis hard or even overwhelm the intrinsic picture. *In situ* TEM tension test was developed later, which is considered as the upgraded technique, especially for studying the ductility of materials. Kiener et al., first introduce this method in 2010 (*65*). Comparing with *in situ* TEM compression, more procedures are required for tension. One additional step is to cut out a micron-sized gripper instead of the flat tip and also the dog-bone shaped tensile specimens. Then the most important step next is to align the gripper and the specimens under TEM. Three dimensional-position adjustment is required by looking at the two dimensional projection of the objects. Figure 1.24 below shows the setup of the in situ TEM tension test. More real time mechanical information can be recorded for analysis, such as the elongation, reduction in area, necking and fracture.

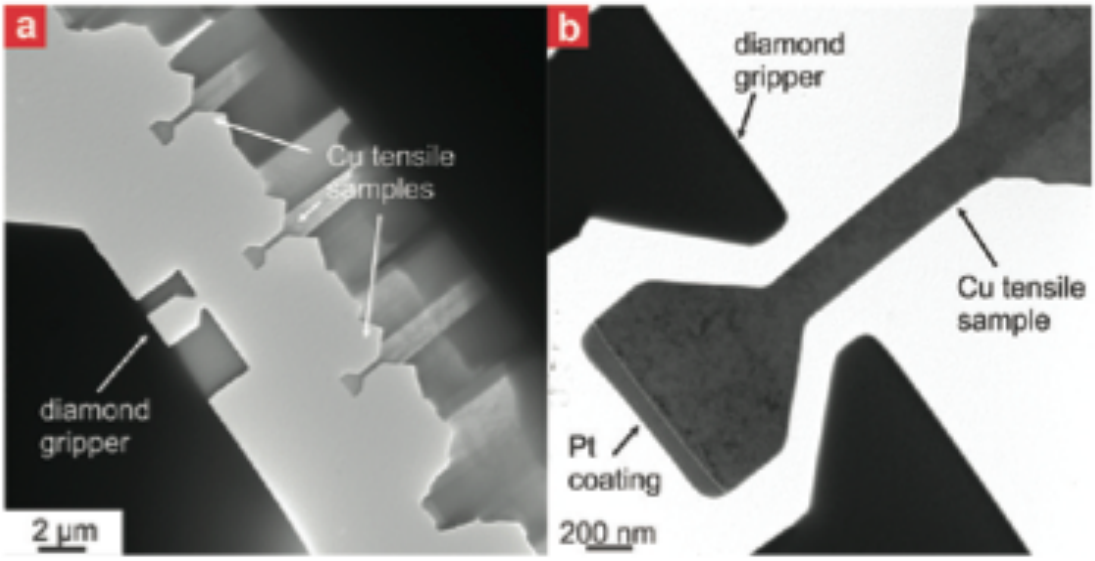

Figure 1.24. The setup of the in situ TEM tension test.(*65*)

1.2 Objective and achievement of the present research work

As we illustrate in section 1.1, the mechanical properties of Mg and Mg alloys strongly affect their application in industry. Even through the light weight of Mg and Mg alloy are attracting more and more attention, the relative poor mechanical performance and the poor formability at room temperature directly hinders their broad application as structural materials. Dimension refinement is a way to tune the mechanical properties for a material with a given chemical composition, but it is evident from the literature that not much work has been done to understand the size-related plastic deformation mechanism of magnesium in comparison to other metals. For example, the size-related twinning behaviors are believed to be different due to the possibly different twinning mechanisms. In addition, the lack of knowledge on fundamental aspects of plastic deformation behavior and deformation mechanisms of magnesium contributes partially to the fact that its development technology is not that advanced. Specifically, when dimension refinement is employed to tune the mechanical properties of materials, the sequence of size-related deformation mechanisms need to be clarified.

So the objectives of the present research work are probing the size-related mechanical properties of Mg and their correlated intrinsic deformation mechanisms by employing *in situ* TEM mechanical tests techniques and microstructure analysis.

The first part of this work focused on the size-related deformation twinning

behavior in single crystal pure Mg and its influence on the mechanical properties of material. The deformation twinning structure was first studied in bulk material, and the interaction of dislocations with the twin boundaries will be discussed. The size effect on deformation twinning is studied by small sample testing. Small specimens were produce by FIB-milling process with the Argon ion cleaning later. *In situ* TEM nanocompression, nanotension and nanobending tests were performed on small specimens. Diffraction analysis, Synchrotron X-ray diffraction analysis and High-resolution TEM analysis were also employed to study the deformed microstructure. Interestingly, the nanostructured origin of deformation twinning was discovered, resulting in great improvement on the mechanical properties of Mg. A nucleation mechanism of deformation twinning was proposed based on the discussion of correlated elastic energy of twinning dislocations.

The second part focused on the size-related dislocation behavior in single crystal pure Mg and also the related mechanical properties of material. We concerned the basal slip system here, which is the most active slip system in Mg. By performing *in situ* TEM nanotension tests on single crystal Mg specimens with external dimensions ranging from about 900 nm to below 100 nm, we studied the effect of crystal size on basal slip behavior and its influence on both the strength and ductility of materials. Here we employed the technique of Focused Ion Beam (FIB) milling and low kV Argon ion cleaning to prepare tensile samples, and used a Hysitron picoindenter to perform the tensile tests. The dislocation structure was studied before and after the deformation for comparison. The dislocation activities during the mechanical tests were recorded by movies. After the *in situ* tensile tests, we were able to identify three different regimes of plastic behavior depending on the sample size. In the largest regime, three-dimensional dislocation plasticity was found to dominate and both the microstructure and the mechanical behavior were similar to those found in the bulk. In the second regime, two-dimensional dislocation plasticity resulted in localized shear. Finally, in the third and smallest regime ultrahigh strength and ductility was obtained and multiple slip systems were activated to contribute to the plastic deformation. The high predominance of basal slip was significantly weakened, representing the reduction of CRSS anisotropy of different slip modes. The *in situ* TEM experiments were compared to detailed molecular dynamic simulations. Consistent with the HRTEM observations, where significant contribution from non-basal slip was observed, the simulation results demonstrated the surface nucleation induced multiple slips and the temporary increase of the dislocation density inside that helped to sustain high flow stress in the smallest regime. These

observations of ultra-high strength plasticity will be discussed in the concept of tuning the anisotropic CRSS of basal and non-basal slips in Mg by regulating the internal or external dimension of crystals. Presumably, the critical size for this engineering concept can be achieved by grain boundary/twin boundary refinement, which may shield light on future processing opportunities for high strength and high ductility structural materials.

The last part is to study the influence of different grain boundary structures on the mechanical properties in polycrystalline Mg small samples. *In situ* SEM/TEM nanocompression tests were performed on samples with several grains. The average grain size is about 100-200 nm. We studied the behaviors of both high angle grain boundary and low angle grain boundary. The results show that the low angle grain boundary acts as the weak barriers for dislocation motion and it might dissociate itself due to the motion of dislocations under high stress. But high angle grain boundary is much more stable which can usually act as the dislocation source to promote dislocation plasticity, enhancing the continuous plastic flow. Nevertheless, grain boundary sliding was also observed in some cases where the grains were too small to sustain intra-grain dislocation activities. These different deformation mechanisms further affect the mechanical behavior of the samples.

Chapter 2

Size-related deformation twinning behavior in single crystal Mg

There have been many efforts over the years to provide a description for the fundamental nucleation and growth mechanisms of deformation twinning in HCP structural materials, but a consensus has not emerged. Certain deformation twinning modes are thought to be beneficial to the ductility of Mg, while others are considered detrimental (*66, 67*). In advanced alloys such as TWIP (twinning induced plasticity) steels, deformation twinning has been engineered to give significantly enhanced ductility and toughness (*68-70*). Since twin boundaries impede dislocation motion, twin boundaries generated during deformation harden the material. However, the reorientation of the crystal due to twinning changes the ability of dislocations to move, which can lead to softening. Thus, deformation twinning can be used to fine-tune the mechanical properties of an alloy to achieve an optimal value of strength and ductility, and understanding the origin of deformation twinning could open up new avenues for alloy design.

Despite the critical importance of deformation twinning to Mg alloys, historically its intricate dependences on ordinary dislocation plasticity and grain size tended to confound alloy developers. Because deformation twins grow so fast, the nucleation structure is difficult to observe experimentally. Also, it is commonly believed that deformation twinning would lose out to ordinary dislocation plasticity at smaller (sub-micron) grain sizes in Mg. Unlike nanoscale twin laths in TWIP steels and nano-twinned Cu, dense arrays of coherent twin boundaries are considered difficult to introduce in pure Mg because the twin boundary energy g_{TB} is much higher (~120 mJ/m^2 in pure Mg, compared to ~15 mJ/m^2 in Cu or hexagonal close packed Co). As the TWIP effect scales with twin density, the lack of nanoscale twins seems to limit the potential efficacy of TWIP for improving the mechanical properties of Mg. Exploiting the intrinsic mechanism of deformation twinning and the size-related deformation twinning behavior is then an interesting topic. Here we performed compression, tension and bending tests on single crystal Mg samples oriented for twinning deformation to systematically study this topic. Detailed microstructure analysis was performed

and the experimental results were discussed with the input of simulation.

2.1. Sample preparation

All the specimens in this study were made from the high purity (99.9995%) single crystal Mg rod supplied by General Motor (Detroit, USA). The crystal orientation of the long single crystal bars was determined by x-ray diffraction, which showed that the length direction of the single crystal rod was parallel to the c-axis. The crystal orientation is schematically shown in Figure 2.1.

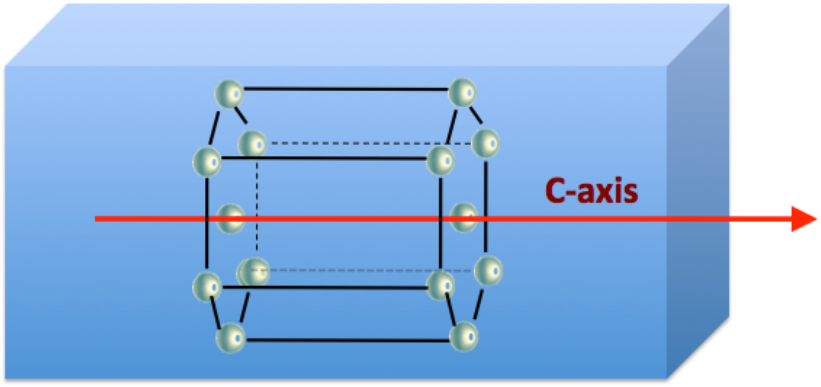

Figure 2.1.The crystal orientation of the bulk single crystal Mg rod.

Bulk sample preparation

We firstly cut out the bulk samples from the single crystal rod by using the electric spark-cutting machine, immersed under dielectric oil. Electrochemistry polishing was performed for surface treatment. The bulk samples were used for compression tests. Their geometry is about 5 mm×5 mm×10 mm and oriented along [0001], as shown in Figure 2.2. As we discussed in chapter 1, if we load the specimens along [0001] direction, the Schmid factor for basal slip will be zero, and 0.4 for <c+a> slip and 0.5 for twinning. So deformation twinning will dominate the plastic deformation. For conventional bulk counterpart, $\{10\bar{1}2\}<10\bar{1}\bar{1}>$ extension twinning is favored under tension, and $\{10\bar{1}1\}<10\bar{1}2>$ contraction twinning is expected under compression.

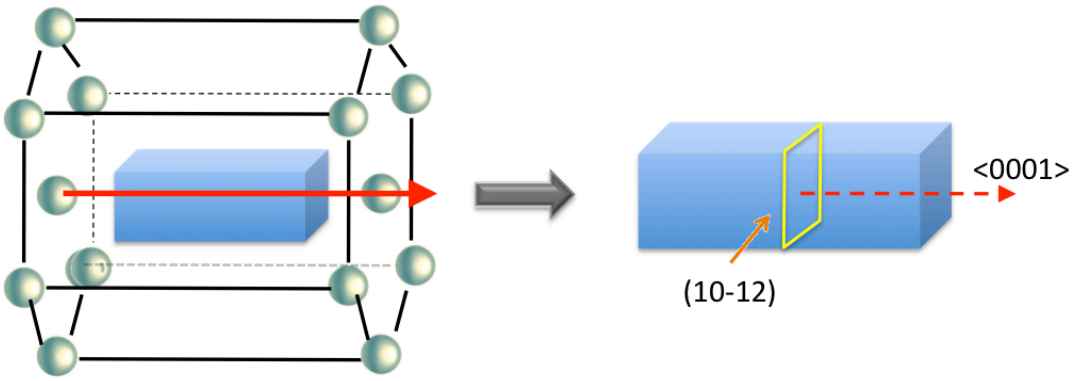

Figure 2.2. The geometry and crystal orientation of bulk compression samples. The loading direction is along [0001].

Small sample preparation

Submicron-sized tension, compression and bending specimens were fabricated with a FEI Strata 235 Dual Beam Focus Ion Beam (FIB). Before FIB milling process, a piece of Mg was cut out from the same single crystal rod. One of the edges of the thin Mg foil was required to be parallel to [0001]. This piece of Mg was further mechanically milled to about 50 micron thick. Ion milling was then used on the thin Mg foil in a Gatan Precision Ion Polishing System (PIPS), which has 2 unique penning ion guns with 10° to -10° milling angles and liquid nitrogen specimen cooling. The beam was centered at the edge of the thin foil, which was normal to [0001] direction. The ion milling process was carried under electron beam with energy at 200 eV for about 1 hour. These procedures are shown in Figure 2.3.

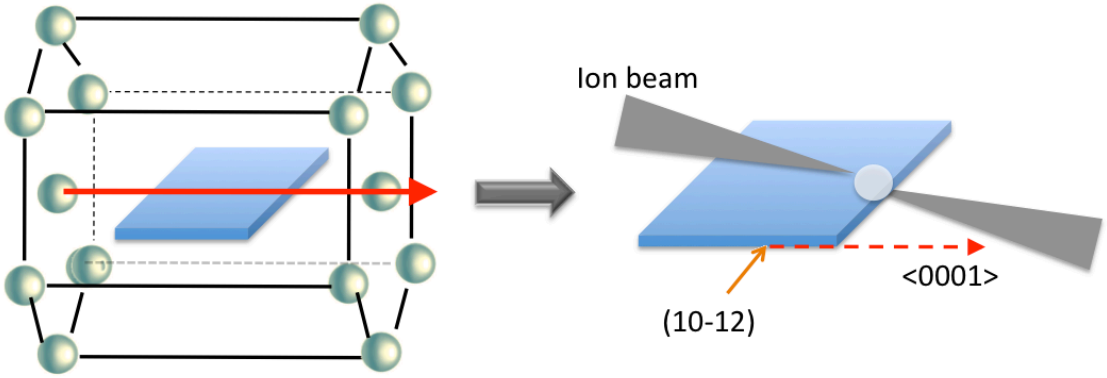

Figure 2.3 The procedures of preparing a thin Mg foil with the electron transparent area near one edge. This edge must be perpendicular to [0001] direction.

As the next step, the thin foil was further glued to an in situ TEM copper stage using colloidal graphite. The TEM stage was then glued to a 45 degree SEM stage. The whole was installed into FIB and the chamber was pumped down to 10^{-5} torr vacuum for operation. Since the angle between ion beam and electron beam in FIB is 52 degree, we firstly tilted the stage by 7 degree, so that the ion beam direction was perpendicular to the edge of the thin foil. FIB-milling process was performed in the sequence of rough cutting with 5000 pA ion beam current and finer cutting with 100 pA ion beam current. These would produce a thinner window with thickness at about 1 micron. These steps are shown in Figure 2.4.

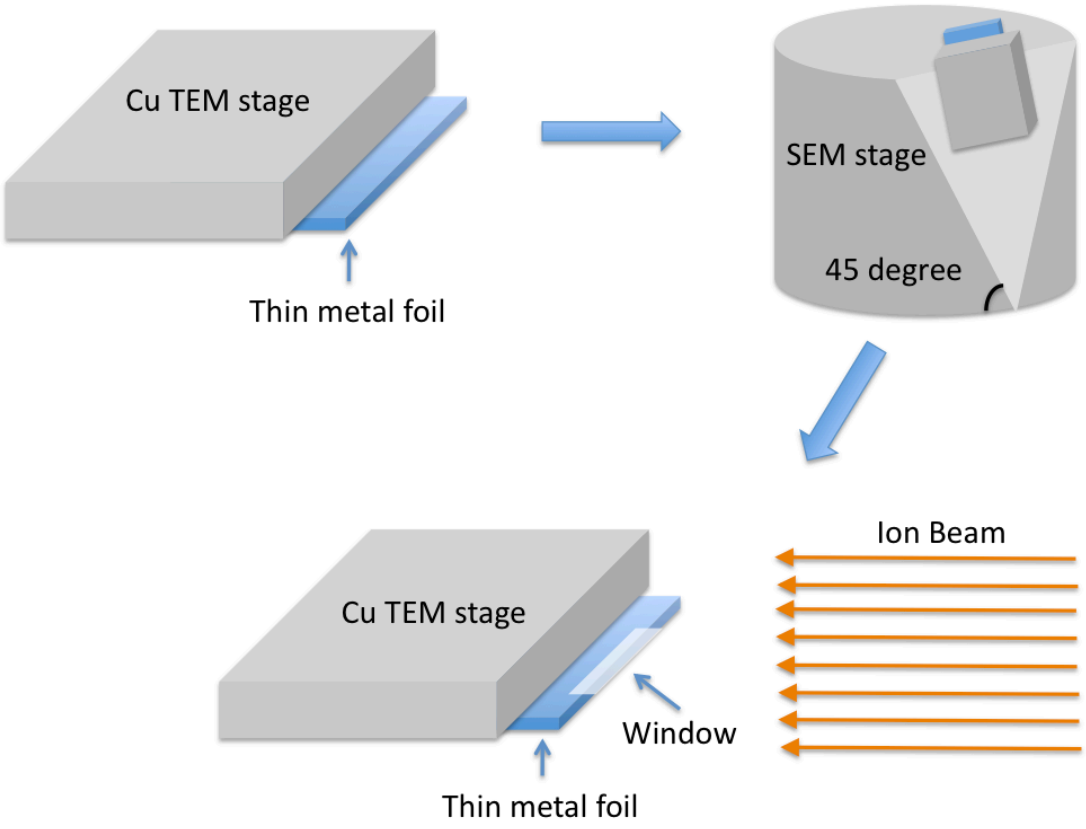

Figure 2.4 The procedures of FIB-milling.

Afterwards, the stage was rotated by 180 degree, so the ion beam was parallel to the edge of the thin film but perpendicular to the normal of the thin film. 10 pA ion beam current was used for the final cutting, which was the critical step to shape the specimens. Samples with different geometry can be produced, including pillar, tensile bar and cantilever beam. Figure 2.5 below shows these procedures. A Fischione 1040 NanoMill with Ar^+ source was employed later to remove the damage layer induced by FIB. The Ar^+ beam in Nanomill has much

lower energy, which is about 1-2 KeV. The beam is perpendicular to the edge of the thin film, so the cleaning process is top-down.

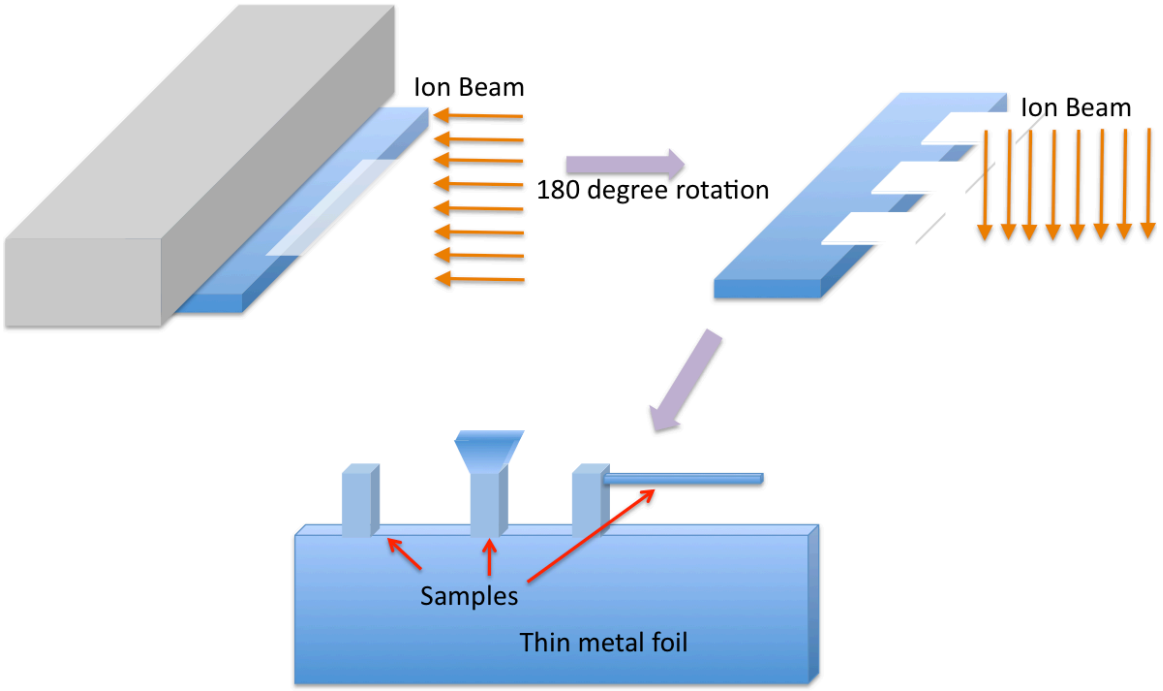

Figure 2.5 The procedures of final cutting in FIB.

Figure 2.6 below shows the typical TEM images of the tension, compression and bending samples before testing, respectively. The diffraction patterns inset confirmed the orthogonal orientation of samples. Here the zone directions were all $[\bar{2}110]$, and the loading direction always came along the [0001] direction. The tensile samples were in the dog-bone shape and were fabricated to be 2-3 μm long, 100-200 nm wide and about 150 nm in thickness; the head was usually 1000 nm wide; bending samples were in the shape of cantilever beam and were 1-2 μm long, about 200 nm in width and about 150 nm in thickness; compression samples were freestanding pillars that made approximately 200 nm in diameter. The distance between each sample was usually more than 5 micron, which was required to be larger than the diameter of the flat diamond tip or the width of the tensile gripper.

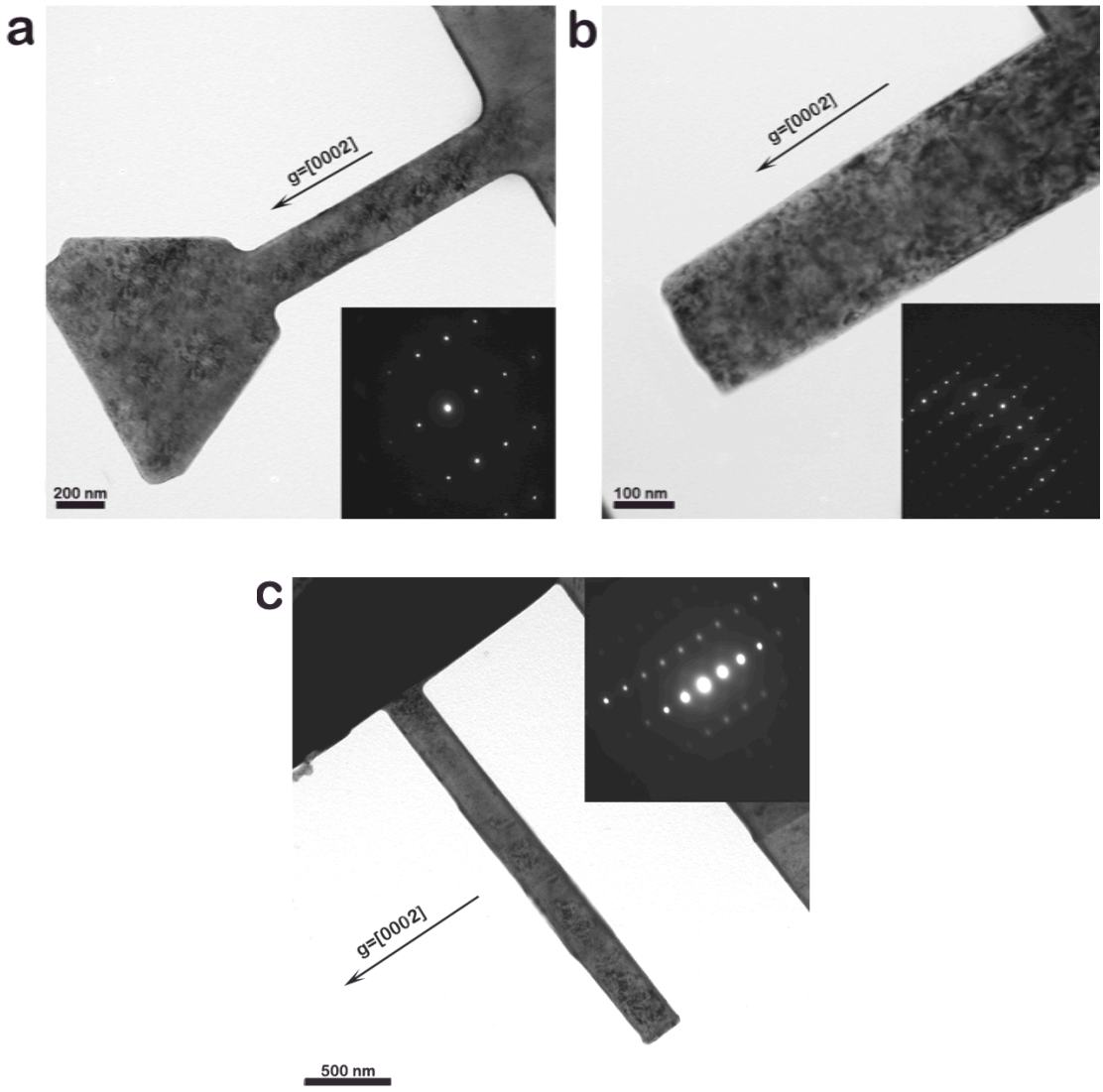

Figure 2.6 The TEM bright field images of the samples before test. (a) tensile sample, (b) compression sample, (c) bending sample. The diffraction conditions are all under g=[0002].

2.2 mechanical tests and microstructure analysis

Magnesium offers a large potential in weight reduction usages because of its lowdensity of about 1.73 g cm^{-3}. However, the relatively low strength and plasticity greatly hinder its wide applications. One effective way that can improve the mechanical property of Mg is grain boundary refinement. Equal channel angular pressing (ECAP) is one promising severe plastic deformation (SPD) technique for refining Mg alloys. W.M. Gan et al., studied the tensile

properties of polycrystalline Mg with (0001) texture, where twinning deformation dominates (*71*). The grains after 4 pass were the smallest one, and the grains after just one pass held the largest size. However from their results, it was found that even in materials with smallest grains, the strength level was only about 70 MPa, as shown in Figure 2.7. The flow stresses can approach about 150 MPa after a significant strain hardening process. However, the fracture strains were all less than 10%, indicating the limited ductility. Consistent with other nanocrystalline materials, the material with smaller grains showed higher strength but lower ductility.

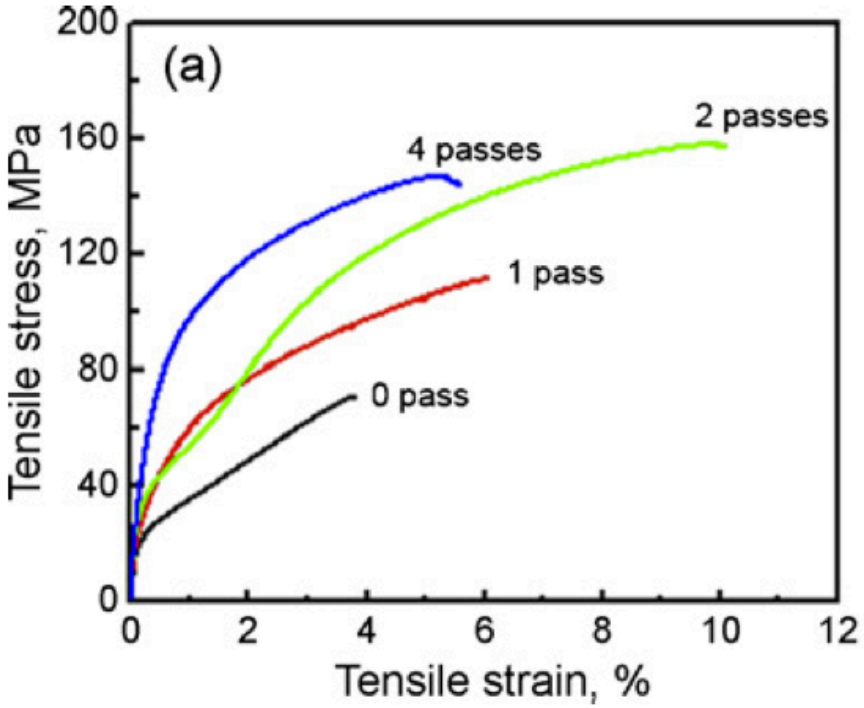

Figure 2.7 The tensile stress-strain curves of polycrystal Mg with {0001} texture. The grain sizes were different after different number of pass. 4 pass presented the smallest grain size.(*71*)

2.2.1 Bulk material behaviors

In our study, the tested material is single crystal but the loading direction is the same, which is along [0001]. Our bulk tensile samples were tested in the Instron tensile and compression press 1195 in the mode of displacement control. The strain rate was about 6×10^{-4}. One typical engineering strain-stress curve is shown in Figure 2.8. From the tensile curve, we can see that the highest flow stress could reach over 150 MPa but the fracture strain was only about 4.3%. The yield

stress was around 28 MPa. Both of the strength and the ductility of bulk single crystals Mg with [0001] orientation are relative poor compared with other structural materials, such as steel and Al alloy.

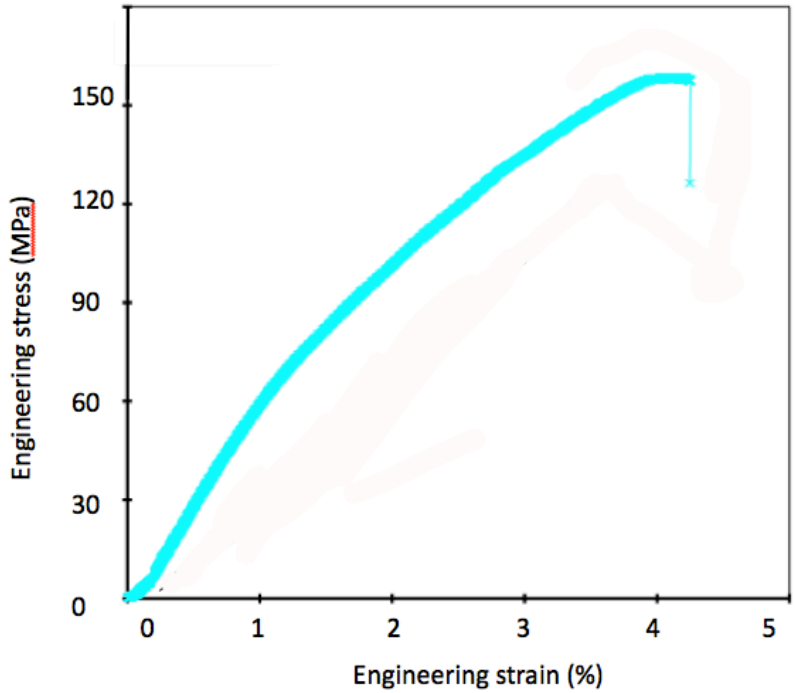

Figure 2.8 One typical engineering strain-stress curve for bulk single crystal Mg oriented along [0001].

The deformed microstructure was investigated by TEM analysis. 3 mm disks were cut out from the deformed bulk samples. Ion mill was used to thin down the disk to be electron transparent. Large numbers of deformation twinning were observed. The twinning bands usually had large length to thickness ratio; most of them were about several micron long and several hundreds nanometer thick. The twinning bands were in the lens shape and the twinning tips were very sharp. The dislocation density was much higher at the twinning tip region either within the twin or in the near-by matrix, which was mainly due to the significant stress concentration induced by the mismatch at the sharp twinning tip. In addition, the dislocation activities were found to be much more intense at the twin boundaries. Different types of dislocations were found and the strong interaction of these dislocations with the twin boundaries were observed. As a consequence, the strain contrast was stronger in the twin boundary region. At some twin boundaries, large number of <a>-type single dislocations with was observed; they interacted with the twin boundaries and generated remarkable strain field. Figure 2.9 shows the typical TEM images of the twinning structure in our bulk materials

after tension, where the long twinning band and the dislocations interaction at the twin boundaries can be seen.

We noticed that the dislocation activities in the matrix were not strong after deformation compared with that within the twin. The reason for this is because that our crystal orientation and the loading direction forbid basal slip and prismatic slip in the matrix. However, the twinning deformation changed the local crystal orientation, which offered a larger Schmid factor for basal slip and prismatic slip in the twinned lattice. So that the basal slip and prismatic slip can all happen within the twin, resulting in much stronger dislocation activities inside.

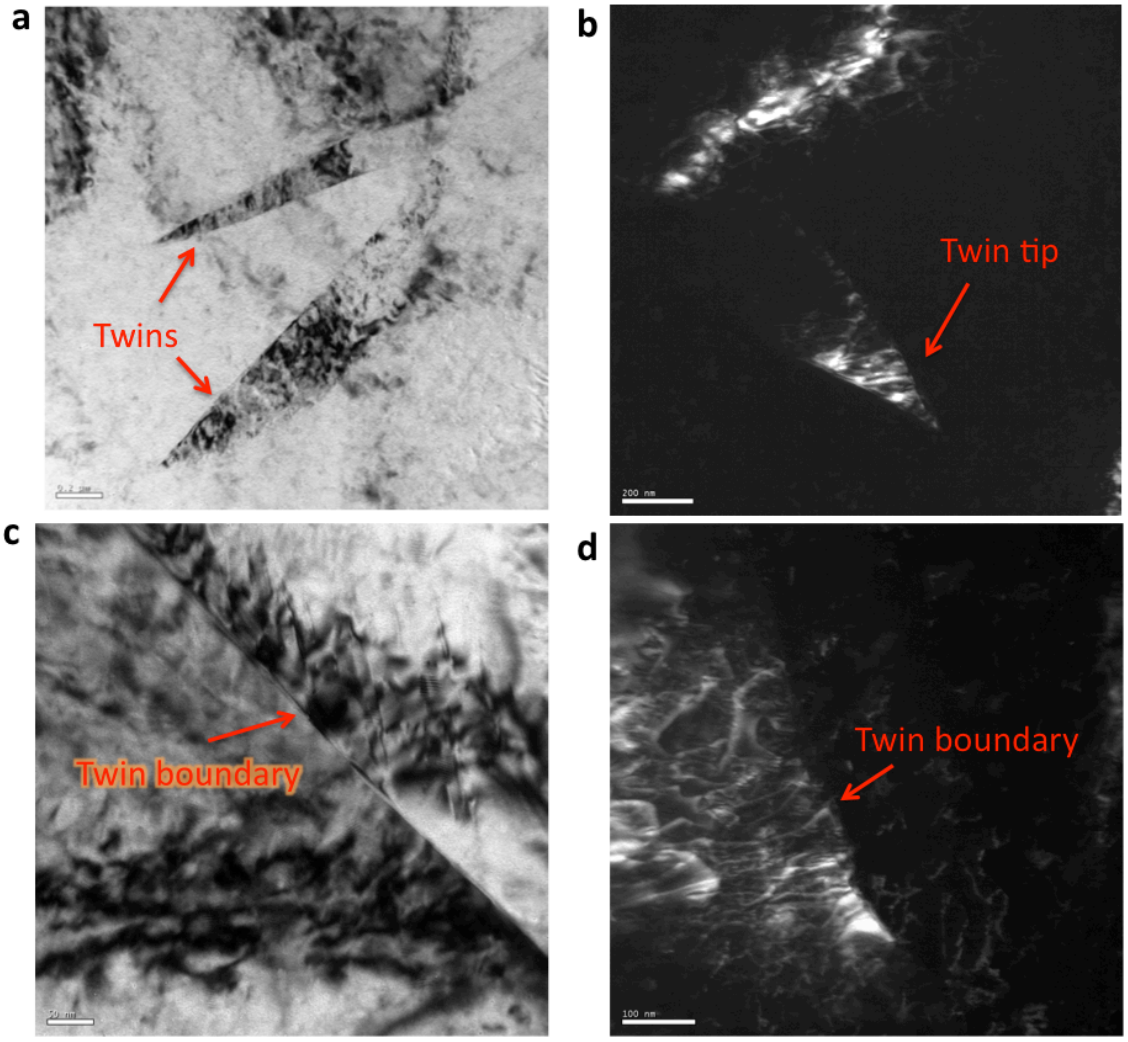

Figure 2.9 The typical TEM images of the twinning structure in our bulk materials after tension, where the long twinning band in the lens-shape can be seen. The dislocations interaction at the twin boundaries is much more intense

than that in the matrix.

2.2.2 Submicron samples' behaviors

From the bulk results above and also the results from others studies, it is realized that both the strength and ductility of bulk Mg with [0001] orientation is relative poor. Twinning deformation dominates the plastic deformation. In the following sections, the size-related twinning behaviors were demonstrated and we observed the strong size effect on the deformation mechanisms and their influence on the mechanical behavior of materials.

2.2.2.1 Nanocompression and nanotension tests

The *in situ* TEM uniaxial tension tests and compression tests were performed along the [0001] direction in a JEOL 3010 TEM with a Hysitron Picoindenter. [0001]-oriented single crystal Mg samples were prepared through Focused Ion Beam (FIB) milling process. For this orientation, basal slip is suppressed, $\{10\bar{1}1\}$ "contraction" twinning is expected under compression, and $\{10\bar{1}2\}$ "extension" twinning is favored under tension (*72*). The crystal orientation of the specimens was confirmed by combining the diffraction analysis and the trace analysis. For example, Figure 2.10 shows a TEM bright-filed image of a tensile specimen and its corresponding diffraction pattern. The diffraction pattern had zone axis along $[2\bar{1}\bar{1}0]$. The connection between the center spot and (0002) spot was parallel to the tensile bar direction and also the loading direction, which indicated that our specimen had a well defined crystal orientation, which was along [0001]. Misorientation happened in some cases, but it was usually less than 5 degrees off. So twinning deformation was the predominant source of plastic deformation. All of the *in situ* TEM mechanical tests were conducted under displacement control mode with displacement rate of 10 nm/s. After the *in situ* tensile, compression and bending tests the sample was further thinned down for high-resolution TEM imaging with a 2kV Ar^+ ion beam. HRTEM study of the atomic structure of the twin was performed in a Philips CM300FEG TEM at 300KV and a FEI Technai F20 at 200kV.

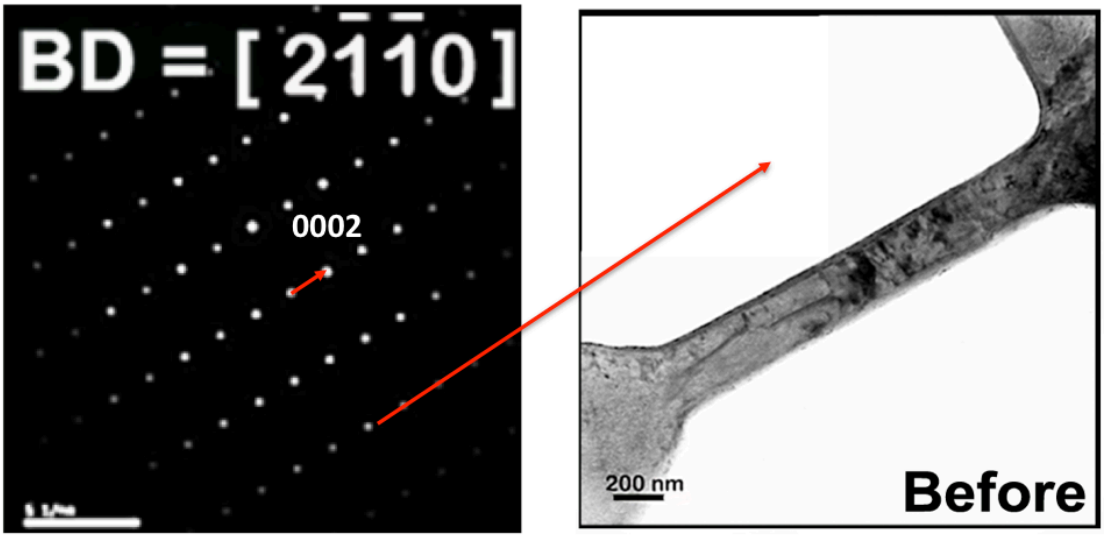

Figure 2.10 A TEM bright-filed image of a tensile specimen and its corresponding diffraction pattern.

Nanocompression tests were using a diamond indenter with a flat tip, which was also fabricated in FIB. The flat tip was about 5 micron wide. Before mechanical tests, the sample was tilted around in TEM in order to achieve a two-beam condition to image the defects, such as dislocations. The alignment of the indenter and the sample was accomplished inside TEM. Nanotension tests used a diamond gripper instead of flat punch. The gripper was 1.4 micron wide and about 1 micron thick, which was fabricated by special designed FIB milling process. Figure 2.11 shows the bright field TEM images at low magnification demonstrating the process of the alignment of the tensile gripper and the sample. To perform the alignment, the sample and the tensile gripper were first brought to eucentric height using the aid of the microscope focus (shown in figure 2.10 left) when these two were out of contact. The gripper was then lowered along the Z-axis and moved forward along the X-axis to be right under the sample. The gripper was then raised back to eucentric height and adjusted along the X and Y axes simultaneously until the gripper was aligned with the sample but still out of contact, as shown in Figure 2.11 right. Tensile testing could then be performed under displacement control in the negative X direction.

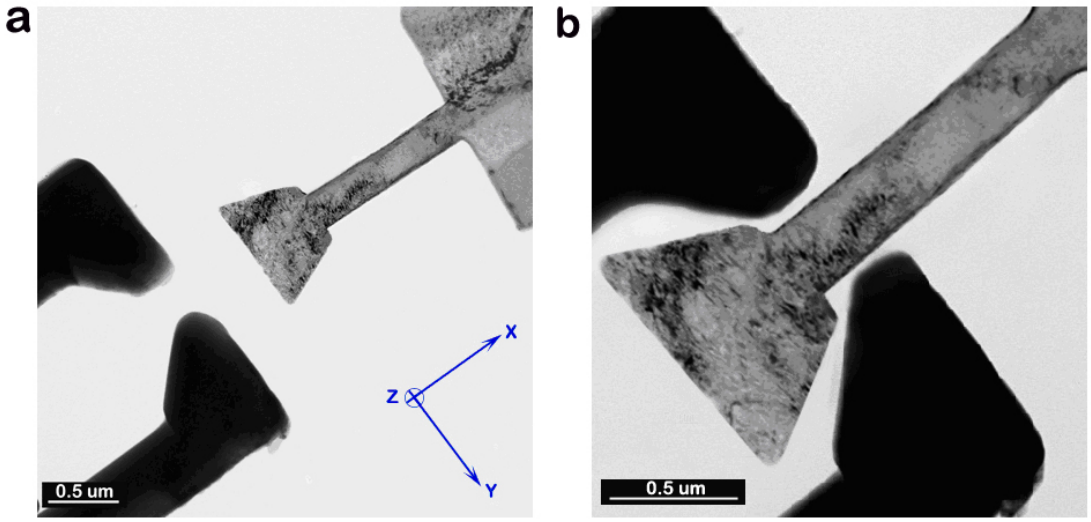

Figure 2.11 The TEM image shows the position of the tensile sample and the gripper. (a) before alignment. (b) after alignment.

Several engineering stress-strain curves from the uniaxial tension and compression are plotted in Figure 2.12 and 2.13, where GPa-level flow stresses were achieved in our small samples; far exceeding previously measured Mg bulk strengths. Based on the TEM videos, the real time mechanical data and subsequent diffraction analyses, it was observed that deformation twins initiated at s~800 MPa under both tension and compression. The initiation of deformation twinning can be observed by the change of local diffraction contrast during the *in situ* test, since the lattice reoriented in the twinned region. These deformation twinning initiation stresses are much larger than the previously reported critical resolved shear stress for $\{10\bar{1}2\}$ and $\{10\bar{1}1\}$ deformation twinning, which were ~3 MPa and ~100 MPa, respectively (*67*). Note, however, that our stresses were measured from such small samples that they can be considered as the "local" or microscopic stresses for deformation twinning initiation, whereas the old values were bulk averaged or macroscopic stresses that do not take into account stress amplifications needed to achieve deformation twinning. In addition, prior to twinning initiation, both the tension and compression tests demonstrated linear hardening. However, after twinning initiation, we found significant differences between the compression and tensile tests in terms of both the twin structures and the corresponding mechanical data, bringing us new insight into the mechanisms of deformation twinning.

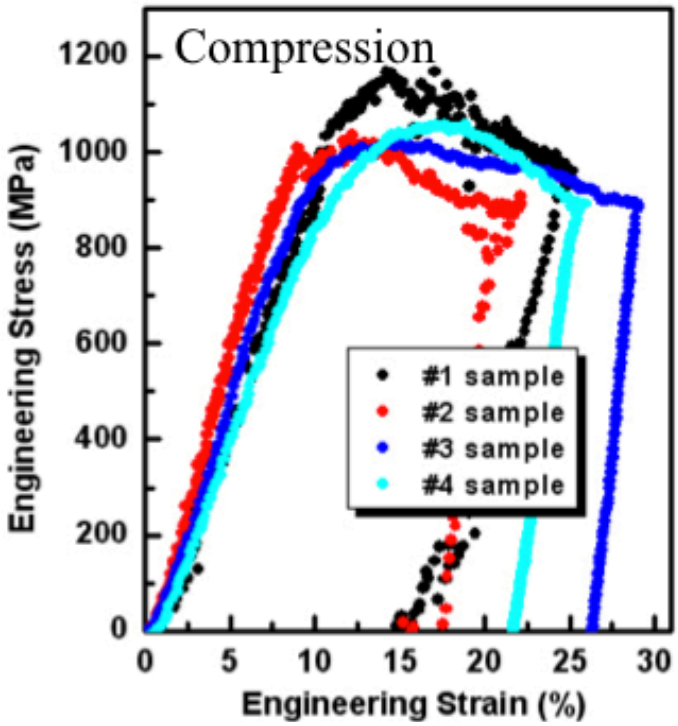

Figure 2.12 The uniaxial compression curves from in situ TEM tensile tests on submicron samples.

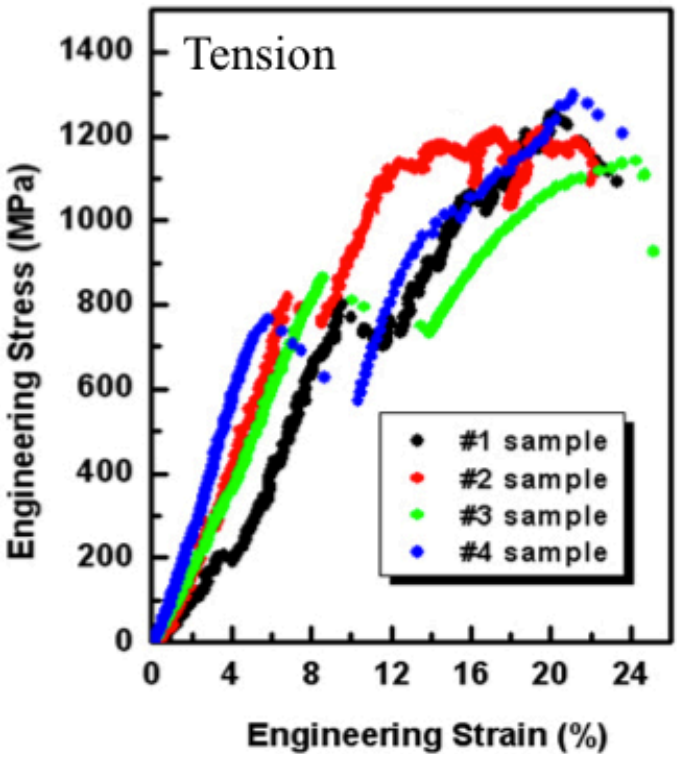

Figure 2.13 The uniaxial tensile curves from in situ TEM compression tests on submicron samples.

Nanocompression

For the compression tests, the nucleation of a single $\{10\bar{1}1\}$ contraction twin always started from the corner of the contact surface between the sample and the indenter. The formation of only a single twin was presumably due to the nano-level roughness of the contact surface, which resulted in stress concentrations leading to preferred nucleation sites. Because there is contact surface in compression and this contact cannot be perfect flat, the roughness of the diamond tip and the top surface of the sample will generate large stress concentrations (*50, 64*). This is in general a significant shortcoming of compression tests on small samples and it is a general phenomenon that deformation initiates from the contact surface in small specimens (pointing out the importance of our tensile results). The result is that in compression there is preferential nucleation of a single twin. This single twin grew gradually as the stress increased continuously until the twin extended across the entire width of the pillar. The growth of a continuous twin produced a shear displacement (marked in red in Figure 2.14). At this point, dislocation activity can be fully accommodated and the escape of dislocations at the surfaces results in significant strain softening, as shown in Figure 2.12. HRTEM study showed the bulk twin structure (see HRTEM image inset in Figure 2.14). The compression test provides a good example of heterogeneous nucleation and growth of the twin due to preferential nucleation at the contact surface and the tapered geometry.

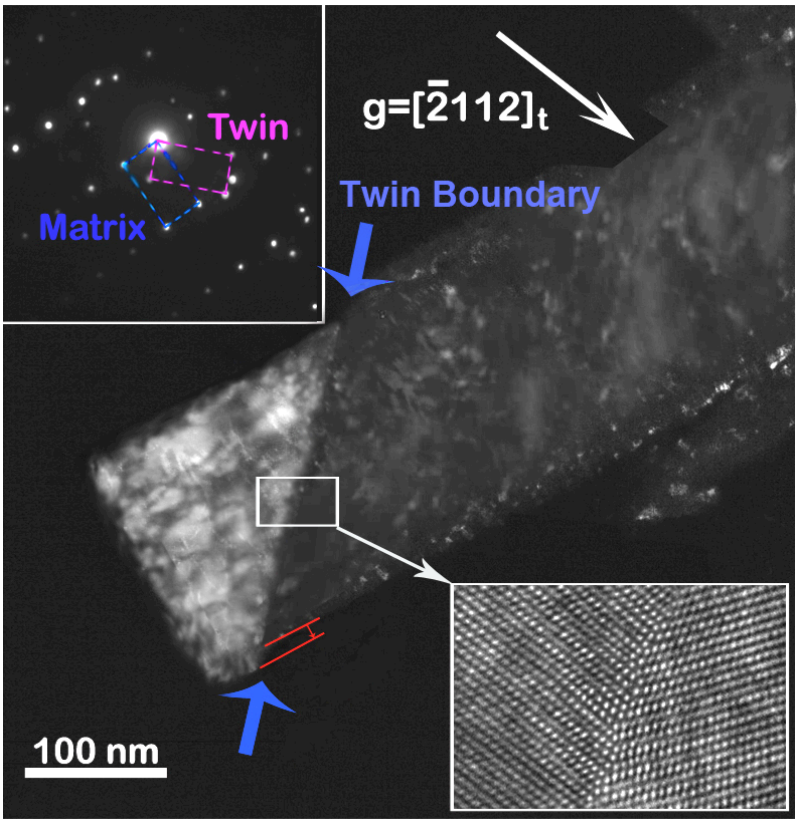

Figure 2.14 TEM from an in situ compression test of [0001] oriented Mg. A dark field image showing the in situ compression sample post-deformation, the diffraction condition is g= $[\bar{2}112]_t$. The twin boundary is indicated by blue arrows, and the shear displacement is marked in red. One typical HRTEM image of compression sample is inserted showing the $\{10\bar{1}1\}$ twinning structure.

The twin type was also confirmed and the induced dislocation structures were investigated by using synchrotron based x-ray Laue microdiffraction (mXRD) technique on Beamline 12.3.2 at the Advanced Light Source of the Lawrence Berkeley National Laboratory. A high brilliance synchrotron polychromatic x-ray beam (5-24 keV) is focused down to 1 mm^2 size by a pair of Kirkpatrick-Baez mirrors. The Mg nanopillar after compression was positioned at the x-ray focal point and a Laue diffraction pattern was recorded by a MAR133 x-ray CCD detector in reflection geometry. The sample and the CCD detector were tilted by 45^o and 90^o with respect to the micro-focused x-ray beam, respectively. The distance from the sample to the center of the MARCCD was about 78 mm. The experimental geometry was calibrated by recording a Laue diffraction pattern on a strain free Si chip. The Diffraction pattern was indexed using the software

package XMAS[2]. By comparing the orientation matrices, it was found that the tilt angle between the matrix and twin domains was 56.4° along $[11\bar{2}0]$ direction, which was close to the calculated angle (56.2°) based on the unstrained lattice parameters corresponding to $(\bar{1}011)$ compression twin. Diffraction peaks from the matrix were observed to be split (Figure 2.15), which indicated that geometrically necessary dislocations (GNDs) were aligned and two subgrains were formed after the compression load. Detailed study of the subpeaks revealed that the tilt angle between the two subgrains was about 1.1°, and the GNDs were $[10\bar{1}0]$ direction. Presumably this subgrain was in the bottom of the pillar and is indicative of heavy deformation below the twinned region.

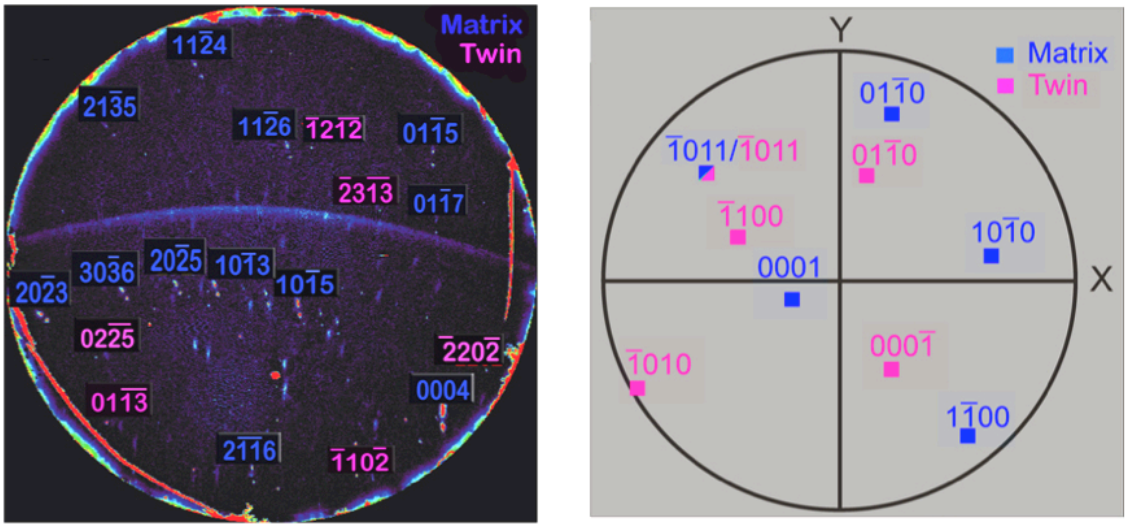

Figure 2.15. Left: mXRD pole figure of the compressed sample. Indexes labeled in blue are from the matrix and those in red belong to the twin. Right: A pole figure showing the corresponding planes of the matrix and the twin.

Nanotension

In tension, the beginning of the elongation occurred with no significant microstructure change. Several pre-existing dislocations were quite stable at this stage. Until the stress went up to about 800 MPa, the pre-existing dislocations suddenly lose of contrast; meanwhile a boundary formed in the tensile specimen. This information indicated the formation of twin. Since the reorientation of the crystal changed the diffraction condition, so that the pre-existing dislocations were no longer under Bragg condition. Diffraction analysis also confirmed the formation of $\{10\bar{1}2\}$ extension twin. Figure 2.15 shows a tensile sample before

test and just after the formation of the twinned region; the related diffraction pattern is inserted into Figure 2.15 right. The initiation of $\{10\bar{1}2\}$ twins resulted in a sudden load drop and was accompanied by a 2-5% strain burst (Figure 2.12). Considering the shear strain of this type of extension twin in Mg (about 10% along the shear direction), the strain burst indicates that the total twinned volume is a large proportion of the sample volume (roughly 50%), which is confirmed by our TEM results. Further TEM and HRTEM analysis showed that nanotwins actually form in tension. Figure 2. 17 shows examples of the formation and structure of nanotwinned arrays formed in tension.

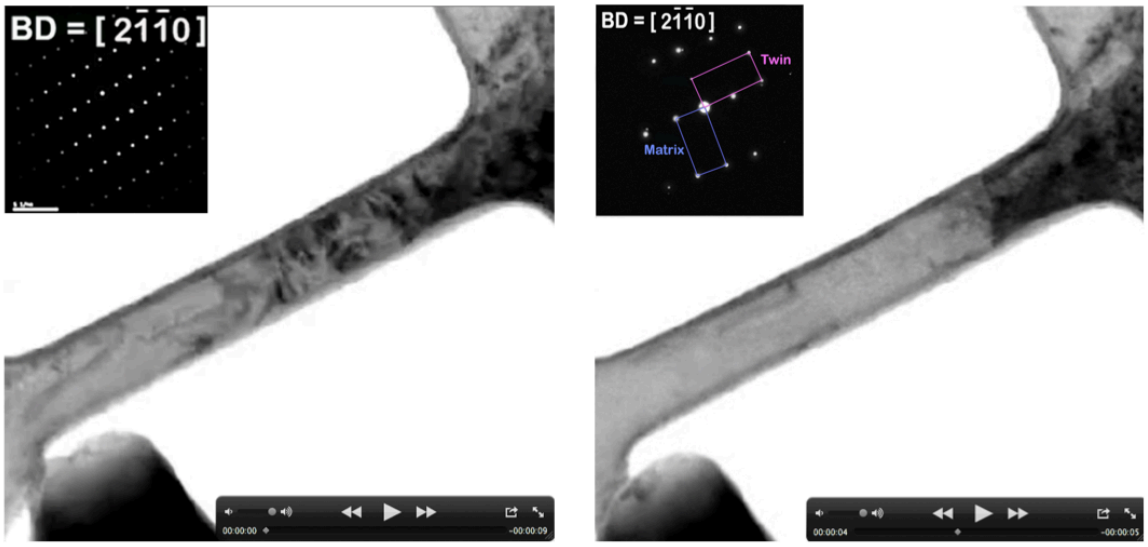

Figure 2.16 A tensile sample before test (left) and just after the formation of twinned region (right); the diffraction pattern for twinning is inserted.

After the formation of nanotwins, homogenous elongation was observed, mainly from the twinned region, and the tensile sample displayed a strain hardening response that lead to 1300 MPa flow stress and ~20% strain. The overall strain contribution of these nanotwins can be roughly estimated as follows: from the TEM images after the test we can roughly estimate the volume fraction of twinned regions, where the average is ~50%. If we consider the $\{10\bar{1}2\}<10\bar{1}\bar{1}>$ twin in Mg, the shear strain along $<10\bar{1}\bar{1}>$ direction is theoretically 0.12. The overall strain along the C axis that would then be generated by these nanotwins is ~5%, a significant part of the total strain (total plastic strain ~20%). The twins contribute a large portion of the total strain because of the small sample volume and the large number of nanotwins (50% volume fraction in this example). Thus,

these nanotwins play dual roles: they provide plastic strain and also facilitate subsequent dislocation plasticity because that the high density of twin boundaries can increase the dislocation storage and result in strain hardening. As an example of this, the BF TEM image of the nanotwins structure in Figure 2.17 shows strong strain contrast within the twins, indicating the intense dislocation activities in the twinned regions. The related diffraction pattern for twin-matrix relation is inserted. The zone axis is $[2\bar{1}\bar{1}0]$.

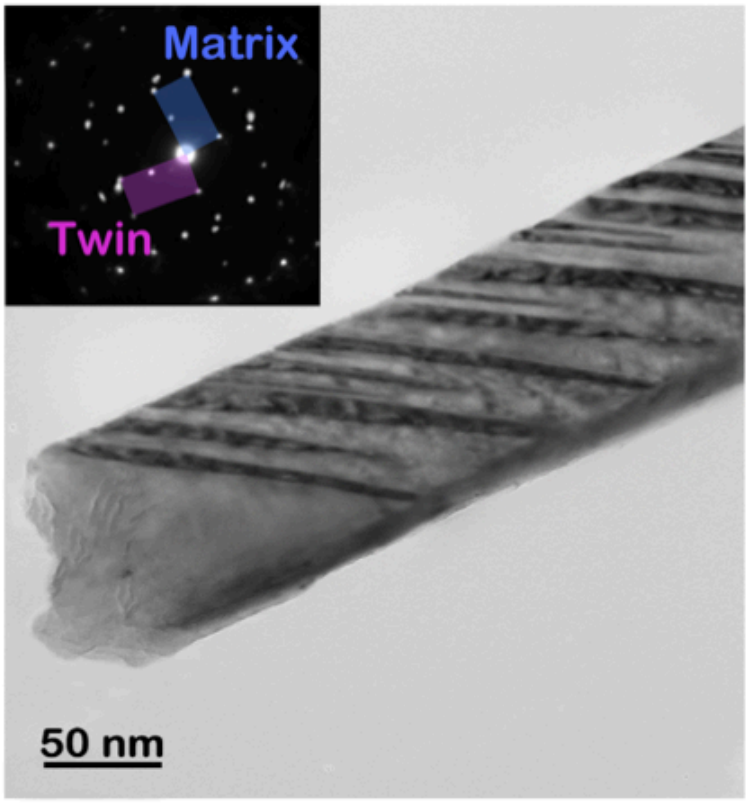

Figure 2. 17 The bright field TEM image that shows an example of the formation of nanotwins and the structure of nanotwinned arrays formed in tension. The related diffraction pattern for the twins and the matrix is also shown.

Fracture occurred at the end of the twinned region (Figure 2. 18 captures one of the fracture events; the image of the same sample before test is inserted for comparison). Compared to the ultimate tensile strength of ~120 MPa and ~5% fracture strain in bulk pure Mg, the mechanical properties of our small sample are impressive: on a per-volume basis our sample absorbs 2000% more mechanical energy (the average is $\sim 1.5\times10^{8}$ J/m^{3}) to failure than microstructure-optimized

bulk pure Mg. We regard this as approaching an upper-bound or "intrinsic" toughness of pure Mg.

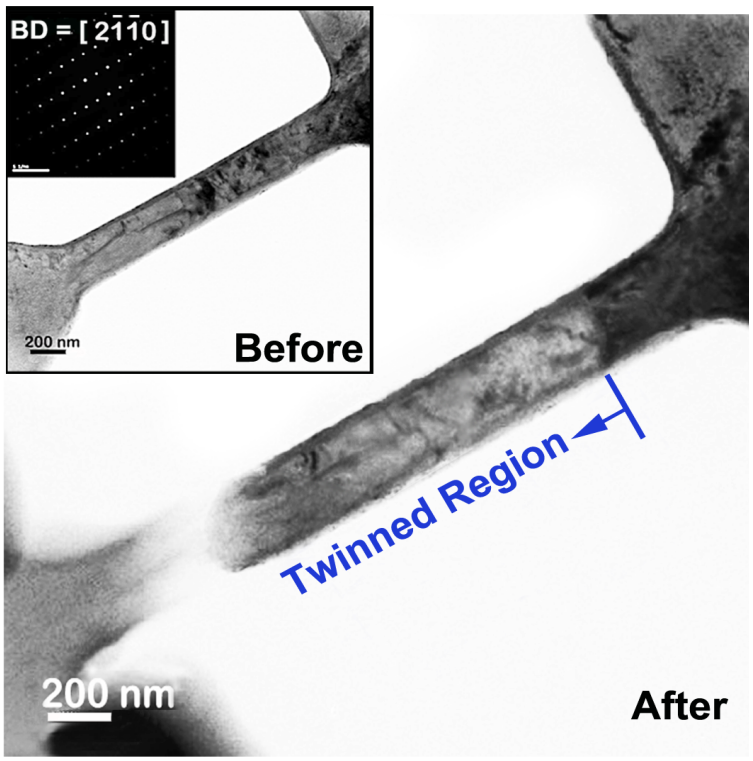

Figure 2. 18 Fracture event in tensile test, which occurred at the end of the twinned region; the image of the same sample before test is inserted for comparison.

Another interesting point is the strain hardening process after the twin formation in tension, which is significantly different from the strain softening we observed in compression. The near-linear strain hardening stage after the strain burst can be observed in most of the tensile curves. This response is similar to the stage 2 in plastic deformation of some bulk materials where the increase in "obstacles" produced by the activity of the primary deformation system strongly influences the activation of the secondary deformation modes. However, in our case, strong dislocation interactions are not expected due to the small sample size and ease of dislocations escaping to the nearby surfaces. What we have instead is a large number of nanotwin boundaries that could serve as "obstacles" and harden the material. As shown in Figure 2.17, in tension multiple nanotwins are distributed along the gauge section. From all the tensile samples, the most common nanotwin thickness was about 5-10 nm. High-resolution TEM analysis revealed even finer

twin structures along the edge of the gage section where the spacing between twins could be only several atomic layers, as shown in Figure 2. 19. The high density of twin boundaries restricts dislocation motion and results in strain hardening, consistent with the "TWIP" concept.

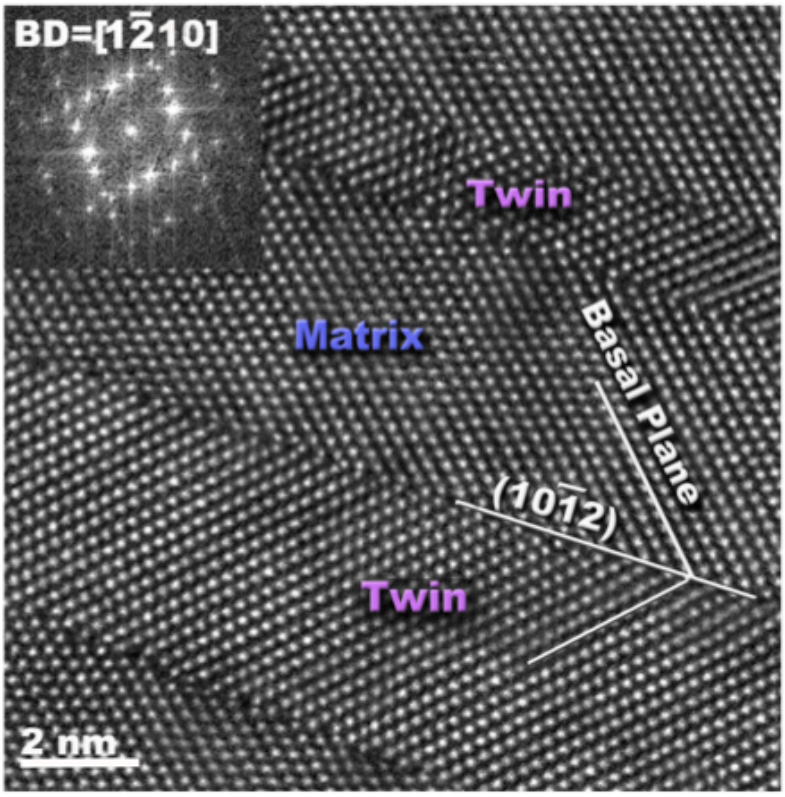

Figure 2. 19 High-resolution TEM image of the nanotwins in deformed tensile sample, which revealed even finer twin structures along the edge of the gage section where the spacing between twins could be only several atomic layers as shown in.

2.2.2.2 Nanobending tests

Deformation nanotwins also appeared under bending at a crack tip. One example is demonstrated here, where the abilities of the nanotwins to accommodate large strain and toughen the sample are demonstrated. In the video, the formation of crack can be observed first. In the specific case that is being shown here, two cracks can be seen to form under bending on the tensile side of the beam about two-thirds of the way down from the tip (the crack positions varied from sample to sample, as a result of the surface roughness). Figure 2.20 shows a bending bar before test and Figure 2.21 shows the image for the crack formation. We have more samples in which the crack formed close to the hinge of the bending where

TEM analysis showed the nanotwined structure also. The main reason for the variation of crack formation sites comes from the surface roughness of the bending specimens.

We can see from the image in Figure 2.20 that the surface of the beam is not perfect flat. Even from this 2-D projected TEM image, we can see the change of width. The width changes only several nanometers, but according to the equation: I=1/12*[h(x)]^3*b(x), and S=w*h*(L-x)/2I, a small change in h(x) and b(x) can significantly change the stress in a small beam with h around 100-200 nm. The non-uniform cross section is mainly introduced when we used Ar+ beam to clean our FIB-machined sample in order to remove the FIB damage. The low energy Ar+ source is not as focused as the Ga+ source. The tradeoff was that we wanted clean samples but this induced a surface roughness.

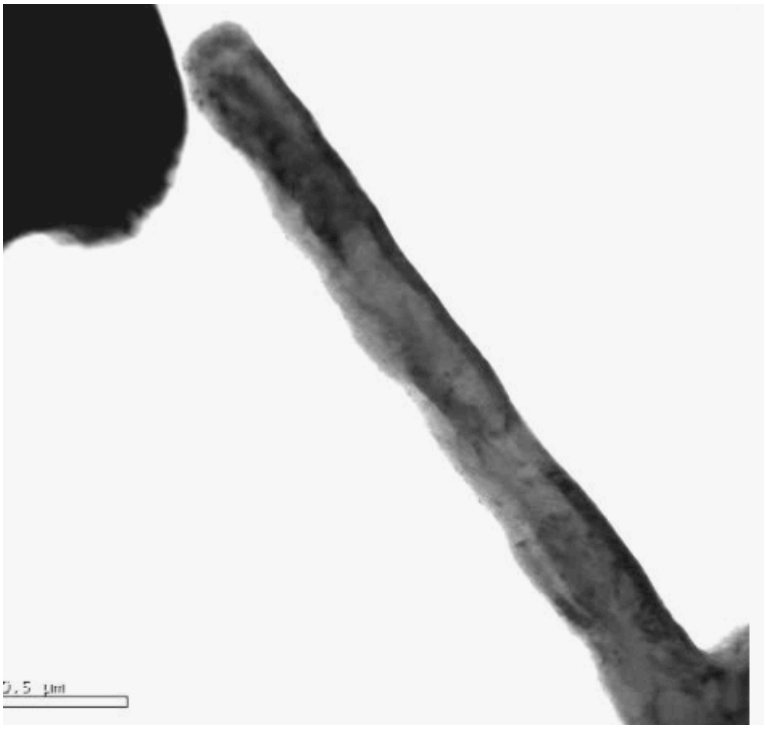

Figure 2.20 The bright field TEM image of a bending bar before *in situ* TEM bending test.

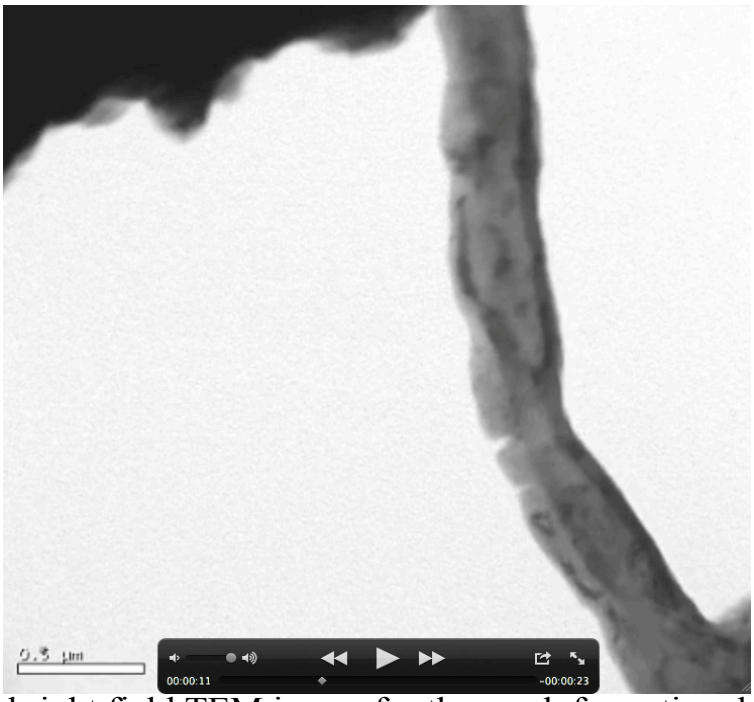

Figure 2.21 The bright field TEM image for the crack formation during bending.

As the larger crack fully opened, the nanotwinned region nucleated and subsequently strongly deflected the crack as shown in Figure 2.22. This is similar to transformation toughening in ceramics, where martensitic transformations near the crack tip increase the fracture toughness, and is also consistent with previous modeling results in which a crack can stimulate twin formation. Subsequent diffraction analysis demonstrated that the twinned region is only localized near the crack tip and is composed of $\{10\bar{1}1\}$ contraction twins, which is not surprising given the large stress gradient.

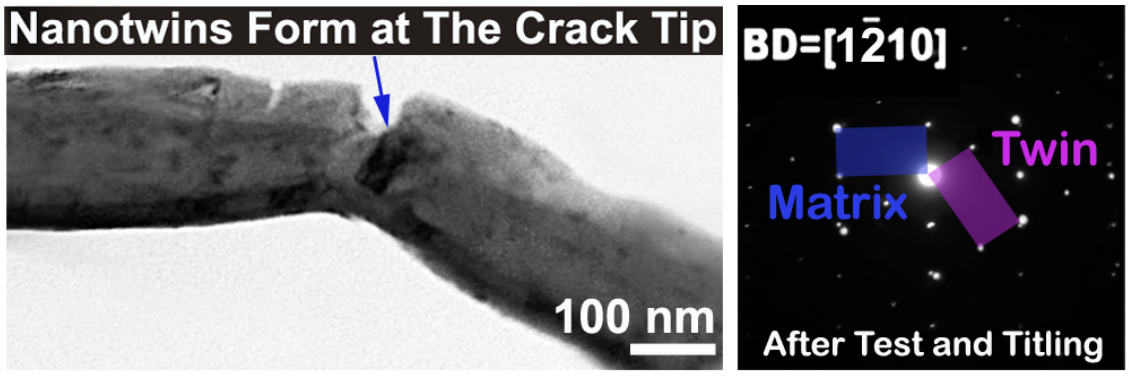

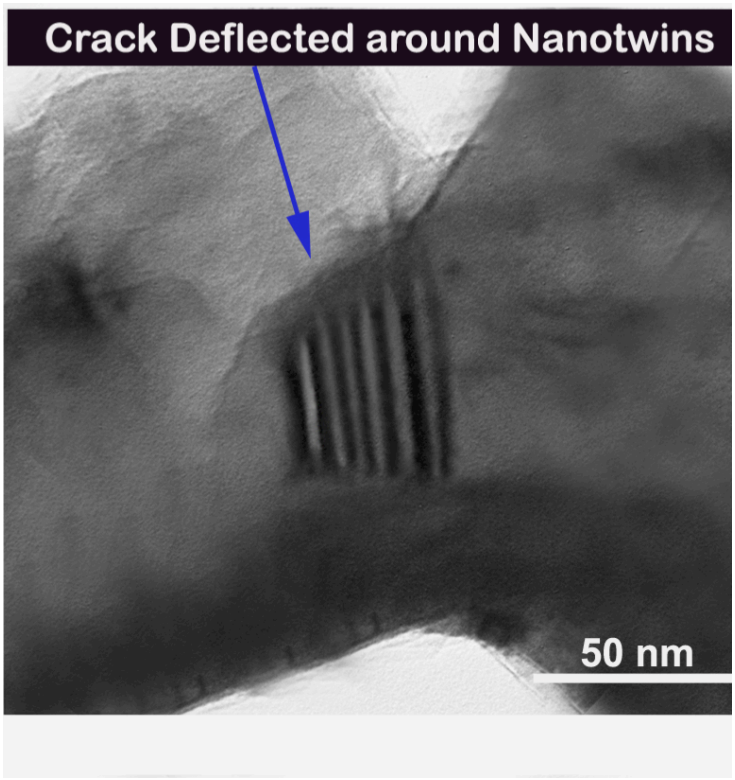

Figure 2.22. The formation of the nanotwinned region at the crack tip, which strongly deflected the crack propagation.

The nanotwined structure can be clearly seen in the HRTEM images, similar to that observed in the tensile samples (Figure 2.23). Extension twins were also found in some bending samples, an example of which is also shown in Figure 2.23. The lattice rotation for about 86 degree can be seen from the extension twin $\{10\bar{1}2\}$. The zone axis is $[1\bar{2}10]$. The lattice rotation for contraction twin is about 137 degree. The HRTEM images clearly show that the twin spacing here is about several nanometer. Large number of twin boundaries can be seen.

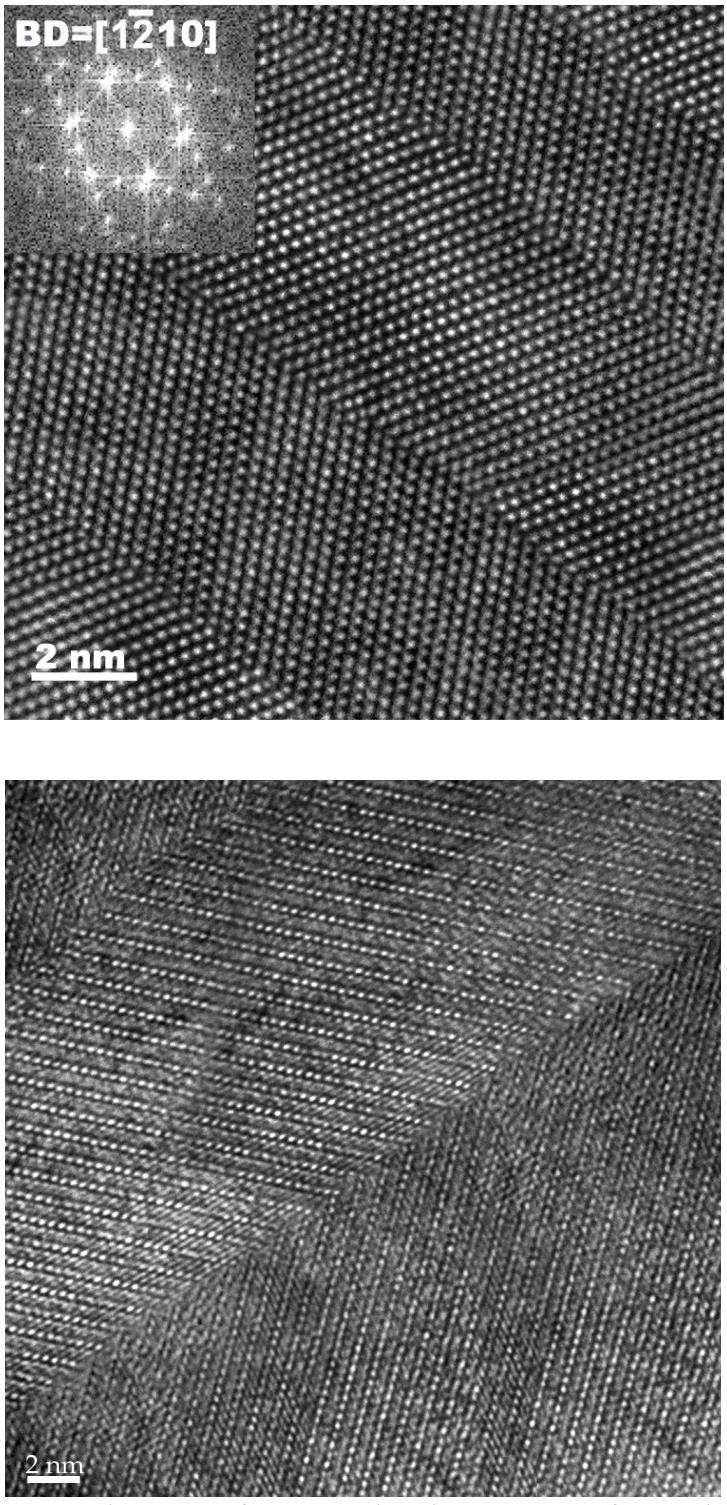

Figure 2.23. HRTEM image of nanotwined structure formed in *in situ* TEM bending tests. Both extension twin and contraction twin were observed.

2.3 Discussion

2.3.1 Twin induced plasticity

These tensile and bending experimental results give a very different picture of deformation twinning in the extremely small samples as compared to the traditional understanding where the entire lattice reorients within a twinned region. The structures are also different from so-called double twinning reported in bulk-textured Mg. Nanotwins structure has been reported in steel and copper, where the Twinning induced plasticity (TWIP) is significant (*68, 73*).

TWIP steel

Steels are currently either strong for the car frame but not very ductile and break when overloaded, or they are ductile for the chassis, but relatively weak. TWIP steel, invented several years ago by Professor Georg Frommeyer, has been engineered for enhanced ductility to absorb energy in the event of a vehicle collision, while maintaining its stability and strength to protect the passenger cabin (*28*). TWIP steel is a high-strength steel concept with superior formability, which may be close to being produced industrially. Comprising about 20% manganese and small quantities of carbon, aluminium and silicon, TWIP steel can be stretched by up to 90% of its length without breaking. The new alloy is similar to transformation induced plasticity (*74*) steels (*74*), which have been on the market for about 10 years. But TWIP steel is said to have greater reserve ductility. The hardening rate – the increase of strength with increasing deformation – of TRIP steels is higher. Therefore, deformability is more quickly exhausted. The better ductility of TWIP steel comes from stacking faults in its crystal lattice. If extra two stacks of atomic planes are introduced to the lattice from above, it disturbs the regular sequencing of the atomic planes, forming a stacking fault on a mirror plane and creating regularly mirrored sections of crystal. Twinning then forms.

B. C. De Cooman et al., (*75*) studied the mechanical properties of TWIP steel and performed the TEM analysis. It is reported that in TWIP steel deformation is achieved by dislocation motion and twinning. The TWIP-effect is mainly due to a dynamic Hall-Petch effect. As the formation of deformation twins induce new crystal orientations, the twin boundaries basically reduce the effective mean free path of dislocations and enhance the dislocation interaction inside. Dislocations will also need to interact with large number of twin boundaries, so that new dislocations may be generated out. The strong dislocation activities further enhance the flow stress, resulting in a high strain hardening behavior. By TEM

studies, they reported that the twinning microstructure was very fine. The dislocations were clearly widely dissociated. In addition, wide stacking faults were often found to be emitted from grain boundaries. At low strains, the dislocation density increases and the grain boundaries seem to be particularly effective source of isolated stacking faults. Therefore, the deformation mechanism of TWIP steel at low strains is considered to be planar slip and the formation of wide stacking faults. The onset of twinning requires multiple slips within deformed grains. Frequently one twinning system is activated, together with dislocation glide. These high aspect ratio twins cross the entire grain. In addition, the twins are internally faulted. High resolution TEM clearly reveals their very narrow width. The twins are very thin and there seems to be a continuous nucleation of new deformation twins of increasingly smaller size.

Twinning-induced plasticity in Mg

The twin boundary energy in Mg is indeed much higher than that in steel or copper. For example, the twin boundary energy for Cu is about 15 mJ/m^{-2}, but the number is 120 mJ/m^{-2} for Mg. So the formation of nanotwins with high density of twin boundary is not energetic favorable. In order to elucidate the origin of this high-energy nanotwinned structure, we have done a series of theoretical studies. We performed molecular dynamics (MD) simulations of single-crystal Mg tensile tests along <0001> direction. The results show that $\{10\bar{1}2\}$ twins nucleate from surface edges and we can extrapolate that the critical nucleation stress should be about 800 ± 200 MPa under low strain rates (10^{-2} s^{-1}), agreeing with our experiments. However, since the high strain rates ($>10^{6}$ s^{-1}) in direct MD simulations are not appropriate for describing the kinetics of multiple deformation twins, we need a mesoscopic model to carefully consider the kinetics of twinning nucleation and growth.

Deformation twinning is a perfectly coherent “stimulated slip” phenomenon, in contrast to the less coherent “spontaneous slip” of ordinary dislocation plasticity(*50*). Slip coherency is catalyzed by promoter defects of different dimensions, which could be screw dislocations (as in the various pole mechanisms of twin nucleation), surfaces or grain boundaries. Figure 2.24 is the single sketch to illustrate this concept.

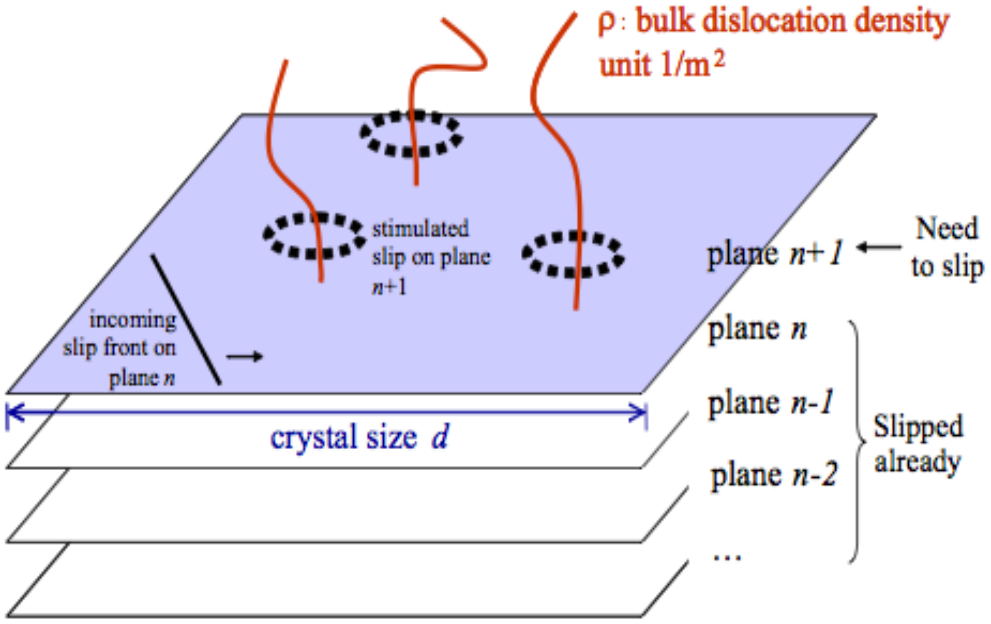

Figure 2.24. The "stimulated slip" model for the formation of deformation twinning.

The promoter defects interact with a gliding twinning dislocation, and subsequently "infect" an atomically adjacent plane to start slipping by the *same variant* of the twinning dislocation Burgers vector b_{TW}. Promoters of different dimensions can be dominant at different length scales. In small samples or near crack tips, the dominant promoter would be the 2D free surface as shown in our MD simulations. Based on this "stimulated slip" concept, we have performed mesoscale kinetic Monte Carlo (kMC) simulations to model the nanotwinning process observed in our experiments.

2.3.2 Molecular Static Simulation for Stress Field of Nanotwin

In order to further investigate the twinning mechanism and to compare with the experimental results, we collaborate with Dr Liang Qi and Ju Li to build the modeling part. A molecular static simulation was performed by LAMMPS Molecular Dynamics Simulator with EAM (Embedded Atom Model) interatomic potential for Mg(*76*). 400000 atoms were used in a 210 nm × 172 nm × 0.32 nm box with free surfaces on both x ($<10\bar{1}\bar{1}>$) and y (perpendicular to $\{10\bar{1}2\}$ plane) directions but periodicity along z direction. A nanotwin (20 nm along $<10\bar{1}\bar{1}>$ direction and 4 nm perpendicular to $\{10\bar{1}2\}$ plane) was produced from the surface by continuous slip of $\{10\bar{1}2\}$ planes with Burgers vector of 0.49 Å along $<10\bar{1}\bar{1}>$

direction. Both top and bottom $\{10\bar{1}2\}$ planes were fixed so that total engineering shear strain along $<10\bar{1}\bar{1}>$ direction was 0.01. Under such a constraint, conjugate gradient relaxation was performed in order to reach the local minimum state. The distribution of atomic shear stress σ_{xy} was calculated and shown in Figure 2.25. The stress intensity decreases from red to blue. So the stress intensity at the twin tip is the highest, consistent with the previous TEM observation. The stress intensity near the twin boundary, however, is lower than that in the area, which is some distance away from the twin boundary.

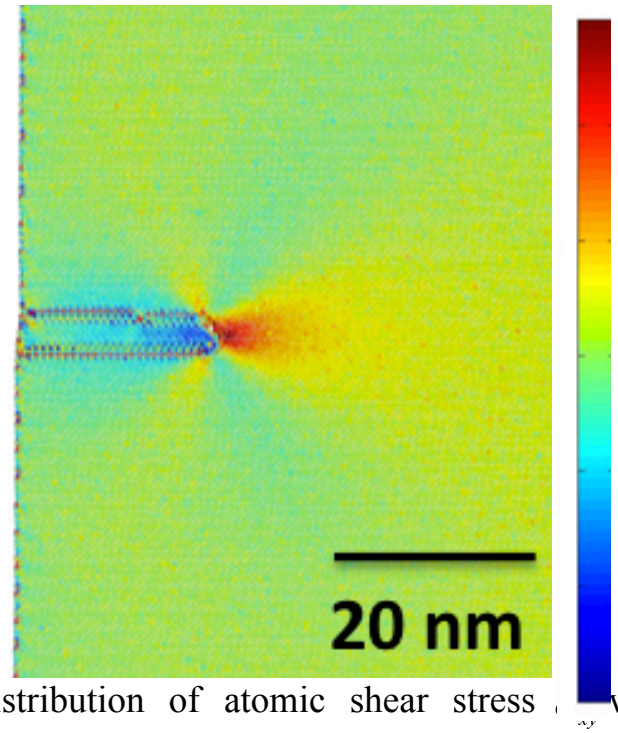

Figure 2.25 The distribution of atomic shear stress σ_{xy} was calculated by molecular static simulation.

2.3.3 Molecular Dynamic Simulation for Twin Nucleation in Tensile Tests

Molecular dynamics simulations were performed by LAMMPS to investigate the nucleation mechanism of deformation twinning in tensile tests of Mg single crystal along $<0001>$ direction, and two different EAM interatomic potentials for Mg were applied to reach consistent results. MD samples were made into rectangular shapes with perpendicular x ($[2\bar{1}\bar{1}0]$), y ($[01\bar{1}0]$) and z ($[0001]$) axis, respectively, and periodic boundary condition along z-axis. All the tensile tests were performed at temperature of 300 K and MD relaxation of 1 nano-second

under 300K was performed before each tensile test. We have tested samples with different sizes, strain rates (10^6 s^{-1} – 10^{10} s^{-1}), surface conditions (clean without vacancies and rough with high concentration of vacancies) and EAM potentials. All the results show that deformation twins nucleate from the edges between the intersections of two facets, and the critical stress for twin nucleation should be in the range of 600~1000 MPa under the strain rate of ~10^{-2} s^{-1} (the strain rate in real experiments) from extrapolation approximations (Details in the following paragraphs), which explains the origin of high stress of twin nucleation observed in the experiments.

Figure 2.26 shows the detailed results for MD tensile test of 10 × 10 × 30 nm^3 sample with clean surfaces under strain rate of 2 × 10^7 s^{-1}. In Figure 2.26 (a), the stress-strain curve initially behaves as a straight line with slope of 56 GPa. When the stress reaches 2.8 GPa, it suddenly drops to almost zero, corresponding to the nucleation and growth of deformation twin as shown in Figure 2.26 (b), (c) and movie, where the twin is nucleated from the edge between two surfaces ($(2\bar{1}\bar{1}0)$ and $(01\bar{1}0)$). To obtain a clear picture of the twin type and formation mechanism, a cross section near $(2\bar{1}\bar{1}0)$ surface is plotted in Figure 2.25 (d) and (e), which clearly show that this twin embryo is $\{10\bar{1}2\}<10\bar{1}\bar{1}>$ type of extension twin, composed by partial dislocations on $\{10\bar{1}2\}$ planes.

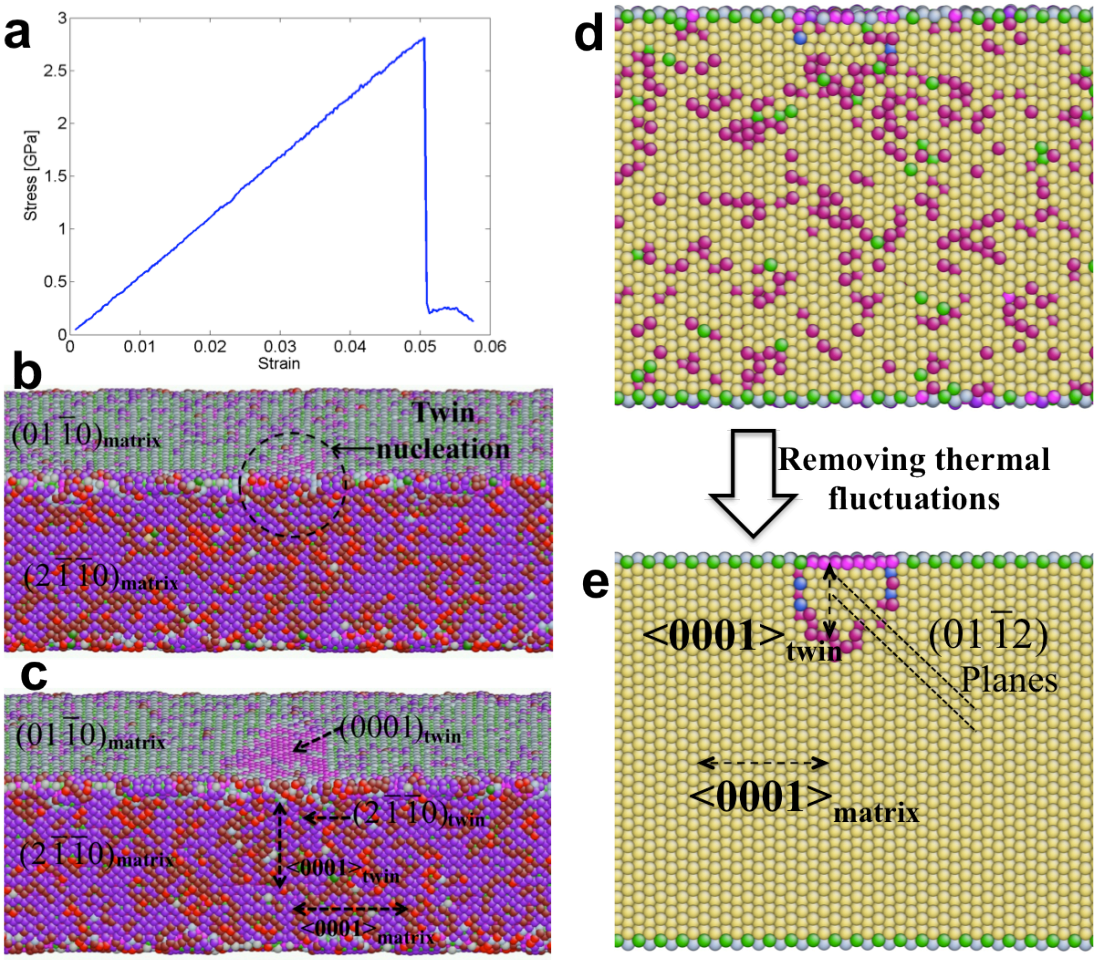

Figure 2.26 (a) Stress-strain curve for MD tensile test of 10 × 10 × 30 nm^3 sample with clean surfaces at T = 300 K and under strain rate of 2 × 10^7 s^{-1}. Mg EAM potential from Ref. 4 was applied. (b) and (c): Nucleation and propagation of extension twin embryo on the edge between two facets at the critical stress obtained from MD simulations. Here two different surfaces of the sample are shown and different colors mean different coordination number (*77*) of atoms (yellow: CN = 12 for Mg in bulk lattice; magenta: CN = 9 for Mg on (0001) surface). The local variations of CN numbers result from thermal fluctuation at T = 300 K. (d): Cross section of a $(2\bar{1}\bar{1}0)$ plane near the sample surface after twin nucleation. (e): 50 steps of conjugate gradient relaxation were performed to the MD configuration of (d) to remove the effect of thermal fluctuation in order to obtain a clear illustration. The boundaries between twin and matrix are partial dislocations on $(01\bar{1}2)$ planes, as shown on the tilted dashed lines. The <0001>

directions of the matrix and the twin are almost perpendicular to each other, which is the typical character of $\{10\bar{1}2\}<10\bar{1}\bar{1}>$ type of extension twin.

However, the critical stress for the twin nucleation (2.8 GPa) from the above calculation is too high compared with our experimental value (~800 MPa). We believe it mainly results from two factors: surface defects and strain-rate effects. In real experiments, all samples are produced by FIB processing and following high-energy Ar^+ cleaning, so the surface should be very rough with high concentration of defects. These defects could facilitate the nucleation process and decrease the critical stress. Meanwhile, the strain-rate in MD (~10^7 s^{-1}) is much higher than that of real experiments (~10^{-2} s^{-1}), which also significantly change the critical stress values. Thus we first produced MD samples with rough surfaces, as shown in Figure 2.27 (a), where the surface roughness was made by superpositions of sinusoidal waves plus random-noise perturbations. Then samples with different sizes and surface conditions (clean and rough) were calculated under different strain rates (from 10^6 s^{-1} to 10^{10} s^{-1}) and EAM potentials. We expect the critical stress and the strain rate have certain power-law relations, thus we plot the $\log_{10}$(critical stress) vs. $\log_{10}$(strain rate) in Figure 2.27 (b) and extrapolate them into the regions of low strain rates. The results show that the surface defects can lower the critical stress by 300~500 MPa under the same strain rate. But more significant effects come from the strain rates: from the calculations of a series of samples, we can see that $\log_{10}$(critical stress) and $\log_{10}$(strain rate) have approximate linear relations; if we extrapolate the strain rate to the experimental value (10^{-2} s^{-1}), the critical nucleation stress could be in the range from $10^{2.8}$ to $10^{3.0}$ MPa (600 ~ 1000 MPa), which is almost the same as the experimental observations.

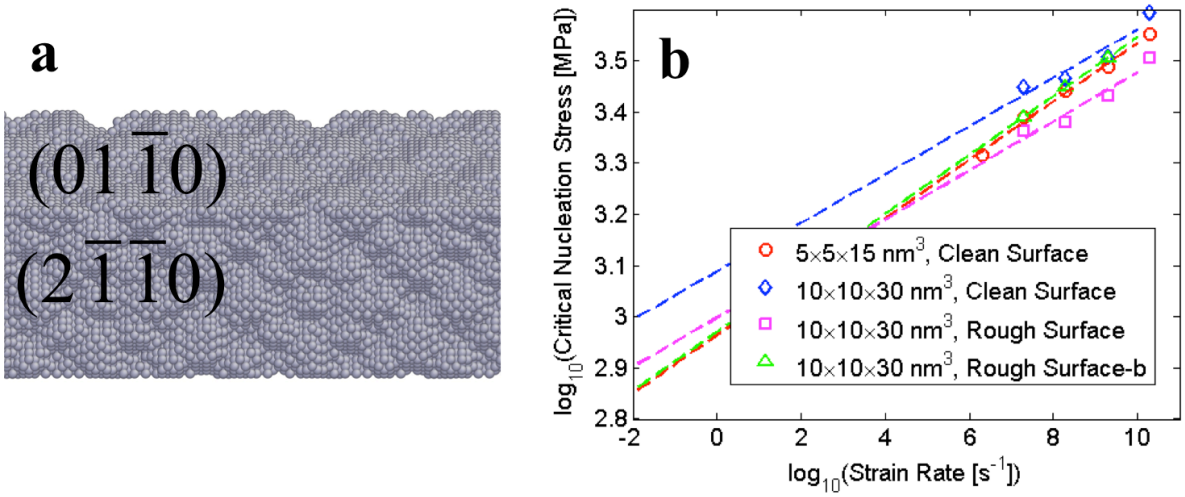

Figure 2.27 (a) MD sample with rough surfaces of $(2\bar{1}\bar{1}0)$ and $(01\bar{1}0)$ and periodic boundary conditions along $<0001>$ directions. (b) Changes of critical nucleation stress of deformation twinning with strain rates for samples with different sizes, surface conditions and EAM potentials. Here except that the "10×10×30 nm^3, Rough Surface-b" sample was performed with potential from Ref. 7, all other samples were tested with potential from Ref. X. Y. Liu, J. B. Adams, F. Ercolessi et al., Modelling and Simulation in Materials Science and Engineering **4** (3), 293 (1996).

It might be worth to point out that these MD simulations cannot repeat the process of dense nanotwin array formation as our experiments. The main reason is also from the strain-rate effects. It is believed that the twinning nucleation is a kinetic phenomenon highly dependent on the strain rate. All our MD calculations can only be performed at extremely high strain rates compared with experiments, so it may reveal the deformation mechanism and dynamics of deformation twinning, but cannot produce the correct kinetics under low strain-rates.

2.3.4 Kinetic Monte Carlo Simulation

A kinetic Monte Carlo simulation was performed based on a 2-D twinning dislocation (TD) model shown in Figure 2.28.

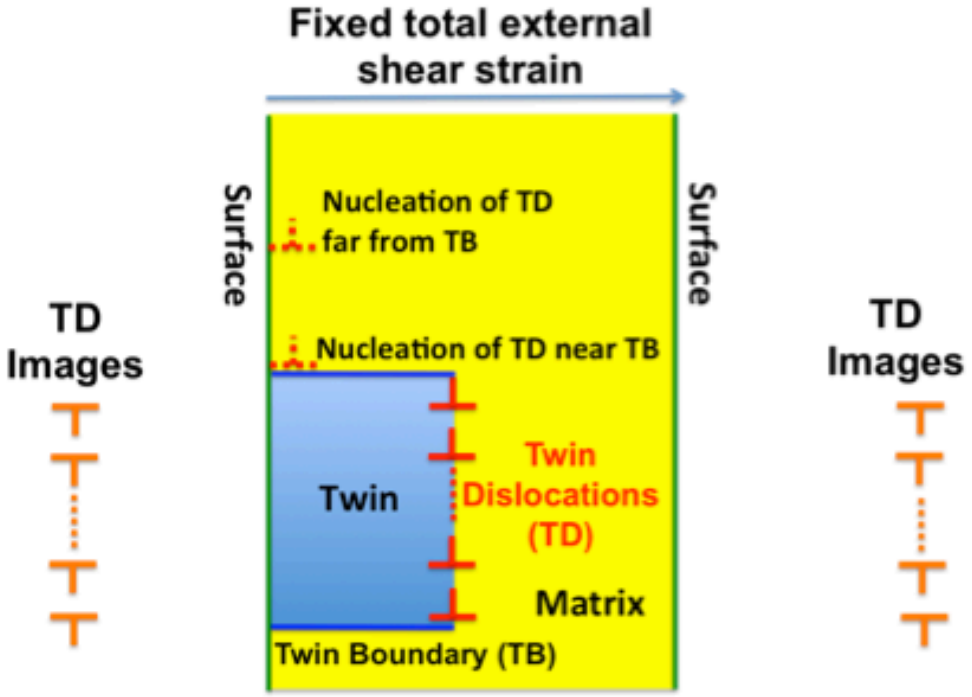

Figure 2.28. 2-D twinning dislocation (TD) model

Once we have a twin embryo, there are two types of possible events: TD nucleate and glide on the atomic plane adjacent to existing twin boundary (TB) (thickening of the existing twin); TD nucleation far from TB (nucleation of a new twin). TD nucleation rate is written as a typical Arrhenius relation (*78*)

$$\nu = \nu_0 \cdot \exp(-\frac{Q(\sigma)}{k_B T}) \quad (16)$$

Here we set $\nu_0 = 1 \times 10^{13}$ s^{-1} and T = 300 K. $Q(\sigma)$ is assumed to be linearly dependent on σ_S, the local shear stress field generated by both external shear strain and all TD, as

$$Q(\sigma) = Q_0 - \sigma_S \cdot \Omega \quad (2)$$

Here Ω is defined as activation volume. TD nucleation on existing twin boundary (TB) would have less Q_0 than those far from TB, because in the former case there is no new TB production. Here we set Q_0 = 0.60 eV for the former and 0.85 eV for the latter. Ω is set as 115 $Å^3$. At each nucleation and migration event, TD moves forward on the slip plane by one lattice spacing. Here the lattice structure and slip system of $\{10\bar{1}2\}<10\bar{1}\bar{1}>$ of Mg are applied so that each time TD migrate

by 7.61 Å, and the distance between adjacent slip planes is d_{SP} = 3.80 Å. The migration rate is also assumed to be linearly dependent on the applied stress:

$$v_S = M \cdot \sigma_S \quad (3)$$

We then set M = 2000 $Pa^{-1}\cdot s^{-1}$ so that the average glide velocity of TD under shear stress σ_S = 500 MPa is approximately 1000 m/s. σ_S is generated by the fixed external shear strain, TD and their surface images. The shear stress field of single TD or TD surface image is described by classical dislocation elastic theory as

$$\sigma_{xy} = \frac{Gb_{TD}}{2\pi(1-v)} \cdot \frac{x(x^2-y^2)}{(x^2+y^2)^2} \quad (16)$$

where x is coordinate along slip direction and y is along direction perpendicular to slip plane. G is shear modulus; here we set G as 19 GPa from first-principles calculations under the slip system of $\{10\bar{1}2\}<10\bar{1}\bar{1}>$ of Mg[6]. b_{TD} is the Burgers vector of TD and equal to 0.49 Å for $\{10\bar{1}2\}<10\bar{1}\bar{1}>$ twin, and it changes the sign for TD surface images[5]. Poisson's ratio is 0.3 here.

The size of simulation cell is 200 nm along $<10\bar{1}\bar{1}>$ direction and 760 nm perpendiculars to $\{10\bar{1}2\}$ plane. The external engineering shear strain is fixed as γ = 0.03, and the external shear stress is calculated as

$$\sigma_S^{ext} = G\,\gamma \cdot (1 - \frac{V_{Twin}}{V_{Tot}} \cdot \frac{b_{TD}}{d_{SP}}) \quad (16)$$

where V_{Twin} and V_{Tot} is the volume of deformation twinning and total simulation cell. So the total shear stress at each investigated point is

$$\sigma_S = \sigma_S^{ext} + \sum \sigma_{xy} \quad (6)$$

where the summation is performed upon each TD and its two images on both surfaces. 130000 simulation steps were performed and the result is shown in movie.

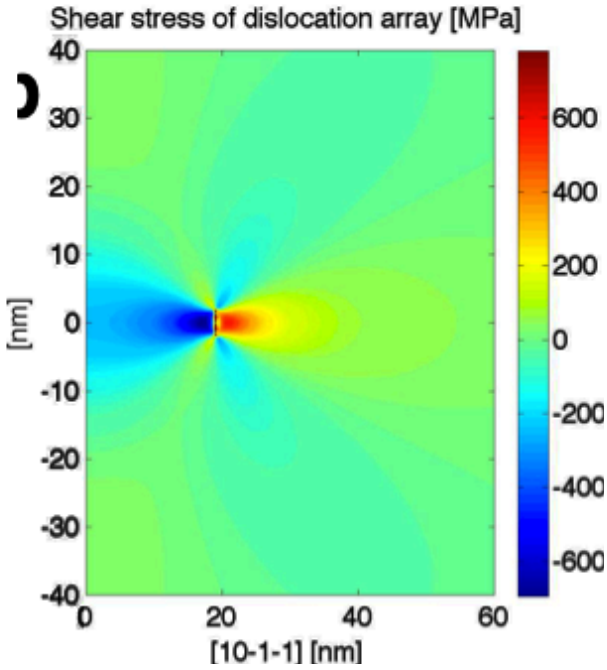

Figure 2.29, The stress filed produced by a twin from continuum calculations.

As shown in Figure 2.29, continuum calculations also indicate that elastic incompatibilities of twinning dislocations in the sample will generate a strong elastic field that biases the nucleation rate of new twinning dislocations on a nearby surface, as:

$$\nu = \nu_0 \cdot \exp(-\frac{Q(\sigma_S)}{k_B T})$$

where $Q(\sigma_S)$ is the stress-dependent activation energy for surface-catalyzed twinning dislocation nucleation, and σ_S is the shear stress at the surface. $Q(\sigma_S)$ can be further approximated by:

$$Q(\sigma_s) = Q_0 - \sigma_S \cdot \Omega$$

where Ω is the activation volume. As shown in Figure 2.30, the simulation super-cell is composed of parallel atomic layers as possible dislocation glide planes, and twinning dislocations can be nucleated on each layer at the surface with the same Q_0 and σ_S initially. Once nucleated, the dislocation glides on this layer with velocity linearly dependent on σ_S, which is updated in the kMC model by summing the stress fields of all twinning dislocations based on classical elasticity theory. Consequently, although a twinning dislocation nucleated adjacent to an

existing twin boundary has a smaller Q_0 than one nucleated further from the boundary, since there would be no increase of twin boundary if an existing twin thickens, the elastic field generated by twinning dislocations of the same sign at the nanotwin tip can suppress nucleation near the twin, but promote nucleation at some distance away from the twin. As a result, the stress field of the twinning dislocations at the tip affects the nucleation of new twinning dislocations; the formation of many nanotwins is actually favored over the thickening of an individual twin (Figures 2.30).

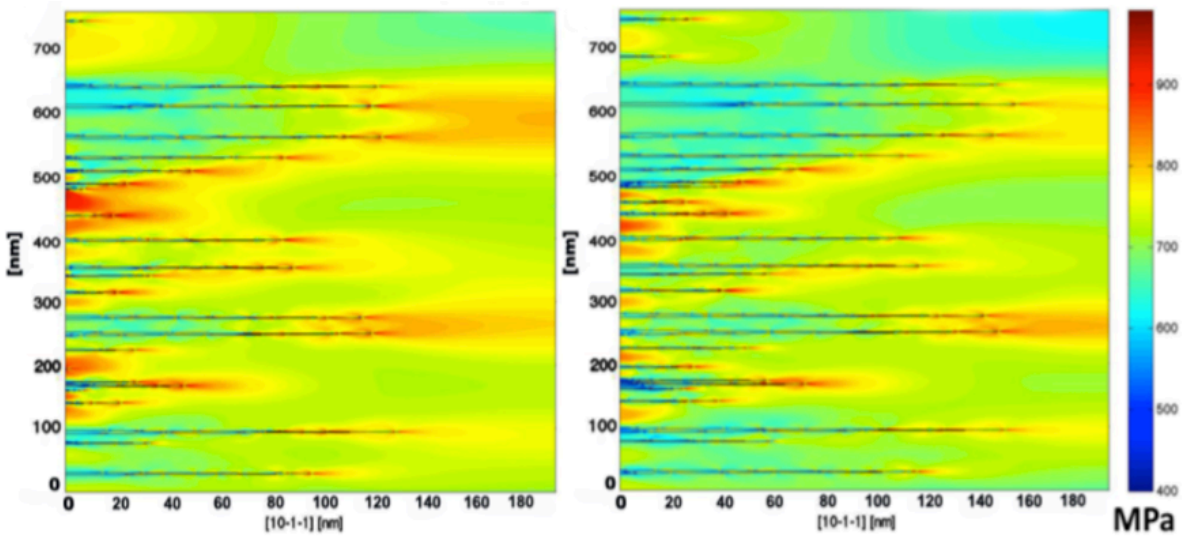

Figure 2.30 kinetic Monte Carlo simulation results of nanotwins and corresponding shear stress field based on model in Figure 2.28. Zero in x-axis is the surface and twin boundaries are plotted in solid lines. Comparing the evolution from left to right, we can clearly see the new TDs nucleated from high stress areas (red color) but no TDs from low stress areas (blue).

2.4 Movies

1 Compression
http://l1.mit.edu/ql/Manuscript/Yu11/Movie/compression.mp4
2 Tension
http://l1.mit.edu/ql/Manuscript/Yu11/Movie/tension.mp4
3 Bending
http://l1.mit.edu/ql/Manuscript/Yu11/Movie/bending.mp4
4 kMC Simulation *(blue: matrix; red: twin)*
http://l1.mit.edu/ql/Manuscript/Yu11/Movie/kMC.avi
5 MD Simulation

http://l1.mit.edu/ql/Manuscript/Yu11/Movie/Nucleation.avi

2.5 Conclusions

The above simulation indicates that high-density nanotwins can be "promoted" kinetically when high density of nucleation sites are correlated by the stress fields of twinning dislocations. As the surface to volume ratio in the nanosized-samples is high, surface nucleation of dislocations is more intense. Similar to the surface sites in our samples, grain boundaries with high densities of dislocations can also achieve this condition. The local stress at the grain boundary is also much higher than that in the grain. Previous study in nanocrystalline materials showed that the local stress at the nano-grain boundary could be extremely high even the global stress is zero (*79, 80*). Thus the correlated formation of nanotwins should be a general phenomenon in deformation twinning nucleation. However, in larger crystals/grain sizes, nanotwin embryos grow to accommodate the same amount of strain, thus what is usually observed in a twinned bulk sample is the final state where multiple nanotwins have merged into a large twin, which is also predicted by our kMC model. In addition, inhomogeneous deformation can lead to stress concentrations and preferential nucleation sites, making it easier for a single twin to thicken, as in our compression experiments. It is expected that the nanocrystalline materials might be able to quench the nanostructured deformation twinning where the grain boundary to volume ratio is high. Higher density of nucleation sites can be reached given the same volume and higher local stress can be achieved also due to the larger curvature of the grain boundary structure and the limited space to release the local stress concentration. So the formation of nanotwins is considered as a size-dependent deformation twinning behavior and is sensitive to the dimension, strain rate, GSF energy and so on.

In summary, we have observed the fundamental embryonic structure of deformation twinning *in situ* in a TEM. We have directly measured the local stress to nucleate deformation twinning and the intrinsic toughness of pure Mg, both of which are much larger than presently achieved in bulk Mg, indicating large headroom for improvement. Combined with the simulation results, we believe that the formation of dense nanotwin arrays is kinetically favorable at the nucleation stage of deformation twinning even in materials with high twin boundary energies. This nanotwinned structure might be quenched down in confined volume. This study develops our understanding on the kinetic nucleation mechanisms of deformation twinning and can further contribute to the future development of advanced structural materials. For example, it is

conceivable that new alloys or processing schemes could be designed to take advantage of kinetics factors that would preserve nanotwinned structures in nano grains to enhance strength and ductility.

Chapter 3

Size-related dislocation behavior in single crystal Mg

In the previous chapter, the size-related deformation twinning behavior in Mg was studied. The nanostructured origin of deformation twinning was discovered, which has positive influence on both the strength and ductility of material. Our small sample testing indicates the possibility to quench down these nanotwins in materials before the significant twin growth (*81*). The future application relating to this could be engineering the nanotwins into polycrystalline Mg and/or other materials, which even have high twin boundary energy. This should be also possible in nano grains since the larger proportion of grain boundaries in nanocrystalline materials could supply denser and more homogenous twinning nucleation sites.

For dislocation plasticity in Mg, it is commonly reported that the basal slips are dominant slip mode. There are three different basal slip systems, but only two of them are independent. Under a defined loading direction, one certain basal slip will hold the highest priority and dominate the plastic deformation. As we discussed in chapter 1 above, a larger amount of strain can be accommodated by basal slip in bulk Mg. From the results of Kelley et al., (1968), about 40 % engineering strain can be consumed by basal slip only(*54*). However, sample rotation has to happen in order to accommodate the shape change, since the only two independent basal slip systems are far from enough to fulfill the Von Mises criterion that requires at least 5 independent slip systems for arbitrary shape changes. The CRSS of prismatic slip and pyramidal slip in Mg are significantly higher than that for basal slip, leading to remarkable CRSS anisotropy between different slip systems. The highly anisotropic τ_{CRSS} values for activation of different slip mechanisms in Mg results in limited dislocation plasticity, leading to relatively poor ductility and formability. In addition, since the basal slip in Mg has very low critical resolved shear stress (CRSS), which is only about 0.5-1.5 MPa, the materials yield by basal slip usually show very low yield strength. As a consequence, the flow stress usually stays at a very low stress level, such as several MPa; no obvious work hardening can be seen. This is called stage 1 in the

plastic deformation of bulk Mg (*30*).

Significant increase of work hardening rate can be obtained in the following stage 2, where other basal slips may be turned on. But even so, the ultimate tensile strength can only be about 12 MPa. So how to balance the strength and ductility of Mg samples with dislocation plasticity is an important issue that requires further investigation.

Dimension refinement is an efficient method to tune the mechanical properties of materials. As discussed in Chapter 1, the "smaller is stronger" phenomenon is general. The significant strengthening of materials can be achieved by reducing the external/internal dimension of materials. However, relatively few experimental studies of size effects on dislocation plasticity in Mg have been undertaken. In this chapter, the size-related dislocation plasticity in Mg was studied by performing *in situ* TEM tensile tests on samples with different sizes. The size-regulated dislocation behavior and the corresponding mechanical response of samples were also discussed. The size-dependent transition of deformation mechanisms was exploited by combining the HRTEM analysis and the molecular dynamic simulation.

3.1. Sample preparation

All the specimens in this study were made from the high purity (99.9995%) single crystal Mg rod supplied by General Motor (Detroit, USA). The crystal orientation of the long single crystal bars was determined by x-ray diffraction, which showed that the length direction of the single crystal rod was parallel to the C-axis. The thin Mg foils were cut out from the rod and the foils normal was 45 degree off the length direction of the rod. The crystal orientation is shown in the simple sketch in Figure 3.1.

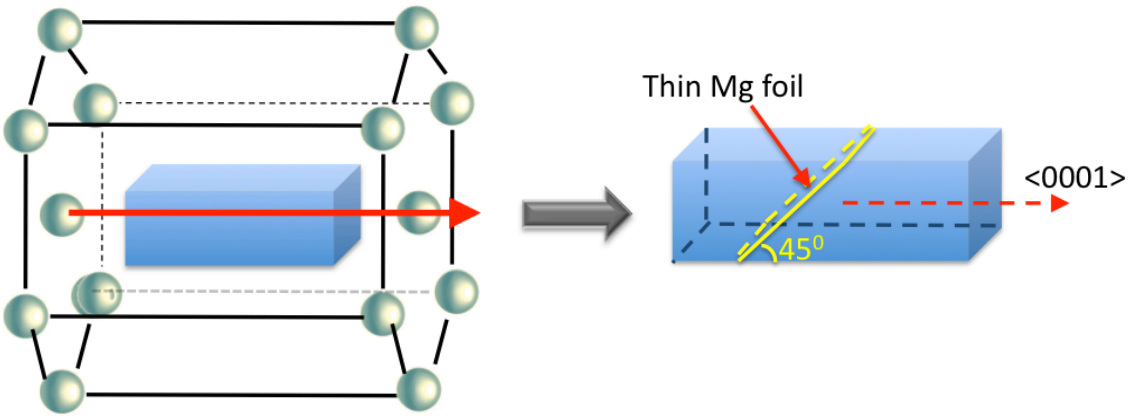

Figure 3.1The crystal orientation of thin Mg foil oriented for basal slip.

All the experiments presented here were performed on pure Mg single crystals loaded in tension along the axis which was 45 degrees off the basal plane normal. The sample orientation is shown in Figure 2.2.

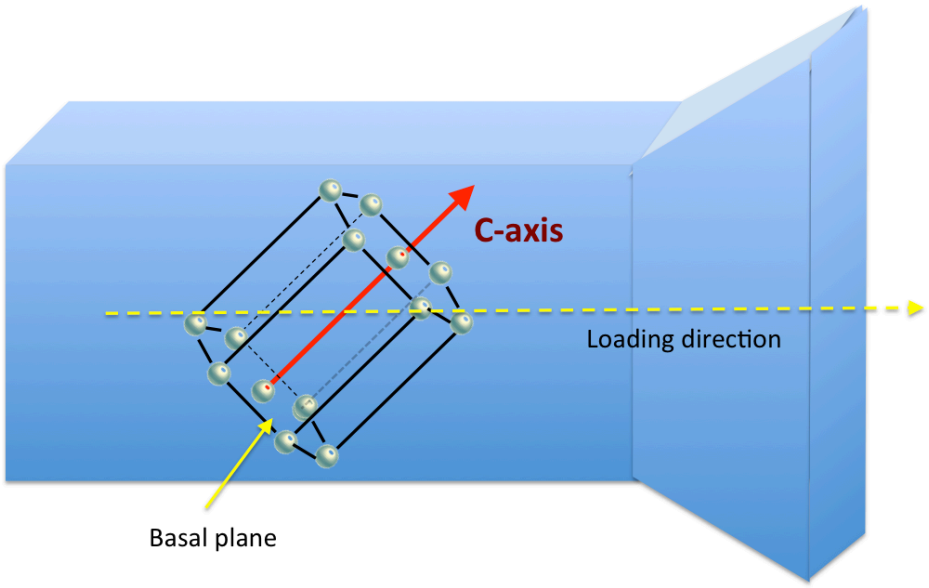

Figure 3.2. The crystal orientation of Mg samples oriented for basal slip.

This orientation was chosen to specifically suppress twinning and facilitate basal slip. As compared to more symmetric cubic crystals such as FCC or BCC metals, the dominance of the basal slip in HCP crystals might simplify the analysis of the plastic behavior. Tensile specimens with gage sizes ranging from 80 nm to 850 nm were machined with a FEI Strata 235 FIB. The milling processes were similar to those described in previous chapter. A Fischione 1040 NanoMill with Ar^+

source was used afterwards to remove the damage layer induced by FIB. *In situ* TEM uniaxial tension tests were performed in a JEOL 3010 TEM with a Hysitron Picoindenter following a method described in previous studies. After the in situ tests, HRTEM studies were performed with a Philips CM300FEG TEM at 300KV and a FEI Technai F20 at 200kV.

3.2. Initial microstructure

Original dislocation structures before mechanical testing were studied first in undeformed samples with different sizes. A series of two beam conditions were used to analyze the Burgers vectors of these pre-existing dislocations. In the largest samples, such as those with width at about 800 nm, dislocation tangling was commonly observed, similar to the microstructure in the bulk Mg material. When the sample size decreased, dislocation tangling became lighter and single dislocation lines or dislocation loops were commonly seen, which laid across the whole width of the gage section. In the samples with extremely small sizes, such as 100 nm and below, dislocation tangling was rarely seen, but single dislocation lines or dislocation loops were still observed. Figure 3.3 below shows the different dislocation structures in different samples before tensile tests.

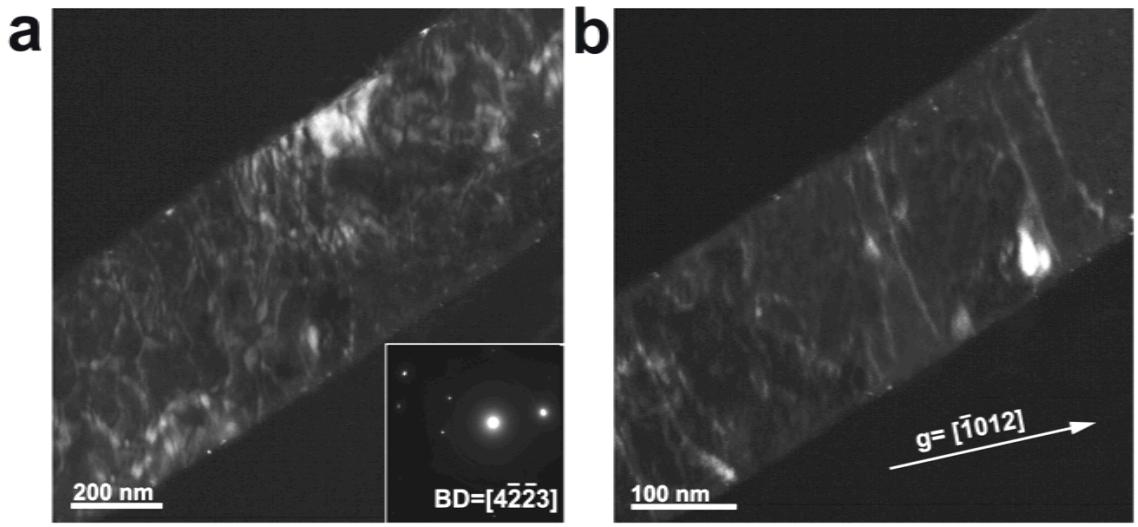

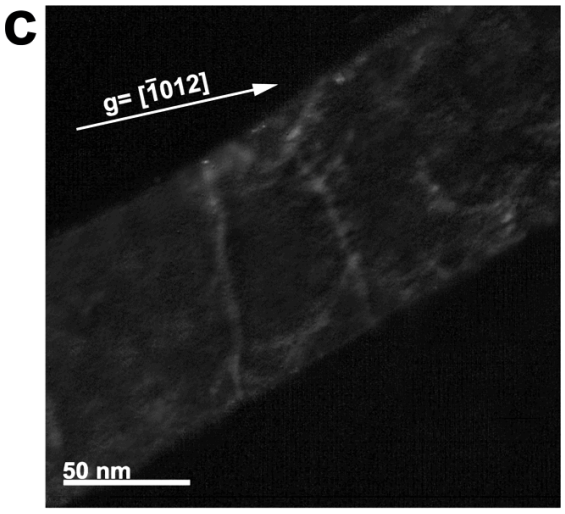

Figure 3.3 (a), (b) and (c) are the dark field images showing the dislocation distribution before tension in samples with size ~600 nm, 200 nm and 80 nm, respectively, g=[-1012].

3.3. Mechanical properties and microstructure analysis from *in situ* TEM testings

3.3.1 DFT Calculation of Ideal Strength of Mg

Sample size effect on the strength of materials has been broadly observed. For comparison, the ideal strength of Mg crystal with this certain crystal orientation was calculated by density functional theory. Dr Liang Qi performed Density functional theory (DFT) calculations by using the Vienna *ab initio* simulation package (VASP). All the calculations were performed in non-spin-polarized condition, and two different types of pseudo-potentials were applied: one is projector augmented wave (PAW) methods with the Perdew-Burke-Ernzerhof (PBE) exchange-correlation functional; the other is ultra-soft (US) pseudo-potential with generalized gradient corrections functional (GGA). Monkhorst-Pack **k**-point grids for the Brillouin-zone integration were applied with **k**-point density higher than 18 per $Å^{-1}$ along each periodic direction in reciprocal space. Partial occupancies of eigenstates were determined by a first-order Methfessel-Paxton smearing of $\sigma = 0.2$ eV. The cut-off energy for the plane wave basis was 400 eV. The relaxed shear stress-strain relation of Mg on basal plane along [11-20] direction is calculated and plotted in Figure 3.4. It shows that the ideal shear stress under such orientation is ~1.8 GPa. If we assume the Schimit factor as 0.5 in our tensile tests, the ideal tensile stress should be ~3.6 GPa.

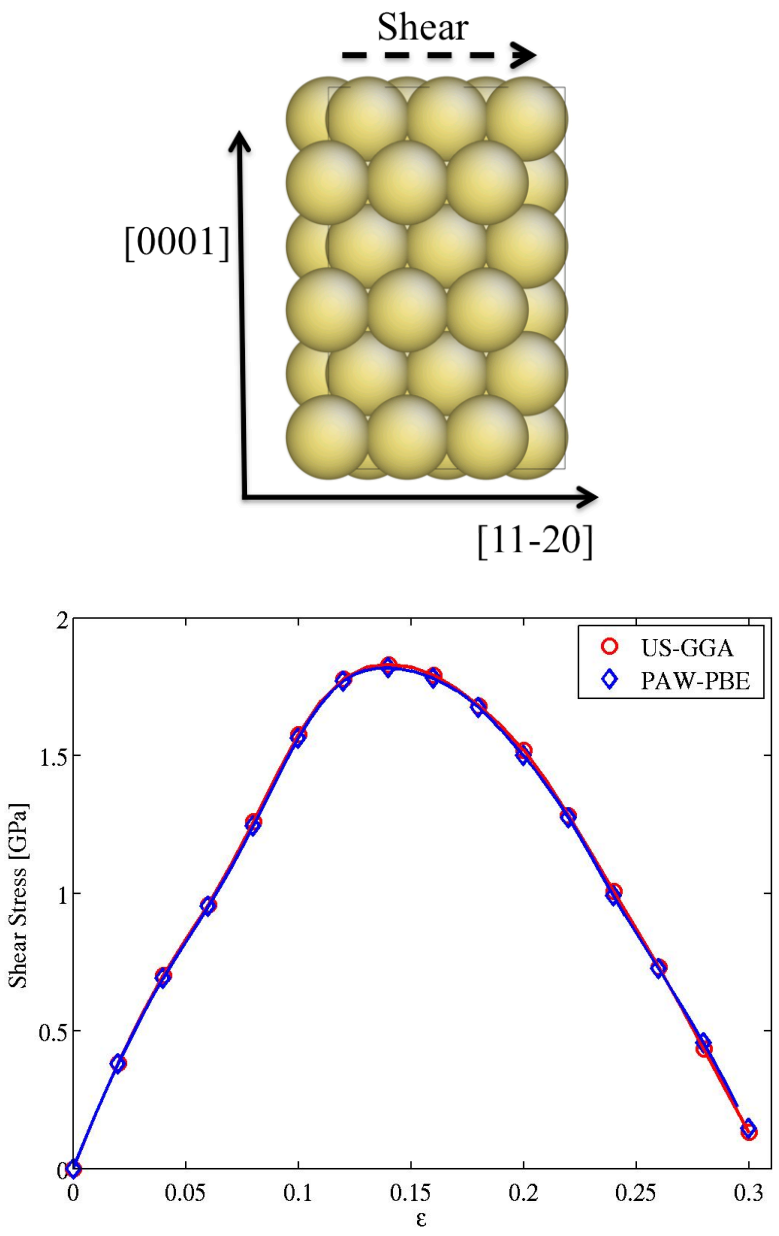

Figure 3.4. The relaxed shear stress-strain relation of Mg on basal plane along [11-20] direction.

3.3.2 Mechanical data

Figure 3.5a shows a comparison of the typical engineering stress-strain curves of samples with different sizes where three types of mechanical behavior can be clearly identified. For the largest samples (from about 900 nm to 400 nm), the curves show a low yield stress and work hardening towards a higher ultimate

yield stress. The “bulk-like” plastic instability is also shown on those curves. For the medium sized samples (from 400 nm to 150 nm) the stress reaches progressively higher values, but the value of plastic strains are limited. The related curves were almost linear; no obvious plastic stage was observed. In the smallest samples (about 100 nm and below), ultrahigh yield stresses, flow stresses and plastic strains were observed. Figure 3.5b plots the yield stress vs. sample size for all of the tested samples (here we define the yield strength as the stress at which the first deviation from linearity is found in the stress-strain curve). To sum, the “smaller is stronger” trend was observed in the entire size regime until the sample size reduced to about ~100 nm; below that critical sample size, the stress saturated and the strength plateau was around 2 GPa. For comparison, the above results of the first principle calculation for theoretical strength of Mg in our orientation gave the value of ~3.6 GPa. The size vs. strength trend demonstrates a power law exponent of around -1, consistent with the description of previous strengthening mechanisms. Coincident with the plateau in strength, there is a significant transition in the total strain achieved by each sample before fracture. This dramatic transition can be seen in Figure 3.5c, which shows that the fracture strain decreases slightly as the sample size decreases from 900 nm to 150 nm; but the values suddenly jump to over ~10% when the sample size is reduced to ~100 nm and can even reach almost 30% fracture strain in some cases. As the data shows, clearly there are very different plastic deformation characteristics in these three different size regimes. The corresponding deformation mechanisms responsible for the size-related mechanical behavior are analyzed below.

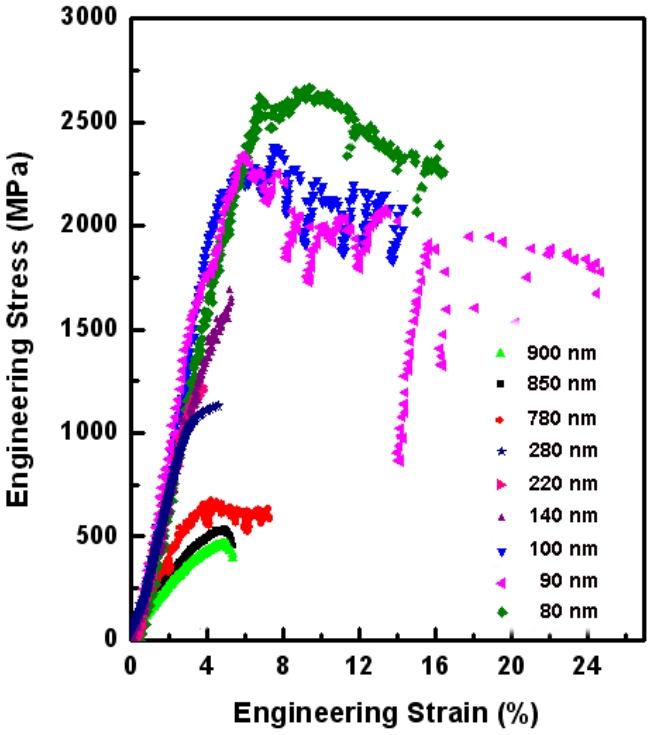
Engineering Stress (MPa)
Engineering Strain (%)
900 nm
850 nm
780 nm
280 nm
220 nm
140 nm
100 nm
90 nm
80 nm

(a)

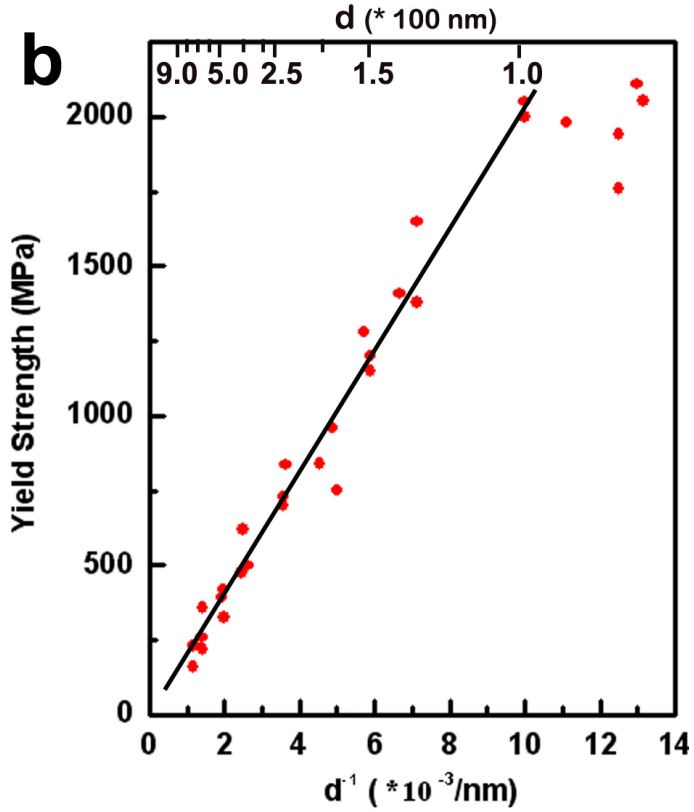
b
d (* 100 nm)
Yield Strength (MPa)
d-1 (*10 -3/nm)

(b)

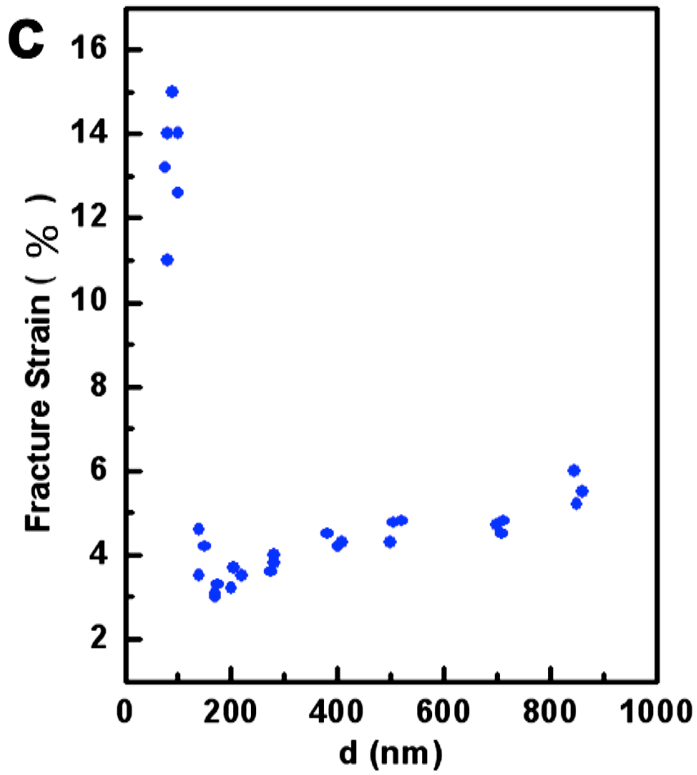

(c)

Figure 3.5 Quantitative mechanical data that shows three different size regimes, in which the samples show different mechanical behavior respectively. (a) The typical stress strain curves of samples with different sizes. Besides the "smaller is stronger" trend, the samples with extremely small size show a dramatically longer plastic stage. (b) The plot of yield strength versus the inverse of the sample gage size, d^{-1}, showing the increase of strength with decreasing size. (c) The plot of fracture strain versus sample gage size d showing a significant transition in plasticity when the sample size approaches ~100 nm.

3.3.2.1 Regime 1- "Bulk" behavior

The largest samples demonstrate the "bulk-like" strain hardening behavior in both their stress strain curves and in their in situ deformation process. As shown in the stress-strain curves of the 900 nm-400 nm samples in Figure 3.5a, a short elastic stage was usually displayed at the beginning followed by a continuous strain hardening. For example, for one curve of 850 nm sample, the plastic instability happened at ~500 MPa, as shown in Figure 3.5a, at which point obvious necking was observed from the related movies. Shortly the samples ran

to failure. Figure 3.6 shows the TEM images captured from one 850 nm sample that display the deformation process described above. For more details, when the external stress was applied onto the specimen, the dislocation activities were observed in multiple regimes through the whole gage section. In this specific case that shown in Figure 3.6, the initial dislocation activities were observed in the area, which was close to the head of the tensile bar, in the middle and also in the bottom of the specimen. Since the thicknesses of these samples were above 400 nm, they were not well electron transparent, so that the detailed dislocation configuration was difficult to identify. However strong dislocation activities can be evidenced from the significant change of strain contours, which was shown in Figure 3.6. The hardening and necking characteristics indicated that the 3D dislocation activities happened. The fracture surfaces were rough, indicating that the fracture events were not dominated by pure shear but more 3-dimensional dislocation glide.

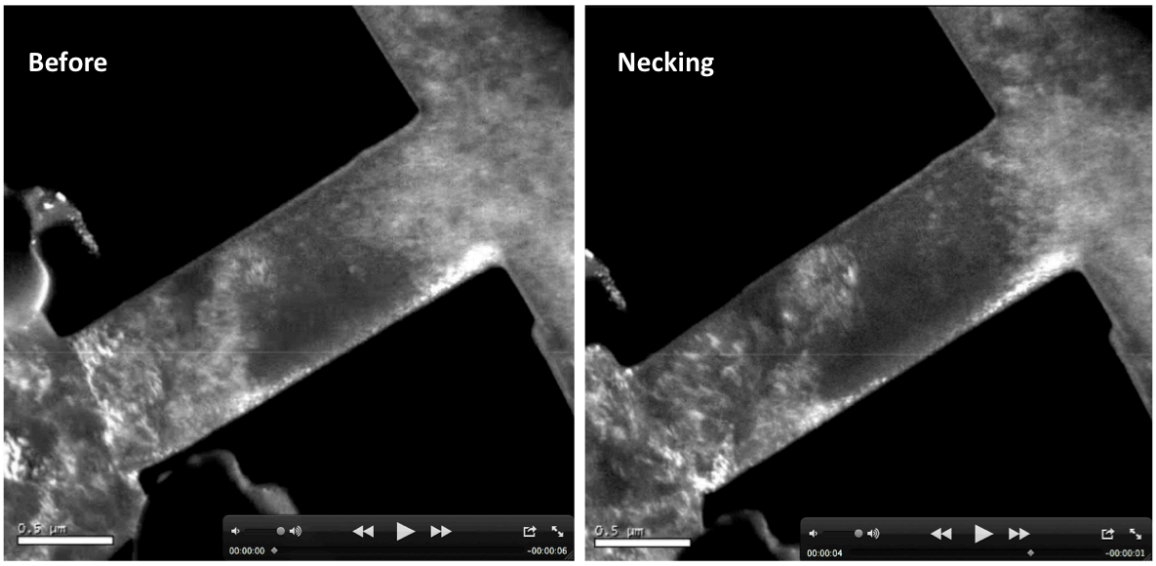

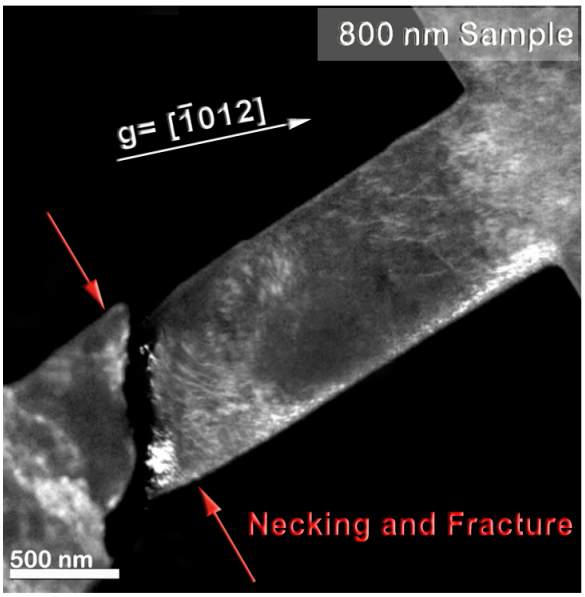

Figure 3.6. The dark field images showing the sample before test, just plastic deformed, necking and failure. The sample size is ~800 nm, g=[10-12].

When the sample size decreased to below about 600 nm, the mechanical behavior was generally the same as that in the larger samples. However, with presumably less pre-existing dislocations than that in the 850 nm samples, we found that the necking may take place in more than one location (Figure 3.7). This indicates that the first necking took place at one location; dislocation interactions and multiplication were believed to happen, generating 3-D dislocation plasticity; however, because of the limited dislocation sources, the further dislocation interactions were not strong; instead dislocations were cleaned out in this certain area, which made this local area even harder. As a result, another necking event may happen at different location. This is a common phenomenon in small sample testing, which is called exhaustion hardening. These phenomena lasted until the sample size decreased to about 400 nm, below which significant necking was rarely seen.

Movies: https://dl.dropbox.com/u/81430932/movie1Mg800nm.mp4
https://dl.dropbox.com/u/81430932/movie2Mg600nm.mp4

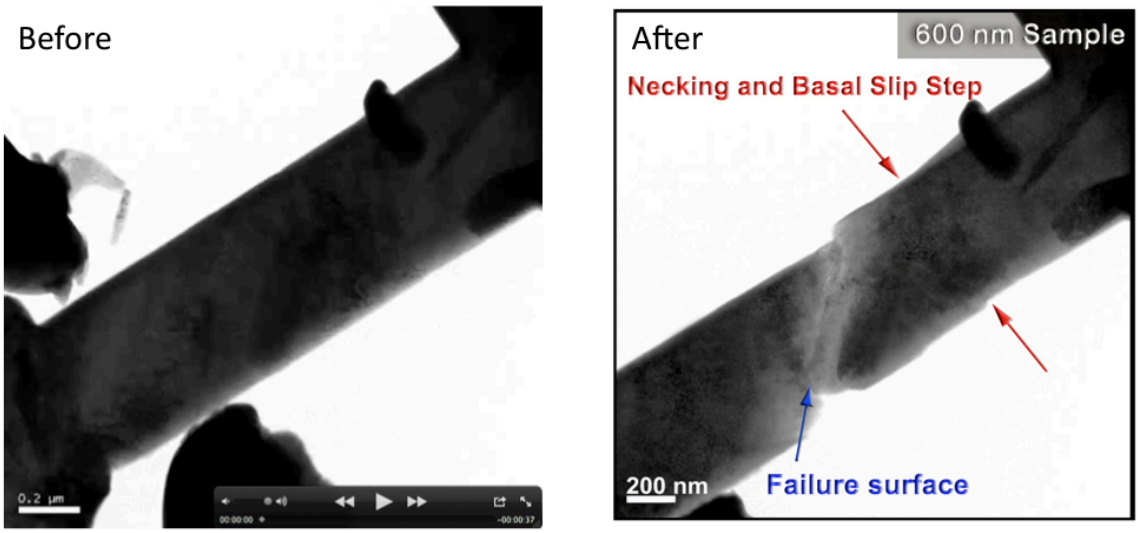

Figure 3.7. The bright field images showing the sample before test and necking and failure. The sample size is ~600 nm, g=[10-12].

3.3.2.2 Regime 2-limited ductility

As sample sizes decreased to ~400 to ~200 nm, the number of pre-existing dislocations decreased and little plasticity was observed both from the mechanical data and the deformation process. The related stress-strain curves usually contained a long elastic stage and a very short strain hardening stage, ended by fracture, which happened at ~ 3%-4% engineering strain. An example of a test from this size regime is shown in Figure 3.8 (also see movie). No significant necking and elongation were observed, which indicated that the 3-D dislocation activities were strongly reduced. The fracture surfaces of samples in this size regime became much flatter and were precisely located at the planes which were ~45 degree off the tensile direction. This is believed to be mainly due to the localized 2D dislocation activities on certain basal plane, where dislocation source operated, generating numbers of dislocations with the same type. These dislocations however had little chance to interact with each other since the sample dimension here was compatible to the mean free path of dislocations in these pure single crystal metals. As a consequence, they quickly slipped out of the sample from the free surface and produced appreciable shear along the direction of sliding, resulting in the shear localization and the fracture of samples from the basal planes. As shown in the middle and bottom images in Figure 3.8, the dislocation activities tend to localize only in certain regions (shown in the middle image in Figure 3.8) compared to the more homogenous dislocation activities in the larger samples. The fracture events happened along

basal plane with ~45 degree off the tensile direction, indicating the leading contribution from the localized 2D dislocation activity. Presumably the easy glide of one leading basal slip on certain plane was the major deformation mode in samples within this size regime.

Single dislocation movement was very hard to capture since the fracture happened quickly once the dislocations were activated. As the sample size further decreased, the hardening region became even shorter and almost undetectable, such as that shown on the 150 nm curve in Figure 3.5.

Movie: https://dl.dropbox.com/u/81430932/movie3Mg280nm.mp4

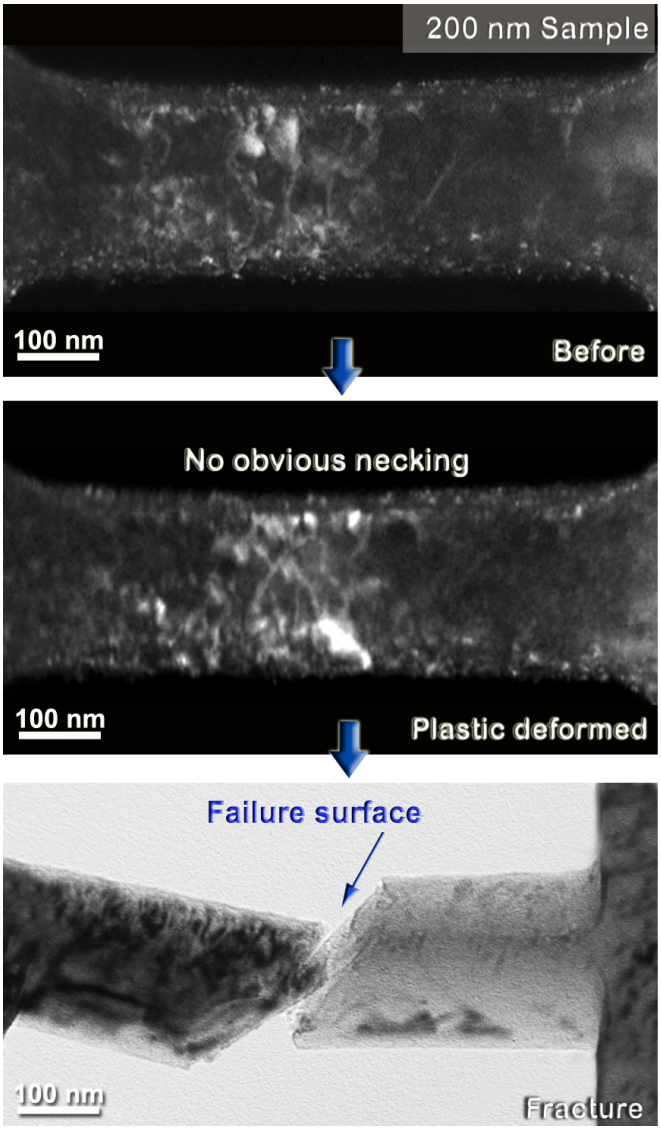

Figure 3.8 The dark field images of a sample with size ~300 nm before deformation, after plastic deformed and after fracture. BD=[4-2-23].

3.3.2.3 Regime 3-ultrahigh strength ductility

As the sample size reduced to below ~100 nm there was a significant shift in deformation behavior seen both from the stress-strain curves (Figure 3.5) and the in situ movies (Figure 3.9). The stress vs. strain behavior shows an extremely long plastic stage with flow stresses close to ~2 GPa. When loaded the specimens, the stress increased quickly up to about 2 GPa. Strong dislocation activities were observed from this moment. Meanwhile, intermitted load drops were observed from the engineering stress-strain curves. The related movies demonstrated that dislocation activity can be observed across the entire gage section and a dramatic amount of elongation occurred. Figure 3.9 demonstrates this dramatic elongation.

Movies: https://dl.dropbox.com/u/81430932/movie4Mg100nm.mp4
https://dl.dropbox.com/u/81430932/movie5%3Cc%2Ba%3Eslip.mp4

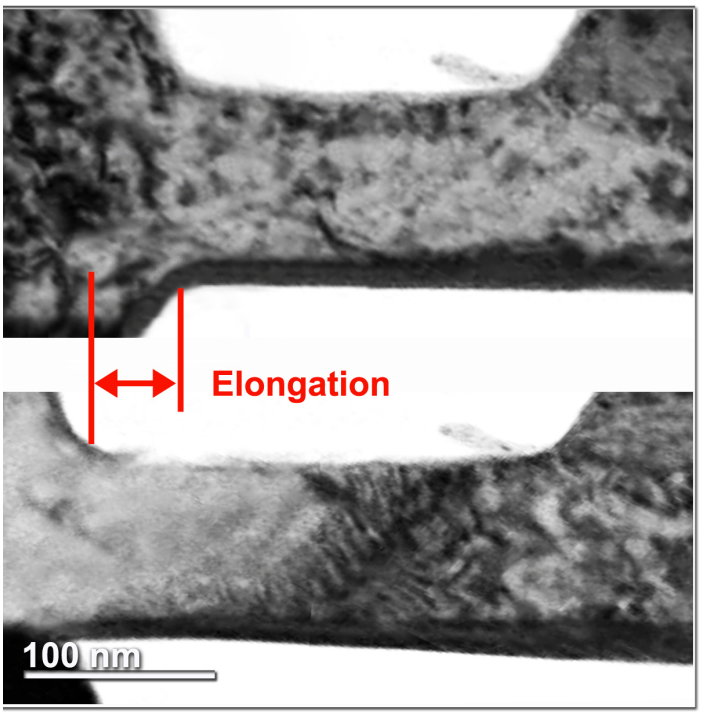

Figure 3.9 Bright field TEM images captured from the movie of the in situ tensile test showing the large elongation in a sample with size ~100 nm. The initial image of the sample is shown on the top.

Importantly non-basal slip was observed during the plastic deformation. Figure 3.10 and the related movie shows an example of the motion of a non-basal dislocation with a Burgers vector along $[11\bar{2}\bar{3}]/[\bar{1}2\bar{1}3]$, even though basal slip is strongly favored in this orientation. The Burgers vector of this dislocation was determined by g•b analysis. A series beam directions were used in this g•b analysis. The dislocation was visible under g= [-1011], [1-101], [2-1-10] and [01-1-1], as shown in Figure 3.11. Thus the Burgers vector of the dislocation can be determined as either [11-2-3] or [-12-13], both of which are <c+a>-type dislocations. In addition, we found that the <c+a> dislocation segments moved in a relatively slow manner. As shown in Figure 3.10, which are the dark field TEM images captured from the movie that showing the dislocation configuration at 2.0 s, 2.8 s, 3.3 s and 4.1 s, the <c+a> dislocation moved in segments, which is consistent with the phenomena of dislocation pinning-depinning processes.

Compared to the easy glide of basal dislocations, the low mobility observed from the pinning-depinning process of the <c+a> dislocation indicates stronger dislocation interactions and a greater likelihood of the crystal maintaining a high dislocation density during deformation. Presumably, this effect leads to more three-dimensional plasticity and the high ductility observed in this size regime.

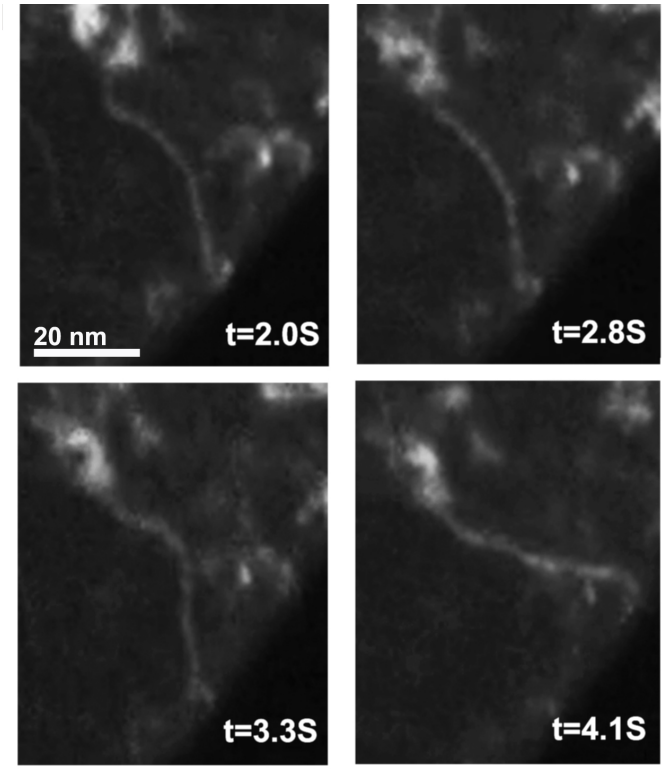

Figure 3.10 The dark field images captured from the movie of a ~90 nm sample showing the motion of a <c+a>dislocation.

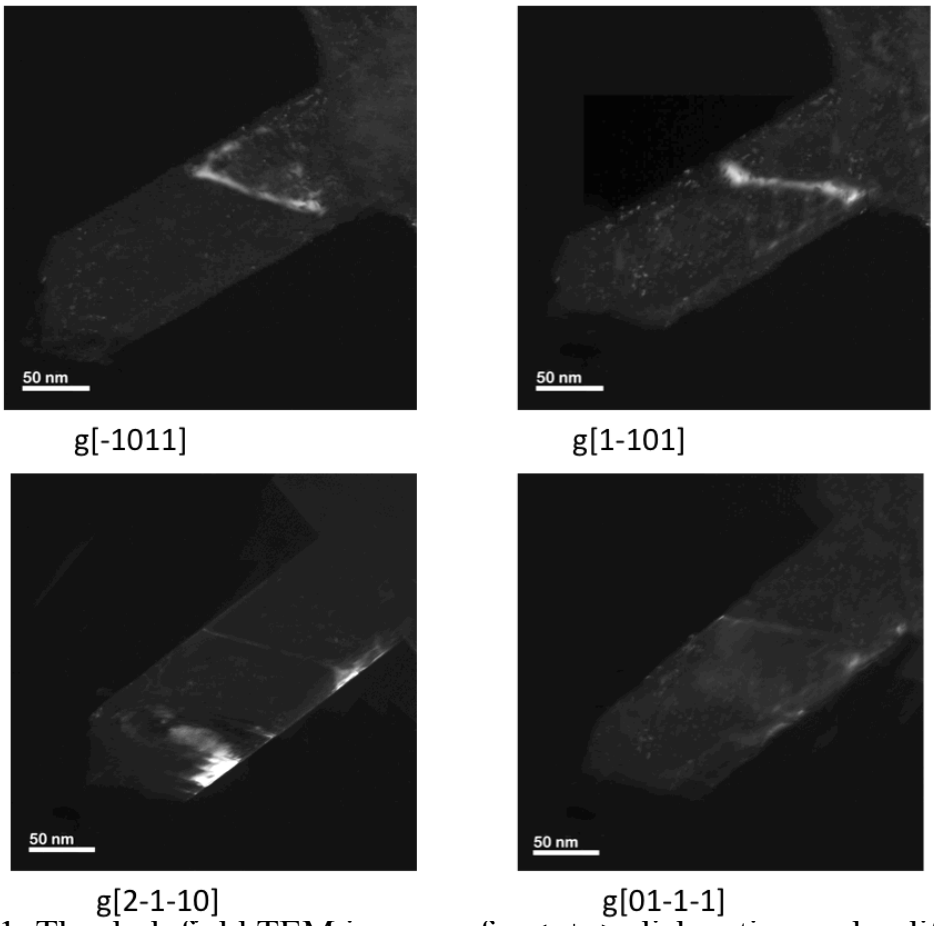

Figure 3.11. The dark field TEM images of a <c+a> dislocation under different g vectors.

A transition of fracture behavior also appeared in this size regime: the failure surfaces changed to a "cup-cone" shape as shown in Figure 3.12 instead of the pure shear fracture that has been seen in the larger samples, indicating the brittle to ductile transition. Multiple slip modes, especially the non-basal slips, are believed to happen at this extremely small size scale. The strong dislocation interaction between different slip modes created the nano voids; the further growth of the voids would result in the fracture in the form of the cup-corn shape. All the phenomena evidenced the significant improvement of the ductility.

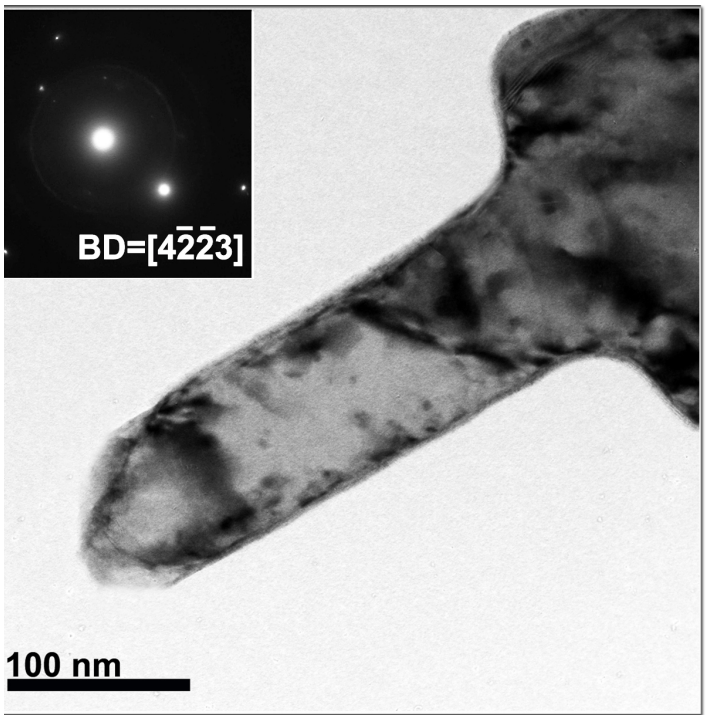

Figure 3.12 The cone shape failure surface in a sample with size ~ 80 nm. BD=[4-2-23].

The HRTEM study was further performed to investigate the slip trace in the extremely small samples. The HRTEM images of samples after failure (Figure 3.13) revealed many small slip steps at the edge of the deformed samples, which were usually several Burgers vector's width. No dramatic shear steps were found, indicating that the predominance of a leading basal slip was strongly reduced. More homogenous deformation was achieved.

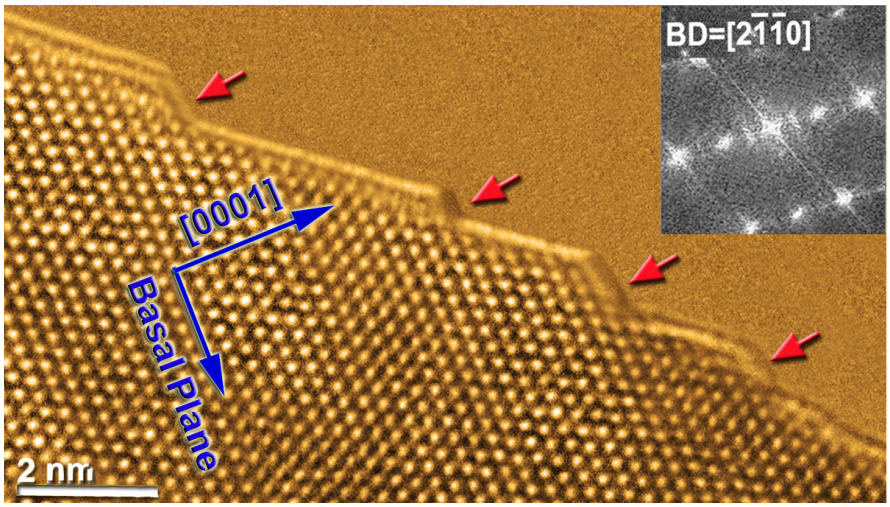

Figure 3.13 HRTEM images of the edge of a deformed sample, where many small slip steps can be seen, BD=[2-1-10].

Secondly the HRTEM images demonstrate multiple types of dislocations (as shown in Figure 3.14) in the deformed microstructure, consistent with the non-basal slip observed from the movie. D1 and D2 were labeled out for two different types of dislocations. Their strain fields interacted with each other as we can see from the lattice distortion in the HRTEM images, respectively. Several D2 were actually pinned at the certain locations. For some reason, the Burges vector of dislocations are difficult to be identify due to the high index of this crystal plane.

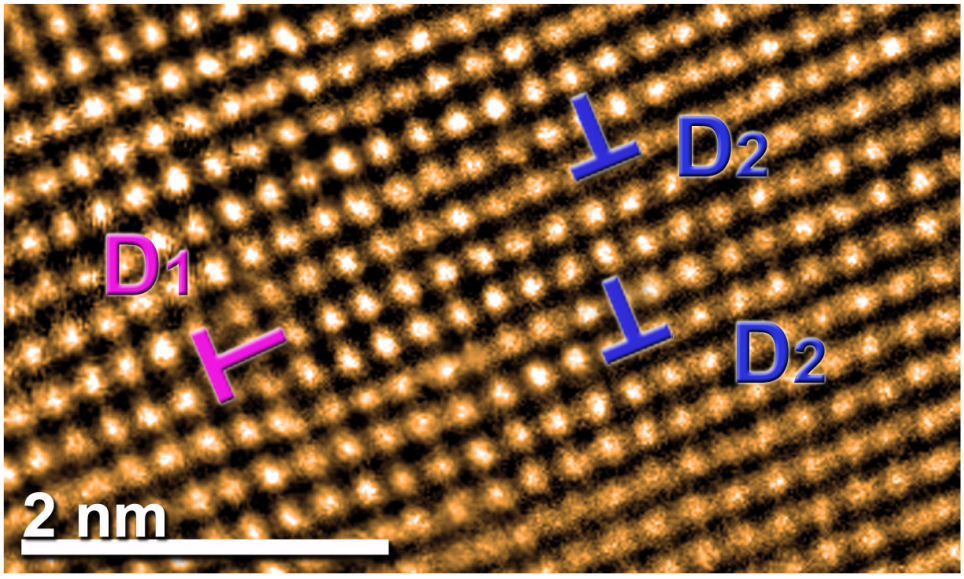

Figure 3.14 The HRTEM image that shows multiple types of dislocations.

However, it is also possible to observe non-basal slip in larger samples as illustrated by previous studies. So the critical mechanism for the improved ductility in the small size regime should be not only the activation of non-basal slip, but also the relative amount of the non-basal contribution. To illustrate this quantitative effect, we further investigated the slip steps at the surface of deformed samples; a typical high-resolution TEM image is shown in Figure 3.15. The zone axis is $[10\bar{1}0]$ and the crystallography viewed from this direction is shown schematically in the lower part in Figure 3.15. The 2D projected morphology of the steps can be clearly seen including steps that would indicate non-basal slip in similar amounts as basal slip.

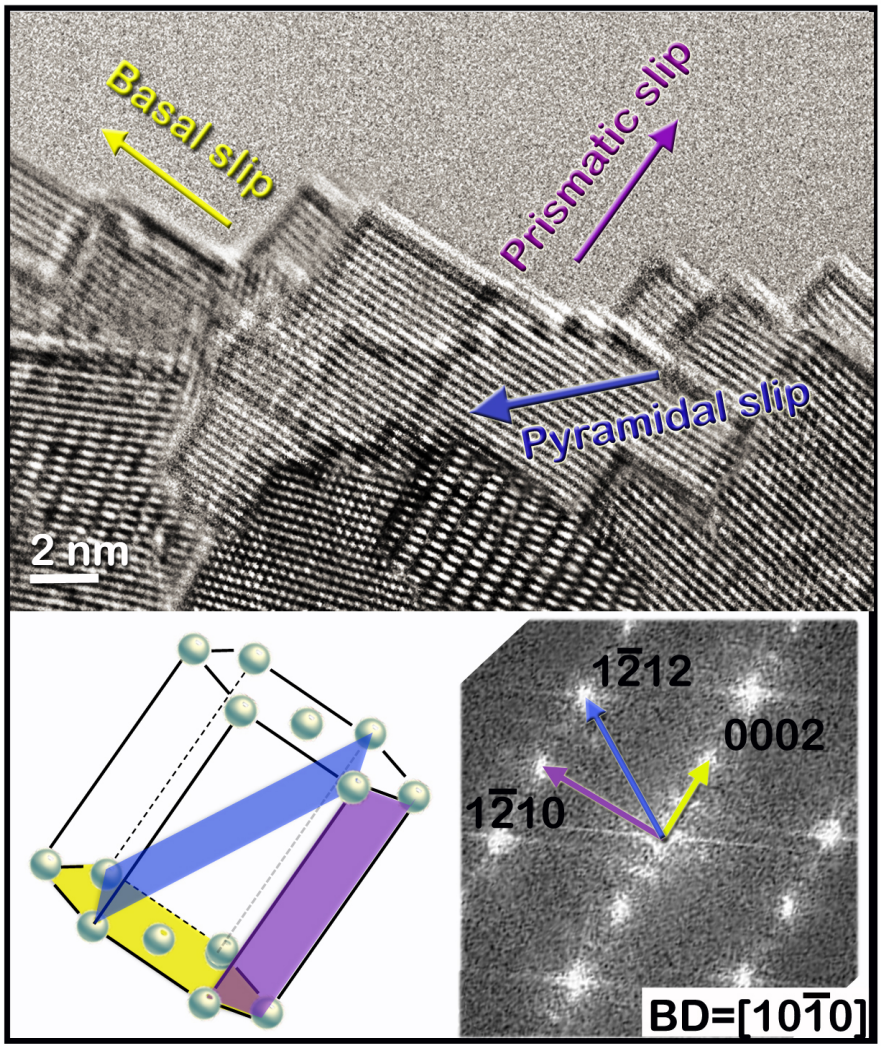

Figure 3.15. The HRTEM image of the slip steps at the surface of a deformed sample with size ~90 nm, Beam Direction=[10-10]. The directions for basal, prismatic and pyramidal slip are all marked. The lower image shows the related crystallography for reference.

The method we used was trace analysis. The related FFT diffraction pattern has been added into Figure 3.15. The beam direction was [10-10]. The plane on which we labeled as "basal slip" is perpendicular to the connection between the origin and [0002] reflection spots, so the slip steps along this orientation correspond to basal slip. Others steps should be produced by non-basal slips. Some of them are nearly 90-degree rotation from the basal slip and perpendicular to the line between the origin and the [1-210] reflection spot, so they are labeled as the slip with component along [0001] (the rotation is also possible, but the 90 degree angle between them is the strong hint of <c> slip). The angle between

some other steps and the line between origin and [1-212] reflection spot are about 79~82 degrees, which are believed to correspond to pyramidal slip.

Regarding the mechanical data from this smallest regime, it is interesting to note that despite several intermitted load drops due to micro-yielding events, the flow stress stays at a very high level, which is close to ~2 GPa throughout the deformation. In almost every way, the samples in the smallest regime seem to deform in a different manner than those in the larger regimes. Non-basal slip is much more intense in extremely small samples, naturally leading to the intriguing question of what mechanism reduces the CRSS anisotropy and generates the ultrahigh strength ductility in this size regime.

3.4 Discussion

The results clearly show that the bulk behavior still hold in large samples. Even though the strength is much higher and the total strain is less than that in bulk materials due to the relative less dislocations in confined volume, the plastic deformation behaviors show the typical bulk characters. We believe that 3-D dislocation activity still dominates; dislocation interaction and multiplication contribute to ductility. The ductility is further affected more significantly as decreasing the sample sizes because of the source limited and the priority of one leading easy slip, which can quickly induce enough shear to accommodate the required strain change. It is believed to be the 2-D dislocation plasticity that dominates, where shear localization is remarkable and main dislocation activities localize on the certain crystal plane instead of the whole volume.

In the smallest size regime, the deformed microstructure indicates that the key difference in the plastic deformation behavior is the much higher ductility, which is due to the activation of multiple slips modes driven by the 2 GPa-level yield stress and stronger dislocation interactions. So it is believed that the anisotropic CRSS for basal slip and non-basal slips was significantly reduced at the extremely size scale. The critical size regime here was around 100 nm. This result indicates that it could be possible to tune the CRSS anisotropy by dimension refinement.

As we described in the chapter 1, as the lightest structural metal, the application of Mg alloys suffers from the relatively low ductility compared with other structural materials. Slip on the basal plane holds the first priority in plastic deformation since its critical resolved shear stress (τ_{CRSS}) is hundreds of times

lower than that for prismatic or pyramidal slip at room temperature. Unfortunately the only two independent basal slip systems are far from enough to fulfill the Von Mises criterion that requires at least 5 independent slip systems for arbitrary shape changes. The highly anisotropic τ_{CRSS} values for activation of different slip mechanisms in Mg results in limited dislocation plasticity, leading to relative poor ductility and formability.

Theoretically, the τ_{CRSS} can be estimated by a simplified formula: $\tau_{CRSS} \sim \frac{\alpha G b}{L} + \tau_0$, where L is the physical dimension of sample, α is geometrical constant ~ 1, G is the shear modulus, b is the Burgers vector and τ_0 is the friction stress. Considering the normal dislocation length in materials is usually in the order of 10^{-6} m, the value of $\frac{\alpha G b}{L}$ is roughly several MPa, so the huge difference between the τ_{CRSS} for basal and prismatic/pyramidal slips is mainly determined by the anisotropic friction stress τ_0. This has been evidenced by previous experiments and simulations, which showed $\tau_{0\text{-basal}} \approx 10^{-2}\ \tau_{0\text{-prismatic}}$. Interestingly, as the dislocation length becomes nano-scale, the value of $\frac{\alpha G b}{L}$ will be hundreds to thousands times larger, then the τ_{CRSS} will be no longer determined by τ_0 but the sample dimension. However, this formula cannot be accurate for extreme small values of "L" because the τ_{CRSS} cannot go infinity. Instead, the maximum τ_{CRSS} is limited by the ideal shear stress, which can be estimated from the maximum slope of the general stacking fault (GSF) energy curve from the origin to the unstable stacking fault energy γ_{us}. Importantly, we note that this anisotropy ratio between the slopes $\left.\frac{d\gamma_{us}}{dx}\right|_{basal}$ and $\left.\frac{d\gamma_{us}}{dx}\right|_{prism/pyramidal}$ is not a factor of 100 but less than 2 for full basal slip and about 3 for partial basal slip from our first-principles calculations (*82*).

Two major consequences of this concept are: 1) the strength of materials can be strongly enhanced with size; 2) the anisotropic τ_{CRSS} for different slip mechanisms can also be significantly reduced with size, leading to more three-dimensional plasticity involving more than just basal slip. This indicates the possibility of tuning the anisotropic deformation properties in Mg to achieve excellent mechanical performance by limiting the size of the dislocations; and our experimental results provide the direct evidence.

To investigate this effect in even smaller samples, we performed a series of molecular dynamics (MD) simulations of tensile tests on Mg nanostructures with the same orientation as that in experiment.

Molecular Dynamics Simulations of Tensile Tests of Mg Nanowires

Dr Liang Qi helped to perform Molecular dynamics simulations by LAMMPS to investigate the deformation mechanism in tensile tests of Mg single crystal along direction 45^{o} with the basal plane. EAM interatomic potential for Mg was applied. The rectangular-shaped samples with periodic boundary condition along z-axis were made according to two different orientations of MD samples, as shown in Figure 3.16. For each orientation, two different sizes (10×10 nm^2 and 20×20 nm^2) were applied to check the size effects. All the tensile tests were performed at temperature of 300 K and MD relaxation of 1 nano-second under 300K was performed before each tensile test. The strain rate was 2×10^7 s^{-1} and the maximum strain is 0.2.

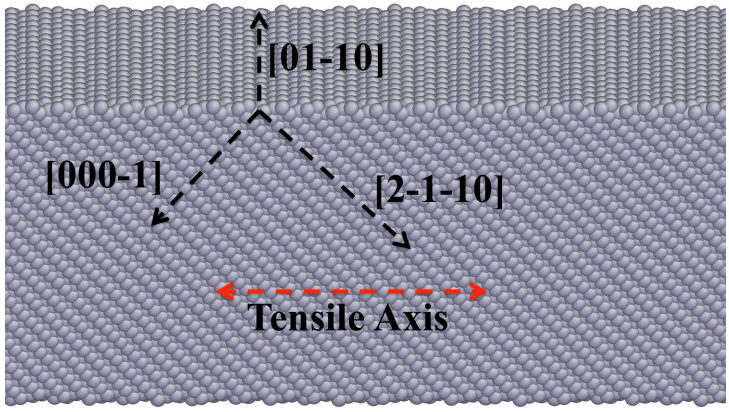

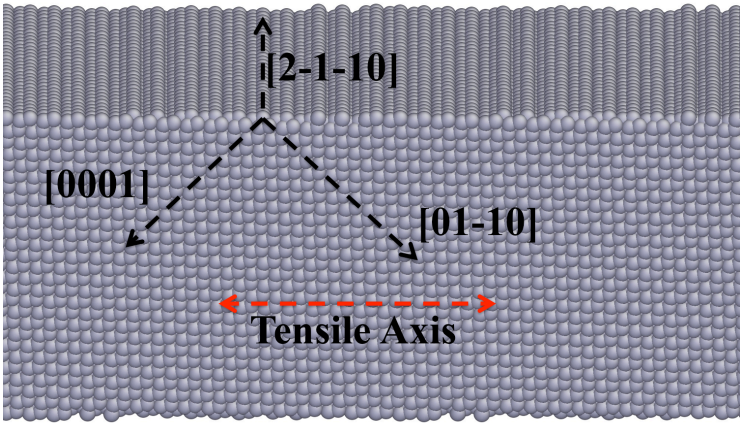

Figure. 3.16: (a) and (b) are MD samples with two different types of orientations. In both samples, the basal plane has 45^{o} angle with the tensile axis. In type A (a), one a-axis ([2-1-10]) has 45^{o} angle with tensile axis, so the corresponding slip system has highest Schmid factor of 0.5. In type B (b), one a-axis ([2-1-10]) has 90 ^{o} angle with tensile axis, so the corresponding slip system has zero Schmid factor. But the other two a-axis ([-12-10] and [-1-120]) have Schmid factor smaller than 0.5.

The stress-strain results are shown in Figure 3.17. Young's modulus in all the samples is 37~38 GPa independent of the detailed orientation. When strain is close to ~0.05 and stress reach ~1.7 GPa, all the samples yield by the nucleation of partial dislocations on basal planes from the corner of surfaces. After yielding, each sample can reach strain of 0.2 without failure facilitated by continuously surface-nucleated dislocations, which would quickly slip out of the samples. The only exception is the sample of 10×10 nm^2 with type A orientation, where twin nucleation occur when strain reaches 0.1. The atomic configurations of samples after deformation are shown in Figure 3.18.

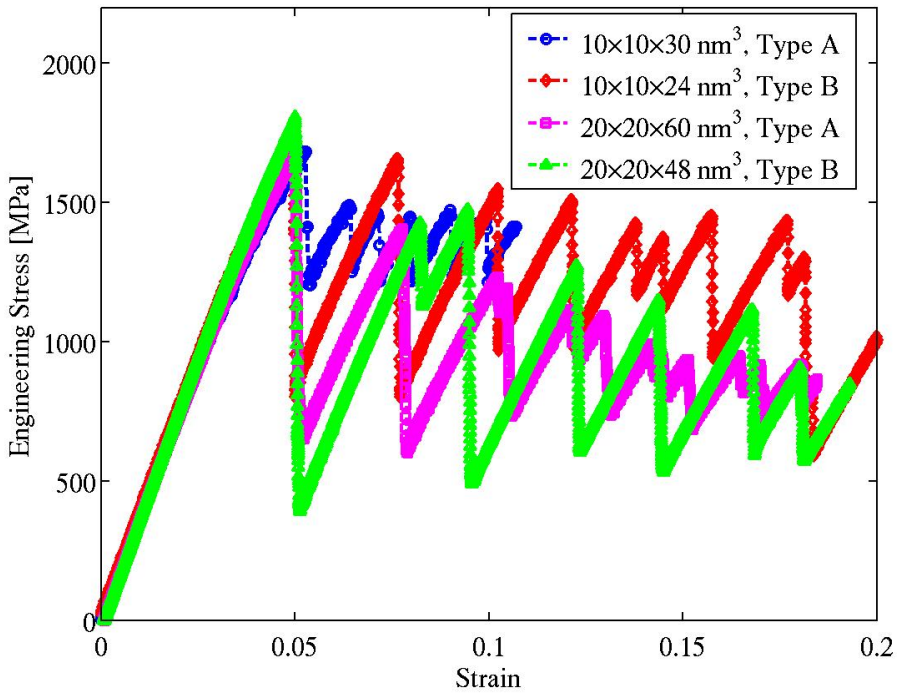

Figure 3.17: Stress-strain curves from MD samples with different types of orientations and different sizes.

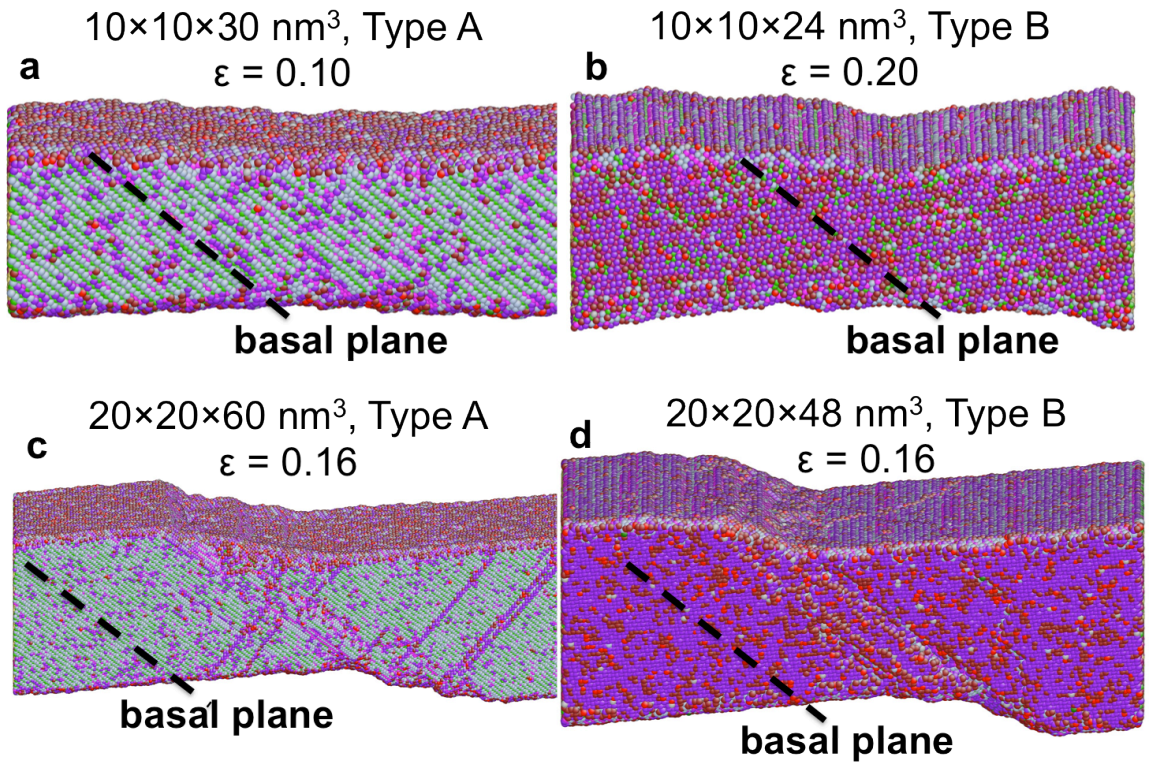

Figure 3.18: The atomic configurations of samples after deformation. Here different colors means different coordinate number, so the tracks of dislocation lines can be observed clearly.

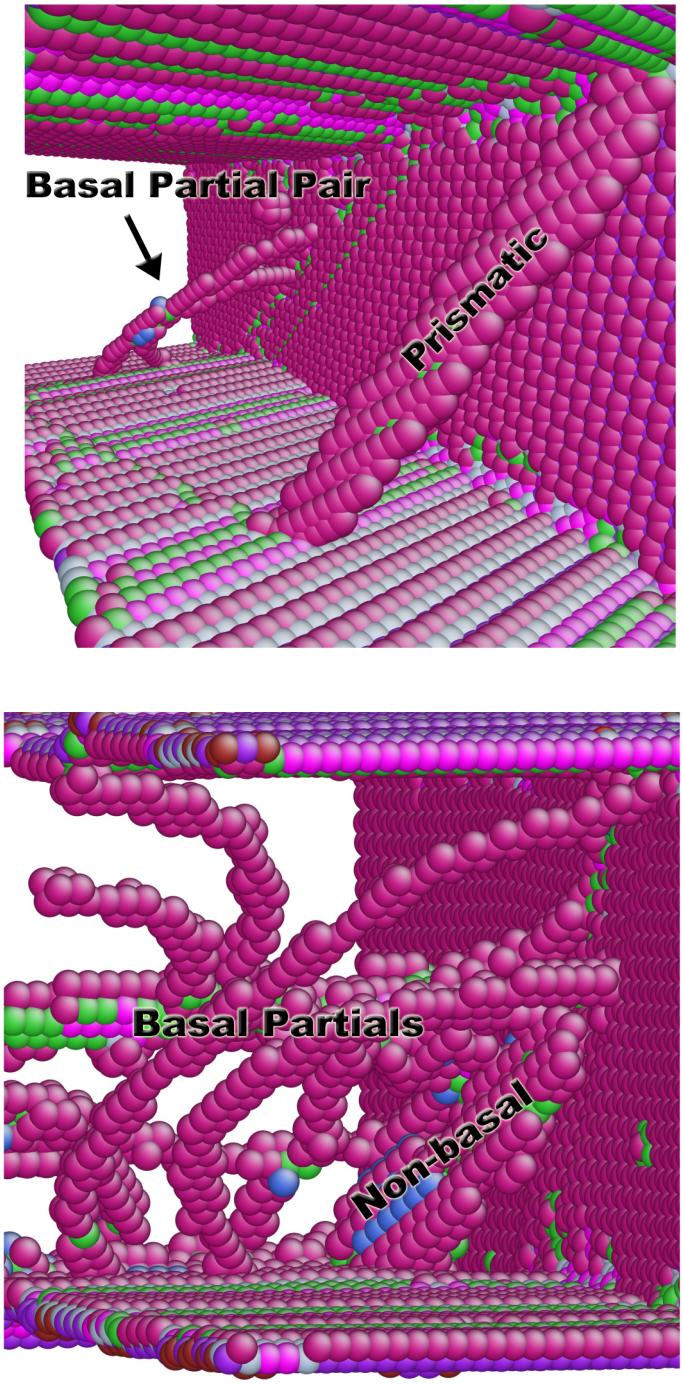

Figure 3.19. The nucleation of multiple types of dislocations, even though the crystal orientation heavily favors basal slip.

As we can see, the simulation results are consistent with the experiment results in a number of ways: 1) the Young's modulus under such orientation is 37.4 GPa, and the experiment value is ~40 GPa. 2) the yielding corresponds to the first

nucleation of dislocation in simulations, which happens at ~1.75 GPa followed by load drop, as compared to the experiment results which give a average yield stress at ~2 GPa. 3) the yield stress does not change with size in our experimental samples with sizes <= 100 nm and MD samples. This is consistent with the previous theoretical studies that the surface nucleation of dislocations should be not very sensitive to the sample sizes (*78*). 4) the flow stress can almost stay at ultra-high level, close to that of yield stress.

Detailed analyses of the simulations reveal further evidence on the origin of the high-strength plasticity in the smallest size regime. Two tendencies can be generalized on these samples. First, both basal and non-basal slip systems can be activated in most cases, even though the crystal orientation heavily favors basal slip (Figure 3.19); their interactions can increase the strength and ductility of samples in real tensile tests (the movie of dislocation interactions can show this). As shown in Figure 3.18 and Figure 3.19, there are many tracks left by dislocation lines that are not on the basal planes, especially those under larger strain. The pre-existing dislocations would escape from the surface under stress, similar to the previous results. Due to a scarcity of dislocation sources and/or the shorter source length, the sample yields at an extremely high stress, which may help to overcome the nucleation barriers of all types of dislocations. As shown in Figure 3.19, both slip of partial dislocations on basal planes and prismatic slip can be observed in most of the cases. In addition, although most of the dislocations eventually slip out of the samples, they may interact with each other and temporarily increase the dislocation density (Figure 3.19b), contributing to the plastic strain and also preserving the flow stress. The concept of multiple types of dislocations being simultaneously active is also consistent with the ductile fracture mode for ~100 nm samples observed in experiments. Second, smaller samples have more homogenous distributions of dislocation nucleation sites, resulting more uniform deformation. We can see dislocations nucleate from multiple places; especially in smaller samples (Figure 3.18(a) and (b)), the distributions of dislocation nucleation locations are more homogenous than larger samples (Figure 3.18 (c) and (d)). Especially for the sample of $10\times10\times30$ nm^2 sample with type A orientation, there is only one partial dislocation pair on basal plane nucleated at each nucleation site (https://dl.dropbox.com/u/81430932/movie6MD1.mov,https://dl.dropbox.com/u/81430932/movie7MD2.mov), and each basal dislocation nucleation corresponds to each stress drop event in stress-strain curve; thus, it has the highest average flow stress as shown in Figure 3.17. In conclusions, interactions of multiple slip systems and homogenous distribution of dislocation nucleation result in uniform

deformation, high flow stress and ductile failure of very small Mg samples. We can clearly see this trend in Figure 3.17, which suggests that 10×10 nm^2 samples have higher average flow stress than those 20×20 nm^2 samples.

Another critical factor for combined ultrahigh-strength and ductility is the dispersed nucleation in the smallest size regime, which facilitates more uniform deformation. Previous studies have shown that shear localization and homogenous deformation are always in competition in single crystals (*83*). Our results show that we are able to favor homogenous deformation by tuning the external dimension of samples. Because the smaller volumes have a higher ratio of possible surface nucleation sites per volume and are deforming at higher stresses due to internal source limitation, surface nucleation dominates and therefore there is actually a larger number of active sources. Our simulations indeed show that smaller samples (10×10 nm^2 cross section) have more uniform deformation and higher average flow stress (Figure 3.17), while some larger ones (20×20 nm^2) have clear shear localization even with obvious shear band. This is consistent with our experimental results where the plastic deformation changes from localized 2D-dislocation plasticity with little plastic strain to nucleation-dominated dislocation plasticity with much larger plastic strain when the sample size decrease below a certain value.

With the systematic investigation on the size-related dislocation behavior in Mg samples with size ranging from about 900 nm to below 100 nm and even smaller in simulation, we are able to map the dislocation plasticity in Mg, as shown in Figure 3.20: 1) bulk behavior regime, where 3-D dislocation plasticity dominates; work hardening and necking are remarkable. 2) limited ductility regime, where 2-D dislocation plasticity drive; almost elastic deformation and little ductility. 3) Ultrahigh strength ductility, where multiple types of slip are turned on and contribute to more homogeneous plastic deformation.

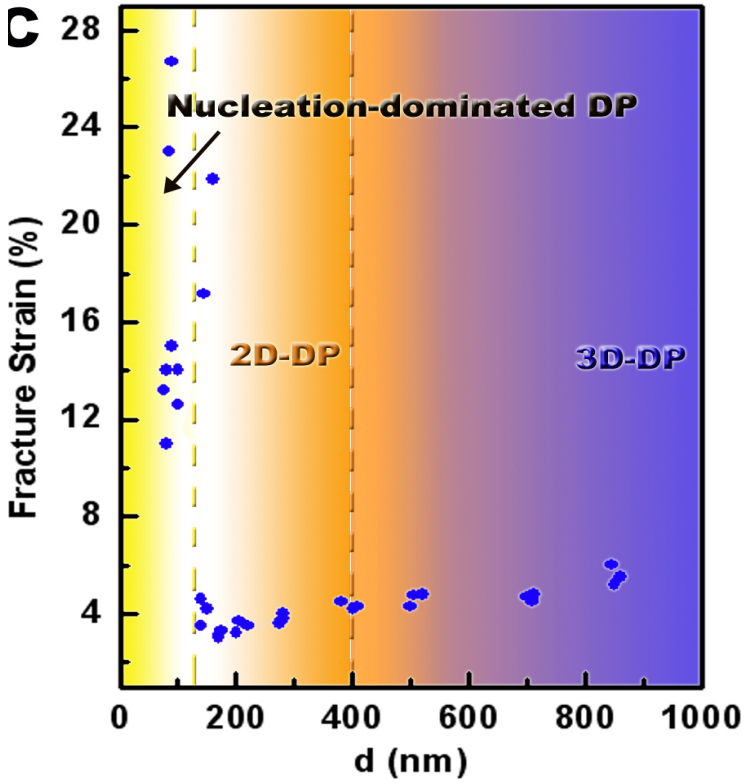

Figure 3.20. Mapping the dislocation plasticity in Mg

By mapping the size-dependent strength and plasticity in Mg, we revealed the possibility to tune the anisotropic CRSS to achieve both high strength and high ductility in Mg by external/internal dimension refinement. The CRSS for basal slip and prismatic/pyramidal slip would be in the same order in confined dimension even though they are strongly anisotropic in larger size. The critical dimension might be material dependent and sensitive to the chemical composition and GSFE. Importantly, we believe that grain boundary or twin boundary should be the efficient carrier for this effect, where the higher possibility of non-basal slip has been reported compared with that within the grain (*84*).

The application of this mechanism is in polycrystalline materials. In polycrystalline materials, the region near the grain boundary undergoes extensive deformation because of limitations involved with grain boundary incompatibility. However in a nanocrystalline material, the effect of grain boundary incompatibility can be secondary if the nanocrystalline material is modified appropriately with alloying addition to reduce GSF energy. The grain boundary

can primarily act as the source for nucleation and emission of dislocations which will play a major role in deformation. In addition, the local stress at the grain boundary can reach an extremely high value (GPa level) even the global stress is low. Presumably, with proper grain boundary engineering, the local stress at the grain boundary can be tuned to a high value, which can satisfy the critical requirement for applying this mechanism of reducing CRSS anisotropy with decreasing size.

This concept can be incorporated into advanced alloy design through microstructure control that exploits the plasticity behavior in polycrystalline samples where grain size and grain orientations or twin spacing can be manipulated to provide the desired effects.

Chapter 4

In situ SEM/TEM study on grain boundary-mediated plastic deformation in polycrystalline Mg

Generally, ductility is accomplished by the motion and propagation of dislocations, while strengthening is often achieved by hindering their motion. Thus, strength and ductility are fundamentally linked in materials and usually a mechanism to improve one almost always leads to a decrease in the other (*85-87*). As an example, for a given alloy, one efficient strengthening mechanism in the materials scientist's toolbox is grain boundary strengthening, which affects the dislocation activities within grains by regulating the length scale between barriers to dislocation motion. This concept is best described by the Hall-Petch relation, which states that the yield strength of a metal is inversely proportional to the square root of the average grain diameter. This empirical relation holds across a very large size range, from millimeters to tens of nanometers. While decreasing the grain size of a material increases strength, it unfortunately leads to a corresponding decrease in ductility (*88*). In addition, there are many previous studies reporting that dislocation plasticity would be dramatically weakened and give rise to grain boundary-mediated plasticity (such as grain boundary sliding, grain boundary rotation) in extremely small grains (~5-10 nm), resulting in inverse Hall-Petch effect and softening of materials (*89-91*).

Interestingly, the grain boundary-mediated plastic deformation is thought to be operating at much larger scale (even micron scale) in Mg, which has significant impact on the strength and ductility of materials (*92-95*). The effect of the grain boundary structures on the deformation response of materials has been examined through various experiments(*92-95*). The grain boundary energies for many kinds of bicrystals with different grain boundary structures have been obtained. Many previous results reported that the deformation behavior near the grain boundaries in Mg and its alloys is quite unique compared to that in other materials. For example, in Mg and its alloy, the possibility of non-basal slip in fine grains was found to be much higher than that in the coarse grains, indicating the higher possibility of non-basal slip at grain boundaries due to the operation of a compatibility stress/strain at the grain boundary (*84, 96*). In addition, the

diffusion pre-exponential factor in Mg is much larger than other metals. Given the similar number of activation energy, the diffusion rate of grain boundary in Mg was reported to be higher (*97*). Understanding the characteristics and the deformation responses of the grain boundary in Mg is then important. However, there is still lack of systematic investigation on the influence of different grain boundary structure on the deformation mechanisms and the mechanical properties of Mg.

It has been shown that grain boundary sliding (GBS), the rigid translation of one grain over another one parallel to the GB interface, mediates plastic flow of polycrystalline materials (*98, 99*). The sliding process has been extensively studied for decades using a variety of experimental and theoretical methods. Even though grain boundary sliding is not considered to be an important deformation mode at ambiant temperature in other metals with relative coarse grains, it is considered as one major carrier of plasticity in polycrystalline Mg. The possibility of grain-boundary sliding (GBS) in Mg alloys below ambient temperature was reported by Hauser et al (*100, 101*). In their paper, the possibility of GBS was examined in pure Mg at room temperature and also at 78 K. Since it was ex situ study, they evidenced the GBS by the displacement of scribed lines at grain boundaries at both temperatures. However, the displacement of the scribed lines at grain boundaries was often accompanied by grain-boundary fracture, so that it was actually difficult to show if the GBS really took place. Gifkins and Langdon also examined the possibility of GBS at room temperature in pure Mg and Mg alloys, which have grain sizes ranging from 100 to 300 μm (*102*). The similar displacement of the scribed lines was observed. However, by examining the strain-related and temperature-related mean step height of the displacement of the scribed lines at the grain boundary, they concluded that GBS does not occur in Mg and its alloys at room temperature and that the step formation was due to localized shear deformation of different magnitudes between adjacent grains, which was the phenomenon of ‘‘zone sliding,’’ but not GBS. J.A. del Valle et al., tested various Mg alloys, which were processed by Equal channel angular pressing (ECAP), large-strain hot rolling (LSHR) and annealing treatments. The results showed evidence of a change in deformation mechanisms with decreasing grain size. They thought that grain boundary sliding might give a plausible explanation of these results(*103*).

The complication of texture in bulk materials, however, made the analysis difficult (*104, 105*). Here we studied the deformation responses of grain boundaries with different structures in polycrystalline Mg small samples by using

in situ SEM/TEM nanocompression testing, where each grain boundary structure can be well defined. Samples with low angle grain boundaries and high angle grain boundaries were tested respectively.

4.1 The grain boundary structures in bulk polycrystalline Mg

The rod of polycrystalline pure Mg was supplied by GM R&D center. 3 mm*3 mm disks were punched out and thinned down to ~200 nm by mechanical milling and ion milling. Microstructure analysis was performed in a 3010 JEOL TEM. Figure 4.1 shows some typical bright field TEM images for the grain boundary structure in bulk Mg. As shown in the TEM images, the grain size was actually inhomogeneous. Some big grains were as large as ~1000 nm, but the smallest ones were around 50 nm. The distribution of grain boundary structures was not homogenous too. As shown in the upper right and the lower right diffraction patterns in Figure 4.1, given the same area, some regime contained more heavily disoriented grains, but others might have more grains with the same orientation and tended to form certain texture.

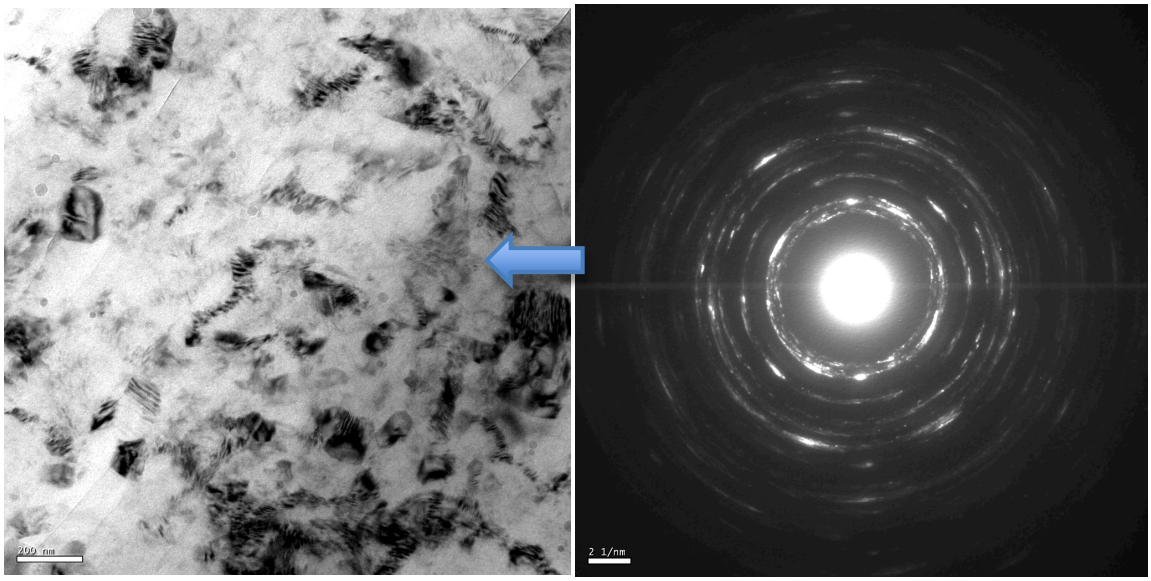

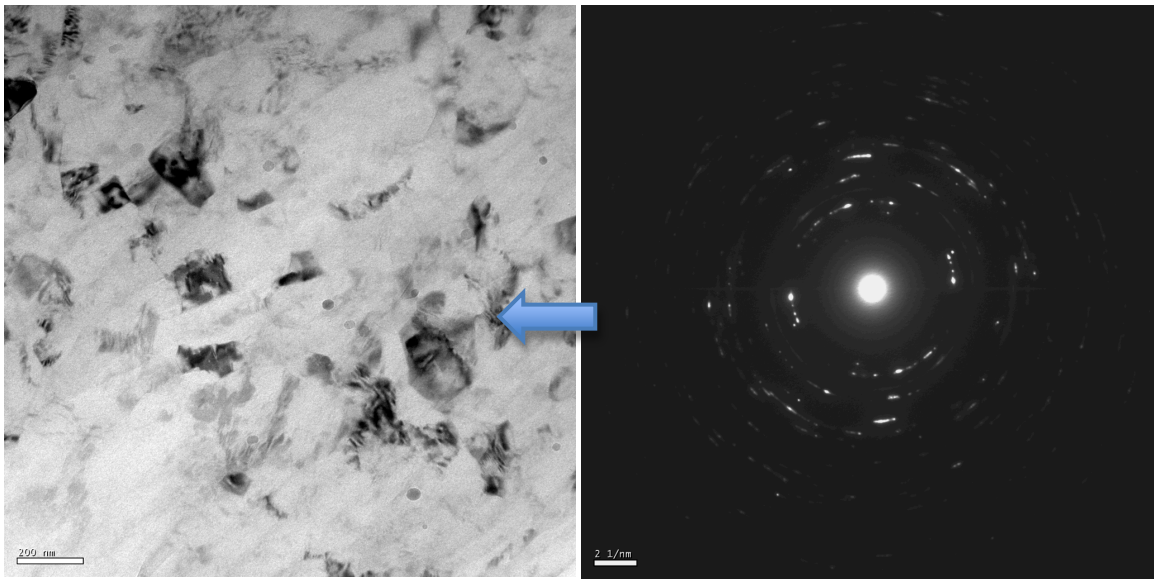

Figure 4.1 The bright field images of nanocrystalline Mg and the related diffraction patterns.

Dislocations were observed even in some finest grains, as shown in Figure 4.2. The straight dislocation lines here were determined as <a>-dislocations lying on the basal planes by g.b analysis. They usually intersected with the grain boundaries and had the average length at about several hundreds nanometer. By comparison, dislocation free grains were also observed and the grain size were usually smaller than 100 nm, as shown in Figure 4.2 c.

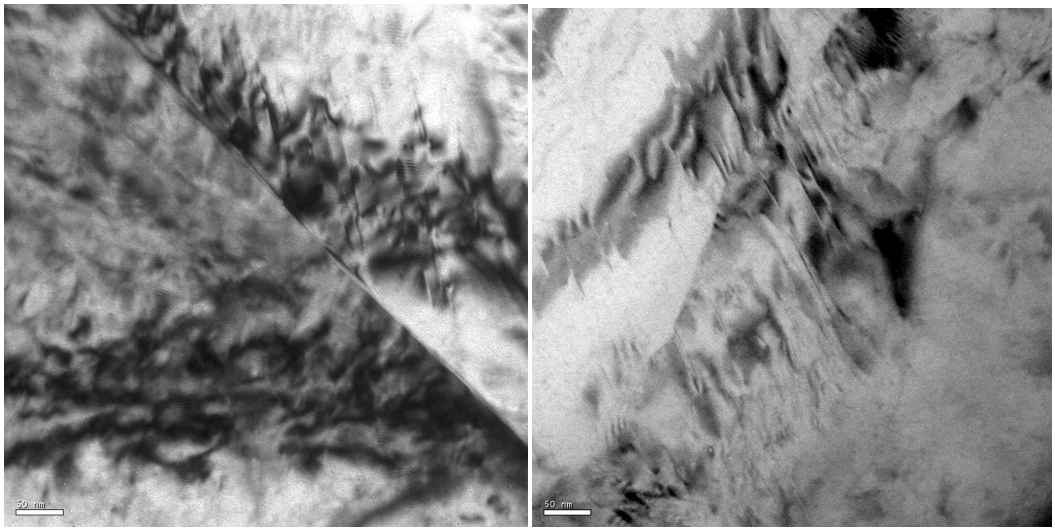

(a) (b)

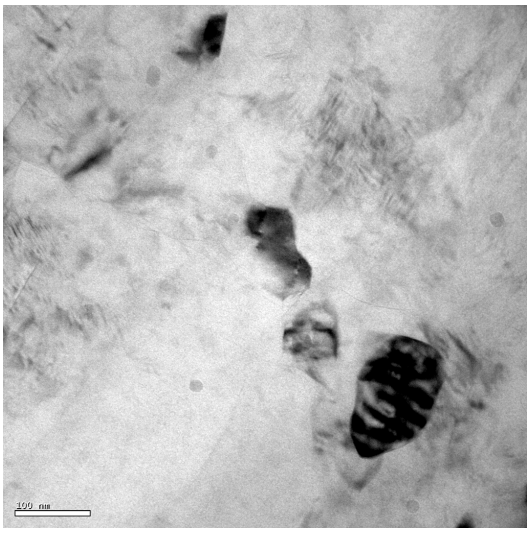

(c)

Figure 4.2. (a) and (b) Dislocations in some nano-sized grains. (c) dislocation-free grains.

4.2 Grain boundary structure in polycrystalline micron/nanpillars

We used FIB-milling process to fabricate the nanopillars for *in situ* SEM/TEM compression test. Figure 4.3 and Figure 4.4 show the SEM image of a micron Mg pillars before test and the bright field images of some of the polycrystalline nanopillars, respectively. Micron pillars were tested in SEM; their size were about 3 um * 3 um * 6 um. Nanopillars were tested in TEM. The diameters of these nanopillars were about 200 nm. The detailed milling procedures were similar to that described in chapter 2. Pillars usually contained different types of grain boundary. As shown in Figure 4.4, in some cases, the nanopillars had a low angle grain boundary (sub grains) inside; but in some other cases, they were high angle grain boundaries. The quantitative analysis of the grain boundary structure was performed based on the combination of the diffraction analysis and trace analysis. For example, as shown in Figure 4.4 (a), from the diffraction pattern, it is observed that the rotation angle between two grains is about 4 degree, which can be easily measured from the relative rotation of two [-1011] reflections from the diffraction patterns, as the grain boundary is parallel to the beam direction. The low angle grain boundary was marked by red dash lines; the sub grain is embedded in the large grain. Some polycrystalline nanopillars had relative higher angle grain boundaries; the rotation angles were about 10 to 16 degree. Figure 4.4 (b) is one example; the zone axis is [01-11]. The misorientation between two [-1011] reflections in the diffraction patterns was about 16 degree, which was still defined as low angle grain boundary.

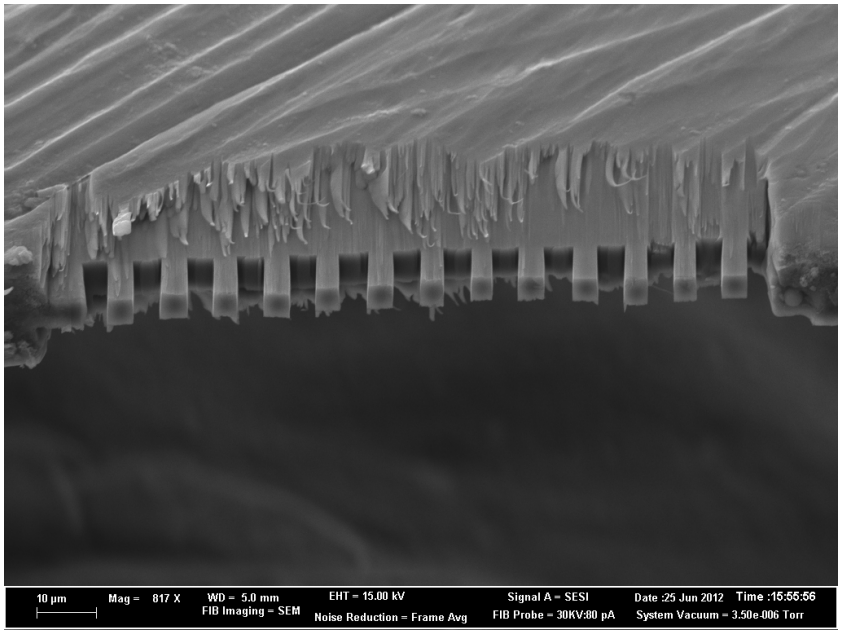

Figure 4.3. The SEM image of micron Mg pillars.

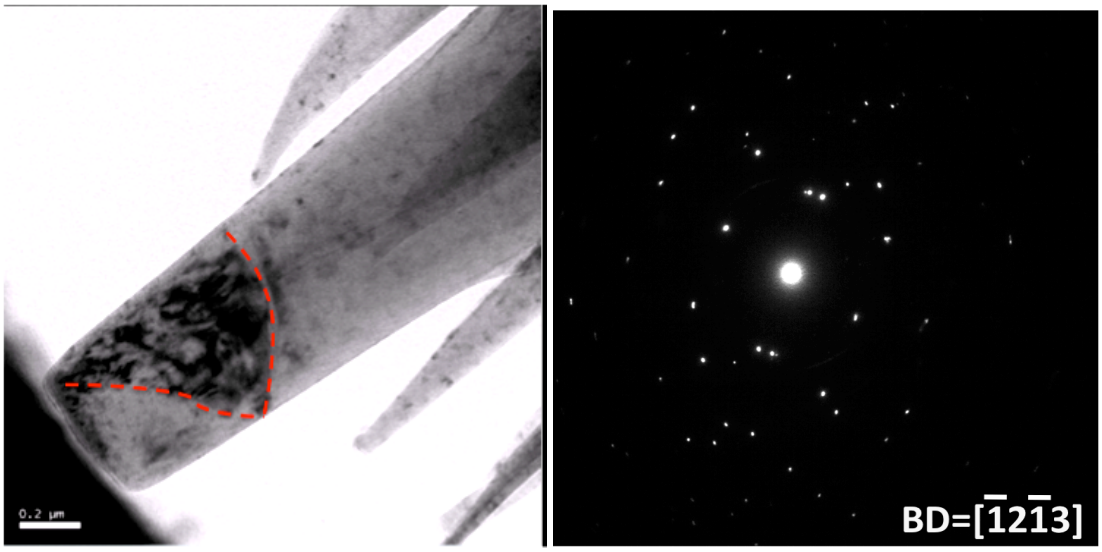

(a)

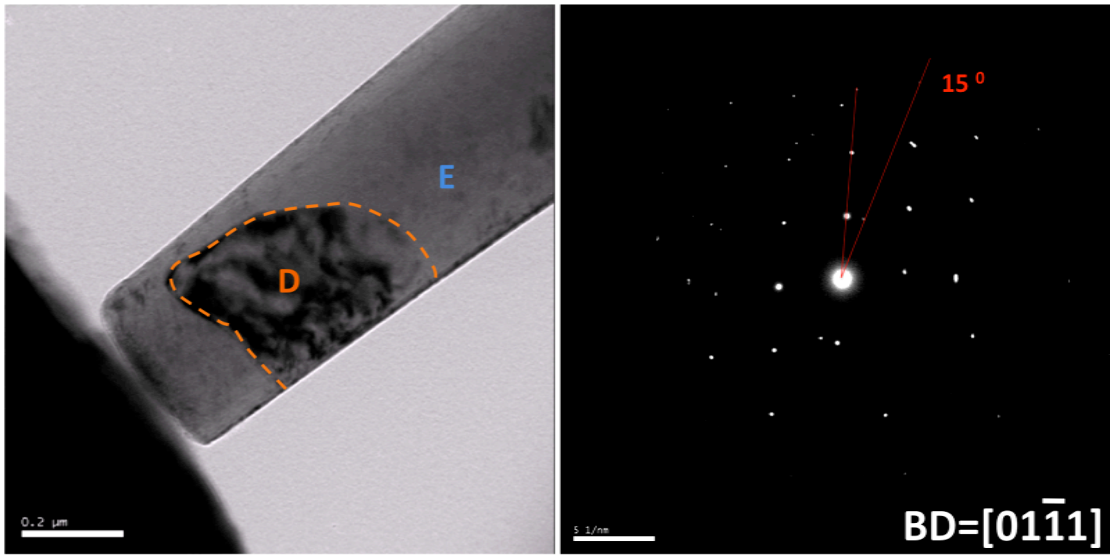

(b)

Figure 4.4. (a) The bright field image of a bicrystalline nanopillar with low angle grain boundary. The related diffraction pattern is shown at right. The rotation angle is only about 4 degree. (b) The bright field image of a bicrystalline nanopillar with low angle grain boundary. The related diffraction pattern is shown at right. Rotation angle is about 15 degrees.

Figure 4.5 shows the examples of nanopillars with high angle grain boundary inside. The high angle grain boundary was marked by the red dash line in the dark field image. The diffraction pattern demonstrated that the rotation angle was about 43 and 52 degrees in these cases, respectively. It was commonly observed that the high angle grain boundary was usually straighter and showed smaller curvature.

The highest angle we observed in the nanopillars was about 108 degree; but the average number was about 50 degrees. In the cases in Figure 4.5, the top part of the nanopillar was a small grain and the rest part of the sample was another larger grain. Since the volume of the second grain was relative small, the intensity of diffraction from this grain was low as shown in the diffraction pattern.

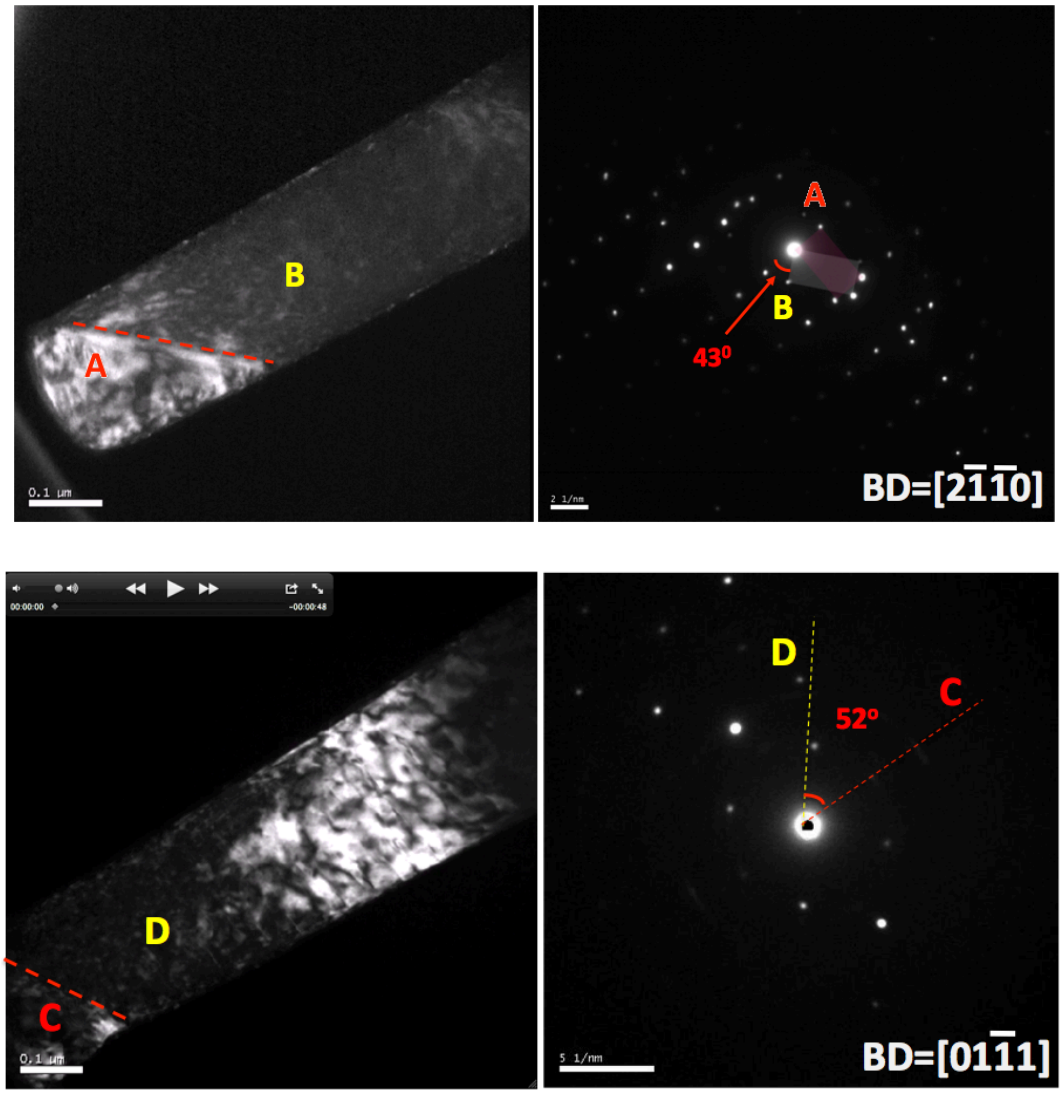

Figure 4.5. The dark field images of a bicrystalline nanopillar with high angle grain boundary. The related diffraction patterns are shown at right. Rotation angle are about 43 degrees and 52 degrees respectively.

4.3 *In situ* SEM/TEM nanocompression

The effect of grain boundary structures on the mechanical behaviors of nanopillars is significant. The polycrystalline pillars with low angle grain boundary usually displayed shear localization and the strain burst on the mechanical curves. Low angle grain boundary was found to be the weak barriers for dislocation motion and it might dissociate itself during plastic deformation. Easy glide then happened as that in single crystal samples, resulting localized shear. In contrast, the high angle grain boundary could facilitate different deformation modes. The pillars with high angle grain boundary could be

deformed either by the twinning deformation or dislocation plasticity, resulting in more continuous plastic flow. Grain boundary sliding was observed also but only in nanopillars with high angle grain boundary and one extremely small grain. The stress to activate grain boundary sliding was higher compared to that for dislocation plasticity in nanopillars with the same size. But the stress was almost a constant during the sliding. No grain boundary sliding was observed in micron pillars and the possibility of grain boundary sliding in nanopillars with high angle grain boundary was 2/6×100%. The *in situ* SEM/TEM mechanical testing also enable us to establish the time to time relationship between each deformation events and the related mechanical response of the material. In the following sections, the detailed analysis would be described.

4.3.1 The deformation of micron/nanopillars with low angle grain boundary

4.3.1.1 In situ SEM mechanical tests

Micron Mg pillars were tested in SEM through the Hysitron PI85 nanoindentation system with a flat diamond tip as shown in Figure 4.6. The tests were in displacement control mode.

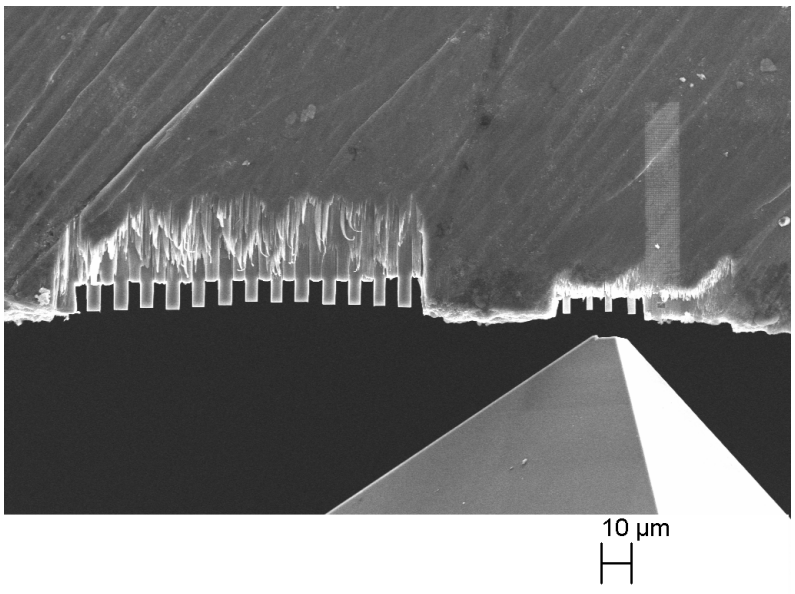

Figure 4.6 The setup of the in situ SEM compression test

One load-displacement curve from the in situ SEM compression tests is shown in

Figure 4.7. During deformation, the cross section area of the specimen gradually increased; formation of several smaller surface slip steps was observed, which was also showing as the small load drops on the Load-displacement curve. The test ended with the sudden shear off of one part of the pillar, which was showing as the big strain burst on the load-displacement curve. The yield strength is about 487 MPa.

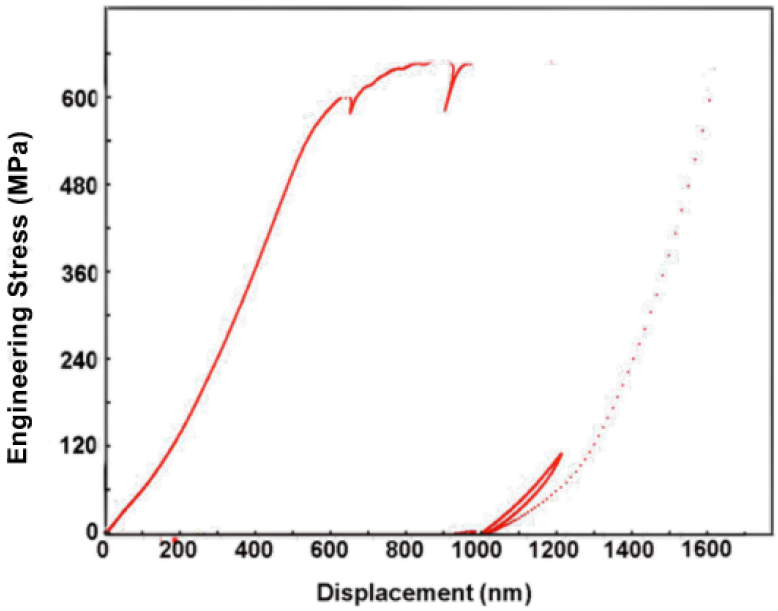

Figure 4.7 load-displacement curve from the in situ SEM compression test on a micron pillar with low angle grain boundary.

The deformed microstructure was further studied by performing EBSD analysis on the micron pillars after compression. Very low energy FIB milling with 1 pA current at 10 KV was used to flatten the deformed surface. The samples were then glued to a SEM holder and tilted to 70 degree in SEM. The EBSD detector was installed in a Zeiss FIB-SEM Crossbeam@workstation. The resolution can reach 10 nm. The EBSD data was cleaned by 3 degrees. Figure 4.8(a) shows the SEM image of a deformed micron pillar and its corresponding EBSD orientation map. The morphology of localized shear is remarkable, which is believed to be due to the easy glide of dislocations in this micron pillar with low angle grain boundary.

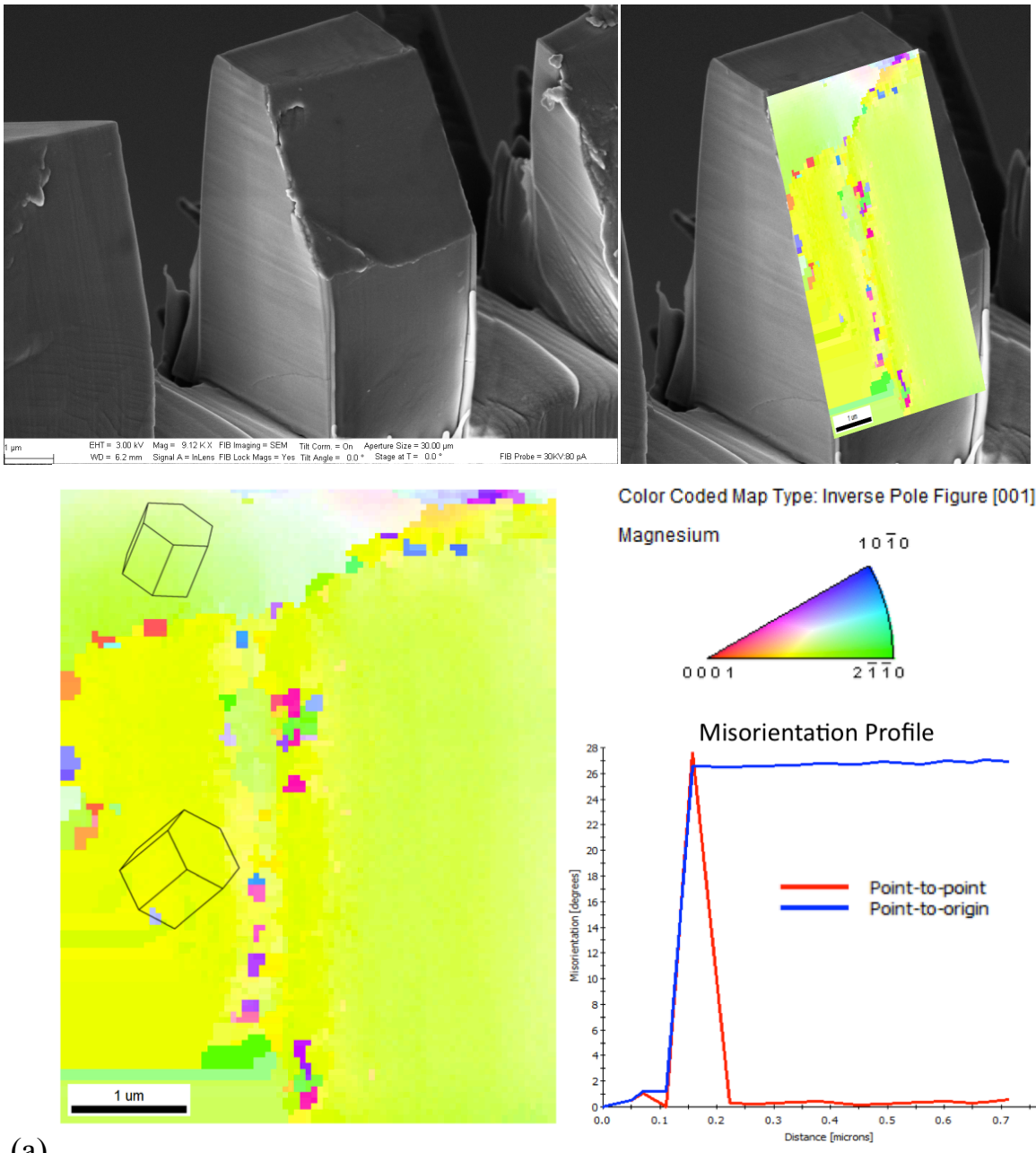

(a) (b)

Figure 4.8 (a) Left: The SEM image of a deformed micron pillar with low angle grain boundary showing the localized shear. Right: the EBSD orientation map of the pillar shown at left. (b) The EBSD map of the pillar in figure 4.7 and the related misorientation profile.

Figure 4.8(b) shows the EBSD map with the misorientation profile. The grain and yellow regimes have about 23 degrees off, which can be read from the

misorientation profile. The crystal orientation in each grain is also shown in the map. It was observed that even in one grain, the color changed gradually. The misorentation within the grain is about 6 degrees, which demonstrates the very intense dislocation activities during plastic deformation.

4.3.1.2 In situ TEM mechanical tests

The typical engineering stress-strain curves of the nanopillars with low angle grain boundary were shown in Figure 4. 9. In Figure 4.9 (a), the pillar yields at about 500 MPa. Here we defined the yield strength as the stress at which the linear relation of stress and strain ended. After yielding, strain hardening was read from the curve and the stress rise up to over 700 MPa; then strain hardening stopped and the curve showed several intermitted small load drops. A larger load drop happened afterwards accompanied by a remarkable strain burst, after which the strain hardening appeared again and the strain change was continuous. Such phenomenon was commonly observed in our nanopillars with low angle grain boundary. In Figure 4.9 (b), this nanopillar shows the yield strength at around 430 MPa and the highest flow stress at about 1 GPa. Similar to the former case in Figure 4.9 a, intermitted small load drops were observed in the plastic deformation stage and a larger load drop appeared latter.

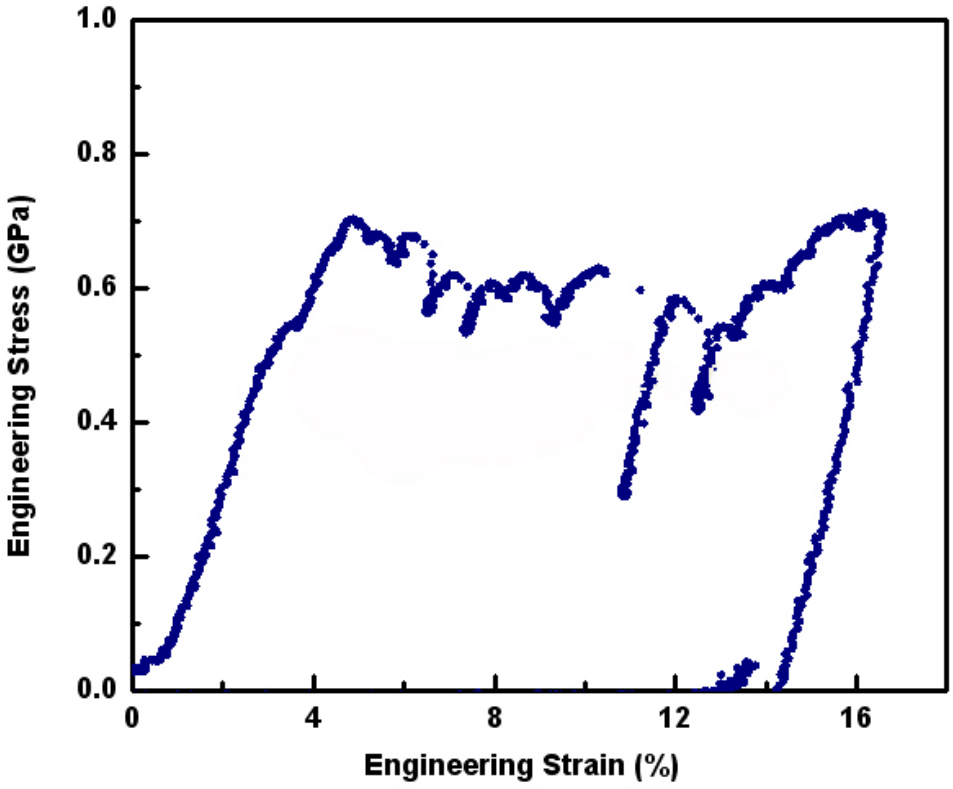
Engineering Stress (GPa)
Engineering Strain (%)
0.0
0.2
0.4
0.6
0.8
1.0
0
4
8
12
16

(a)

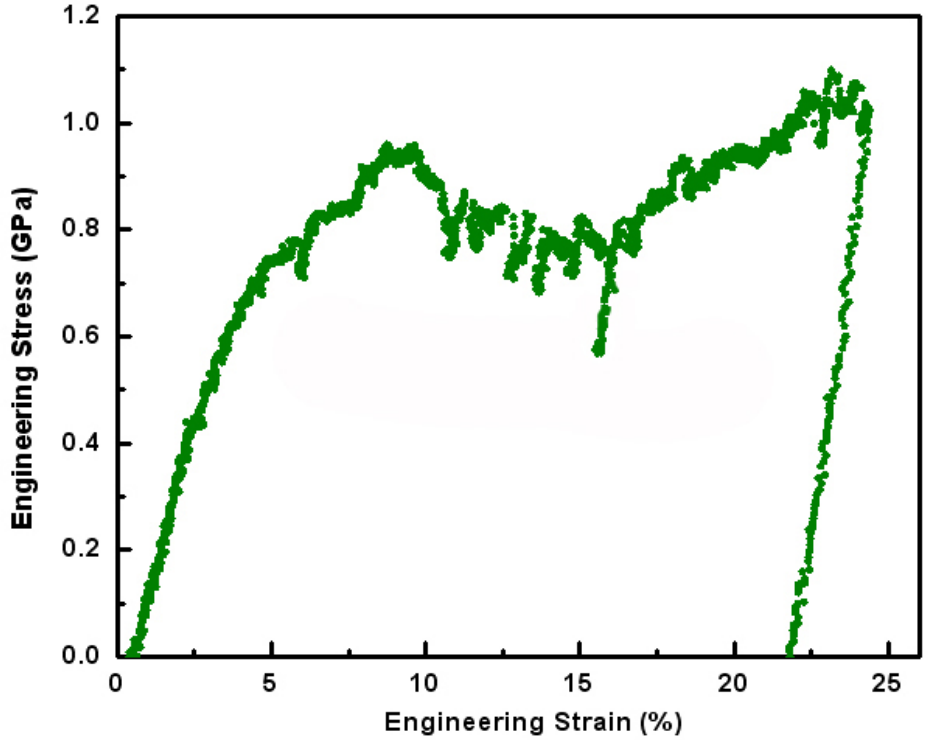
Engineering Stress (GPa)
Engineering Strain (%)
0.0
0.2
0.4
0.6
0.8
1.0
1.2
0
5
10
15
20
25

(**b**)

Figure 4. 9 (a) and (b) The typical engineering stress-strain curves of the nanopillars with low angle grain boundary.

Relating the movies with the mechanical curves, better understanding on the mechanical behaviors can be achieved. From the movie https://dl.dropbox.com/u/81430932/s3.00%20selected.mp4, which corresponds to the curve in Figure 4.9 b, the dissociation of low angle grain boundary was observed. Figure 4.10 shows the bright field TEM image of the nanopillar before the compression test. One relative large grain was sitting in the top part of the pillar, which was labeled as grain "A". Another sub-grain with low angle grain boundary was sitting in the middle of the pillar, which was labeled as grain "B". Grain "C" located at the bottom of the nanopillar and had a large angle grain boundary with grain "A". The related diffraction pattern clearly showed the reflection spots corresponding to each of the grains.

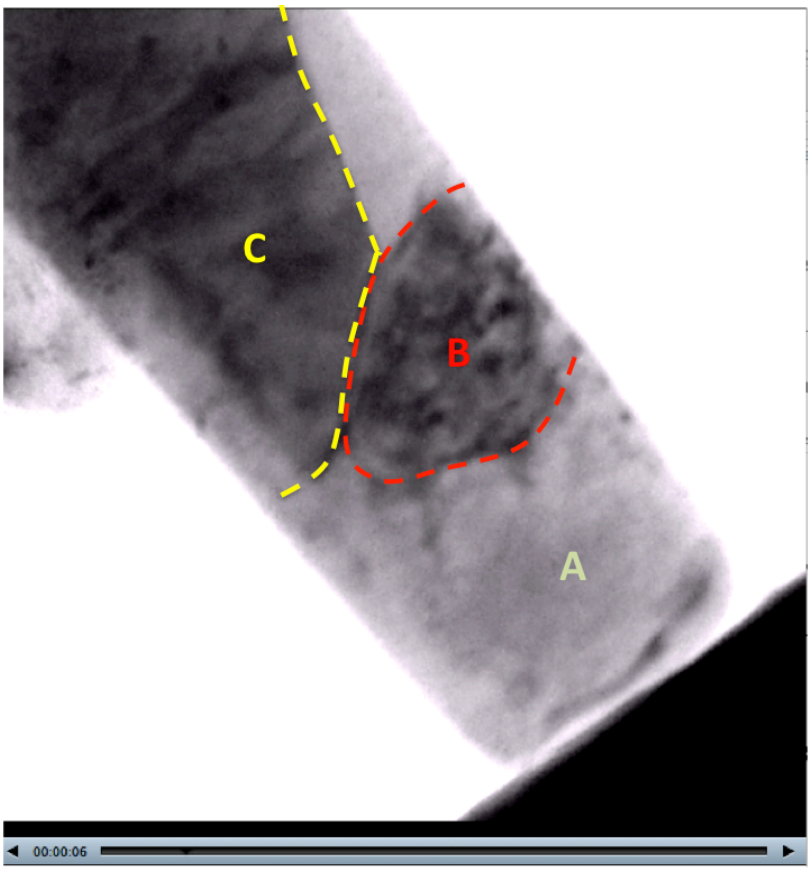

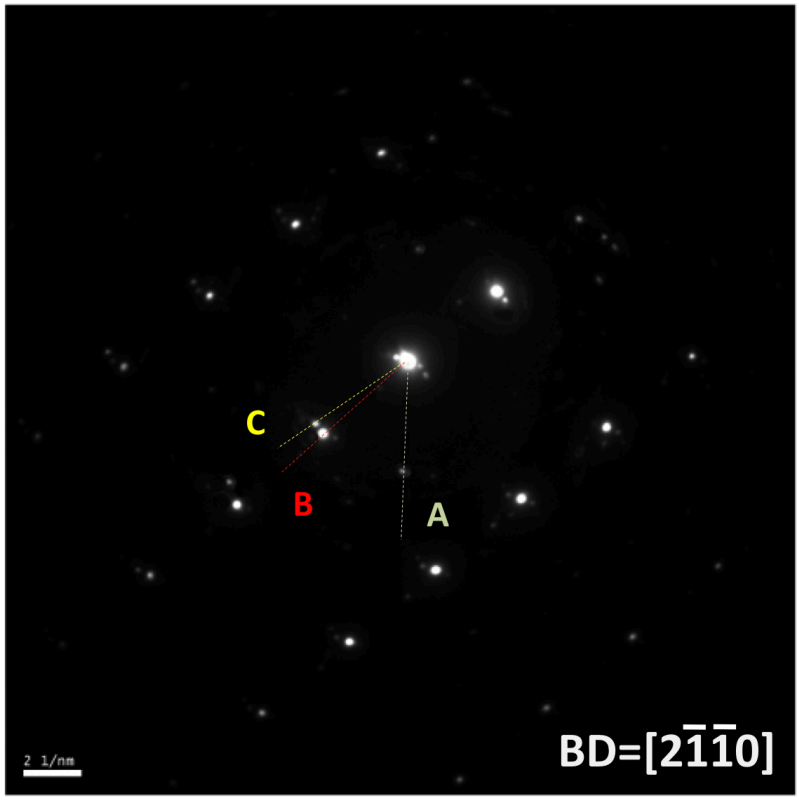

Figure 4.10 The bright field image of a nanopillar before the compression test and the related diffraction patterns.

During the compression test, it was observed that the dislocation activity first initialized from the contact surface and quickly infected the regime just below it; meanwhile the sample yield and strain hardening appeared on the curve. Figure 4.11 is the bright field image captured from the movie during this process. When the stress reached about 700 MPa, the grain boundary structure of grain "B" changed. The grain boundary dissociated gradually from top to bottom with the motion of dislocations, as showing in Figure 4.12 (a) and (b); several intermitted load drops appeared on the curve. The amplitude of the small load drops was about 50 MPa each.

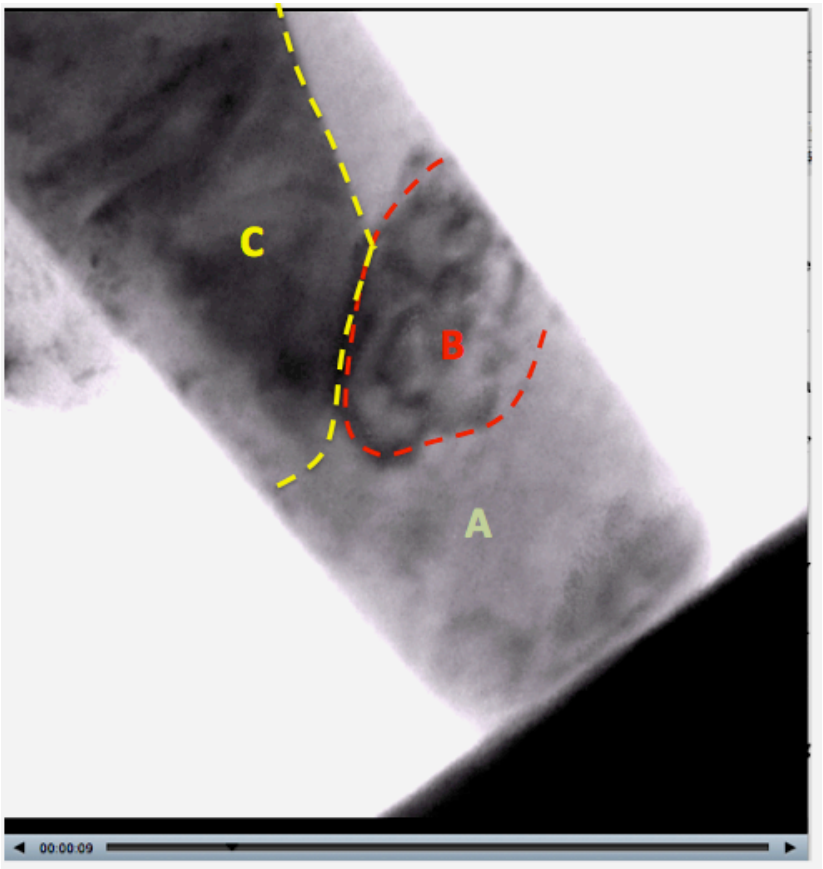

Figure 4.11 The bright field image captured from the movie to show the dislocation activities from the contact surface.

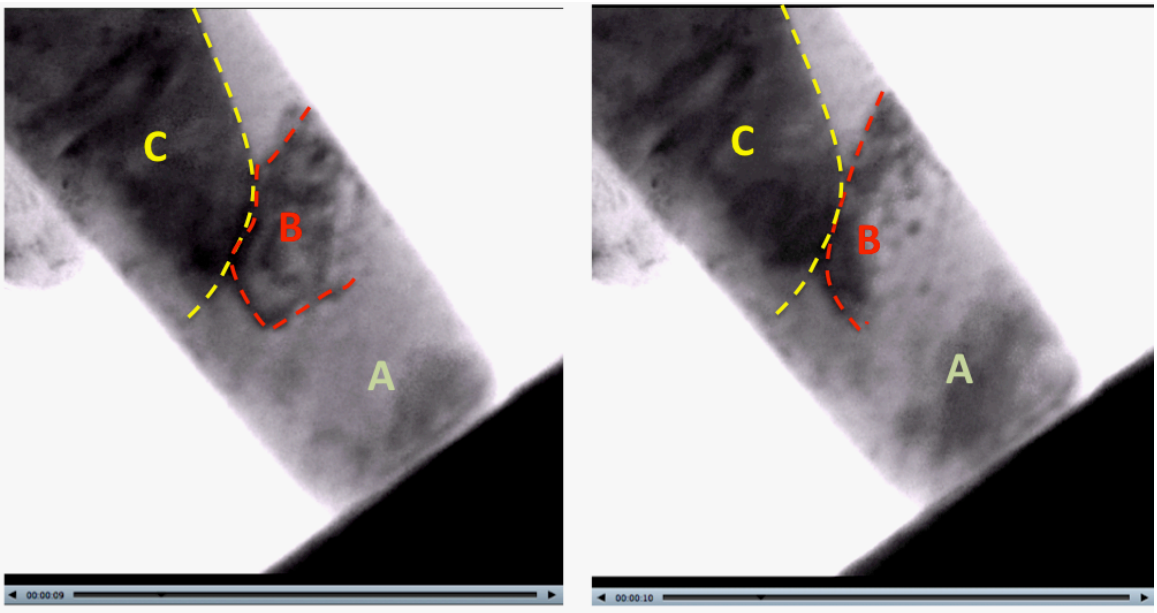

Figure 4.12. The grain boundary dissociated gradually from top to bottom with

the dislocation motion.

A larger load drop happened latter with almost 300 MPa stress change. At this moment, strong strain contour appeared, indicating the heavy dislocation activities in both grain “A” and grain “C”. Continuous strain hardening was read from the curve afterwards and the diameter of the pillar increased significantly, which was mainly due to the further dislocation interactions. Figure 4.13 shows the nanopillar after compression; only grain “A” and grain “C” can be seen. Consistently, the related diffraction pattern also showed the disappearance of reflection spots from original grain “B”.

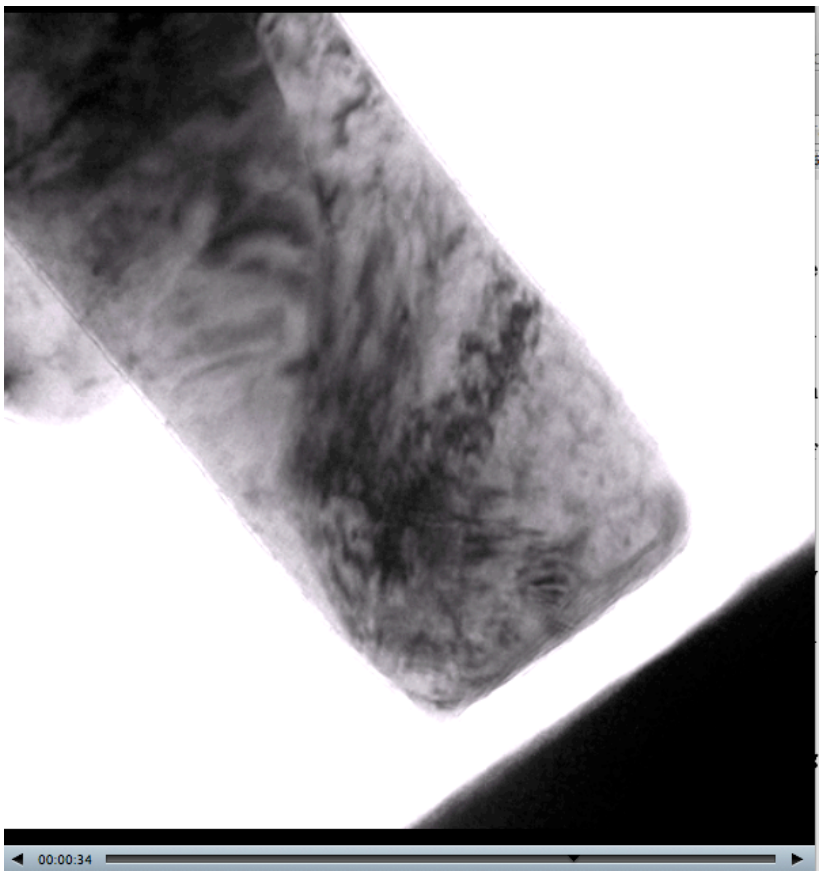

Figure 4.13 The nanopillar after compression, bright field image and diffraction pattern; only grain “A” and grain “C” can be seen. Grain “B” disappeared. BD=[2-1-10].

In the nanopillar that corresponded to the curve in Figure 4.9 a, two grains were observed, which were marked as grain “D” and grain “E”. Grain “E” was a sub grain and had low angle grain boundary with grain “D”. Figure 4.14 shows the bright field TEM image of this nanopillar before compression test.

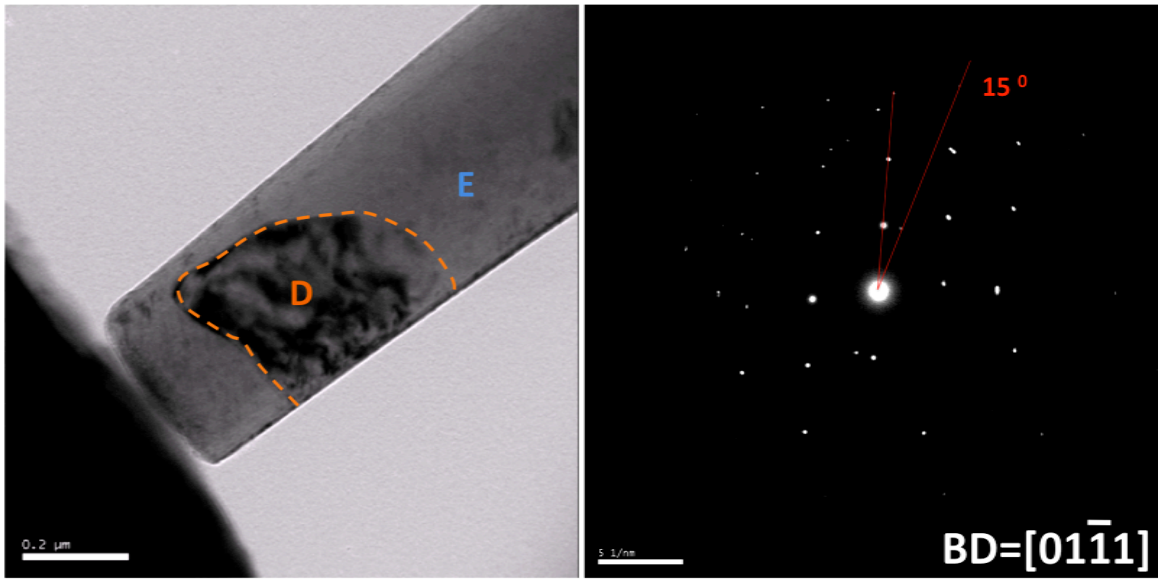

Figure 4.14 The bright field image of the nanopillar in figure 4.9 (b) before compression test.

The related diffraction patterns before the tests showed the diffraction spots from the two individual grains. During the deformation, the dissociation of the low angle grain boundary processed gradually. Similar to the other cases with low angle grain boundary-mediated deformation; intermittent small load drops appeared during the dissociation of the grain boundary. Figure 4.15 shows images captured from the movie, the dissociation of grain boundary was observed. During the dissociation of the grain boundary, the dislocation activities in grain "E" became much stronger. The diameter of the nanopillar at the top part increased due to the significant plastic deformation in grain "E".

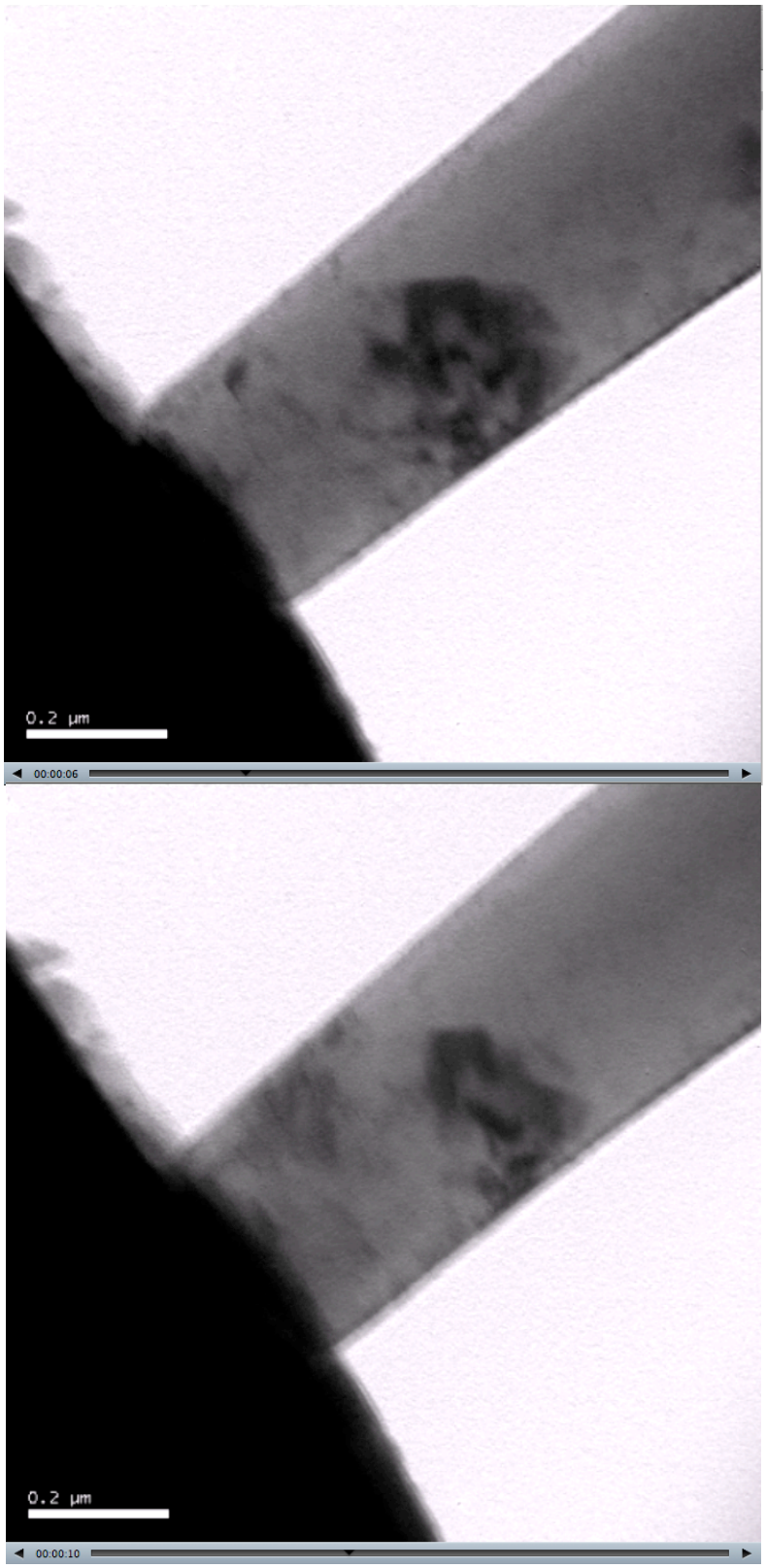

Figure 4.15 The bright field images captured from the movie, the dissociation of

grain boundary processed gradually.

After the completion of the grain boundary dissociation, the whole pillar became a single crystal; no grain boundary was observed anymore, but the load was still increasing. At a certain moment, a shear event happened suddenly, which corresponded to a large load drop on the engineering stress-strain curve. Meanwhile, a big strain burst was detected from the mechanical data, which was responsible for about 2.5% strain change. Consequently, a small shear step appeared; the offset along the shear direction was about 12 nm.

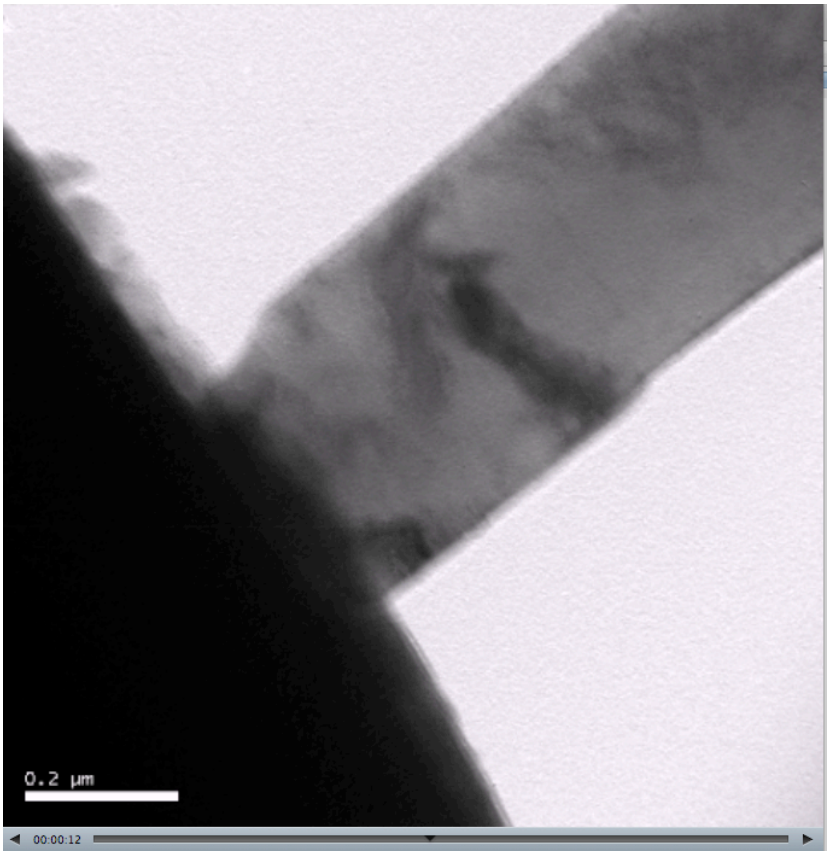

Figure 4.16. A significant shear step was produced; the offset along the shear direction was about 20 nm.

During the further deformation, the top part started to slip off further; and strain hardening appeared on the curve. Finally, a significant shear step was produced; the offset along the shear direction was about 20 nm, as shown in Figure 4.16. The related diffraction pattern showed the single crystal spots, the diffraction spots from original grain “D” disappeared (Figure 4.17).

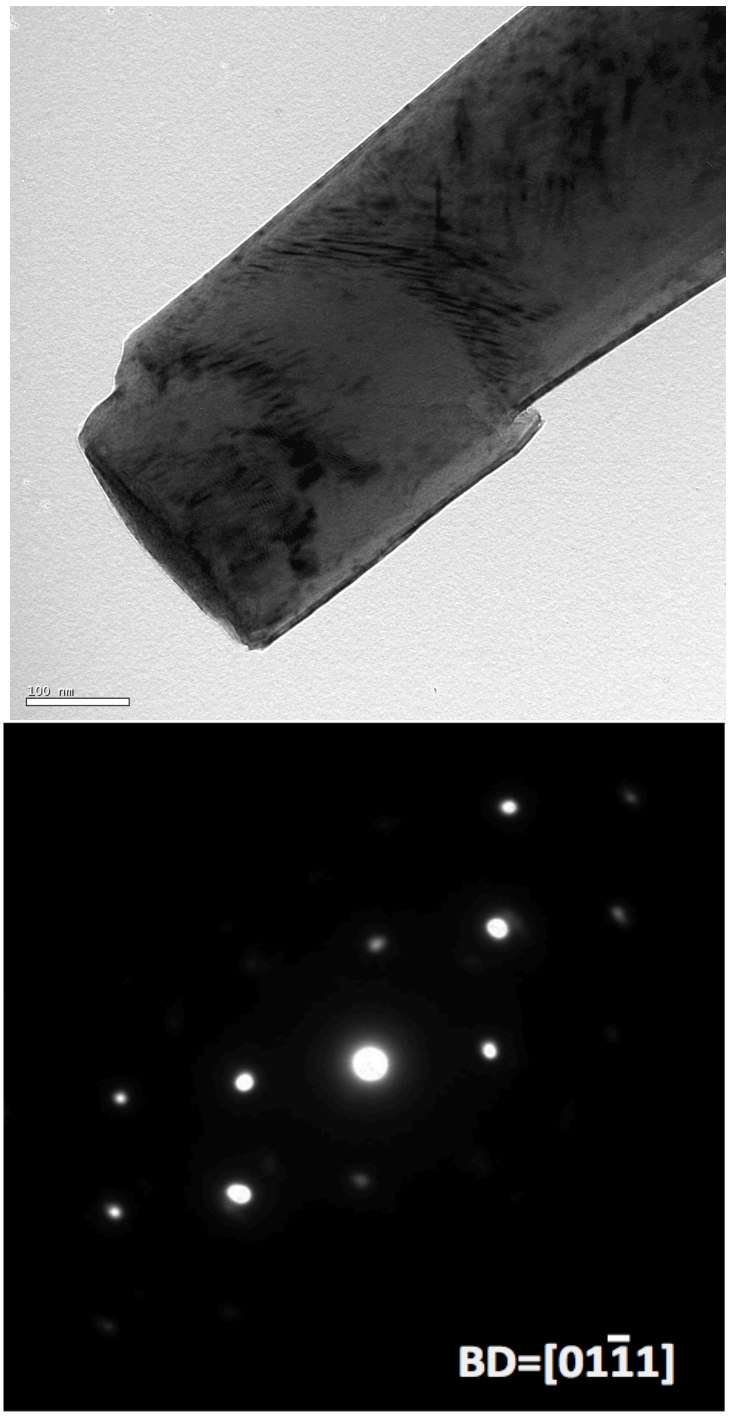

Figure 4.17. The pillar after compression test. The related diffraction spots from original grain “D” disappeared.

4.3.2 The deformation of micron/nanopillars with high angle grain

boundary

High angle grain boundaries are much more stable than low angle grain boundaries. From the results of micron/nanopillars with high angle grain boundary, grain boundary dissociation had not been seen. Instead twinning deformation and dislocation activities dominate the plastic deformation within the grains and also at the grain boundaries. Grain boundary sliding was also observed in nanopillars during in situ TEM compression; but it only happened in some specific case where the pillar contained one extremely small grain.

4.3.2.1 *In situ* SEM compression tests

The micron pillars with high angle grain boundary were studied in the same method as described in 4.3.1. The mechanical behavior of these pillars is significantly different from that in the pillars with low angle grain boundary. Figure 4. 18 shows one of them, from which we can see the continuous plastic flow. Several small plateaus were observed from the load-displacement curve, which were believed to be the typical sign for the formation of deformation twinning. The yield strength in this case is about 530 MPa.

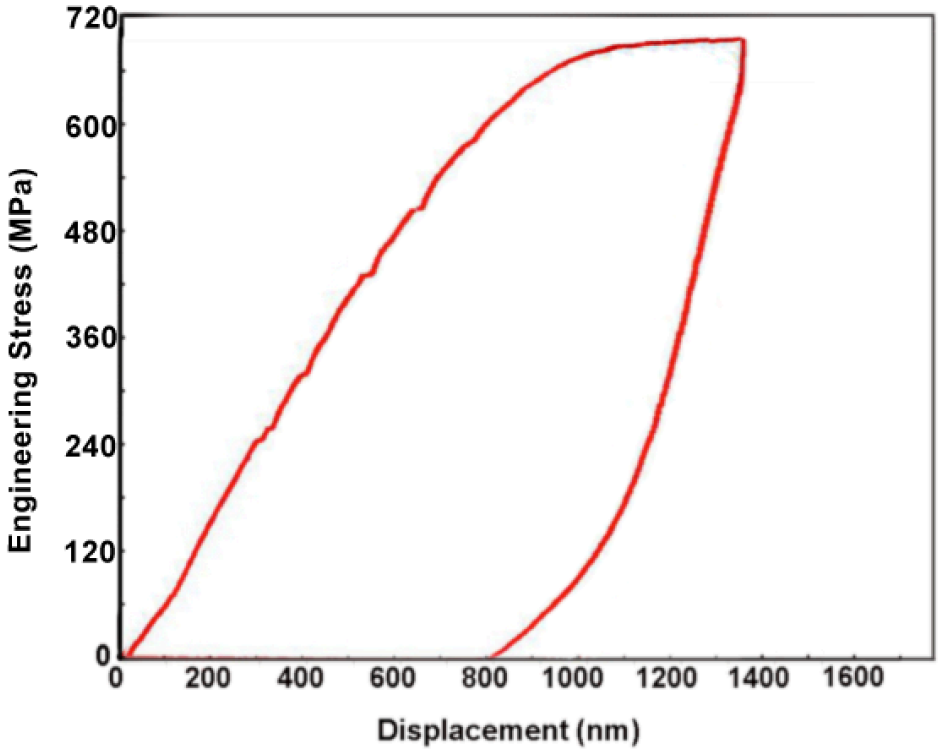

Figure 4.18 The load-displacement curve from a micron pillar with high angle grain boundary.

The morphology of the deformed micron pillar and the related EBSD orientation map are shown in the SEM image in Figure 4.19. Both extension twin and contraction twin were observed in the deformed microstructure. The deformation twins were in the lens shape, consistent with the TEM observation.

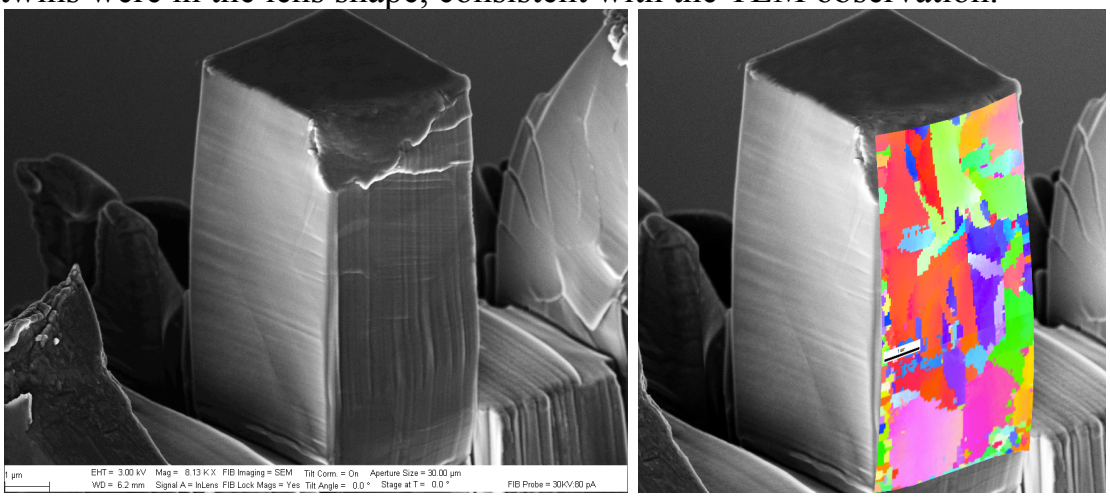

Figure 4.19 The SEM image of the deformed micron pillar and its corresponding EBSD map.

The EBSD orientation map and the misorientation profile are shown in figure 4.20. The grain boundaries in this pillar were all high angle grain boundaries. The misorientation angles between each of them were larger than 40 degrees. Interestingly, some deformation twinning started/ended at the grain boundary, but some of them were sitting inside of the grain. So we can see that it is not necessary to form the deformation twinning with the help of grain boundary. Similar to the low angle grain boundary cases, the color within the grain also changed. For example, in the red grain, at some location, the color changed to near orange; the misorientation between red and orange was about 5 degrees, indicating the strong dislocation activities in the grain. The dislocation activity was usually more intense near the grain boundary. As the example, the pink grain shows light pink near the grain boundary with misorientaion angle at about 6 degrees.

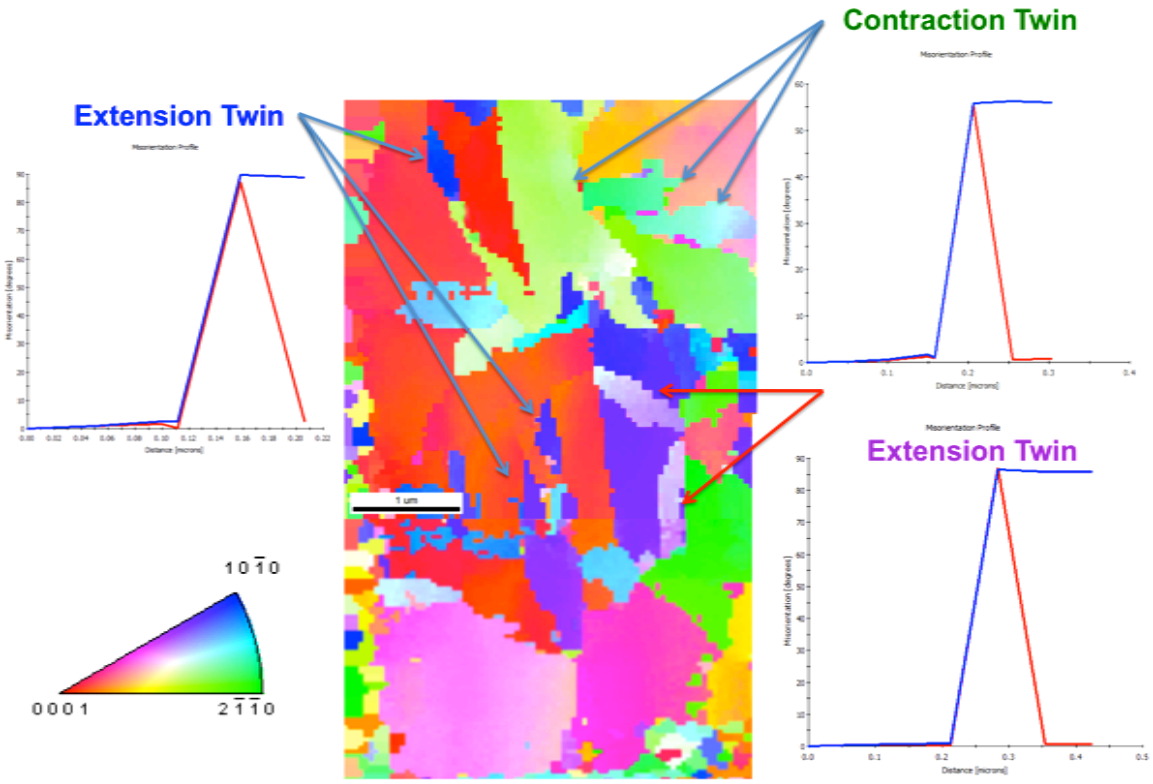

Figure 4. 20 The EBSD orientation map and the misorientation profile of the micron pillar in figure 4.19.

4.3.2.2 In situ TEM compression tests

4.3.2.2.1 Grain boundary-enhanced dislocation plasticity

Figure 4.21 shows an example of nanopillars with high angle grain boundary. The dark field TEM image shows two individual grains, which are marked as grain "A" and grain "B" and their related diffraction spots are shown in the diffraction pattern on right. The related engineering stress-strain curve is shown in Figure 4.22, which has the continuous plastic flow.

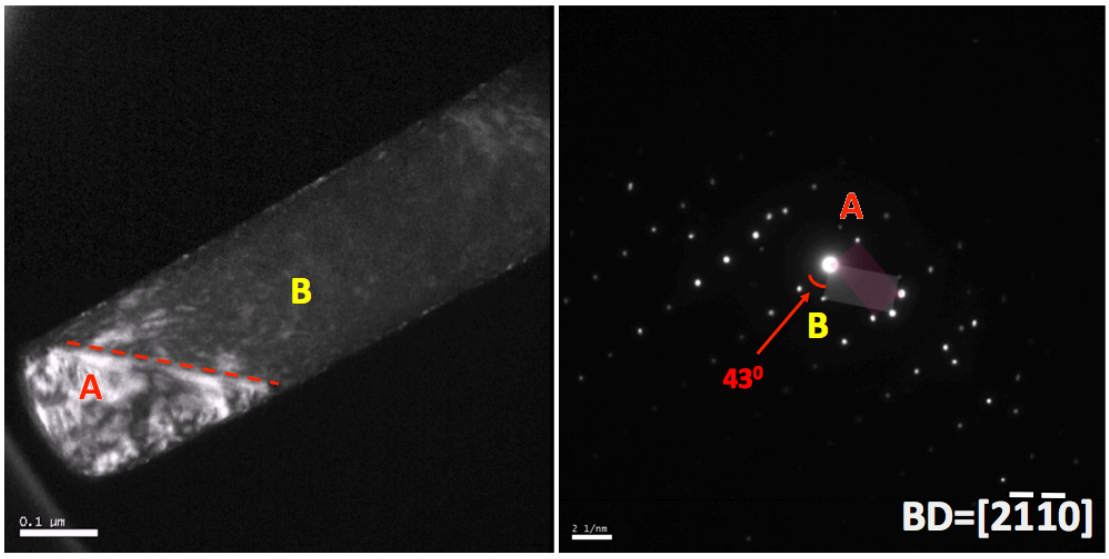

Figure 4.21 Example of a nanopillar with high angle grain boundary. The dark field TEM image shows two individual grains, which are labeled as grain "A" and grain "B" and have their related diffraction spots shown in the diffraction pattern.

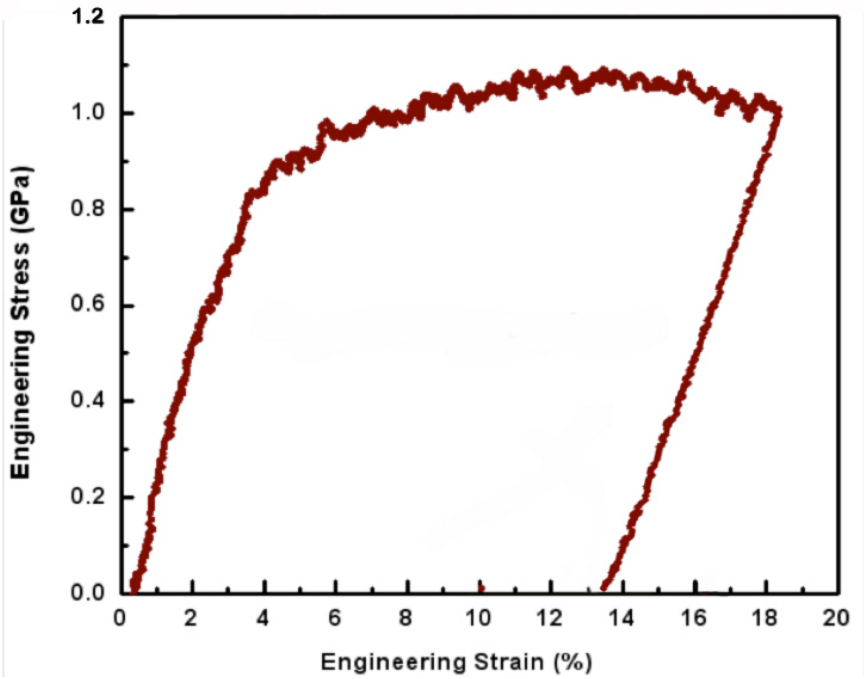

Figure 4.22 The engineering stress-strain curve corresponding to the nanopillar in Figure 4.21.

Relating the movie with the mechanical curve, detailed correlation of the microstructure evolution and deformation response of the material can be

analyzed. The dislocation activity was first activated in grain “A”. It has been commonly agreed that the taper of the nanopillar and the nano-level roughness of the contact surface would facilitate the dislocation activity starting from the contact surface, as shown in Figure 4. 22 left. The curve shows the deviation from linearity at about 500 MPa. Significant work hardening phenomenon was observed from the curve until the stress reached about 800 MPa, after which remarkable dislocation activity was observed in grain “B”; started from the grain boundary and quickly infected the rest of the pillar (shown in Figure 4.23 right). Work hardening can be still read from the stress-strain curve, but the work hardening rate decreased comparing with that in the previous stage. The deformation was continuous and no strain burst appeared. The maximum flow stress reached about 1.1 GPa. No grain boundary dissociation, migration and sliding was observed.

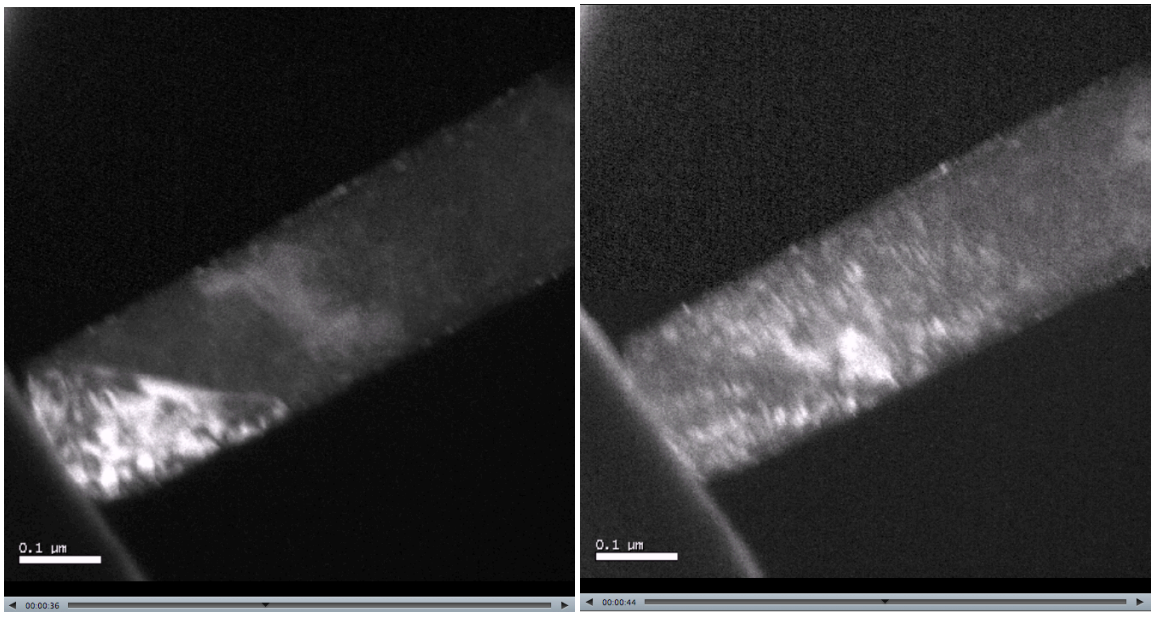

Figure 4.23 The evolution of dislocation activities during the compression test (left to rigth).

4.3.2.2.2 Grain boundary sliding

It was observed in some cases that the nanopillars with high angle grain boundary deformed by grain boundary sliding, especially in pillars containing a extremely small grain.

As shown in Figure 4.24, before compression test, grain “C” and “D” were observed. The rotation angle was about 52 degrees. Grain “C” was located at the

top and had relative small volume fraction.

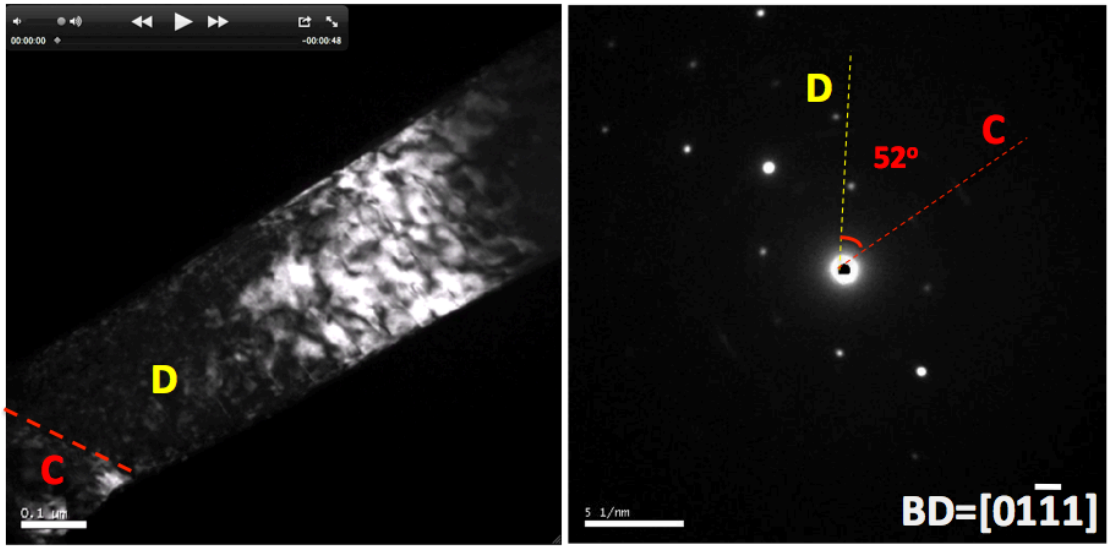

Figure 4.24 The dark field image of the pillar before the test and the related diffraction pattern that shows the ~52 rotation angle.

Figure 4.25 shows the related engineering stress-strain curve of this sample. As the load applied, the stress increased linearly to about 700 MPa; beyond this point, the curve showed the deviation from the linearity. Meanwhile some dislocation activities were observed from grain "C", but not intense. Work hardening rate was high, which was believed to be the exhausting hardening. The maximum flow stress can reach 1000 MPa. Grain boundary sliding happened next and the stress dropped to about 750 MPa. It was clear that the grain "C" slipped off along the grain boundary. Meanwhile, strong dislocation activities initialized at the grain boundary, which can be evidenced from the significant change of the local strain contour. We noticed that the stress to activate the grain boundary sliding in this case was about 1000 MPa. Once started, the stress that kept the sliding decreased to about 800 MPa and stayed as almost a constant. The grain boundary sliding processed gradually. Different from the strain burst that commonly is observed in small sample testing, the strain change was almost continuous even though several drops of stress were observed. No significant dislocation activities were observed from the other parts of the pillar.

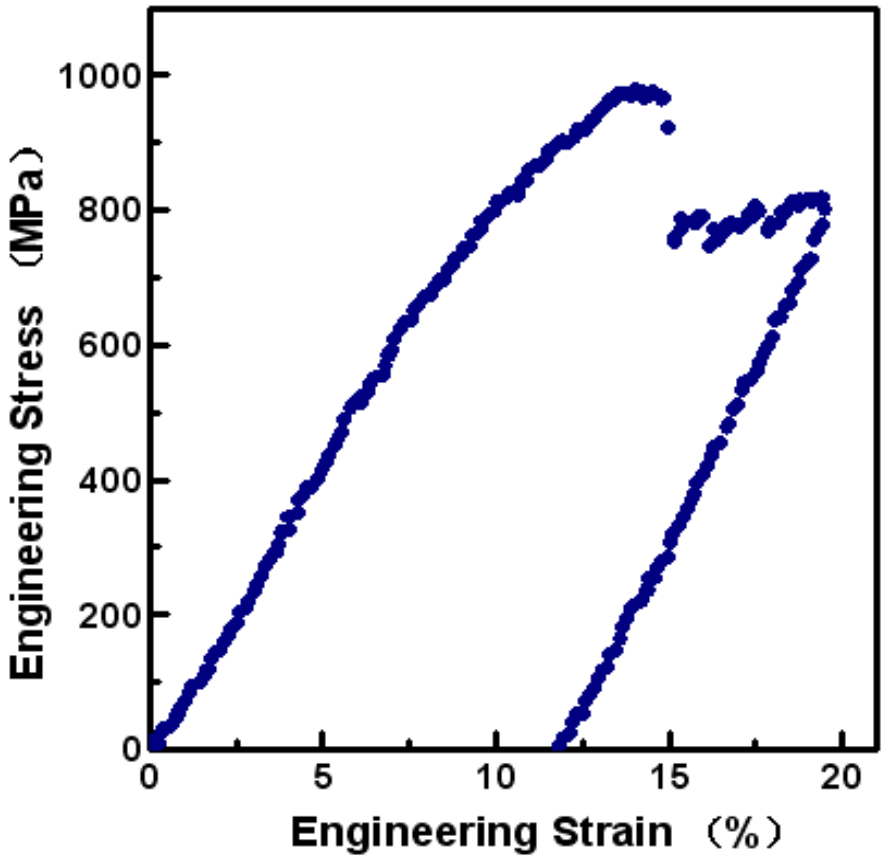

Figure 4.25 The related engineering stress-strain curve for the sample in figure 4.24.

4.4 Discussion

Our experimental results show that the influence of different grain boundary structure on the deformation mechanisms and the mechanical properties of Mg are very different. Low angle grain boundary was found to be the weak barriers for dislocation motion and it might dissociate itself during plastic deformation. Easy glide then happened as in single crystal samples, resulting in localized shear. In contrast, the high angle grain boundary could facilitate different deformation modes. The pillars with high angle grain boundary could be deformed either by the twinning deformation or dislocation plasticity, resulting in more continuous plastic flow. Grain boundary sliding was observed also but only in nanopillars with high angle grain boundary and one extremely small grain.

In theory, low angle tilt grain boundaries are generally considered to be composed of edge type of perfect dislocations, where Burgers vector of the

perfect dislocations corresponds to a translation vector in the crystal structure. It was found from the recent bicrystal experiments, however, that some of low angle grain boundaries in ceramics were composed of dissociated dislocations, where individual dislocation was divided into partial dislocations with very narrow separation distance, forming a stacking fault between partial dislocations (*106*).

D. L. Medlin et al also reported the similar dislocation reaction in gold (*107, 108*). Their high resolution transmission electron microscopy (HRTEM) observations and atomistic simulations of {11 ⅂}/{121} facets in a gold 90° tilt boundary showed the presence of a 10 A˚ wide layer with stacking faults distributed one to every three close-packed planes. This interfacial reconstruction, which formed the rhombohedra 9R stacking arrangement, was similar to that found in low stacking fault energy metals. They believed that the formation of stacking faults at the boundary was the consequence of the dissociation of full dislocation into Shockley partial dislocations.

In our Mg study, high resolution TEM (HRTEM) was employed to study the atomic structure of the grain boundaries before the tests. In the nanopillar shown in figure 4.14, dislocation arrays were observed at the grain boundary. As shown in Figure 4.26, the grain boundary area was about 5 to 7 atomic spacing wide. High density of dislocations was observed at the grain boundary compared with that within the grain. Only one type of dislocation was identified. The dislocation arrays induced lattice distortion and resulted a tilting angle at about 5 degrees between grain “A” and grain “B”. No stacking faults formed at the grain boundary, which was mainly because of the high stacking faults energy in Mg.

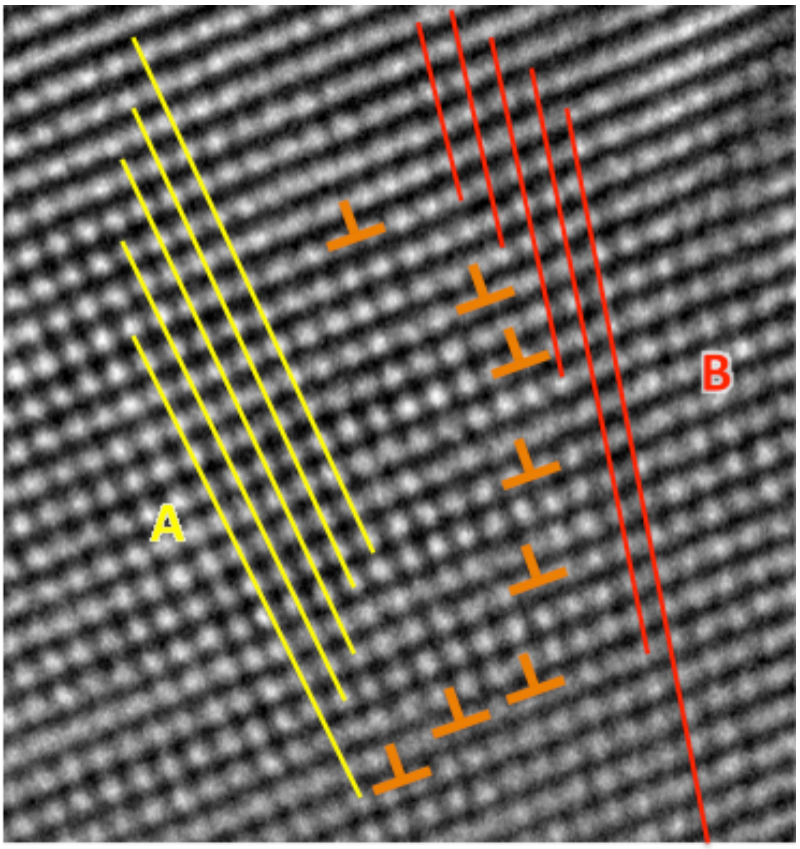

Figure 4.26 HRTEM image of the low angle grain boundary, dislocation arrays were observed at the grain boundary.

The engineering stress before the deviation from the linearity in the in situ TEM nanocompression tests was usually ~600 MPa in low angle grain boundary cases. With such high stress, it is not a surprise that the dislocations at the grain boundary are mobile. Based on the recorded tilting angle x and y of a certain TEM image, we can calculate the angle between the grain boundary normal and the loading direction of the sample. For the nanopillar, from which the HRTEM image in Figure 4.26 was taken, the relationship of lattice orientation and the sample orientation was shown in Figure 4.27. It was estimated that the angle between the dislocation slip direction and the loading direction should be larger than 19 degrees. So similar to the mechanical annealing phenomenon reported in FCC Ni and BCC Mo, the high stress provided large shear component along the slip direction of dislocations, driving the dislocations out of the sample from the free surface. Dissociation of the low angle grain boundary happened due to the dislocations motion and the dissociation of the grain boundary dislocation walls. Since the grain size here was in the same order as the length of dislocations, we considered the stress as the local stress for the dissociation of grain boundary.

Further plastic deformation was similar to that in single crystal samples with the same sample size, where a leading dislocation source operated at certain crystal plane, generating big shear step along the slip direction.

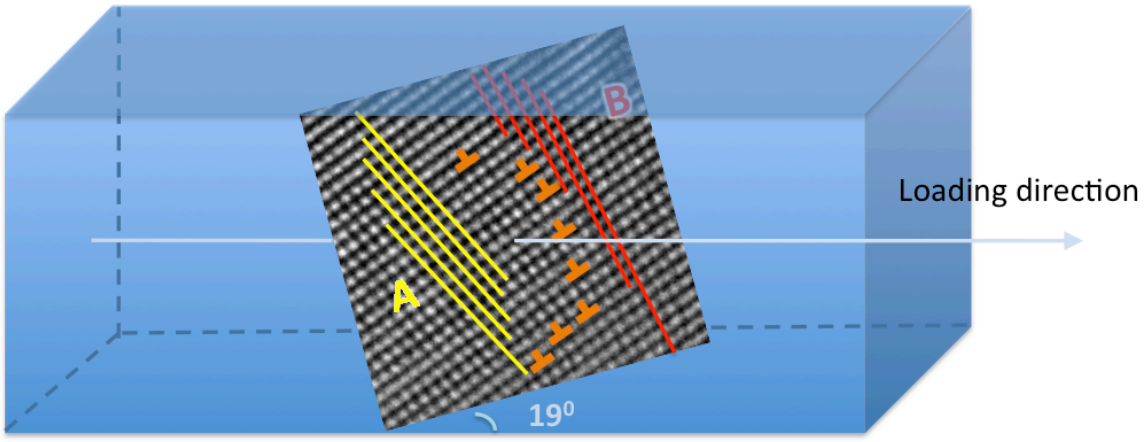

Figure 4.27 The lattice orientation in the nanopillar shown in figure 4.14

High angle grain boundary is much more stable than low angle grain boundary. A HRTEM image of the high angle grain boundary in the original microstructure is shown in Figure 4.28.

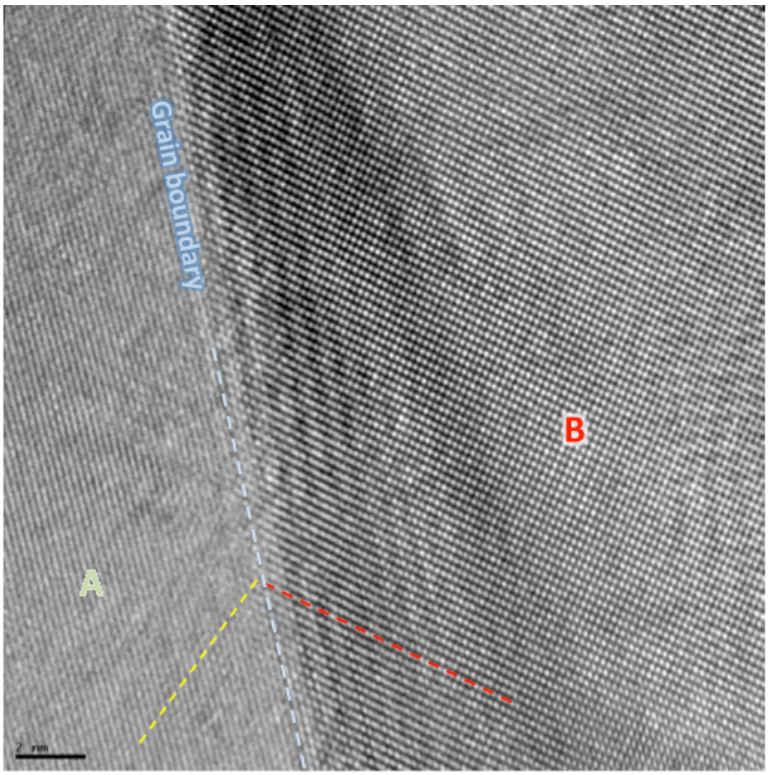

Figure 4.28 A typical HRTEM image of the high angle grain boundary before compression.

Because of the technique difficulty to orient the nanopillars in TEM, it was hard to tilt the high angle grain boundary to be parallel to the beam direction. Moire fringes were observed in Figure 4.28 due to the overlapping of two grains at the grain boundary. However, the tilting angle between these two grains can be roughly estimated by the lattice rotation, which gave a number around 100 degrees. Even though the detailed atomic structure analysis at the grain boundary cannot be carried out, it is believed that there is no significant thickness of amorphous layer at the grain boundary. These high angle grain boundaries were observed to facilitate the dislocation activity by serving as the dislocation sources.

There have been many reports both from experiment and simulation to demonstrate that the grain boundary can be either the dislocation source or sink (*109, 110*). K. S. Kumar et al performed tension test on nc Ni; their TEM results showed that in *nc* Ni with grain size in the 30-40 nm regimes, ample dislocation emission was triggered at the crack tip, and this process could extend over several grains ahead of the crack tip. In addition, it appeared that these dislocations were generated at grain boundaries, and preceded to the adjacent/opposite boundary where they were absorbed.

In our study, it was obvious that the dislocation activity in the grain below initialized from the high angle grain boundary and then the whole pillar was infected. Work hardening was preserved due to the strong dislocation interaction at the grain boundary and within the grain afterwards. *Ex situ* TEM analysis after the compression tests showed the dislocation configuration in the deformed pillar where dislocation tangling was clearly seen. Under two-beam condition, the dislocations in the lower grain showed up; the grain boundary area had the higher dislocation density. Dislocation lines intersected with the grain boundary, which were considered as outgoing dislocations that originally emitted from the high angle grain boundary. The reason that grain boundary can serve as the dislocation source comes from the mismatch between two grains at the grain boundary. Higher disordering at the grain boundary produces local stress concentration and also supplies large number of vacancies. Dislocation nucleation is easier than that within the grain. The twinning deformation also happened to accommodate the plastic deformation in micron pillars.

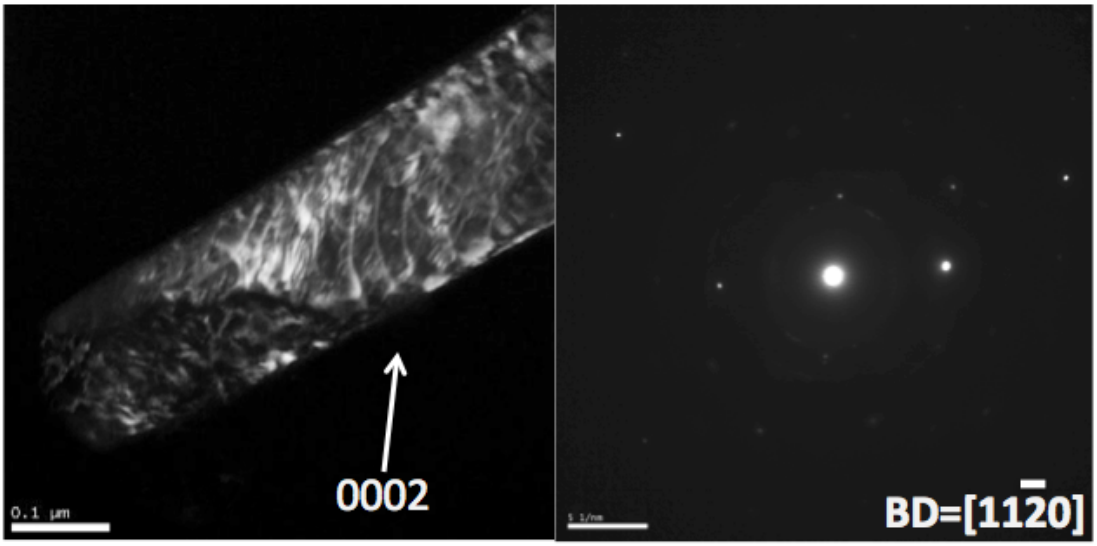

Figure 4.29 A typical dark field image for the high angle grain boundary after compression; large number of dislocations can be observed near the grain boundary. The related diffraction pattern is shown at right.

A large proportion of the nanopillars with high angle grain boundary deformed in the form of dislocation plasticity and the micron pillars deformed by the combination of twinning deformation and dislocation plasticity. However, it was also observed that grain boundary sliding happened and dominated the plastic deformation in some cases when the top grain was too small to sustain dislocation activities.

The stress level in those cases was indeed higher than that for dislocation plasticity, indicating the higher energy cost for grain boundary sliding. It was also noticed that the grain boundary sliding differed from the localized shear from several sides. First the grain boundary sliding processed gradually with almost the constant rate; no significant strain burst appeared even the load drops were dramatic. In comparison, the localized shear in single crystal pillars usually happened promptly and was accompanied by remarkable strain burst. Secondly dislocation activities can be observed near the grain boundary in both grains during the grain boundary sliding; the thickness of the area where strong dislocation activities happened was about 100 nm. Different from the localized shear in single crystals where the slip happens on certain crystal plane and little dislocation activity can be observed from the adjacent regime, the differences here indicate that grain boundary sliding is associated with three-dimensional dislocation plasticity but localized shear is mainly accomplished by two-dimensional dislocation plasticity.

From the description of previous literatures, grain-boundary sliding is the relative translation of a pair of grains by a shear movement at their common interface. This definition is meant to include cases where shear takes place in a zone of finite width around the boundary, and cases in which sliding is a shear confined completely to the interface (*111-115*). Our results confirmed the former one since the 100 nm thick deformation zone can be clearly see during the grain boundary sliding. The theories of grain boundary sliding have been discussed for decades. Stevens reviewed the related studies in 1965 and suggested several possible mechanisms: 1) migration theory; 2) deformation theory (*116, 117*). Intrater and Machlin proposed that migration is the rate-limiting process. An elastic shear relaxes the stress on to "jogs" on the boundary. This causes the jogs to migrate, expanding the relaxed area. When the relaxed area reaches a critical size, fracture of tension jogs and deformation of compression jogs occur to give a pulse of sliding (*117*). However, this theory suggested a jump on the sliding/time curve, which was not observed in some others results and also ours.

Weertman suggested that macroscopic sliding is a shear in the boundary region caused by dislocation movement (*118*). The dislocations arrive at the boundary from within the grains, and climb along the boundary. If the slip plane is not perpendicular to the boundary, slip will take place in addition to climb, thus shearing the boundary zones. Nix et al also believed that the sliding of grain boundaries in polycrystalline solids needed to be accommodated either by diffusional flow or by dislocation slip in the adjoining grains (*119*). Figure 4.30 shows the basic concepts.

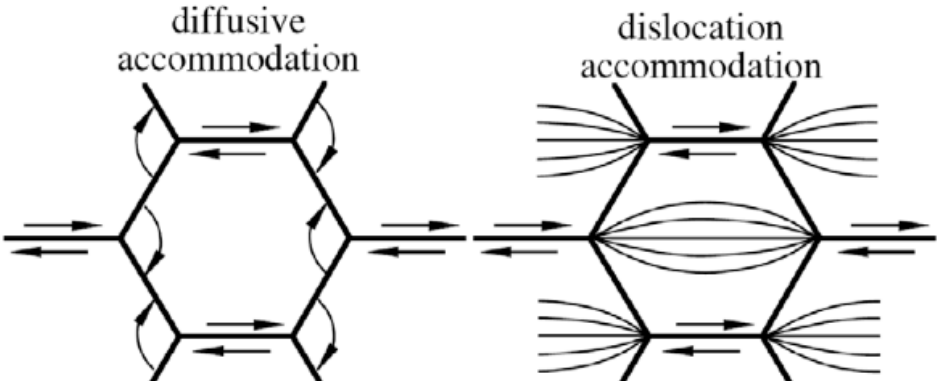

Figure 4.30 Illustration of both diffusional and dislocation accommodation of grain boundary sliding in a polycrystalline solid (*119*).

Our results from the ambient temperature testing showed agreement with the deformation theory, especially the dislocation accommodation of grain boundary sliding (*120, 121*). We also believe that diffusion must be the important mechanism for grain boundary sliding at elevated temperature. Dislocation accommodation of grain boundary sliding observed here generated strain change by the shear deformation of the grain boundary and the dislocations activities in adjacent regimes. No detectable plastic deformation was observed in the other parts of the samples.

Considering the high stress to initialize the grain boundary sliding and the limited strain relaxation associates with grain boundary sliding at room temperature, we doubt that if the grain boundary sliding itself can lead to the better ductility in Mg and superplasticity at even elevated temperature. However, our results provided direct observation to support the deformation zone and dislocation accommodation in grain boundary sliding. The detailed dislocation interaction at the grain boundary still needs further theoretical investigation.

Chapter 5

Conclusions

5.1 Summaries

The size related deformation mechanisms and mechanical properties in single crystal and polycrystalline Mg were studied by employing *in situ* TEM mechanical testing techniques including tension, compression and bending. Because of the HCP structure, which limits the number of slip systems, we are able to design the crystal orientation to study the individual deformation mechanisms. The size-related deformation twinning behavior, dislocation behavior and grain boundary behavior were investigated respectively in this way; the corresponding mechanical properties of the materials were also studied.

5.1.1 Size-related deformation twinning behavior

By studying the deformation twinning behavior in submicron samples stressed into tension, compression and bending, we have observed the fundamental embryonic structure of deformation twinning. We have directly measured the local stress to nucleate deformation twinning and the intrinsic toughness of pure Mg, both of which are much larger than presently achieved in bulk Mg, indicating large headroom for improvement. Combined with the simulation results, we believe that the formation of dense nanotwin arrays is kinetically favorable at the nucleation stage of deformation twinning even in materials with high twin boundary energies. We tested the possibility of nanotwins formation in nanocrystalline Mg and obtained deformation nanotwins in grains with about 50 nm size. Recent experimental results in nanocrystalline Mg study also reported the formation of nanotwins in the small grains near the crack tip, which confirmed our theory (*49*). This study develops our understanding on the kinetic nucleation mechanisms of deformation twinning and can further contribute to the future development of advanced structural materials. For example, it is conceivable that new alloys or processing schemes could be designed to take advantage of kinetics factors that would preserve nanotwinned structures to enhance strength and ductility.

5.1.2 Size-related dislocation behavior

In situ TEM tension tests were employed to study the dislocation behavior with varying external dimension of samples. By mapping the size-dependent strength

and plasticity in Mg, we reveal the evolution of dislocation behaviors that occur as the external dimension of crystal is decreased. The trend of size-related transitions in dislocation behavior from 3D-activity to localized 2D-activity and then to homogeneous nucleation-dominated dislocation activity should be intrinsic to all metals but the exact transition sizes would depend on the material (alloy composition), strain rate etc. since the CRSS of different slip systems is size-dependent, small dimensions lead to high strengths and the reduction in CRSS anisotropy. The activation of multiple slip systems creates strain along different directions to satisfy the arbitrary shape change, leading to much better ductility. In the case of Mg, the high strengths activate non-basal slip systems, but in the case of cubic alloys certain alternative deformation modes (non-Schmid systems) might be activated at high stresses. Importantly, this is a possible way to tune the CRSS anisotropy of slip systems to achieve simultaneous ultra-high strength and ductility by constraining the external dimension of materials below a certain value, a concept that can be incorporated into advanced alloy design through microstructural control that exploits the plasticity behavior in polycrystalline samples where grain size and grain orientations can be manipulated to provide the desired effects. The hints have already been shown in some previous studies on grain boundary refinement and/or twin boundary refinement.

5.1.3 Grain boundary-mediated plasticity in polycrystalline Mg

The behavior of low angle grain boundary and high angle grain boundary were studied respectively. The yield stress can all reach about 600 MPa. The low angle grain boundary acts as weak barriers for dislocation motion; it was found to be metastable, which dissociated itself under high stress. So the easy glide is easier in samples with low angle grain boundaries, resulting in shear localization. The samples with high angle grain boundary deformed differently. In most cases, grain boundary-enhanced dislocation plasticity dominates the plastic deformation. High angle grain boundary can act as the dislocation sources and promote the dislocation activities, especially in the near-boundary regime, resulting in continuous plastic flow. Twinning deformation also happened in micron pillars with high angle grain boundaries. Grain boundary sliding was observed in the cases where the grain size is too small to accommodate dislocation plasticity. Nevertheless, our in situ study demonstrates that the sliding is accomplished in the form of deformation zone with dislocation activities.

5.2 Future work

Expanding upon my *in situ* TEM compression/tension/bending work, the combination of nanoscale *in situ* and *ex situ* mechanical tests with high resolution TEM analysis of nanostructured bulk materials and nanoscale materials (pillar structures, nanowires, etc.) is a field that new instrumentation and techniques can make a large impact on. One of the most important challenges that I believe these experimental techniques can address is to close the length and time-scale gaps that exist not only between experimental and computational materials science, but also between experimental investigations and realistic applications. In both computational materials science and realistic applications, there are many fundamental problems (creep, fatigue, crack, etc.) that are related to physical phenomena at different length and time scales. *In situ* electron microscope mechanical testing is currently developed as an efficient tool that can directly aim to close these gaps by probing the intrinsic deformation mechanisms, and then to improve the processing procedures for applications. Specifically for some advanced materials such as hcp Ti and Mg, where the deformation mechanisms are relatively complicated, I see there is large headroom for exploiting these techniques. There are three topics that could be the focus of future work: 1) to develop *in situ* electron microscope tension, bending and fatigue testing, to establish the time-to-time relation between individual mechanical response of materials, such as the necking, nucleation and propagation of crack and fracture, and the microstructure evolution, such as the dislocation activities, phase transformation and twinning, which can lead to a direct and profound understanding on materials' mechanical behaviors. 2) to exploit the possible "critical size" and/or "critical rate" for deformation modes transition by varying the internal dimensions (gain size) or external dimensions (physical dimension) of materials, such as the behind of the Hall-Petch to inverse Hall-Petch relation transition and the plasticity transition in my previous work, or varying the strain rate in the fatigue/creep experiments. Such transitions could be universal phenomena, which will strongly change the mechanical behaviors of materials. 3) to directly correlate and integrate these measurements into computational simulations to probe the intrinsic mechanisms, and use these improved understanding on future materials design and processing.

Reference:

1. Gulnaz Nurislamova, Xavier Sauvage, Maxim Murashkin, Rinat Islamgaliev, Ruslan Valiev, Nanostructure and related mechanical properties of an Al-Mg-Si alloy processed by severe plastic deformation. *Philosophical Magazine Letters* **88**, 459 (2008).
2. John Alico, Introduction to magnesium and its alloys. *Ziff-Davis Publishing Company,* , (1945).
3. Henry Marshall Leicester, Herbert S. Klickstein, A Source Book in Chemistry *New York: McGraw Hill*, 1400 (1952).
4. R. Reed-Hill, *Acta Met* **5**, 728 (1957).
5. J. W. Christian, deformation twinning. *Progress in Materials Science* **39**, 1 (1995).
6. M. R. Barnett, Twinning and the ductility of magnesium alloys Part I: "Tension" twins. *Materials Science and Engineering A* **464**, (2007).
7. G. Partridge, The crystallography and deformation modes of hexagonal close-packed metals. *Met. Rev.* **12**, 169 (1967).
8. C. S. BARRETT, T. B. MASSALSKI, The structure of metals. *McGraw-Hill, New York.*, (1966).
9. Berghezan, Fourdeux, AmeHnckx, *Acta MetalL* **9**, 464 (1961).
10. Legrand B, *Phil. Mag.* **49**, 171 (1981).
11. J. C. Williams, M. J. Blackburn, The identification of a non-basal slip vector in titanium and titanium-aluminum alloys. *Phys Status Solidi,* **25**, (1968).
12. Hutchinson.W.B, Barnett.M, Effective values of critical resolved shear stress for slip in polycrystalline magnesium and other hcp metals. *Scripta Materialia* **63**, 737 (2010).
13. Koike.J *et al.*, The activity of non-basal slip systems and dynamic recovery at room temperature in fine-grained AZ31B magnesium alloys. *Acta Materialia* **51**, 2055 (2003).
14. Hosford W.F, The mechanics of Crystals and Textured Polycrystals，1st ed. *Oxford Univ. Press，New York.*, (1993).
15. Cahn R.W, *Acta Met* **1**, 49 (1953).
16. Cahn R.W, Twinned Crystals，. *Adv. in Phys*， **3**, 363 (1954).
17. I. J. B. L. Capolungo, Nucleation and stability of twins in hcp metals. *PHYSICAL REVIEW B* **78**, (2008).
18. Y. Wang, L. Q. Chen, Z. K. Liu, S. N. Mathaudhu, First-principles calculations of twin-boundary and stacking-fault energies in magnesium. *Scripta Materialia* **62**, 646 (2010).
19. N. Thompson, D. J. Millard, TWIN FORMATION IN CADMIUM. *Philosophical Magazine* **43**, 422 (1952).
20. M. L. Kronberg, Atom movements and dislocation structures in some common crystals. . *Acta Met* **9**, 970 (1961).
21. D. G. Westlake, {10.1} twinning in the h.c.p. structure,. *Acta Metall.* **14**, 442 (1961).
22. R. C. Pond, J. P. Hirth, Solid state physics academic, New York, NY: Plenum Press. **47**, 287 (1994).

23. W. T. R. OROWAN. E, JR., AND W.SHOCKLEY., *Dislocations in metals*. C. M, Ed., (American Institute of Mining and Metallurgical Engineers, New York, 1954).
24. P. B. Price, Nucleation and Growth of Twins in Dislocation-Free Zinc Crystals. *Proc. R. Soc. Lond. A* **260**, 251 (1961).
25. R. G. H. J. Wang, J.P. Hirth, L. Capolungo, I.J. Beyerlein and C.N. Tome, Nucleation of a (-1012) twin in hexagonal close-packed crystals. *Scripta Materialia* **61**, 903 (2009).
26. J. P. H. J. Wang, C.N. Tome, (-1012) Twinning nucleation mechanisms ihexagonal-close-packed crystals. *Acta Materialia* **57**, 5521 (2009).
27. B. Li, E. Ma, Atomic Shuffling Dominated Mechanism for Deformation Twinning in Magnesium. *Phys. Rev. Lett.* **103**, 4 (Jul, 2009).
28. Slutsky L.J, Garland C.W, *Phys. Rev.,* **107**, 4 (1957).
29. Burke E.C, Hilbbard W.R Jr., *J. Metals, Trans. AIME,* **295**, (1952).
30. Hirsch P.B, Lally J.S, *Phil. Mag.,* **12**, 595 (1965).
31. Tsui R T C, Internal friction and transmission electron microscopy studies of magnesium. *Acta Materialia* **15**, 1723 (1967).
32. B. Bhattacharya, M. Niewczas, Work-hardening behaviour of Mg single crystals oriented for basal slip. *Phil. Mag.* **91**, 2227 (2011).
33. Groves G.W, Kelly A, *Phil. Mag.,* **8**, 877 (1963).
34. Agnew S.R, Horton J A , Yoo M.H, Metall. Trans. A, . *Metall. Trans. A,* **33A**, (2002).
35. Stohr J.F, Poirier J.P, *Phil. Mag.* **25**, 1313 (1972).
36. Obara T, Yoshinga H, Morozumi S, *Acta Materialia* **21**, 845 (1973).
37. Ando S, Tonda H, *Mater. Trans., JIM,* **41**, 1188 (2000).
38. Yoo M H, Agnew S.R, Morris J.R, Ho KM, *Mater. Sci. Engng, A,* **87**, 319 (2001).
39. Frank F.C, Nicholas J.F, *Phil. Mag.* **44**, 1213 (1953).
40. Liang M.H, Bacon D.J *Phil. Mag., A,* **53**, 205 (1986b).
41. Liang M.H, Bacon D.J, Phil. Mag., A, . *53*, (1986a).
42. Minonishi Y, Morozumi S, Yoshinaga H., *Scripta Materialia* **16**, 427 (1986).
43. Morris J.R, Ho K.M, Turner D.E, Ye Y.Y, Yoo M.H, *Phil. Mag., A* **76**, (1997).
44. Ward Flynn P, Mote J, Dorn J.E, *Trans. metall. Soc. AIME,* , 1148 (1961).
45. Couret A, Caillard D, *Acta Materialia* **33**, 1447 (1985).
46. S. Morozumi, M. Kikuchi, H. Yoshinaga, Electron microscope observation in and around f11 0 2g twins in magnesium. *Trans. JIM* **17**, 158 (1976).
47. S.R. Agnew, O. Duygulu, Plastic Anisotropy and the Role of Non-basal Slip in Magnesium Alloy AZ31. *Inter. J. Plasticity* **21**, 1161 (2005).
48. Y.T. Zhu *et al.*, Formation of single and multiple deformation twins in nanocrystalline fcc metals. *Acta Materialia* **57**, 3763 (2009).
49. XL Wu et al., Deformation twinning in a nanocrystalline hcp Mg alloy. *Scripta Materialia* **64**, 213 (2011).
50. Q. Yu *et al.*, Strong crystal size effect on deformation twinning. *Nature* **463**, 335.
51. E. Lilleodden, Microcompression study of Mg (0001) single crystal. . *Scripta Materialia,* **62**, 532 (2010).
52. Cynthia M Byer, Bin Li, Buyang Cao, K T Ramesh, Microcompression of single-crystal magnesium. *Scripta Materialia* **62**, 536 (2010).

53. J. Ye, R. K. Mishra, A. K. Sachdev, A. M. Minor, In situ TEM compression testing of Mg and Mg–0.2 wt.% Ce single crystals. *Scripta Materialia* **64**, 292 (2010).
54. Kelley E.W, Hosford Jr. W.F, *Trans. metall. Soc. AIME,* , 654 (1968).
55. Hirth J P, Lothe J, *Theory of dislocations. New York: McGraw-Hill,* , (1968).
56. O. Kraft, P. A. Gruber, R. Monig, D. Weygand, in *Annual Review of Materials Research, Vol 40*. (Annual Reviews, Palo Alto, 2010), vol. 40, pp. 293-317.
57. Allison Kunz, Siddhartha Pathak, Julia R. Greer, Size effects in Al nanopillars: Single crystalline vs. bicrystalline. *Acta Materialia* **59**, 4416 (2011).
58. M. Dietiker, S. Buzzi, G. Pigozzi, J.F. Lo¨ffler b, R. Spolenak, Deformation behavior of gold nano-pillars prepared by nanoimprinting and focused ion-beam milling. *Acta Materialia* **59**, 2180 (2011).
59. H. Bei, S. Shim, E.P. George, Compressive strengths of molybdenum alloy micro-pillars prepared using a new technique. *Scripta Materialia* **57**, (2007).
60. Qiaoyan Sun *et al.*, Size effects in strength and plasticity of single-crystalline titanium micropillars with prismatic slip orientation. *Scripta Materialia*, (2011).
61. M. D. Uchic, D. M. Dimiduk, J. N. Florando, W. D. Nix, Sample dimensions influence strength and crystal plasticity. *Science* **305**, 986 (2004).
62. David. B. Williams, C. Barry Carter, Transmission Electron Microscopy - A Textbook for Materials Science *Plenum Press.*, (1996).
63. Andrew M. Minor, S. A. Syed Asif, Zhiwei Shan, Eric A. Stach, Edward Cyrankowski, *Nature Materials* **5**, 697 (2006).
64. Z. W. Shan, R. Mishra, S. A. Syed, O. L. Warren, A. M. Minor, *Nature Materials* **7**, 115 (2008).
65. D. Kiener, A. M. Minor, In situ Tensile testing .. . .. (submitted).
66. M. R. Barnett, Twinning and the ductility of magnesium alloys. Part I: "Tension" twins; Part II: "Contraction" twins. *Materials Science and Engineering A* **464**, 1 (Aug, 2007).
67. J. KOIKE, Enhanced Deformation Mechanisms by Anisotropic Plasticity in Polycrystalline Mg Alloys at Room Temperature. *Metallurgical and Materials Transactions a-Physical Metallurgy and Materials Science* **36A**, (2005).
68. G. Frommeyer, U. Brux, P. Neumann, Supra-ductile and high-strength manganese-TRIP/TWIP steels for high energy absorption purposes. *Isij International* **43**, 438 (2003).
69. O. Bouaziz, S. Allain, C. Scott, Effect of grain and twin boundaries on the hardening mechanisms of twinning-induced plasticity steels. *Scripta Materialia* **58**, 484 (Mar, 2008).
70. T. Zhu, J. Li, A. Samanta, H. G. Kim, S. Suresh, Interfacial plasticity governs strain rate sensitivity and ductility in nanostructured metals. *PNAS* **104**, 3031 (Feb, 2007).
71. W.M. Gan *et al.*, Microstructure and tensile property of the ECAPed pure magnesium. *Journal of Alloys and Coompounds* **470**, 256 (2009).
72. H. Miura, T. Sakai, Orientation dependence of ductility of Mg single crystals at elevated temperature. *Materials Science Forum* **488-489**, (2005).
73. K. Lu, L. Lu, S. Suresh, Strengthening Materials by Engineering Coherent Internal Boundaries at the Nanoscale. *Science* **324**, 349 (2009).

74. Triplicane A. Parthasarathy, Satish I. Rao, Dennis M. Dimiduk, Michael D. Uchic, Dallas R. Trinkleb, Contribution to size effect of yield strength from the stochastics of dislocation source lengths in finite samples. *Scripta Materialia* **56**, 313 (2007).
75. B. C. De Cooman et al., state of the science of high manganese TWIP steels for automotive applications, . *microstructure and texture in steels* 165 (2009).
76. Xiang-Yang Liu, James B Adamsy, Furio Ercolessiz, J. A. Moriarty, EAM potential for magnesium from quantum mechanical forces. *Modelling Simul. Mater. Sci. Eng* **4**, 293 (1996).
77. Bringa.E.M *et al.*, Fivefold twin formation during annealing of nanocrystalline Cu. *Scripta Materialia* **59**, 1267 (2008).
78. T. Zhu, J. Li, A. Samanta, A. Leach, K. Gall, Temperature and strain-rate dependence of surface dislocation nucleation. *Phys. Rev. Lett.* **100**, (2008).
79. E.M. Bringa, *Scripta Materialia* **59**, 1267 (2008).
80. K. Reimann, R. Würschum, *J. Appl. Phys.* **81**, 7186 (1997).
81. Qian Yu *et al.*, The Nanostructured Origin of Deformation Twinning. *Nano Letters* **12**, 887 (2012).
82. Qian Yu, Liang Qi, Raja K. Mishra, Ju Li, Andrew M. Minor, Reduction of CRSS anisotroy with size in Mg. *submitted*, (2012).
83. Frederic Sansoz, Atomistic processes controlling flow stress scaling during compression of nanoscale face-centered-cubic crystals. *Acta Materialia* **59**, 3364 (2011).
84. J. Koike *et al.*, The activity of non-basal slip systems and dynamic recovery at room temperature in fine-grained AZ31B magnesium alloys. *Acta Materialia* **51**, 2055 (2003).
85. A. S. Argon, Physics of Strength and Plasticity. *The MIT Press Classics Series*, (1969).
86. Robert O. Ritchie, The conflicts between strength and toughness. *Nature Material* **10**, 817 (2011).
87. Sidney Yip, Mapping Plasticity. *Nature Material* **3**, 11 (2004).
88. S. Yip, Nanocrystals - the strongest size. *Nature* **391**, 532 (1998).
89. G. A. Malygin, Plasticity and Strength of Micro- and Nanocrystalline Materials. *Physics of The Solid State* **49**, 1013 (2007).
90. M.A. Meyers, A. Mishra, D.J. Benson, Mechanical properties of nanocrystalline materials. *Progress in Materials Science* **51**, 427 (2006).
91. C.E. Carlton, P.J. Ferreira, What is behind the inverse Hall–Petch effect in nanocrystalline materials? *Acta Materialia* **55**, 3749 (2007).
92. M.R.Barnett, D.L.Atwell, A.G.Beer, Grain size in Mg alloys: recrystallization and mechanical consequences. *Materials Science Forum Vols* **558**, 433 (2007).
93. Pavel Lukáč, Z. Trojanová, Influence of grain size on ductility of magnesium alloys. *Materials Engineering - Materiálové inžinierstvo* **18**, 111 (2011).
94. Pavel Lukáč, Zuzanka Trojanová, The Effect of Grain Size on the Deformation Behaviour of Selected Mg Alloys. *Materials Science Forum Vols* **567**, 85 (2008).
95. S. I. H. W.J. Kim, Y.S. Kim, S.H. Min, H.T. Jeong,, J. D. Lee, Mg alloy fabricated by equal channel angular pressing. *Acta Materialia* **51**, 3293 (2003).
96. J. R. Rice, Dislocation nucleation from a crack tip: an analysis based on the Peierls concept. . .*J.Mech. Phys. Solids* **40**, 239 (1992).

97. Frost HJ, A. MF., Deformation-mechanismmap. *Oxford:PergamonPress*, (1982).
98. R.Ohyama, J. Koike, T. Kobayashi, M. Suzuki, K. Maruyama, *Materials Science Forum* **419**, 237 (2003).
99. Hidetoshi Somekawa, Toshiji Mukai, Effect of grain boundary structures on grain boundary sliding in magnesium. *Materials Letters* **76**, 32 (2012).
100. F. E. Hauser, P. R. Landon, J. E. Dorn, *Trans. ASM* **48**, 986 (1956).
101. F. E. Hauser, C. D. Starr, L. Tietz, J. E. Dorn, *Trans. ASM* **47**, 102 (1955).
102. R. C. Gifkins，, T. G. Langdon，, *J. Inst. Metals* **93**, 347 (1964).
103. J.A. DEL VALLE, M.T. PÉREZ-PRADO, O.A. RUANO, Deformation Mechanisms Responsible for the High Ductility in a Mg AZ31 Alloy Analyzed by Electron Backscattered Diffraction. *Metallurgical and Materials Transactions A* **36A**, 1427 (2005).
104. W.J. Kim, S.J. Yoo, Z.H. Chen, H.T. Jeong, ain size and texture control of Mg–3Al–1Zn alloy sheet using a combination of equal-channel angular rolling and high-speed-ratio differential speed-rolling processes. *Scripta Materialia* **60**, 897 (2009).
105. S.R. Agnew, J.A. Horton, T.M. Lillo, D.W. Brown, Enhanced ductility in strongly ... produced by equal channel angular processing. *Scripta Materialia* **50**, 377 (2004).
106. Atsutomo Nakamura, Eita Tochigi, Naoya Shibata, Takahisa Yamamoto, Yuichi Ikuhara, Structure and Configuration of Boundary Dislocations on Low Angle Tilt Grain Boundaries in Alumina. *Materials Transactions* **50**, 1008 (2009).
107. H. Ichinose, Y. Ishida, N. Baba, K. Kanaya, *Philos. Mag. A* **52**, 51 (1985).
108. A. G. Crocker, B. A. Faridi, *Acta Materialia* **Acta28**, 549 (1980).
109. Kumar KS, Suresh S, Chisholm MF, Horton JA, W. P., *Acta Materialia* **51**, 387 (2003).
110. K.S. Kumar, H. Van Swygenhoven, S. Suresh, Mechanical behavior of nanocrystalline metals and alloys. *Acta Materialia* **51**, 5743 (2003).
111. M.F. Ashby, R.A. Verrall, *Acta Materialia* **21**, 149 (1971).
112. W.A. Rachinger, *J. Institute of Metals* **81**, 33 (1952).
113. M. S. Daw，, M. I. Baskes, *Phys. Rev. Lett.* **50**, 1285 (1983).
114. M.J. Mayo, W.D. Nix, *Acta Metallurgica* **37**, 1121 (1989).
115. D. Lee, *Metall. Trans. A,* **1**, 309 (1970).
116. R. N. Stevens, Grain-Boundary Sliding in Metals. *Metallurgical Reviews* **11**, 129 (1966).
117. J. INTRATER，, E. MACHLIN, *J. Inst. Metals* **88**, 305 (1959－1960).
118. J. Weertman, High temperature creep produced bydislocation motion. *J.C.M. Li and A.K. Mukherjee, eds., Rate Processes in Plastic Deformation, Amer. Soc. for Metals, Metals Park, OH, 315.*, (1975).
119. William D. Nix, Merrilea J. Mayo, A Model for Superplasticity not Controlled By Grain Boundary Sliding. *imechanica.org*, (2006).
120. J.R. Spingarn, W.D. Nix, *Acta Materialia* **27**, 171 (1979).
121. G.B. Viswanathan, V. K. Vasudevan，, M.J. Mills, *Acta Materialia* **47**, 1399 (1999)